Multi-Axis Analog Adaptive Feedforward Cancellation of Cryocooler Vibration

by

Simon Andrew Collins

B.A.Sc. University of Toronto (1988)
S.M. Massachusetts Institute of Technology (1990)

SUBMITTED TO THE DEPARTMENT OF
AERONAUTICS AND ASTRONAUTICS
IN PARTIAL FULFILLMENT OF THE REQUIREMENTS
FOR THE DEGREE OF
Doctor of Philosophy
at the
Massachusetts Institute of Technology
May, 1994

Signature of Author _____
Department of Aeronautics and Astronautics
April 8, 1994

Certified by _____
Prof. James D. Paduano
Thesis Supervisor, Assistant Professor of Aeronautics and Astronautics

Certified by _____
Prof. Andreas H. von Flotow
Adjunct Professor of Aeronautics, University of Washington

Certified by _____
Prof. Nesbitt W. Hagood IV
Assistant Professor of Aeronautics and Astronautics

Certified by _____
Dr. David W. Miller
Principal Research Scientist, Department of Aeronautics and Astronautics

Certified by _____
Dr. James L. Fanson
Jet Propulsion Laboratory, California Institute of Technology

Accepted by _____
Prof. Harold Y. Wachman
Chairman, Department Graduate Committee

Multi-Axis Analog Adaptive Feedforward Cancellation of Cryocooler Vibration

by

Simon Andrew Collins

Submitted to the Department of Aeronautics and Astronautics
on April 8, 1994, in partial fulfillment of the
requirements for the degree of
Doctor of Philosophy

Abstract

The vibration produced by Stirling cryocoolers is incompatible with spacecraft-borne precision-pointing imaging instruments. Thermal considerations prevent the addition of sufficient mechanical isolation to eliminate the effects of this vibration. The objective of this research is the design, analysis, and experimental verification of a multi-axis vibration cancellation system for the expander of a split Stirling cryocooler.

Cancellation of the periodic cryocooler vibration is achieved with a set of load cells, a custom three-axis electrodynamic actuator, and a narrowband adaptive feedforward controller. In order to size the actuator, a simple model of the cryocooler's vibration is combined with a first-order analysis of a four-magnet two-return-plate forcing element. While the resulting actuator has sufficient force capability, it exhibits significant nonlinearity A nonlinear actuator model is developed that accounts for in-plane flexure restraint due to both large-amplitude static deflections and large-amplitude vibrations. Numerical solutions of the nonlinear model accurately reflect jump phenomena and higher harmonics observed in the actuator's response.

The adaptive feedforward controller employs the filtered-x least-mean-square (FXLMS) algorithm to update an adaptive filter. Rather than implementing this filter with a digital signal processor (DSP), for which there is little flight heritage, a continuous-time analog realization of the FXLMS filter is selected. Theoretically, the FXLMS filter may be represented by an equivalent linear transfer function. However a comprehensive treatment of factors associated with the actual implementation reveals the limitations of the transfer function representation. Factors such as harmonic distortion of the reference signal and imperfect quadrature are shown to result in frequency-shifted terms in the filter's output. The presence of these output components is confirmed experimentally, and their effect on performance is illustrated.

Multi-axis, multi-harmonic vibration cancellation is successfully demonstrated using independent two-weight FXLMS filters. Some cross-axis coupling is observed due to the actuator's off-diagonal response. Despite this, approximately 30 dB of axial cancellation and 20 dB of lateral cancellation are simultaneously achieved. This vibration cancellation system provides high levels of performance without the cost or complexity of DSP-based systems.

Thesis Committee: Prof. James D. Paduano, Thesis Supervisor
Assistant Professor of Aeronautics and Astronautics

Prof. Andreas H. von Flotow
Adjunct Professor of Aeronautics, University of Washington

Prof. Nesbitt W. Hagood IV
Assistant Professor of Aeronautics and Astronautics

Dr. David W. Miller
Principal Research Scientist, Department of Aeronautics and Astronautics

Dr. James L. Fanson
Member of Technical Staff, Jet Propulsion Laboratory, California Institute of Technology

Dedicated to the memory of

Attilio Vivian

and

Frank van Humbeck

Acknowledgments

At this time I would like to thank all those who have acted as my thesis supervisor. Prof. Andy von Flotow deserves special mention for serving as my technical supervisor, and much of the work presented in this thesis may be traced back to discussions at his blackboard. Dr. Sandy Alexander also helped get the project going, especially the analog implementation of the controller. Prof. Jim Paduano guided this work through its final stages and posed many thought-provoking questions, directing me to research areas I might have otherwise left unexplored.

The assistance of many people at JPL must be acknowledged. Dr. Jim Fanson, in addition to serving on my thesis committee, helped arrange two summers of research at JPL which led directly to the work presented in this thesis. During those summers, I worked under Dr. Ron Ross, who was most helpful and also suggested a number of changes to my actuator design. Dr. Dean Johnson and all the other members of Dr. Ross's group made those summers particularly enjoyable, greatly easing my entry into the world of cryogenics.

All the members of the SERC lab contributed to its unique personality, making it a pleasure to work there. Many thanks to all those who helped me in the lab and in the computer room. Victor Owuor deserves particular recognition for fabricating the controllers and making the measurements of the actuator's nonlinearity.

Finally, I'd like to thank all the members of my family. My parents always provided me with wonderful educational opportunities—they deserve much of the credit for who I am today. And of course Lisa has been a constant source of support. She had much more faith in my ability than I ever did, and was always there with encouragement whenever I needed it. I have devoted much of my time over the last several years to work; Lisa's tolerance of that has never received enough recognition, but it is greatly appreciated.

Contents

1 Introduction **17**
- 1.1 Cryocooler Vibration Reduction . . . 18
- 1.2 Thesis Overview . . . 24

2 Vibration Reduction Systems **27**
- 2.1 System Architecture . . . 27
  - 2.1.1 Noise Source . . . 30
  - 2.1.2 Vibration Reduction System . . . 45
- 2.2 Sensor Selection . . . 46
- 2.3 Actuator Selection . . . 47
  - 2.3.1 Electromagnetic Forcers . . . 47
  - 2.3.2 Electrodynamic Forcers . . . 48
  - 2.3.3 Piezotranslators . . . 49
- 2.4 Summary . . . 50

3 Multi-Axis Electrodynamic Actuator **51**
- 3.1 Magnetic Design . . . 52
  - 3.1.1 Magnetic Circuit Analysis . . . 53
  - 3.1.2 Coil Trade-Offs . . . 58
- 3.2 Mechanical Design . . . 60
  - 3.2.1 Configuration . . . 61
  - 3.2.2 Performance Evaluation . . . 65
  - 3.2.3 Dynamics . . . 67
  - 3.2.4 Flexures . . . 69
- 3.3 Drive Electronics . . . 73
  - 3.3.1 Coordinate Transformations . . . 74
  - 3.3.2 Power Amplifiers . . . 77
- 3.4 Measured Performance . . . 79
- 3.5 Summary . . . 84

4 Nonlinear Actuator Dynamics **85**
- 4.1 Initial Observations . . . 86
- 4.2 Nonlinear Vibration Analysis . . . 89
- 4.3 Steady-State Solutions . . . 101
  - 4.3.1 Simple Harmonic Motion . . . 104

4.3.2 Two-Harmonic Motion . . . 111
4.3.3 Three-Harmonic Motion . . . 115
4.4 Higher-Order Transfer Functions . . . 118
4.5 Effect on Linear Cancellation . . . 124
4.6 Summary . . . 128

5 Controller Design and Realization **131**
5.1 Adaptive Feedforward Disturbance Rejection . . . 131
5.1.1 Stochastic Disturbance Rejection . . . 132
5.1.2 Harmonic Disturbance Rejection . . . 135
5.2 Factors Affecting Performance . . . 141
5.2.1 Imperfect Quadrature . . . 142
5.2.2 Leaky Integrator . . . 144
5.2.3 Integration Bias Error . . . 146
5.2.4 Noisy Reference Signal . . . 146
5.2.5 Periodic Reference Signal . . . 147
5.2.6 Plant Modes . . . 149
5.3 Implementation . . . 151
5.3.1 Reference Signal . . . 151
5.3.2 Quadrature Filters . . . 153
5.3.3 Multipliers and Integrators . . . 154
5.4 Measured Performance . . . 157
5.4.1 Reference Signal . . . 157
5.4.2 LMS Input-Output Behavior . . . 158
5.4.3 Imperfect Quadrature . . . 162
5.4.4 Periodic Reference Signal . . . 163
5.5 Summary . . . 165

6 Cancellation System Performance **167**
6.1 Fixed Filters . . . 167
6.1.1 Error Filters . . . 168
6.1.2 Compensation Filters . . . 170
6.2 Loop Transfer Functions . . . 174
6.3 Single-Axis Cancellation . . . 176
6.3.1 Axial Cancellation . . . 176
6.3.2 Lateral Cancellation . . . 183
6.3.3 Transient Response . . . 185
6.3.4 Frequency-Tracking Cancellation . . . 190
6.4 Multi-Axis Cancellation . . . 192
6.5 Summary . . . 196

7 Conclusions **199**
7.1 Summary . . . 199
7.2 Conclusions and Contributions . . . 201
7.3 Recommendations . . . 209

List of Figures

1-1 Vibration levels for the BAe 80K cooler 21
1-2 Open- and closed-loop vibration levels of the BAe 80K compressor . 23

2-1 AIRS block diagram 29
2-2 Axial force spectra. (a) BAe 80K expander; (b) Hughes expander . 32
2-3 Time trace of axial force generated by Hughes expander 33
2-4 Single-degree-of-freedom expander model 34
2-5 Bumper-limited stroke of displacer in Hughes expander 36
2-6 Computed axial force spectrum for Hughes expander 38
2-7 Effect of drive frequency on harmonic amplitudes 39
2-8 Coordinate axes for expander vibration measurements 43
2-9 Typical vibration levels generated by the expander 44

3-1 Cross-section of a four-magnet two-return-plate forcing unit 53
3-2 B–H curve for a typical permanent-magnet material 56
3-3 Layout and cross-section of the multi-axis actuator 63
3-4 Photograph of the multi-axis actuator 64
3-5 Current and voltage required to generate specified force levels for various coil wire gauges 67
3-6 Single degree-of-freedom model of the forcer dynamics 68
3-7 Transmissibility as a function of the normalized frequency 70
3-8 Block diagram of cancellation system 75
3-9 Functional elements of a variable-gain summer 76
3-10 Variable-gain summer circuits 76
3-11 Voltage-controlled current-source circuit 78
3-12 Actuator MIMO transfer function in local coordinates 81
3-13 Actuator MIMO transfer function in global coordinates 83

4-1 Two-flexure actuator model and effect of various loadings 87
4-2 One- and two-flexure actuator models with distributed and concentrated loads 90
4-3 Nondimensional mid-span static deflection as a function of the system's mass ratio 97
4-4 Linear natural frequency as a function of the system's mass ratio . . 98
4-5 Parameters α_i in Duffing's equation as a function of the system's mass ratio 100

4-6 Backbones of Duffing's equation 106
4-7 Forced response of the undamped symmetric and asymmetric systems 108
4-8 Geometric derivation of the frequency response 109
4-9 Forced response of the undamped asymmetric system with the second harmonic 112
4-10 Forced response of the undamped asymmetric system with the third harmonic 114
4-11 Stable forced response of the damped asymmetric system 116
4-12 Estimated and measured higher-order transfer function 121
4-13 Duffing forced response 123

5-1 Adaptive feedforward disturbance rejection 132
5-2 Adaptive feedforward disturbance rejection with the filtered-x LMS algorithm 135
5-3 Two-weight continuous-time filtered-x LMS adaptive feedforward disturbance rejection 136
5-4 Geometric interpretation of $1 + e^{j2\theta_q} = \beta e^{j\theta_q}$ 142
5-5 Bode plot for leaky FXLMS controller and second-order plant . . . 150
5-6 Functional block diagram of the reference-signal generation network 152
5-7 Circuit diagram for a noninverting unity-gain allpass filter 153
5-8 Circuit diagram for the leaky integrator 156
5-9 Spectrum of the second-harmonic reference signal 157
5-10 Bandpass filter used to extract the second-harmonic reference signal 159
5-11 Harmonic amplitudes in the second-harmonic reference signal 159
5-12 Adaptive filter output with a sinusoidal reference signal 160
5-13 Adaptive filter's transfer function with a sinusoidal reference signal 161
5-14 Ratio of nonlinear component gain to linear component gain 162
5-15 Adaptive filter output with a triangular reference signal 163
5-16 Adaptive filter's transfer function with a triangular reference signal 164

6-1 Error signals caused by cryocooler vibration 169
6-2 Error-filter transfer function 170
6-3 Effect of error filters on open-loop error signals 171
6-4 Axial compensation-filter transfer function 172
6-5 Plant transfer-function matrix including cancellation filters and error filters 173
6-6 Axial loop transfer functions 175
6-7 M_x loop transfer function with first-harmonic controller 175
6-8 Open- and closed-loop axial vibration spectra with the third-harmonic axial controller 177
6-9 Open- and closed-loop vibration spectra with five axial controllers . 180
6-10 Ratios of lateral to axial actuator output in response to a commanded axial force 181
6-11 Open- and closed-loop lateral vibration spectra with five axial controllers, with actuator-generated torques 182

6-12 Open- and closed-loop lateral vibration spectra with first-harmonic lateral controllers 183
6-13 Open- and closed-loop F_z and M_x vibration spectra with a first-harmonic M_x controller 184
6-14 Open- and closed-loop disturbance-to-output transfer function . . . 185
6-15 Transient response of the first-harmonic axial adaptive filter to a step 186
6-16 Transient response of the first-harmonic axial adaptive filter to a ramp 188
6-17 Transient response of the first-harmonic axial adaptive filter to rapid drive-voltage changes 188
6-18 Transient response of the first-harmonic M_x adaptive filter at a low drive frequency 189
6-19 Transient response of the first-harmonic M_x adaptive filter at a high drive frequency 190
6-20 Axial and lateral cancellation achieved at the first four harmonics as a function of drive frequency 191
6-21 Open- and closed-loop vibration spectra with five axial controllers and two lateral controllers 194
6-22 Open- and closed-loop vibration spectra with third-harmonic controllers 195

List of Tables

3.1 Magnetic properties 58
3.2 Flexure design trades 72

5.1 Comparison of analog multiplier ICs 155
5.2 Harmonic content of the reference signal 164

6.1 Axial cancellation levels achieved with a single axial controller 178
6.2 Lateral cancellation levels achieved with a single axial controller . . . 178
6.3 Axial cancellation levels achieved with multiple axial controllers . . . 179
6.4 Lateral cancellation levels achieved with multiple axial controllers . . 179
6.5 Cancellation levels achieved with multiple controllers on multiple axes 192
6.6 Cancellation levels achieved with third-harmonic controllers on multiple axes 193

Chapter 1

Introduction

The increasing demand for long-wavelength infrared (IR) imaging instruments on scientific spacecraft and the development of the long-life Oxford-type Stirling cooler has resulted in a great deal of interest in mechanical cryocoolers. This has included a recognition of the unique requirements associated with spacecraft-borne instruments. The most difficult requirement for cryogenic refrigerators to meet has been that of long operational lifetimes with very high reliabilities. However, when the cryocooler is to be used with a precision-pointing imaging instrument, there are also very stringent limits on the cooler-generated vibration. The objective of this thesis is to develop and demonstrate a novel vibration reduction system for cryocoolers.

The predominant source of vibration in these coolers is the Stirling cycle itself: cooling is achieved through the controlled motion of mechanical elements (a piston and a displacer) to compress and then expand a working fluid. The linearly reciprocating motion of these elements gives rise to a momentum imbalance. Although the piston is typically driven with a sinusoidal signal, it oscillates against the nonlinear gas spring of the compression space, resulting in a nonsinusoidal piston motion. This manifests itself in the cooler-generated vibration through the presence of harmonics of the piston's drive frequency.

A variety of techniques are being investigated for cryocooler vibration reduction. Examples include passive vibration isolation, drive-signal conditioning, active vibration cancellation, and active control of coldfinger deformation. Most of these systems

are designed to reduce the axial component of the cooler's vibration; impressive levels of performance have been demonstrated on rigid foundations. In general, these reduction systems have had little effect on the other vibration components, preventing several coolers from meeting the specifications associated with particular instruments.

The high-performance systems invariably rely on closed-loop control. Indeed, it is informative to view cryocooler vibration reduction as an application of closed-loop disturbance rejection; the periodic nature of the vibration encourages the use of narrowband techniques. Narrowband disturbance rejection has received considerable attention in fields such as active vibration isolation, active control of sound, and helicopter vibration reduction. The analytical techniques and the implementation experience developed in these applications are of direct utility to the cryocooler community.

After reviewing the work to date on cryocooler vibration reduction, a brief overview of the thesis will be presented.

1.1 Cryocooler Vibration Reduction

The primary purpose of a cryocooler is to provide sufficient cooling power at a specified temperature to a heat load; the required input power to the cooler should also be minimized. While vibration is a secondary characteristic of the cryocooler, its importance should not be underestimated. It can be a decisive factor during initial trade studies, especially for imaging-instrument applications. For example, Stirling coolers were eliminated from consideration for a second-generation Hubble Space Telescope instrument (the Near-Infrared Camera and Multi-Object Spectrometer) due in large part to the unacceptable cryocooler-induced vibration levels [1].

Burt [2] listed four major effects of vibration on state-of-the-art detectors: motion of pixels resulting in image smearing; motion of signal wires in electromagnetic fields resulting in induced currents; frictional effects of signal-lead motion resulting in triboelectric charge generation; and microstress-induced piezoresitive voltages in certain detector materials. The relative significance of these effects depends on many

application-specific details. However, a sense of scale may be gained by noting that a typical pixel size is 50×50 μm, while inter-pixel spacing ranges from 0.25 μm to 10 μm [2]. In order to limit detector motion to less than 5 μm, force levels on the order of 0.2 N are considered acceptable [3].

Of course, the cooler-induced vibration is strongly dependent on the cryocooler design. A broad range of Stirling coolers have been proposed for spacecraft-borne applications, with uncompensated peak vibration levels ranging from less than 5 N for a Texas Instruments 1/5-W 80K cryocooler [4] to over 400 N for a Philips 5-W 65K cryocooler [5].

Some of the cooler-induced vibration may be prevented from reaching the detectors with thoughtful design of the cryosystem. If a split Stirling coolers is used, it might be possible to mount the compressor on a separate structure, isolating it from the detectors. This could, however, prove challenging on a microsat due to the compact size of the spacecraft [6].

The cryocooler expander cannot be isolated in the same way, since a highly conductive path is required between the cooler's coldfinger and the detectors. In order to avoid placing appreciable side loads on the coldfinger, the thermal link typically consists of bundles of thin copper wire [7] or layers of copper foil [8]. Research is being conducted on characterizing and improving the vibration transmission properties of these thermal links [9].

A number of modifications have been made to the design of the cryocooler itself in order to improve its reliability and its vibration characteristics. For example, in one of the first spacecraft-borne applications of cryocoolers, four Stirling coolers provided cooling for two gamma ray spectrometers aboard the P-78-1 spacecraft, launched in February 1979 [10]. The coolers were developed by the Philips Laboratories and used a rhombic drive mechanism, which established the correct phase relationship between the piston and the displacer and used counter-rotating weights for dynamic balancing. The resulting motion at the cold tip was less than 4 μm [11]. However this drive mechanism was abandoned because of performance degradation due to leakage and contamination of the working fluid after less than 1000 hours of operation.

Lifetimes in excess of 2000 hours were achieved with rotary-drive coolers [12]. The vibration produced by these coolers could be tolerated by employing a split configuartion, in which the compressor and the expander are housed in separate modules. The noisy compressor could then be removed from the vicinity of the sensitive detector.

Further lifetime gains were made by replacing the rotary drive with a linear motor. The compressor vibration may then be reduced by using a dual opposed piston design, in which a pair of pistons operate on a common compression space [13]. It appears, however, that other design modifications arising from the use of linear motors have increased the vibration generated by the expander [14]. There are few examples of the expander using dual opposed displacers for dynamic balancing [15].

Most of the mature Stirling cooler designs consist of a single-piston compressor and a single-displacer expander. These coolers may be dynamically balanced by operating two back-to-back units 180 degrees out of phase. This is typically achieved by using position feedback and common drive electronics for the two units. Ellis *et al.* [16] discuss an infrared instrument at the Kitt Peak National Observatory that is cooled by a pair of back-to-back expanders; in conjunction with passive isolation, this arrangement reduces the cooler-induced vibration by almost 60 dB. The Improved Stratospheric and Mesopheric Sounder aboard the Upper Atmosphere Research Satellite uses a pair of 80K Stirling coolers developed by Oxford University [17]. Both the expanders and compressors are mounted as balanced pairs, which reduced the compressor-induced vibration by 40 dB [7].

The Oxford cooler was subsequently commercialized by British Aerospace (BAe). Ross *et al.* [18,19] have conducted a detailed characterization of the BAe 80K cooler's vibration. They demonstrated that, while the back-to-back arrangement significantly reduced the axial and lateral RMS vibration levels [18], it was not successful at cancelling the higher harmonics, as shown in Figure 1-1 [19]. The higher harmonics exceeded the vibration specifications for the next generation of cryogenically-cooled instruments [18].

Hopkins *et al.* [1] provide several additional examples of the use of back-to-back coolers. They also note some of the problems with this arrangement. Quite often,

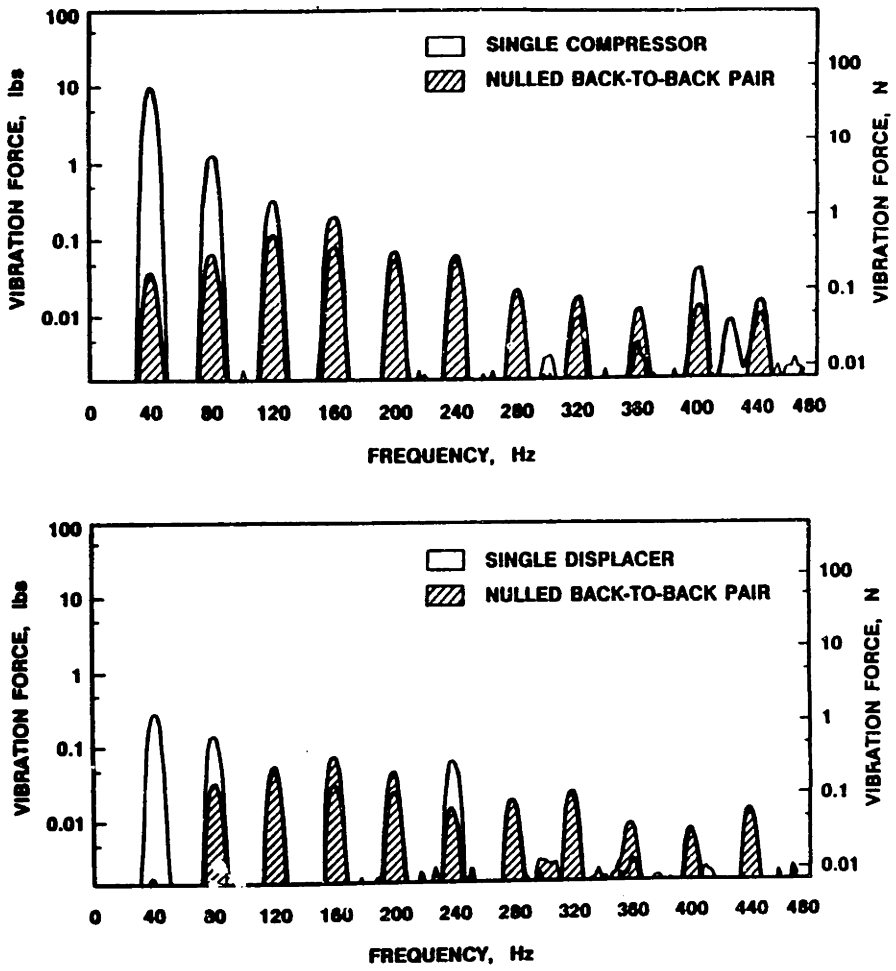

Figure 1-1: Compressor- and displacer-generated vibration levels for the BAe 80K cooler. Shown for single and back-to-back units. From Reference [19].

the second cooler's only purpose is vibration reduction; a single cooler can satisfy the thermal requirements. While the pair of coolers are dynamically well-matched, they require significant levels of input power, making this a rather inefficient approach to vibration cancellation. Furthermore, redundancy is not improved by using two coolers, since the subsequent failure of a single cooler eliminates the benefits of the balanced pair. For this reason, the cryogenic subsystem of the AXAF X-Ray Spectrometer includes *four* Stirling coolers.

Rather than using a pair of coolers, many designs include a passive counterbalance. Examples range from a 1/4-W 85K tactical cooler [20] to an enormous 150-W 90K industrial cooler [21]. While smaller than a second cooler, the counterbalance can still add considerable mass to the system. For example, the counterbalance assembly

for a 36-kg triple-expansion Stirling cooler weighed 17 kg [22]. The counterbalance is typically a tuned mass/spring system that is designed to cancel the axial vibration at the cooler's drive frequency.

A thorough description of one such system may be found in Reference [5]. The counterbalance in this case consisted of a 3.0-kg moving mass on leaf springs with a measured damping ratio of 0.14%, while the 63-kg cooler included a 1.9-kg piston and a 0.4-kg displacer. Stolfi *et al.* demonstrated 25 dB of cancellation at the fundamental; the vibration at the second and third harmonics was modified by less than 2 dB. These results rely on operating the cooler at the natural frequency of the counterbalance assembly. Unfortunately, the counterbalance dynamics and the mass of the cooler also interact to create an additional resonance, at which the cooler's vibration is strongly amplified. These two frequencies were separated by only 0.5 Hz for this cooler, necessitating careful tuning of the counterbalance's moving mass.

It was often noted that the counterbalance could be used to cancel the higher harmonics if a linear actuator and a control system were added to the reaction mass [13]. The cooler itself already featured drive electronics, actuators, and position sensors in order to maintain the desired phase relationship between the piston and the displacer, so several researchers attempted to eliminate the higher harmonics by using position feedback to enforce sinusoidal motion of the moving components [5,22]. This was not very successful; much better results were achieved with force feedback.

The higher harmonics of the BAe 80K cooler were successfully reduced using force feedback [23, 24]. In these tests, a digital signal processor (DSP) was used to implement a classical narrowband disturbance rejection scheme, which modified the cooler's drive signal. Johnson *et al.* [23] eliminated five of the compressor's higher harmonics in this way, demonstrating up to 50 dB of cancellation. Jones and Scull [24] reduced the compressor's higher harmonics to less than 0.2 N and the expander's harmonics to less than 0.05 N.

The self-cancellation scheme is not able to cancel the fundamental component—this component is providing the cooling action. Aubrun *et al.* [25] combined a back-to-back cooler pair with a force feedback system to cancel both the fundamental

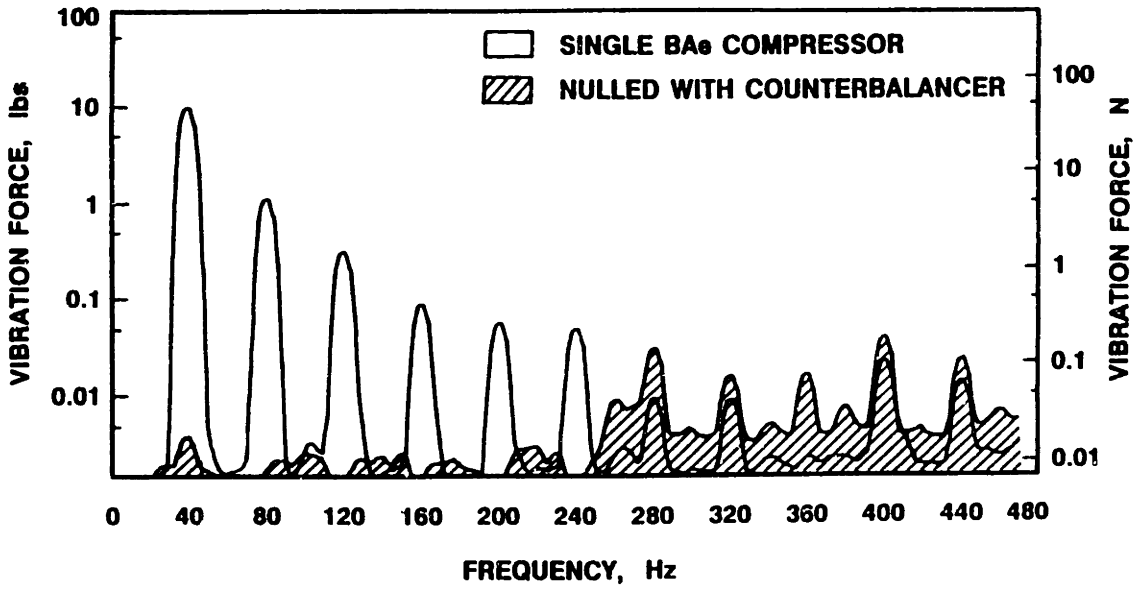

Figure 1-2: Open- and closed-loop vibration levels of the BAe 80K compressor. From Reference [27].

and the higher harmonics. The compressor's RMS axial vibration was reduced by almost 60 dB, although the lateral vibration was basically unaffected. The expander exhibited more coupling between the axes: the axial vibration was reduced by 54 dB, the axial torque was reduced by 26 dB, and the lateral force was reduced by 11 dB. The difference between the effect on the compressor and on the expander might be due to the fact that the compressor dynamics are determined primarily by the gas dynamics, whereas the expander dynamics are dominated by the displacer-supporting flexures [26] and the control system is modifying the displacer's motion.

The ability to cancel the fundamental and the higher harmonics has also been demonstrated using force feedback and an active counterbalance [27,28]. The control system is the same as for self-cancellation, however, the control signal drives a reaction mass rather than modifying the cooler's drive signal. Typical results are shown in Figure 1-2 [27]; the effect on the lateral vibration was not reported. Wu [29] has also proposed an adaptive feedforward technique to control the reaction mass.

There has also been some research on coldfinger motion. Even when the cryocooler is rigidly mounted, the thin-walled coldfinger experiences displacements in all three dimensions on the order of microns [4, 19]. Glaser *et al.* [4] describe two systems

based on piezoelectric actuators and adaptive feedforward controllers designed to suppress the coldfinger motion; preliminary results [30] indicate that the fundamental component is practically eliminated, although significant higher harmonic content remains.

1.2 Thesis Overview

In this thesis, a novel multi-axis vibration cancellation system for the expander of a Stirling cooler is designed, analyzed, implemented, and tested. The objective is to improve significantly on the performance of passive counterbalances without incurring the cost or complexity of DSP-based systems. Furthermore, this system provides multi-axis cancellation directly rather than relying on fortuitous coupling of the various cryocooler vibration components.

The overall vibration reduction system is considered in Chapter 2. This includes modelling the cryocooler vibration in order to select appropriate sensors and actuators for active control. Magnetic and piezoelectric actuator options are presented.

A custom multi-axis electrodynamic actuator is presented in Chapter 3. The actuator combines a simple compact mechanical design with sophisticated electrodynamic forcing elements in order to provide sufficient force capability without the need for high-power drive electronics. A first-order analysis of both the magnetic and the mechanical behavior of the actuator is conducted. Experimental measurements are also presented.

In the course of these measurements, significant nonlinear response was noted. In Chapter 4, an explanation of the nonlinearity is proposed: the flexures that support the actuator's outer ring experience substantial in-plane tension due to both the outer ring's static deflection and its vibratory motion. A nonlinear actuator model is derived, and numerical solutions for the harmonic frequency response are computed. The actuator's higher-order transfer functions are measured and found to be in good agreement with the analysis. A describing-function analysis based on the nonlinear model is also conducted; the actuator nonlinearity is shown to have little effect on a

narrowband controller for the expected range of parameter values.

Adaptive feedforward disturbance rejection is examined in Chapter 5. The ideal response to stochastic and harmonic disturbances is derived for the continuous-time filtered-x LMS algorithm. Factors that affect the achieved performance are then analyzed. An analog implementation is described, and the input-output behavior of the one such controller is measured. For the most part, the controller's behavior is linear, although some distortion is noted near the harmonics of the reference frequency, in agreement with the analysis.

The controller and the actuator are combined in Chapter 6. Some additional filters are presented in order to boost the loop gain, allowing better vibration reduction. Loop transfer functions are measured, confirming the narrowband nature of the system. Results of cancelling the cryocooler's vibration are then presented, using single- and multi-axis controllers.

Finally, in Chapter 7, the design and performance of the multi-axis cancellation system is summarized, the contributions of this thesis are noted, and recommendation for future research are made.

Chapter 2

Vibration Reduction Systems

> There are many applications for an electronic vibration reducer which decreases the coupling between an offending vibration producer and a terminal location in which vibrations are undesirable.
>
> —H. F. Olson, 1956.

This chapter examines the selection and arrangement of transducers for an active vibration reduction system. The system is designed specifically to reduce cryocooler-induced vibrations in spacecraft-borne imaging instruments. Single-degree of freedom models of a long-life cooler and of a tactical cooler are presented. These models are used to make estimates of the vibration levels in order to size sensors and actuators. Multi-axis measurements are made of the tactical cooler's vibration. After contrasting vibration isolation and vibration cancellation, appropriate sensors for closed-loop control are chosen, and several actuation alternatives are evaluated.

2.1 System Architecture

There are many ways to reduce the vibration associated with cryocooler operation, making it worthwhile to compare the possibilities at a systems level before selecting one for implementation. To permit a more detailed comparison, it will be assumed that the cryocooler is a component of an AIRS-like instrument, *i.e.* the cooler is used to cool the focal plane of a high-resolution IR spectrometer on board a spacecraft. The vibration environment in such an instrument must be such that the opto-mechanical

system is able to provide a stable and accurate light path from the outermost aperture to the final detector. Other important instrument attributes include mass, power, volume, the ability to survive launch, and the ability to operate reliably in the space environment. The choice of this application for the cryocooler will affect the configuration and components chosen for the vibration reduction system; a substantially different system might be appropriate for other cryocooler applications.

Before proceeding to the design of the vibration reduction system, the salient features of the Atmospheric Infrared Sounder (AIRS) will be described, with the following caveat: this instrument, and indeed the entire Earth Observing System (EOS), is presently in the development stage and as such may be subject to substantial revision. The configuration portrayed here represents the design as it stood at the end of 1991. Subsequent changes to the design are immaterial to this discussion, as the objective is not to solve the vibration problems of a particular instrument, but rather to assess generic architectures for vibration reduction systems given a basic description of this type of instrument.

The AIRS instrument consists of three spectrometers, covering the visible/near-infrared (VIS/NIR) region (0.4–1.7 μm), the shortwave infrared (SWIR) region (3.4–8.6 μm), and the longwave infrared (LWIR) region (8.6–15.4 μm) [31]. AIRS is one of several instruments on the EOS-PM platform; each one is connected to the platform via a payload mounting plate (PMP). Hard-mounted to, but thermally isolated from, the AIRS PMP is a tubular outer frame which supports all the instrument's systems; the major systems and interfaces are illustrated in Figure 2-1. The physical dimensions of the outer frame are $0.80 \times 0.95 \times 1.16$ m, and the instrument's mass is 114 kg.

When assessing the effect of cryocooler vibration, an important element in the AIRS instrument is the optical bench. This is supported from the outer frame by glass-epoxy tubes and is radiatively cooled to 155 K, serving as a base for both IR spectrometers. It also supports the dewar assembly that houses the IR spectrometers' focal plane arrays (FPAs) and the cryocooler expander. (Notice that the cryocooler compressor, on the other hand, is supported by the instrument's outer frame.) The

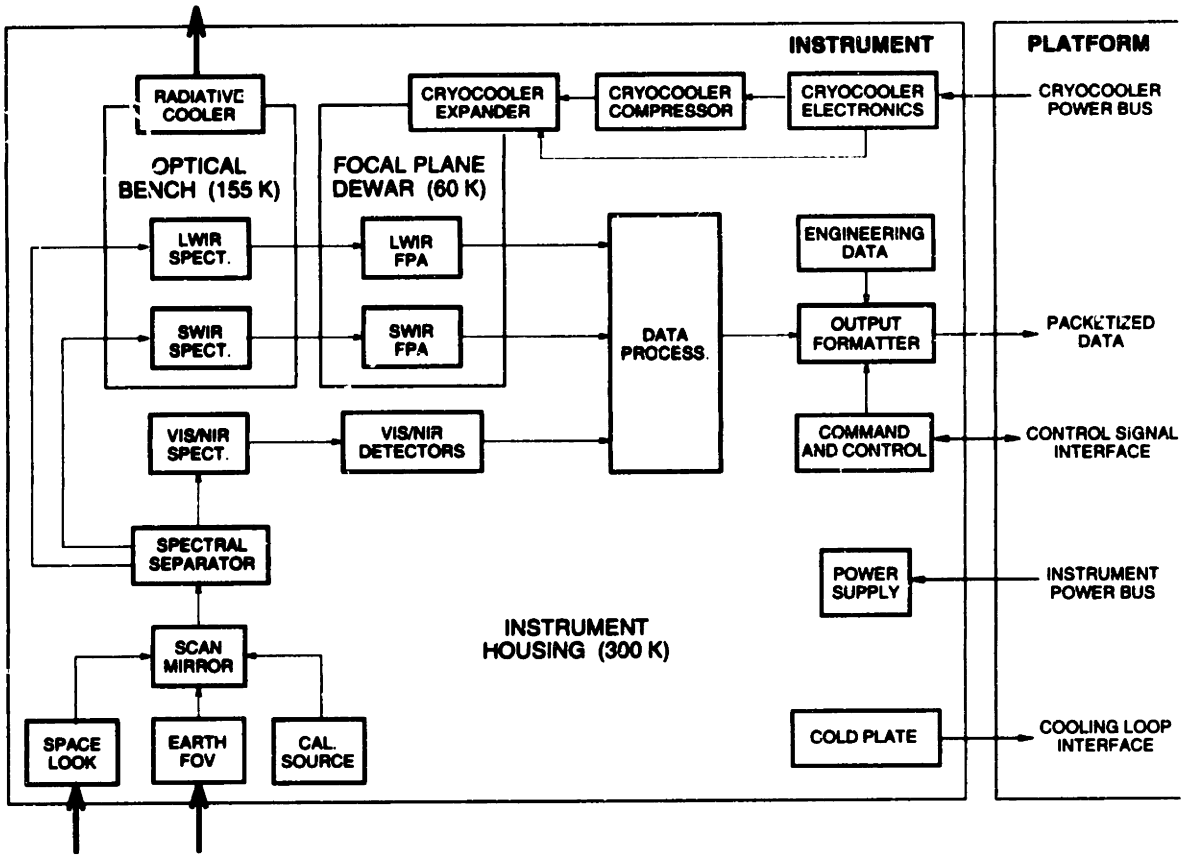

Figure 2-1: AIRS block diagram [31], illustrating major systems and interfaces.

dewar provides thermal isolation from the optical bench, and the cryocooler actively cools the FPAs to 60 K, with coupling between the coldfinger and the FPAs achieved by a thermal link.

Even this brief description of the AIRS instrument can be simplified to include only the three subsystems fundamental to its structural dynamics: a noise source, a vibration reduction stage, and a foundation. The noise source might consist of the cryocooler compressor, the expander, or both; the vibration reduction stage can be passive or active, providing isolation or cancellation; and the foundation can range from a rigid ground-based test stand to a flexible spacecraft. Although these are separate subsystems, it is their interaction that determines the instrument's vibration environment. To assure the lowest possible vibration levels, the vibration reduction stage should be designed with the charactersitics of both the noise source and the foundation in mind. However, only the noise source will be considered in detail here.

The interaction of the vibration reduction stage and the foundation dynamics is a subject unto itself; Blackwood [32] provides an extensive treatment of both passive and active reduction stages.

2.1.1 Noise Source

The most critical component in the AIRS optical system is the IR focal plane. The combination of high spectral resolution ($\lambda/\Delta\lambda = 1200$) and fast optics (f/1) leads to a 1.0-μm mechanical accuracy requirement at the focal plane between calibrations [33]; a calibration sequence is performed every 2.7 seconds. Much of the focal plane motion can be attributed to cooler-induced vibration, for which there are three distinct transmission paths: from the compressor to the focal plane via the outer frame, the optical bench, and the dewar assembly; from the expander to the focal plane via the dewar assembly; and from the expander to the focal plane via the thermal link. A Loral study [34] found that these paths contribute 0.01 μm, 0.025 μm, and 0.04 μm respectively to the focal plane motion, assuming the compressor generates a harmonic blocked force of 0.05 lb_f (0.2 N) and the expander generates a harmonic blocked force of 0.01 lb_f (0.04 N). These figures suggest that, despite the smaller blocked force, the expander-induced vibration has a greater effect on the instrument's performance than the compressor-induced vibration, making it appropriate to focus on the cryocooler expander as the system's noise source.

Two distinct cryocoolers are considered in this chapter. Both are split-cycle Stirling coolers, but one is a tactical or short-life cooler whereas the other is a long-life cooler designed for use on spacecraft. The tactical cooler is the Hughes 7014H 1/4-W cryocooler. This cooler will act as the noise source in the experimental demonstration of the vibration reduction system, so the tactical cooler's characteristics are used to size the components of this system. However, the tactical cooler differs in both size and operation from the long-life coolers that would be used on an AIRS-like instrument. Some functional requirements may be assessed more realistically using the characteristics of the long-life British Aerospace (BAe) 80K cryocooler.

There is a considerable difference in the vibration produced by these two coolers.

Spectra of the axial force generated by the cryocooler expanders when rigidly mounted are shown in Figure 2-2. Both display narrowband components at the cooler's drive frequency and higher harmonics. (The BAe harmonics appear to be wider because of differences in the signal processing used to obtain the two spectra.) Note that the vertical scales are not the same; the fundamental component of the BAe expander's vibration is an order of magnitude larger than the fundamental of the Hughes expander's vibration. This is to be expected, as the moving mass, the drive frequency, and the stroke are all greater in the BAe expander. The other major difference is that in the BAe spectrum the higher harmonics are significantly smaller than the fundamental component, which is not true in the Hughes spectrum. The distinct structure of the higher harmonics is due to each expander's particular mode of operation.

The BAe expander has a driven displacer, with an electrodynamic linear motor providing a harmonic driving force. However, the displacer in this cooler is supported by spiral flexures that produce nonlinear as well as linear spring forces. The displacer also oscillates against a volume of gas, which acts as a damper in parallel with a nonlinear spring. It is these nonlinearities that give rise to the higher harmonics observed in Figure 2-2a.

The Hughes expander, on the other hand, has a free displacer, which is driven by the pressure wave generated by the compressor. The stroke of the displacer is limited by bumpers, resulting in an impact at each end of the stroke, as is evident in an axial-force time trace (Figure 2-3). The spectrum of this force (Figure 2-2b) approximates the spectrum of an impulse train, which features harmonics of equal amplitude. It should be noted that the highly impulsive character of the vibration seen here is unusual even among tactical coolers. Hughes offers a version of the same cooler with the compressor's rotary motor replaced by a linear motor. While this cooler also has a free displacer, it no longer strikes the bumpers, greatly reducing the higher harmonics [14]. In other coolers, the bumpers are replaced by springs. Finally, long-life coolers never feature such impulsive vibrations, as all forms of contact within the cooler are avoided because of the deleterious effects on long-term reliability.

The particular structure of the Hughes spectrum can thus be safely neglected for

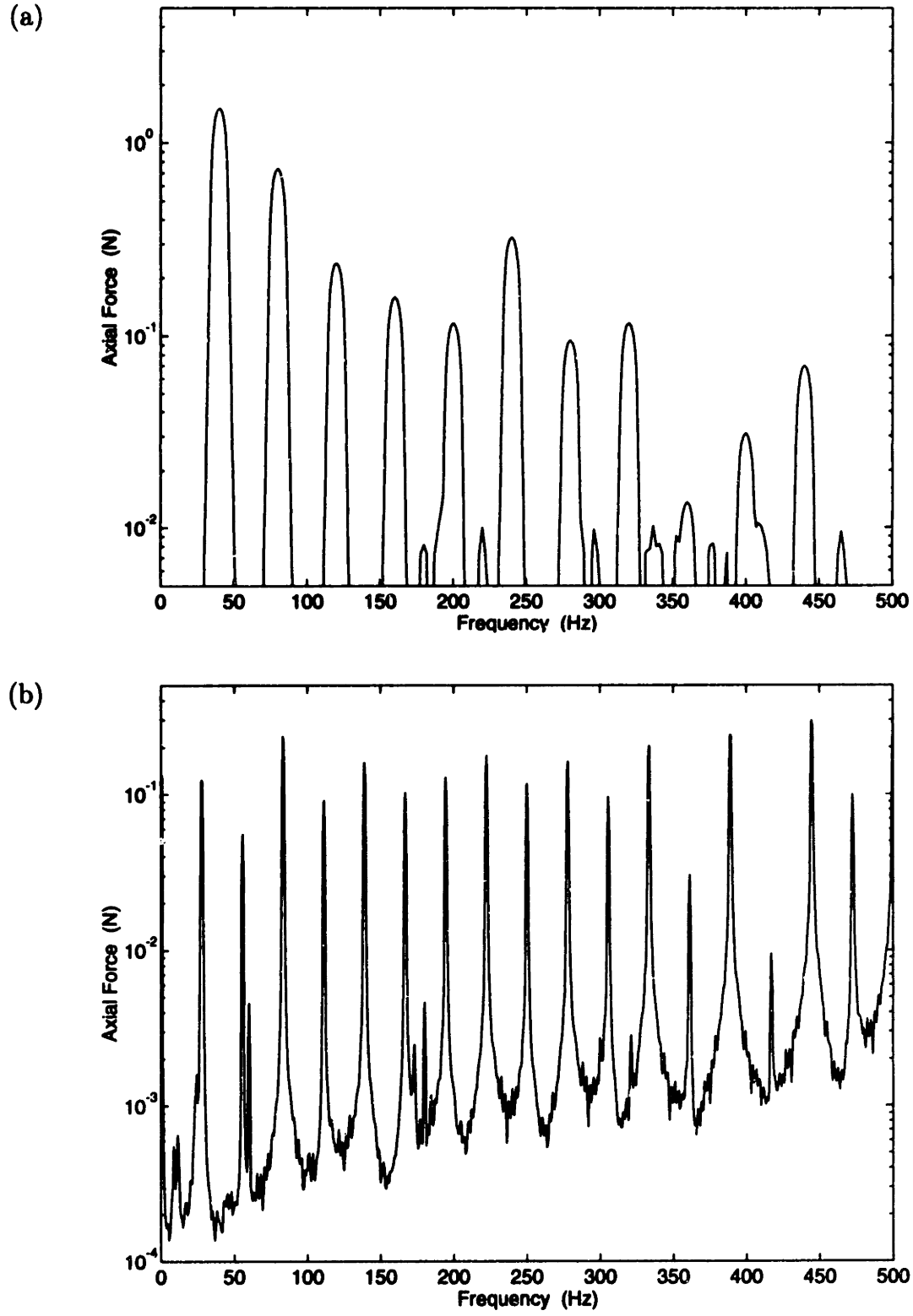

Figure 2-2: Axial force spectra. (a) BAe 80K expander (adapted from [19]) ; (b) Hughes expander.

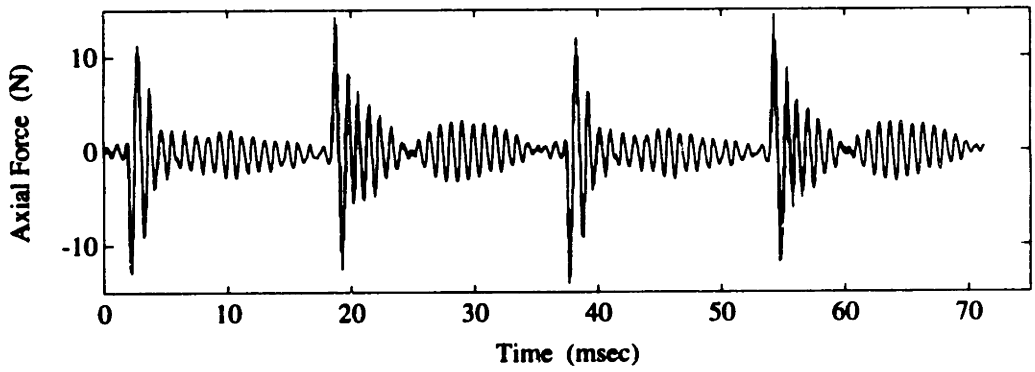

Figure 2-3: Time trace of axial force generated by Hughes expander.

spacecraft applications. But is the BAe spectrum acceptable? How much performance must be expected from the vibration reduction system? The Loral study mentioned above suggested that for AIRS, ten harmonics of 0.04 N would not result in excessive focal plane motion. The first eight harmonics of the BAe expander's vibration exceed this level, necessitating vibration reduction over a significant bandwidth. Although second-generation long-life coolers produce lower vibration levels, greater demands are being placed on the new coolers, with target levels of 0.01 N [28]. Even given this trend, it appears that vibration reduction is required over a relatively small number of harmonics, say five to ten.

The noise source must be characterized over this decade-wide frequency bandwidth in order to compare vibration reduction systems in a quantitative manner and then to size the components of these systems. Some *a priori* estimates of the disturbance levels can be made with a simple single-degree-of-freedom (SDOF) model. However it would require a more complicated model to predict details such as the higher harmonics and the non-axial disturbances; these details can often be extracted more easily from measurements of the expander's vibration.

Noise Source Model

In an ideal expander, the displacer executes strictly axial motion. This unbalanced reciprocating motion is the primary cause of expander vibration and can be represented by a SDOF model, shown in Figure 2-4 in both a rigidly-mounted and a

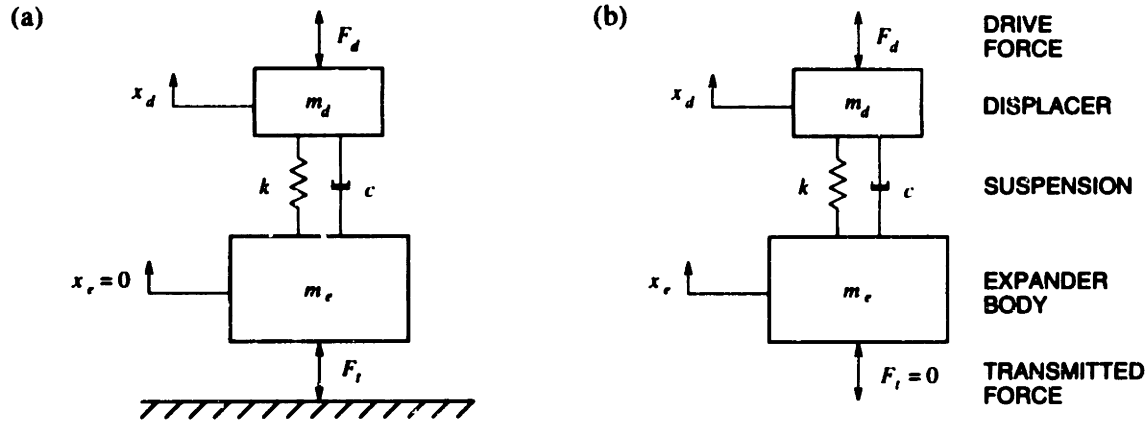

Figure 2-4: Single-degree-of-freedom expander model. (a) Rigidly mounted; (b) freely suspended.

freely-suspended configuration. While the operation of the long-life cooler is quite different from the tactical cooler, both cooler types can be described by this model. In the case of the long-life cooler the drive force F_d is generated by a linear motor, and the stiffness, k, of the displacer's suspension system is a combination of mechanical and gas spring constants. In the tactical cooler, on the other hand, F_d is generated by a pressure wave, and k is solely determined by the gas dynamics within the expander. Finally, the bumpers in the Hughes cooler may be included by limiting the stroke x_d of the displacer.

Consider first of all the rigidly-mounted configuration, which is the typical way to measure the cooler's vibration. The displacer's equation of motion is

$$m_d\ddot{x}_d + c\dot{x}_d + kx_d = F_d \tag{2.1}$$

while the force transmitted to the expander body and the rigid foundation is

$$F_t = kx_d + c\dot{x}_d \tag{2.2}$$

Long-life coolers are usually operated with position feedback, adjusting the drive force $F_d(t)$ to ensure the displacer follows the desired profile, commonly $x_d(t) = x_0 \sin \omega t$. The drive force required to satisfy Equation (2.1) is

$$F_d(t) = P_0 \sin(\omega t + \phi_d) \tag{2.3}$$

where

$$P_0 = x_0 m_d {\omega_n}^2 \sqrt{[1-(\omega/\omega_n)^2]^2 + (2\zeta\omega/\omega_n)^2}$$

$$\tan\phi_d = \frac{2\zeta\omega/\omega_n}{1-(\omega/\omega_n)^2}$$

with $\omega_n = \sqrt{k/m_d}$ and $\zeta = c/2m_d\omega_n$. Assuming $F_d(t)$ can indeed be generated, the harmonic displacement $x_d(t)$ can be substituted directly into Equation (2.2), yielding

$$\begin{aligned} F_t(t) &= x_0\sqrt{k^2+(c\omega)^2}\,\sin(\omega t+\phi_t) \\ &= x_0 m_d {\omega_n}^2 \sqrt{1+(2\zeta\omega/\omega_n)^2}\,\sin(\omega t+\phi_t) \end{aligned} \tag{2.4}$$

where the phase angle is $\tan\phi_t = c\omega/k = 2\zeta\omega/\omega_n$.

The parameters that appear in Equation (2.4) are physically meaningful and are relatively easy to determine. The displacer mass m_d, the amplitude of the displacer stroke x_0, and the drive frequency ω can be obtained from a rudimentary description of the cryocooler. The nominal values for the BAe 80K cooler are $m_d = 35$ g, $x_0 = 1.3$ mm, and $\omega = 2\pi(40$ Hz) [24]. Good cooler designs place the system's natural frequency ω_n near the drive frequency, because the power required to drive the linear motor is minimized when the system is operated at resonance [35]. For example, the BAe cooler features a drive frequency of 40 Hz and the displacer's natural frequency is approximately 36 Hz [36]. The damping ratio is difficult to predict, but it can be extracted from measurements of the work performed on the gas in the expander; typical values range from 0.2 to 0.3 [26]. Substituting the BAe cooler's parameters into Equation (2.4) yields a transmitted force of 2.7 N, which is within a factor of two of the axial force's fundamental component reported in References [19] and [24]. This is close enough for initial sizing of the vibration reduction system, although margin must be included to allow for the higher harmonics not predicted by this model.

If the tactical cooler's displacer executes harmonic motion, the transmitted force will also be determined by Equation (2.4). But because of the bumpers, the displacer in the Hughes cooler vibrates periodically rather than harmonically. Estimates can still be made of the transmitted force. The displacement is first described as a function of time, incorporating the effect of the bumpers, and the Fourier series of

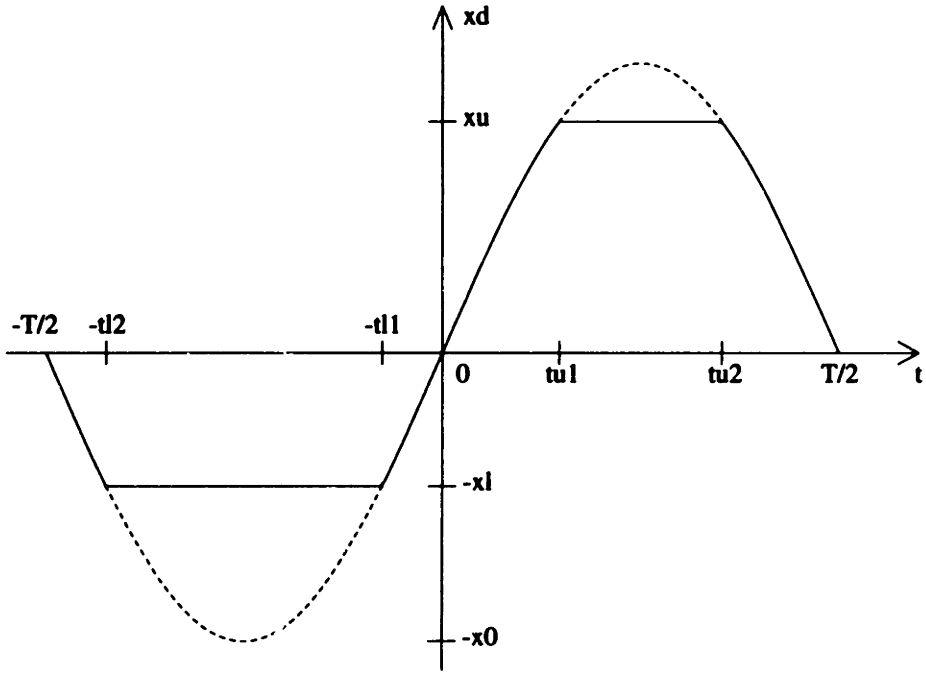

Figure 2-5: Bumper-limited stroke of displacer in Hughes expander.

this function is then computed. Once the displacement is separated into harmonic components, Equation (2.4) may be used to determine the transmitted force caused by each harmonic.

Assume that the displacer moves harmonically when not in contact with the bumpers. There is an offset to the displacer's position when the expander is mounted vertically in a gravity field, so it cannot be assumed that the stroke is limited by the same amount in each direction. Referring to Figure 2-5, denote the distance from the displacer's equilibrium position ($x_d = 0$) to the upper bumper and to the lower bumper by x_u and x_l respectively. Let t_{u1} and t_{u2} be the times at which the harmonic motion intersects the upper bumper's position, with a similar definition for t_{l1} and t_{l2}. Then the displacement is given by

$$x_d(t) = \begin{cases} x_u, & t_{u1} \le t \le t_{u2} \\ x_0 \sin \omega t, & -T/2 < t < -t_{l2} \quad \text{or} \quad -t_{l1} < t < t_{u1} \\ & \quad \text{or} \quad t_{u2} < t < T/2 \\ -x_l, & -t_{l2} \le t \le -t_{l1} \end{cases} \tag{2.5}$$

where the period is $T = 2\pi/\omega$. This function may also be expressed in terms of its Fourier series:

$$x_d(t) = \frac{a_0}{2} + \sum_{p=1}^{\infty}(a_p \cos p\omega t + b_p \sin p\omega t) \tag{2.6}$$

where

$$a_p = \frac{2}{T}\int_{-T/2}^{T/2} x_d(t)\cos p\omega t\, dt, \qquad p = 0,\ 1,\ 2,\ \ldots$$

$$b_p = \frac{2}{T}\int_{-T/2}^{T/2} x_d(t)\sin p\omega t\, dt, \qquad p = 1,\ 2,\ \ldots$$

From Equation (2.4), the Fourier series of the transmitted force is then

$$F_t(t) = |G_0|\frac{a_0}{2} + \sum_{p=1}^{\infty}|G_p|[a_p \cos(p\omega t + \phi_p) + b_p \sin(p\omega t + \phi_p)] \tag{2.7}$$

where

$$|G_p| = \sqrt{k^2 + (cp\omega)^2} = m_d{\omega_n}^2\sqrt{1 + (2\zeta p\omega/\omega_n)^2}$$

$$\tan\phi_p = cp\omega/k = 2\zeta p\omega/\omega_n$$

The harmonic components may be determined by substituting Equation (2.5) into the Fourier integrals. The force generated by the Hughes expander may then be estimated by evaluating Equation (2.7) using the harmonic components and parameter values. The nominal drive frequency of the 7014H cryocooler is 28 Hz, with a displacer mass of 3 g and a total stroke, $x_l + x_u$, of 2.8 mm; the displacer is in contact with the bumpers about 60% of the time [37]. Free-displacer Stirling coolers rely on the dynamics of the SDOF system to establish the correct phase relationship between the displacer and the compressor; cold production is maximized when $\omega_n/\omega \approx 1.25$ [35]. Finally, the damping ratio is assumed to be similar to the BAe cooler's.

The harmonic amplitudes over a 500 Hz bandwidth were computed and are shown in Figure 2-6. Clearly there are differences between this computed spectrum and the measured one (Figure 2-2b), but the overall structure is similar and the amplitudes are comparable. Even the higher harmonics are reasonably approximated here—the nonlinearity that caused them, *i.e.* the presence of the bumpers, was simple to model. Nonlinear spring elements could be included in the long-life cooler model,

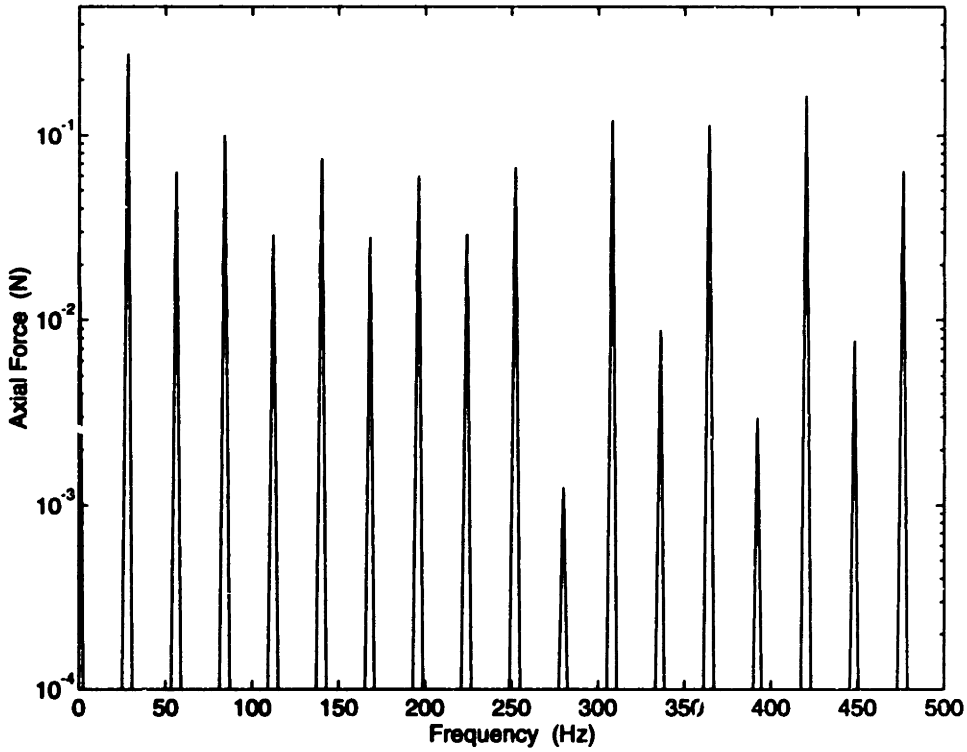

Figure 2-6: Computed axial force spectrum for Hughes expander.

but much more detail would be required to achieve good *a priori* estimates of the higher harmonics. The general agreement between the computed spectrum and the measured spectrum suggests that the SDOF model may be used for rough sizing of the vibration reduction system before accurate measurements are available.

The model may also be used to assess the effect on the vibration of changing the drive frequency. For drive frequencies below roughly $2\omega_n$, Equation (2.4) shows that the amplitude of the transmitted force is approximately

$$|F_t| \approx x_o m_d \omega_n{}^2 [1 + 2\zeta^2(\omega/\omega_n)^2] \tag{2.8}$$

So higher drive frequencies result in higher forces.

The tactical cooler model was used to predict the amplitude of the first eight harmonics as a function of drive frequency. The computed amplitudes are compared with measured values in Figure 2-7. While the relative order of the harmonics does not agree (the model's largest component is the first harmonic, whereas the largest measured component is the third harmonic), the behavior with respect to the drive

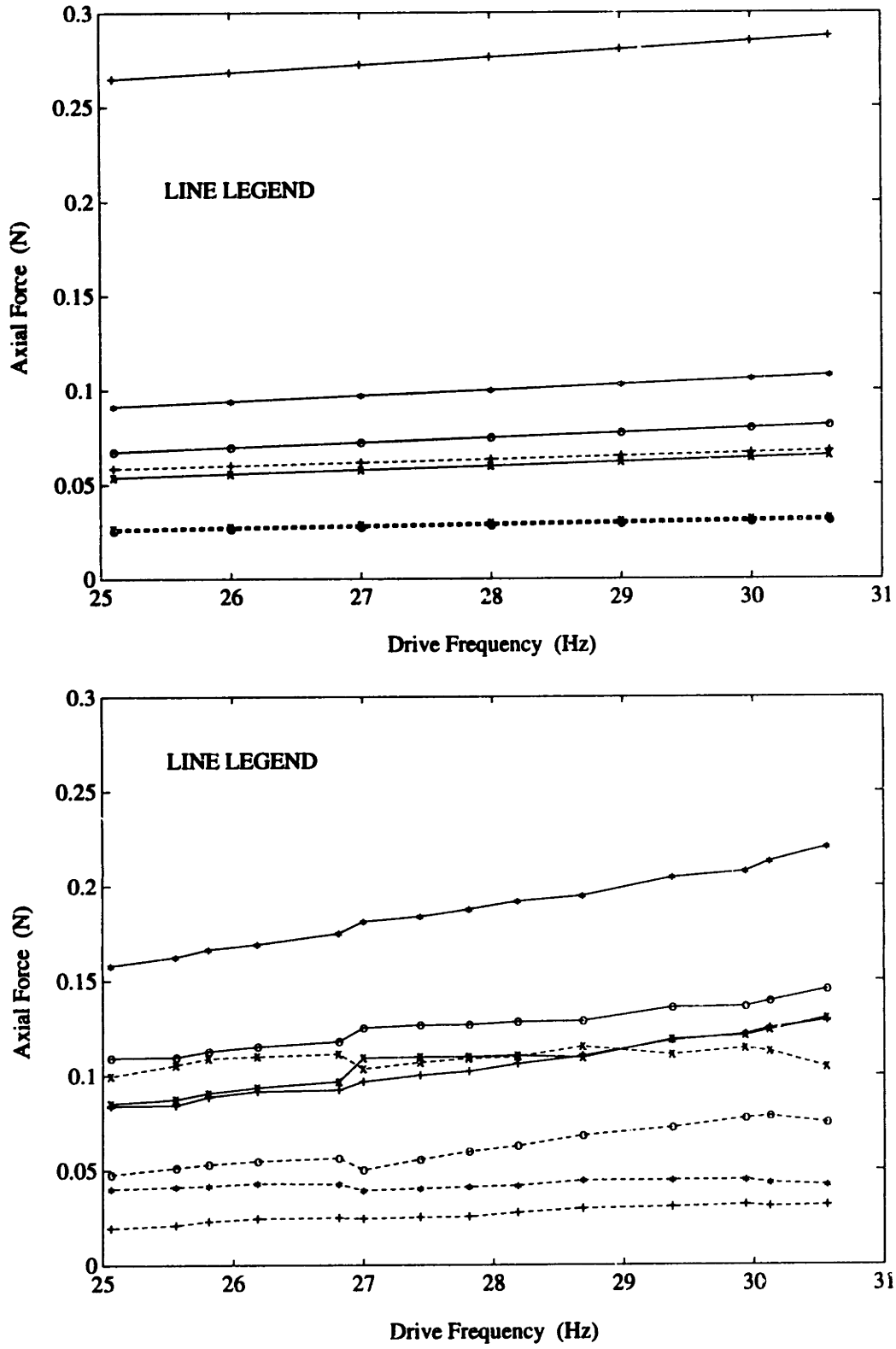

Figure 2-7: Effect of drive frequency on harmonic amplitudes. (a) Computed; (b) measured.

frequency is accurately reflected by the model. Thus the frequency dependence of the disturbance level may be considered explicitly when designing the vibration reduction system, or more conservatively, the system may be designed for the disturbance level generated at the highest drive frequency.

Finally, the freely-suspended configuration of the SDOF model (Figure 2-4b) is worth examining. This configuration is occasionally used for ground-based testing [25], as it avoids the rigidly-mounted configuration's need for a large seismic mass. More importantly, if the vibration reduction system makes extensive use of isolation, the expander will appear to be freely suspended.

In this configuration both the displacer and the expander body are free to move. Denoting the relative motion of these masses by $x_r = x_d - x_e$, the systems' equations of motion are

$$\begin{aligned} m_d\ddot{x}_d + c\dot{x}_r + kx_r &= F_d \\ m_d\ddot{x}_e - c\dot{x}_r - kx_r &= 0 \end{aligned} \tag{2.9}$$

With the rigid configuration, the imposed motion was $x_d(t) = x_0 \sin \omega t$. However, since the position transducers used for feedback in long-life coolers measure *relative* displacement, the imposed motion in the free configuration is $x_r(t) = x_0 \sin \omega t$. The required drive force is still $F_d(t) = P_0 \sin(\omega t + \phi_d)$, but the gain and phase of this force are now

$$\begin{aligned} P_0 &= \frac{x_0 m_d {\omega_n}^2}{\alpha} \sqrt{[1 - \alpha(\omega/\omega_n)^2]^2 + (2\zeta\omega/\omega_n)^2} \\ \tan\phi_d &= \frac{2\zeta\omega/\omega_n}{1 - \alpha(\omega/\omega_n)^2} \end{aligned} \tag{2.10}$$

where $\alpha = m_e/(m_d + m_e)$. Equations (2.3) and (2.10) define the force required to impose the specified relative motion in the rigidly-mounted and the freely-suspended configurations respectively. Observe that a greater drive force is required in the free configuration; the resonant frequency is also greater. Both effects are determined by α, the ratio of the mass of the expander body to the total mass of the expander. If $m_e \gg m_d$, then $\alpha \approx 1$, and the two configurations require the same drive force.

As the relative motion of the two masses is prescribed to be the same in both configurations, the spring and damper forces applied to the expander body must be

identical. Rather than being transmitted to a foundation, these forces accelerate m_e when the expander is freely suspended. Thus, the free displacement of the expander body is

$$x_e(t) = F_t(t)/m_e\omega^2 \tag{2.11}$$

where F_t is given by Equation (2.4).

Estimates of the free displacement are important when designing the vibration reduction system; an ideal isolation system would require sufficient travel to allow motion on the order of the expander's free displacement. The BAe expander has a total mass of 0.9 kg [36], so $m_e = 0.865$ kg and $\alpha = 0.96$. Combining this with the previous estimate of $|F_t| = 2.7$ N yields a free displacement of 50 μm at the 40 Hz drive frequency. The vibration of the Hughes expander is most easily handled in terms of its Fourier series, applying Equation (2.11) to each harmonic. Although the amplitude of each harmonic of the transmitted force is quite small, the Hughes expander is very light ($m_e = 63$ g, $\alpha = 0.95$), resulting in large displacements. For example, at the 28 Hz drive frequency the fundamental component of the free displacement is approximately 120 μm. Of course, these values should be treated as order-of-magntiude estimates and should only be used for initial sizing of the vibration reduction system.

Noise Source Measurements

There are many ways to improve the expander model: additional degrees of freedom could be added, more nonlinearities could be introduced, or the lumped masses could be replaced by general impedance elements to account for structural flexibility within the expander. These improvements might be appropriate for a high-fidelity cooler development model, but they represent excessive detail for a noise source model. A better approach is to make measurements of the actual disturbance levels produced by the expander. This will not provide the insight that a model does, but it will capture the net effect of all contributing phenomena.

The sensors used to make these measurements might be the actual sensors that will be used in the vibration reduction system (*q.v.* Section 2.2), or they might be

sensors selected for their convenience and availability. The demands on resolution and noise levels are less stringent here because the original vibration levels are being measured rather than the reduced ones. Estimates of the axial vibration, which is the predominant component, have already been derived using the SDOF model. These estimates may be used as an aid to sensor selection.

Are the other vibration components negligible? The answer to this question will determine the number and arrangement of sensors needed to characterize the expander's vibration. Estimates of these components can sometimes be made in the cases where a clear mechanism exists to convert axial vibrations into reactions about or along the other axes. For instance, in the long-life coolers, the suspension's spiral flexures produce a torque about the longitudinal axis in response to the displacer's axial motion. But even if such a mechanism is known, several additional parameters that are difficult to determine, such as the torsional stiffness of the flexures, may be required to convert estimates from the SDOF model into the non-axial vibration components.

Little guidance is to be found in the literature; the axial component is usually the only component reported. Although several researchers have published values for the axial and lateral forces as well as the axial torque generated by long-life expanders [18,24,25], the values appear to be quite sensitive to cooler and measurement details: BAe 80K expanders were tested in References [18] and [24], yet Reference [18] reported peak forces and torques of 2.5 N, 5.1 N, and 3.2 N·cm respectively, whereas Reference [24] reported 5 N, 1.5 N, and 2 N·cm. Changing cooler types causes even greater variation. In Reference [25] a somewhat smaller expander which operated at 55 Hz rather than 40 Hz was tested; the same set of reactions were 3.6 N, 11 mN, and 0.18 N·cm. These examples suggest that, given only a measurement (or an estimate) of the axial force, no conclusions can be drawn about the lateral forces or the axial torque.

Measurements would ideally be made of all six reactions. Indeed, the development and use of six-axis force dynamometers seems to be a common theme in the cryocooler community [8, 18, 25], although the full set of reactions is never reported. The usual

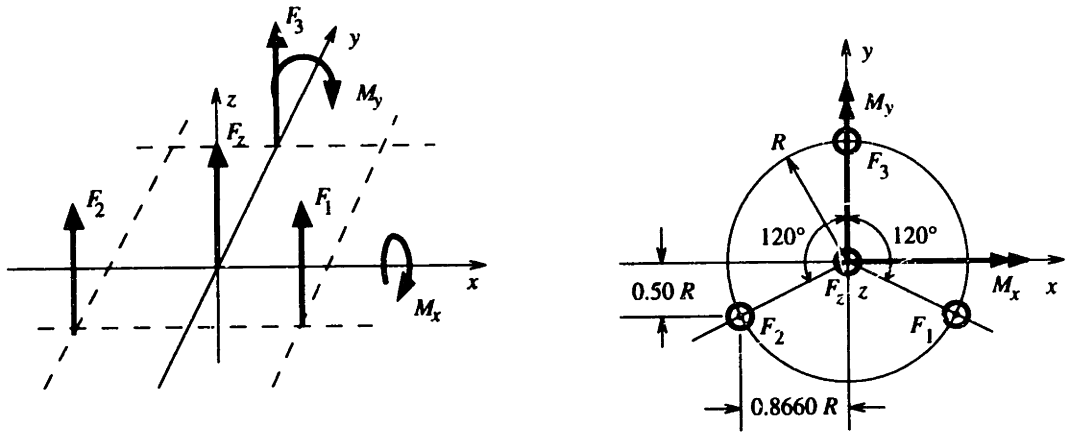

Figure 2-8: Coordinate axes for expander vibration measurements.

subset of the axial and lateral forces and the axial torque appears to have arisen from concerns about the spiral flexures in the long-life coolers.

A different set of three reactions will be considered here, namely the axial force and the torques about two orthogonal lateral axes (Figure 2-8). This set was chosen in part because of the importance of the coldfinger–thermal link vibration path in the Loral study [34], which suggests that the most significant vibration components are those that cause coldtip vibration. It is assumed that the structure to which the expander is mounted is quite stiff laterally, minimizing the effect of F_x, F_y, and M_z on the coldtip. (These reactions will, however, be transmitted to the focal plane via the dewar assembly.) The vibration of the coldtip will then be determined primarily by F_z, M_x, and M_y.

This set of reactions was also chosen because it allows an elegant transducer implementation. All three components may be determined by measuring the expander's vibration with three axial sensors some distance from the longitudinal axis. Similarly, three axial actuators may be used to generate the three components needed to counter the expander's vibration. An analogous arrangement of three lateral sensors and three lateral actuators could be added to include all six reactions, should this prove necessary.

The vibration generated by the Hughes expander was measured on a mount formed by several elements. The expander was mounted on a plate that included a vacuum

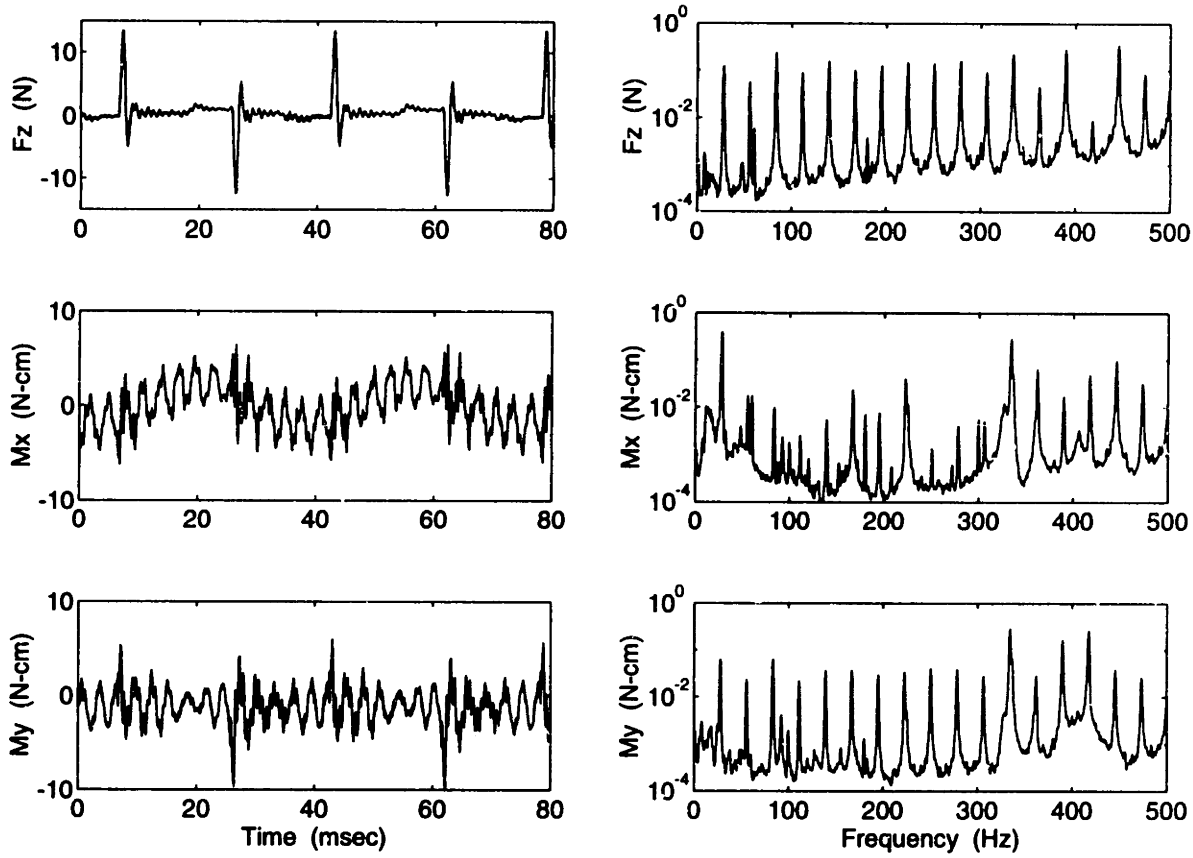

Figure 2-9: Typical vibration levels generated by the expander.

dewar for the coldfinger. This plate was connected to an aluminum mounting fixture by means of three load cells, which allowed the transmitted force to be measured. The mounting fixture was bolted to a plate that was embedded in a 230-kg concrete block. The block, in turn, rested on four pneumatic isolators. The dynamic behavior of this foundation was characterized by Blackwood [32]. The natural frequency of the block's bounce mode is 5.4 Hz, with rocking modes at 4.4 Hz and 8.3 Hz. These modes have little effect on the measurements as the cooler's drive frequency is always greater than 25 Hz. After these low-frequency modes, the embedded plate has resonances that start at approximately 1 kHz. Tap tests revealed additional lateral modes near 400 Hz.

The measured time traces and spectra are shown in Figure 2-9. The impact of the displacer against the top bumper and then the bottom bumper results in sharp peaks in the axial force time trace. The structural modes of the foundation amplify

the harmonics near 1 kHz, as can be seen in all three time traces.

The first ten harmonics of the cooler's drive frequency were considered when designing the active vibration reduction system. Although the vibration levels do not roll off significantly over this bandwidth, this was due to the particular design of the Hughes rotary cooler. As noted above, most coolers do not feature such harmonically-rich vibration.

A conservative description of the disturbance is to assume that all harmonics are of equal amplitude, using the greatest amplitude in this bandwidth. Less conservative approaches might replace this amplitude with a logarithmic or linear average. Depending on the complexity desired, the assumed design amplitude might or might not account for the effect of drive frequency variations too (Figure 2-7). For actuator design purposes, values of 0.25 N and 0.1 N·cm per harmonic were assumed, both of which are quite conservative.

2.1.2 Vibration Reduction System

The two primary alternatives here are isolation and cancellation. While both systems are composed of similar elements, they achieve the vibration reduction in two distinct ways.

An isolation system separates the noise source from the foundation, ideally providing the noise source (the cryocooler expander) with freely-suspended boundary conditions. As shown in Figure 2-4, this eliminates the force transmitted from the expander to the foundation, although much greater expander motion occurs. The resulting displacement of the expander body is given by Equation (2.11). Based on the assumed force level of 0.25 N per harmonic, the expander mass of 63 g, and a drive frequency of 31 Hz, the worst-case displacement associated with the first ten harmonics of the Hughes expander is 160 μm. (Active narrowband isolation provides rigid coupling at the other harmonics, so they do not contribute to the displacement of the expander.) This free displacement represents a significant stroke for the active system's actuator. Furthermore, this stroke must be accommodated by the thermal link between the coldfinger and the focal plane.

In a cancellation system, the expander is firmly connected to the foundation, which minimizes the relative motion between the expander and the focal plane. An actuator drives a reaction mass so as to cancel the cooler's momentum, thereby reducing the net force transmitted to the foundation. This system was selected in preference to the isolation system because the thermal link does not become a critical factor; the design of the cancellation may then be driven by the vibration requirements and the design of the thermal link by the thermal requirements.

2.2 Sensor Selection

The vibration reduction system can only cancel the expander's vibration to the extent that the vibration can be measured. Since the closed-loop vibration will be much smaller than the open-loop levels, high-resolution low-noise sensors with a very large dynamic range are required.

Several types of sensors are commonly used in the active control of vibration. These include load cells, gap sensors, and accelerometers. The accelerometers can be mounted on the expander body or on the foundation.

The sensor type has a strong effect on the coupling between the control system and the structural flexibility of either the expander or the foundation. Since the cryocooler is physically very compact, most of its flexibility occurs at high frequencies, making interaction with foundation modes the most likely problem. Blackwood and von Flotow [38] considered the suitability of the various sensors for active isolation in the presence of foundation dynamics. They confirmed the observation made by Watters *et al.* [39] that using the foundation acceleration results in very strong coupling between the controller and the foundation dynamics. Assuming some passive isolation is present, gap sensors achieve good decoupling below the passive mount resonance, while force sensors provide good decoupling above this resonance. Force sensors are therefore an attractive means of decoupling the controller from mid-range instrument resonances, provided some degree of passive isolation is included in the system.

The transmitted force may be measured directly with load cells, or it may be inferred from accelerometers mounted on the expander body. Load cells are preferable when the cryocooler is supported by a relatively rigid base.

As indicated by Figure 2-9, the cryocooler vibration levels are quite low, making resolution much more critical than range when selecting a load cell. The PCB Model 208B load cell features good resolution (1 mN) and more than adequate range (±45 N). A stiffness of 1750 N/μm ensures that the load cells do not introduce any additional low-frequency modes.

2.3 Actuator Selection

The actuator consists of a reaction mass and three parallel single-axis forcing elements. By properly phasing these elements, the cryocooler's momentum can be cancelled. Due to existing components, the space available for the actuator is restricted to a cylinder with an inner diameter of 40 mm, an outer diameter of 85 mm, and a height of 30 mm.

The design vibration levels are 0.25 N and 0.1 N·cm per harmonic. In order to cancel all three axes of vibration given the worst possible phasing of the axial vibration and the two lateral torques, each forcing element must be capable of generating 0.1 N per harmonic, presuming the three forcing elements are arranged in a 32-mm radius ring. A conservative requirement for a ten-harmonic cancellation system is therefore 1 N per forcing element.

Two types of magnetic forcers were considered, as were several commercial piezoelectric translators.

2.3.1 Electromagnetic Forcers

Electromagnetic forcers rely on external magnetic fields, applied by means of current-carrying coils, to control the magnetic flux in a soft magnetic material. When an air gap is included in the magnetic circuit, the resulting mechanical forces are directed so as to reduce the circuit's reluctance, *i.e.* the magnetic system attempts to close

the air gap [40]. An example of such an actuator is a solenoid.

A preliminary design was developed for an electromagnetic forcer. High force constants (the force generated per unit current) are fairly easy to achieve with this design. However, electromagnetic forcers are strictly attractive, requiring a second opposed forcer or a spring to provide a restoring force. Furthermore, the force is proportional to the current squared [40]. This relationship is usually linearized by applying small control currents along with a substantial bias current, which eliminates much of the advantage of the high force constant.

This design was abandoned due to the mechanical complexity associated with a system based on attractive forcers and due to the large bias currents required to linearize the force-current relationship.

2.3.2 Electrodynamic Forcers

A second type of magnetic forcer is the electrodynamic forcer. In this type, a mechanical force (the so-called Lorentz force) results from the interaction of a magnetic field and an electric current. The magnetic field is typically established by permanent magnets. The magnetic circuit includes an air gap, into which is placed a current-carrying coil mounted on the moving element. Examples of electrodynamic forcers include voice coils and small shakers.

Even a small commercial shaker such as the Wilcoxon 1-lb_f shaker has much more force capability than required, 4.5 N vs. 1 N. Furthermore, three of them do not fit in the available space. Similarly, most commercial linear actuators are physically too large. This led to development of a custom electrodynamic forcing element.

This design was much less complex than the design of the electromagnetic forcer. The Lorentz force is directly proportional to the applied current, eliminating the need for opposing forcers or bias currents. The force constant is determined by the geometry of the forcer and by the magnetic flux density in the air gap. Force constants on the order of 6 N/A have been achieved with comparably sized units using rare-earth permanent magnets [41]. Thus, the assumed force level of 1 N per forcer requires less than 0.2 A per forcer; currents of this amplitude are easily supplied by power

operational amplifiers [42].

The relative mechanical simplicity and the low-power drive electronics make the electrodynamic forcer much more viable than the electromagnetic design.

2.3.3 Piezotranslators

Finally, several commercial piezotranslators were considered. When combined with a reaction mass, these will act as displacement actuators below the piezo/reaction mass resonance. Above this resonance, they will act as force actuators. In the displacement regime, they must match the displacer's mass-stroke product in order to cancel the displacer's momentum. For the Hughes cooler, this product is 8 g·mm. As this figure only accounts for the axial vibration, the mass-stroke product was increased to 10 g·mm for multi-axis design purposes. It is assumed that each of the three translators has the same stroke capability. All three might support a single reaction mass, or each one might have its own reaction mass.

Physik Instrumente (PI) has an annular three-axis levelling stage, the P-741 [43]. Unfortunately it is much too large for this cryocooler application: its *inner* diameter is 100 mm, whereas the outer diameter of the available actuator space is 85 mm. This multi-axis actuator is intended for static positioning applications; subsequent tests revealed significant nonlinearities when used dynamically [44].

PI also makes a range of compact single-axis translators. Several models were examined. The low-stroke models require large reaction masses to match the displacer's mass-stroke product. For example, the P-770.10 Microstage has a full stroke of 7 μm at 100 V. In order for three of these to achieve the 10 g·mm mass-stroke product, each would have to support a 0.475 kg reaction mass. Some models offer greater stroke capability, but the lever action used to achieve this also results in lower resonant frequencies. For example, the unloaded resonant frequency of the P-771.00 Mini-Block is 200 Hz. Since the cooler's first ten harmonics range from 31 Hz to 310 Hz, this resonance complicates (but does not prevent) operation. The cost of three Mini-Blocks and the associated drive electronics was almost $6000 in 1992.

The decision was made to pursue the design and fabrication of a multi-axis elec-

trodynamic actuator. This appeared to offer a simple compact solution that could be driven by low-power electronics.

2.4 Summary

The architecture of and the transducers for an active vibration reduction system were selected in this chapter. The manner in which cryocoolers are integrated into spacecraft instruments makes it difficult to use active vibration isolation; an active vibration cancellation system is more easily accommodated. The vibration environment generated by both long- and short-life Stirling coolers was modelled, and multi-axis measurements were made of the vibration associated with the Hughes expander.

Based on these measurements and the comparison with long-life coolers, conservative bounds on the disturbance levels were determined. The bounds were used to size the cancellation system's transducers. Commercial load cells were selected, and a custom electrodynamic actuator was proposed.

Chapter 3

Multi-Axis Electrodynamic Actuator

> This problem of closing the gaps and making the thing work in the most practical way is *engineering*. It requires serious study of design problems, although there are no new basic principles from which the forces are obtained.
>
> —R. P. Feynman, 1964.

The comparison of the previous chapter suggests that adequate performance can be achieved with an electrodynamic actuator in which the magnetic flux is established by permanent magnets. This design is used in loud-speaker voice coils and in small shakers, and a wide range of linear magnetic actuators are commercially available. Most of these systems, however, have more capability than required to cancel the vibration of the Hughes cryocooler expander. Not only are they overdesigned for this application, they simply would not fit in the available space. Thus, a custom multi-axis actuator was designed and built.

The forcing elements in this actuator are based on a relatively unusual magnetic configuration. However, the equivalent magnetic circuit is no more complicated than a first-order model of a voice coil. An analysis of the magnetic circuit is presented, and some design considerations are discussed. The mechanical design of the actuator allows simple fabrication and assembly while also providing dynamic characteristics that are compatible with the active cancellation system. Both the magnetic design and the mechanical design have a direct effect on the drive electronics; the sizing

of these elements permits the use of a low-power voltage-controlled current source. Finally, the measured performance of the electrodynamic actuator is presented.

3.1 Magnetic Design

Electrodynamic actuators utilize the Lorentz force which results from the interaction of a magnetic field and an electric current. In a typical design, permanent magnets produce a magnetic flux in an air gap. A current-carrying conductor placed in this air gap will then experience a Lorentz force

$$\mathbf{F} = -I \int \mathbf{B} \times d\mathbf{l} \tag{3.1}$$

where I is the current, $\mathbf{B}$ is the magnetic flux density, and $d\mathbf{l}$ is a vector directed along the conductor axis in the direction of positive current; the integration is performed over the entire length of the conductor. (Observe that $\mathbf{F}$, $\mathbf{B}$, and $d\mathbf{l}$ are vector quantities while I is a signed scalar.) The actuator's force constant, $|\mathbf{F}/I|$, is therefore determined by the magnetic flux density and the conductor geometry.

The design possibilities have been greatly enhanced by the advent of commercial rare-earth permanent magnets. The energy product $BH_{\max}$ of these magnets is four to six times that of traditional Alnico permanent magnets, yet the material density is approximately the same. Thus, actuators based on rare-earth magnets have much better force-to-mass and force-to-volume ratios.

If the force requirements are relatively low, the high energy product of rare-earth magnets may be used to increase the size of the air gap while maintaining sufficient flux density. This is important in large-stroke applications such as microgravity magentic suspensions [45, 46]. It is also important in multiple-degree-of-freedom (DOF) robotic fine-positioning devices, as it maximizes the workspace through which the device can move without internal interference. For example, Higuchi *et al.* [47] describe a five-DOF "intelligent hand" supported by DC electromagnetic bearings with air gaps of 1–2 mm, whereas Hollis *et al.* [41] developed a six-DOF "magic wrist" that incorporates Lorentz-force actuators in which the air gaps exceed 6 mm. In addition

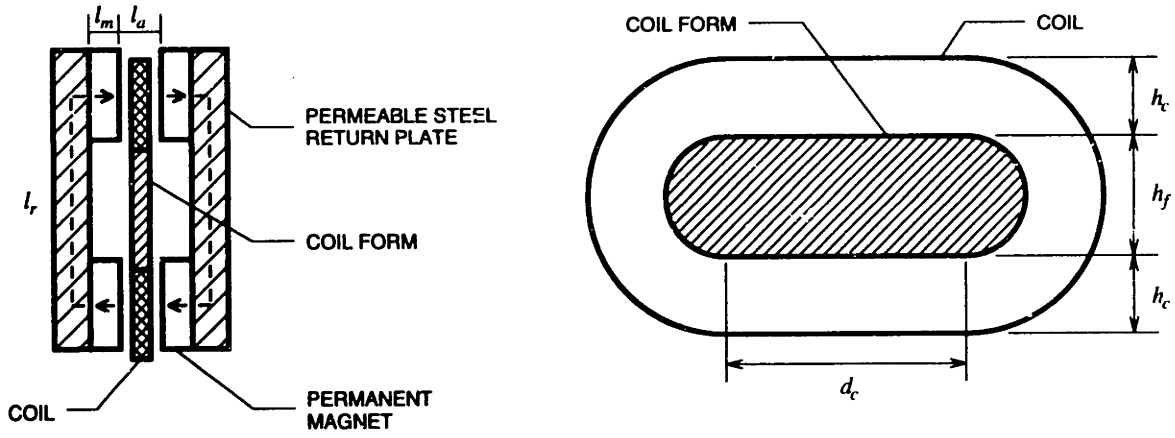

Figure 3-1: Cross-section of a four-magnet two-return-plate forcing unit. The coil and the coil form are also shown.

to expanding the workspace, the larger air gaps reduce the need for active gap control.

The single-axis forcing elements in the magic wrist are wide-gap flat-coil electrodynamic actuators. They were derived from narrow-gap units used in disk drives [41]. Hollis *et al.* refined the wide-gap design through numerical and experimental analyses of the magnetic flux distribution as a function of gap length and magnet dimensions. They reported a measured force constant of 6.2 N/A for a single forcer, which incorporates four magnets and two return plates in a 30 × 36 × 32 mm configuration. This design provides a much higher force constant than comparably-sized commercial linear actuators and was therefore chosen as the baseline configuration for the forcers in the cancellation system's three-DOF actuator.

3.1.1 Magnetic Circuit Analysis

A cross-section of a simplified four-magnet two-return-plate configuration is shown in Figure 3-1. By analyzing this configuration, the relationship between the magnetic parameters, the geometric parameters, and the force constant may be established. This relationship will be used to guide material selection and component sizing.

The magnets are rectangular bars with the long axis extending into and out of the page. They are polarized through the thickness, so the mean length of the flux path l_m in each permanent magnet is equal to the thickness of the magnet. Similarly,

denote the mean length of the flux path in each air gap and in each return plate by l_a and l_r, respectively.

Ampère's circuital law states that the line integral of the magnetic field intensity around a closed path is equal to the enclosed current, that is

$$\oint \mathbf{H} \cdot d\mathbf{s} = I_{\text{encl.}} \tag{3.2}$$

Assume that the magnetic field is sufficiently uniform to allow a one-dimensional analysis. The positive direction of current is out of the page for the upper half of the coil and into the page for the lower half. The circuital law is then

$$4H_m l_m + 2H_a l_a + 2H_r l_r = N_e I \tag{3.3}$$

where H_i is the magnitude of $\mathbf{H}_i$ and N_e is an effective number of turns in the coil to account for asymmetric placement with respect to the flux path; if the coil were truly centered, the net enclosed current would be zero.

The magnetic field intensity in the air gap H_a is related to the magnetic flux density B_a by the relation

$$\mathbf{B}_a = \mu_0 \mathbf{H}_a \tag{3.4}$$

where the magnetic constant μ_0 is the permeability of free space. Magnetic quantities are commonly specified in one of two systems of units. In the SI metric system, the magnetic field intensity is given in amperes per meter (A/m). The standard unit of magnetic flux is the weber (Wb), and the unit of flux density is the tesla (T), where $1\ \text{T} = 1\ \text{Wb/m}^2$. The value of the permeability of free space is then defined as $\mu_0 = 4\pi \times 10^{-7}\ \text{Wb/A·m}$. The other system is the CGS metric system, in which the magnetic field intensity unit is the oersted, $1\ \text{Oe} = (1000/4\pi)\ \text{A/m}$, the flux unit is the maxwell, $1\ \text{Mx} = 10^{-8}\ \text{Wb}$, and the flux density unit is the gauss, $1\ \text{G} = 10^{-4}\ \text{T}$. Thus, in the CGS system, $\mu_0 = 1\ \text{G/Oe}$.

Assume that the magnetic flux is confined to effective areas A_m, A_a, and A_r in the permanent magnets, the air gaps, and the return plates, respectively. Continuity

of magnetic flux around the circuit requires that

$$B_m A_m = B_a A_a = B_r A_r \tag{3.5}$$

If the areas are approximately equal, the flux density will be approximately constant around the circuit. The magnetic field intensity in the back plates is then negligible, since $H_r = B_r/\mu_r\mu_0 \approx H_a/\mu_r$, where μ_r is the relative permeability of the back-plate material, and $\mu_r \approx 3000$ for transformer-grade steel [48].

The load line defines the relationship between the flux density and the field intensity in the permanent magnets. Upon neglecting the return-plate terms, Equations (3.3)–(3.5) may be combined to yield the load line

$$B_m = -\mu_0 \frac{A_a}{A_m}\left(\frac{2l_m}{l_a}H_m - \frac{1}{2l_a}N_e I\right) \tag{3.6}$$

The flux density and the field intensity are also related through the characteristic B–H curve of the permanent-magnet material. The intersection of the load line and the B–H curve determines the (B, H) operating point of the magnetic circuit [40].

The slope of the load line is dictated by the dimensions of the magnet and the air gap. Equation (3.1) shows that the force constant is proportional to the magnetic flux density. Thus the design problem consists of selecting the forcing element's dimensions so as to maximize the air-gap flux density B_a. One approach is to minimize the permanent-magnet volume V_m, which will help reduce the mass and cost of the system too. The offset introduced by the applied current I may be neglected during preliminary sizing. For a given size air gap, Equations (3.3)–(3.5) show that the magnet volume required to produce B_a is

$$\begin{aligned} V_m &= l_m A_m \\ &= |(-l_a H_a/2H_m)\,(A_a B_a/B_m)| \\ &= \frac{V_a B_a^2}{2\mu_0 |B_m H_m|} \end{aligned} \tag{3.7}$$

The permanent-magnet volume is proportional to the air-gap volume and the square of the air-gap flux density. Fixing these values, the magnet volume is minimized

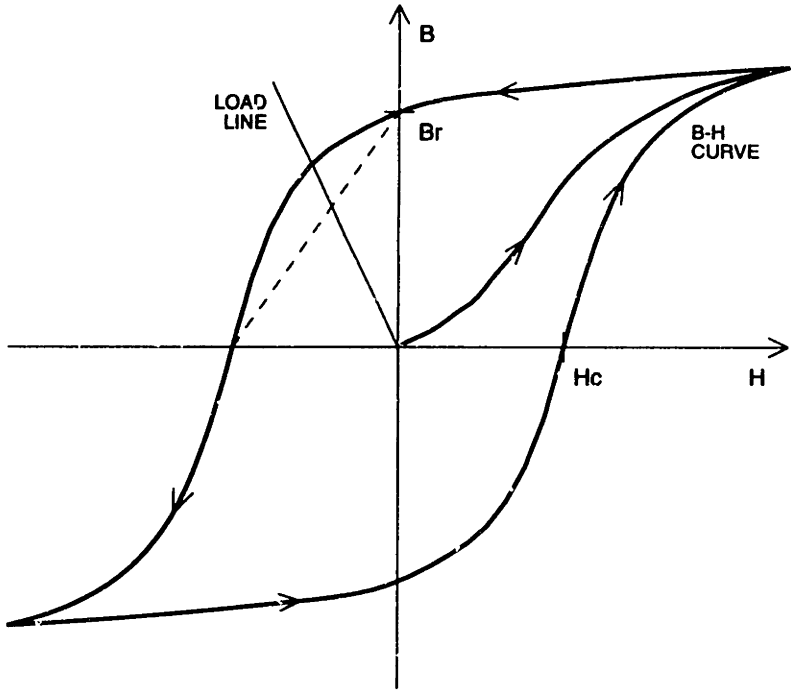

Figure 3-2: B–H curve for a typical permanent-magnet material. Load line and assumed demagnetization curve (dashed line) are also shown.

by operating on the load line that maximizes the energy product $|B_m H_m|$. Magnet selection tables typically include $BH_{\max}$ and the slope of the load line at $BH_{\max}$ for a given material. The magnets and the air gap may then be sized so that the system's load line, Equation (3.6), has this optimal slope.

The saturation and hysteresis properties of magnetic materials result in complicated B–H loci that depend on the material's magnetization history. An envelope that is convenient for material characterization is the B–H curve that describes the state of the material in a closed magnetic circuit as it is brought to saturation, demagnetized, saturated in the opposite direction, and then demagnetized again under the influence of an external magnetic field (Figure 3-2). Two critical parameters may be obtained from such a curve [40]. The residual flux density B_R is the maximum flux density under closed-circuit conditions that remains after removal of the external field, and the coercive force H_C is the external field intensity required to demagnetize the material completely after saturation.

Once a permanent magnet has been initially magnetized, the standard practice

is to subject it to a demagnetizing magnetic field of intensity H_s that is stronger than the fields expected during use. The operating point will then lie on the so-called demagnetization curve [40]. If the value of H_s is not known, a conservative approximation is to use the line between $-H_C$ and B_R; this will underestimate B_m for most values of H_m.

Assume the demagnetization curve is simply $B_m = B_R(1 + H_m/H_C)$. This expression may be used to eliminate H_m from Equation (3.6). The flux density in each permanent magnet is then

$$B_m = \frac{B_R}{1 + \alpha_{ma}} \left(1 + \frac{1}{4H_C l_m} N_e I\right) \tag{3.8}$$

where

$$\alpha_{ma} = \frac{B_R}{\mu_0 H_C} \frac{A_m}{A_a} \frac{l_a}{2l_m}$$

The parameter α_{ma} includes characteristics of both the B–H curve and the load line.

Given B_m, the actuator's force constant may be determined. From Equation (3.5), the flux density in each air gap is $B_a = (A_m/A_a)\, B_m$. Let $A_m = d_m h_m$ and $A_a = d_a h_a$, where d_m is the out-of-plane dimension of the magnet (the length of the rectangular bar) and d_a is the width of the flux path in the air gap. Assume that N_1 turns of the coil lie in the flux path of the upper air gap and that N_2 turns lie in the flux path of the lower air gap. When the coil carries a current I, the resultant Lorentz force is

$$\begin{aligned} F &= d_a B_a (N_1 + N_2) I \\ &= d_a (N_1 + N_2) \frac{A_m}{A_a} \frac{B_R}{1 + \alpha_{ma}} \left(1 + \frac{1}{4H_C l_m} N_e I\right) I \end{aligned} \tag{3.9}$$

This force is oriented vertically; positive values correspond to upward forces. If the coil lies completely in the flux path, then $N_1 = N_2 = N$ where N is the total number of turns in the coil. The force constant is then

$$F/I = 2 d_a N \frac{A_m}{A_a} \frac{B_R}{1 + \alpha_{ma}} \tag{3.10}$$

If $N_e \neq 0$, notice that Equation (3.9) is a nonlinear function of the current I.

The forcing elements should be designed to maximize the force constant, since

Table 3.1: Comparison of permanent-magnet characterisitics.

Material	B_R (kG)	H_C (kOe)	$BH_{\max}$ (MG·Oe)	Slope at $BH_{\max}$	Curie Temp. (°C)	Density (g/cm^3)	Relative Cost
NdFeB	12.3	11.3	35	1.1	310	7.4	65
SmCo	9.5	8.6	22	1.0	825	8.3	100
Alnico	12.8	0.64	5.5	18	890	7.3	15
Ceramic	3.8	2.4	3.4	1.1	460	5.0	3

this minimizes the current required to produce a given force; low currents simplify the drive electronics and minimize the I^2R losses. The range of values for d_a and N are limited by the actuator geometry, while B_R is determined by the material properties of the permanent magnet. Both the geometry and the material properties affect α_{ma}.

As mentioned above, rare-earth elements are the material of choice for compact electrodynamic actuators. The two common compositions for rare-earth permanent magnets are neodymium iron boron (NdFeB) and samarium cobalt (SmCo). Some important characteristics of these materials are presented in Table 3.1; values for Alnico and ceramic permanent magnets are included for comparison [49]. NdFeB magnets have an extremely attractive B–H curve as measured by B_R, H_C, and $BH_{\max}$. They are also less dense, less susceptible to cracking and chipping, and less expensive than SmCo magnets. On the other hand, SmCo magnets are less susceptible to corrosion and can be used at much higher temperatures. These last two factors do not play a role in the cryocooler-vibration cancellation application, so NdFeB magnets were selected.

3.1.2 Coil Trade-Offs

Before moving on to the detailed sizing of the actuator, some trade-offs associated with the coil deserve attention. The NI term in the Lorentz-force equation is just as important as the B term. Moreover, it is the coil that determines the electrical properties and the power consumption of the actuator.

Hollis *et al.* devoted a considerable amount of effort to developing an efficient coil

design [41]. Each coil consists of 95 turns of flat copper wire with high-temperature insulation. This is wound onto a 25 × 4 mm coil form and sandwiched between thin aluminum sheets with high-temperature epoxy. The aluminum sheets provide a conductive heat path, allowing the coil to carry currents as high as 3 A before the insulation reaches its break-down temperature of 220°C. The coil resistance is 2.1 Ω, and the inductance is 0.24 mH.

This design could not be duplicated for the multi-axis actuator; thin flat wire is exorbitantly expensive. Of course, conventional round wire can be used instead. The wire gauge is then a design parameter.

Retaining the magnetic circuit notation, denote the thickness of the coil by l_c: the "length" of the flux path through the coil. The coil must obviously fit in the air gap, so $l_c < l_a$. Let the perpendicular dimensions be d_c and h_c, and assume these match the air gap dimensions d_a and h_a. For preliminary sizing, consider a coil form with a rectangular central section and semi-circular ends of diameter h_f (Figure 3-1).

Given this coil geometry, consider making the coil by winding wire of radius r_w onto the form. The coil's entire cross-sectional area $A_c = l_c h_c$ will not consist of conductive material; assume a conductor fill factor of β to account for packing inefficiency, insulation, and epoxy. The total number of turns in the coil is then

$$N = \beta A_c / \pi r_w^2 \tag{3.11}$$

and the average length of a turn is

$$l_w = 2d_c + \pi(h_f + h_c) \tag{3.12}$$

The number of turns may be increased by selecting finer gauge wire.

The electrical properties of the coil may be determined from the dimensions of the wire and from the magnetic circuit analysis. The resistance of a conductor of length l and cross-sectional area A is $R = l/\sigma A$ where σ is the material's conductivity, *e.g.* $\sigma = 58 \times 10^6$ S/m for copper [48]. Thus the coil's resistance is

$$R_c = N l_w / \sigma \pi r_w^2$$

$$= \beta l_w A_c / \sigma \pi^2 r_w^4 \tag{3.13}$$

Notice that the resistance is proportional to $1/r_w^4$; any attempt to increase N by using fine wire will also drastically increase R_c.

Assume that the current has negligible effect on the magnetic flux density. Then, from Equation (3.10), the current required to generate a force F is

$$\begin{aligned} I &= F/(2d_a N B_a) \\ &= \frac{F}{2d_a B_a} \frac{\pi r_w^2}{\beta A_c} \end{aligned} \tag{3.14}$$

The current is proportional to r_w^2, so finer wire will reduce the current for a given force level. The power loss associated with this current is

$$P = I^2 R = \left(\frac{F}{2d_a B_a}\right)^2 \frac{l_w}{\sigma \beta A_c} \tag{3.15}$$

Notice that the design of the magnetic circuit and the overall coil geometry affect the power loss, but the wire gauge does not appear explicitly. A more accurate model might modify the fill factor: $\beta = \beta(r_w)$.

Assume that the coil's impedance is primarily resistive in the bandwidth of the cooler's first few harmonics. Then the current from Equation (3.14) is associated with a voltage drop

$$V = IR = \frac{F}{2d_a B_a} \frac{l_w}{\sigma \pi r_w^2} \tag{3.16}$$

Thus, the coil's drive electronics must provide a current which is proportional to r_w^2 and a voltage which is proportional to $1/r_w^2$. Once the other parameters have been specified, Equations (3.14) and (3.16) may be used to select a value of r_w that does not put unreasonable demands on the drive electronics.

3.2 Mechanical Design

Several factors govern the design of the actuator's configuration and its dynamics. The functional requirement of being able to generate an axial force and two orthogonal lateral torques means that the actuator must incorporate at least three single-axis

forcers. The space available for these forcers is constrained by the desire for compatibility with existing hardware. But compactness must be traded off against fabrication complexity. Furthermore, as this is a prototype, the design should facilitate disassembly and re-assembly for inspection or replacement of any component. Finally, in order to simplify the design of the active cancellation system, the bandwidth spanned by the cooler's first few harmonics should be relatively free of actuator dynamics.

3.2.1 Configuration

A vacuum bonnet had been built previously for the expander of the Hughes cryocooler. It provides a vacuum housing to reduce the heat load on the expander, and it acts as a mounting fixture for vibration characterization on JPL's Six-Axis Dynamometer. The decision was made to size the actuator so as to allow integrated testing of both the cooler and the cancellation system using the vacuum bonnet and the dynamometer. However, the actuator should not impede access to the cryocooler.

The mounting flange on the expander has an outer diameter of 1.50 in. (38.1 mm), and the vacuum bonnet has an outer diameter of 3.25 in. (82.6 mm). These two dimensions define an annulus in which the forcers must fit. The expander protudes 0.94 in. (23.9 mm) above the upper surface of the vacuum bonnet; the actuator height should not greatly exceed this.

Hollis *et al.* adopted a hexagonal ring structure for the magic wrist [41]. Six forcers are alternately arranged horizontally and vertically around the ring. The inner and outer permanent magnets are fixed to the base and form the stator element. The "flotor" element is a hexagonal shell containing the coils and supporting a work platform. The flotor is levitated by means of a DC current; a payload of 32.5 N requires a 60 W power expenditure.

The multi-axis actuator requires only three vertical forcers. The hexagonal layout of the magic wrist is retained, but the horizontal forcers are replaced by flexures. The flexures support the moving mass without requiring power. This is important for spacecraft applications, since it eliminates the need for a power-up launch.

The stroke associated with a given force F is $x = F/m\omega^2$ in the mass-dominated

region of the flexure dynamics. The magic wrist's moving-coil flotor minimizes the moving mass, which might lead to unacceptably large motion. Excessive motion stresses the flexures, and it modifies the actuator's force constant by changing N_e. Additionally, if rotations are involved, the size of the air gap limits the available travel. Rather than a moving coil, the multi-axis actuator uses a moving-magnet arrangement. Desirable stroke levels may be achieved through the design of the structure housing the magnets.

This structure should not consist of too many elements, due to the limited space. In an attempt to reduce the part count and the complexity of the actuator, only the outer ring of magnets is free to move. The inner ring of magnets is incorporated into the actuator's base, to which the coils are also attached (Figures 3-3 and 3-4). While this configuration sacrifices half of the actuator's force capability, it simplifies the connections between the moving and the stationary components. It also permits an assembly sequence that provides good access to all fasteners.

The first step in the detailed sizing of the actuator was determining the dimensions of the magnets. Due to the limited number required, the magnets were selected from the supplier's available stock [49]. The supplier also performed all needed machining of the rare-earth magnets, which are quite brittle. Rectangular bars of NdFeB 35, 0.79 in. (20.0 mm) long and 0.30 in. (7.6 mm) wide, were ground to a thickness of 0.110 in. (2.79 mm), and 30° chamfers were added to the upper and lower edges. Other components mate to the chamfers to clamp the magnets in place, eliminating the need for adhesives.

Each pair of magnets is attached to a return plate made of permeable 1018 steel. The width of the return plate matches the length of the magnets, 0.79 in. (20.0 mm), while the 1.00 in. (25.4 mm) height was selected to ensure minimal interaction between the fields of the two magnets. The steel is 0.125 in. (3.18 mm) thick, which represents a compromise between minimizing the volume required for each forcer and providing a large enough flux path to prevent saturation of the steel.

An aluminum keeper with chamfered edges separates the magnets on the return plate. Its dimensions are $0.79 \times 0.525 \times 0.090$ in. ($20.0 \times 13.34 \times 2.29$ mm). It is held

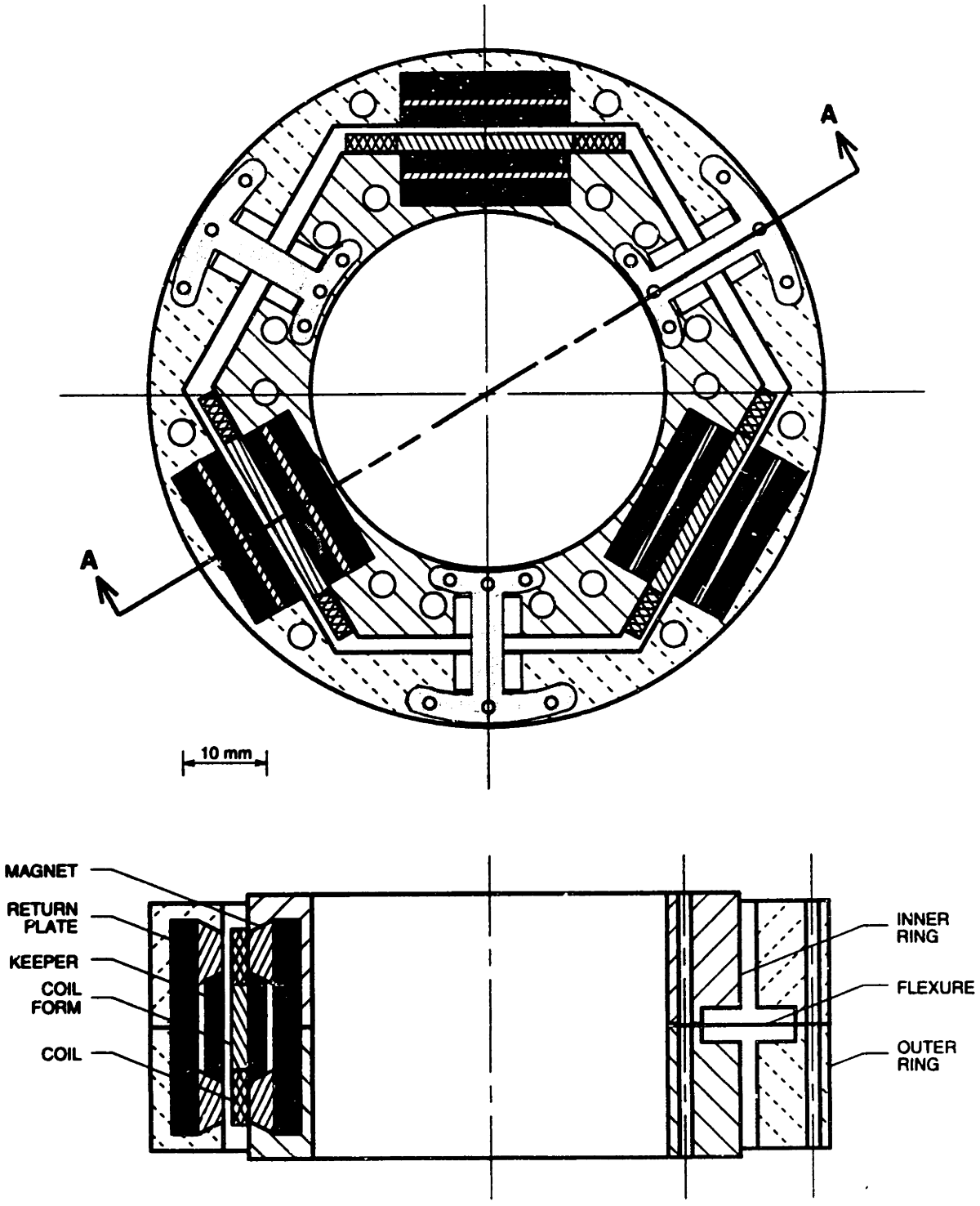

Figure 3-3: Layout and cross-section of the multi-axis actuator. Drawn to scale; the outer diameter of the outer ring is 80.8 mm.

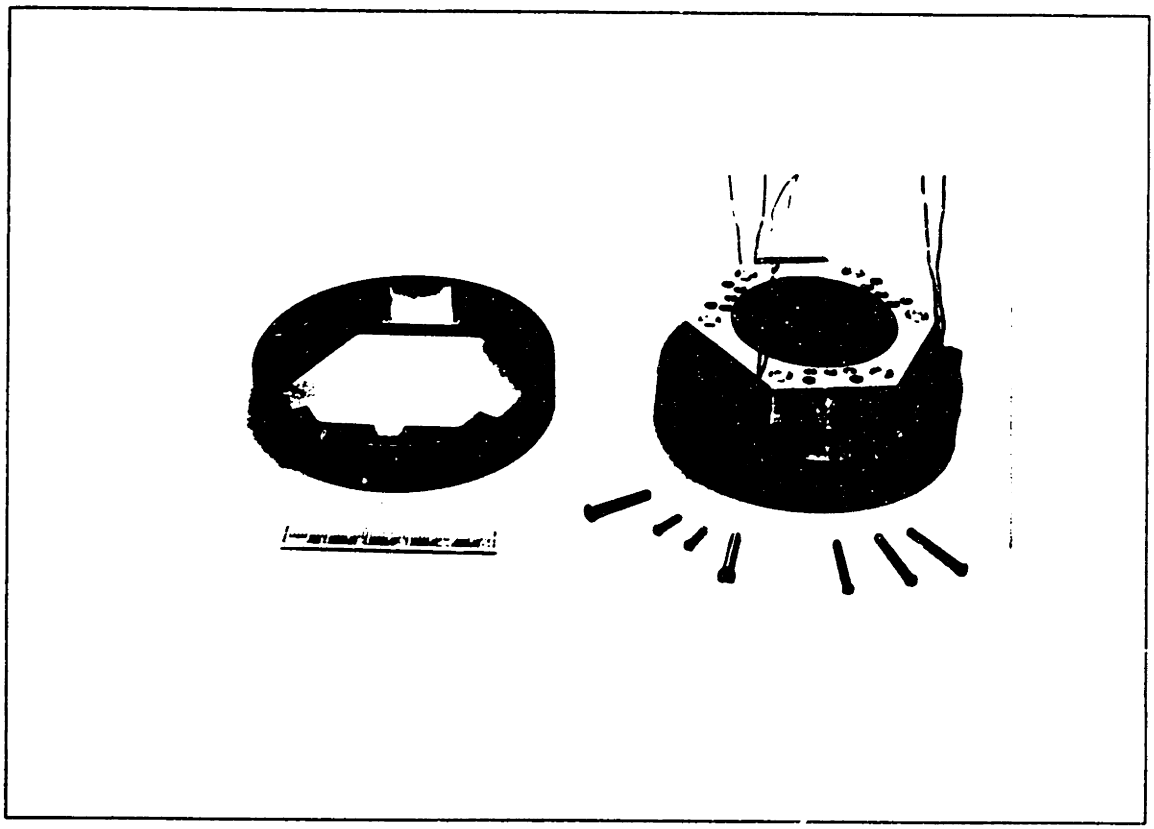

Figure 3-4: The multi-axis actuator with the upper half of the outer ring removed.

in position by machine screws that pass through the rings housing the magnets.

In the case of the inner ring, these screws also pass through an aluminum coil form, which is 0.80 × 0.40 × 0.090 in. (20.3 × 10.2 × 2.29 mm) with rounded corners. During manufacture of the coils [50], each coil form was sandwiched between Teflon and aluminum sheets. Wire of the desired gauge was embedded in high-temperature epoxy (241A/B) and then wound onto the form to a height of 0.25 in. (6.4 mm). The entire coil was then impregnated with 235A/B epoxy, and the Teflon and aluminum sheets were removed. The epoxy protects the wire and helps conduct heat to the coil form, which is thermally coupled to the keeper and the housing structure by means of Thermalloy thermal grease.

The inner ring is the stationary element that is attached to the vacuum bonnet. It is made of aluminum to reduce the weight of the actuator. It has a cylindrical cut-out, 1.68 in. (42.7 mm) in diameter, to make room for the cooler's expander. The outer surface is an irregular hexagon, with long faces of 1.410 in. (35.81 mm) alternating

with short faces of 1.252 in. (31.80 mm)—this provides clearance for the coils. The ring is composed of an upper and a lower half, both of which have cut-outs on the long faces to accommodate the magnets, the return plates, and the keepers. The cut-outs have chamfered lips to retain the magnets. There are also cut-outs on the short faces for the flexures. The total height of the inner ring is 1.25 in. (31.8 mm).

The moving outer ring is supported from the inner ring by means of the flexures. Its basic structure is similar to the inner ring: it has an upper and a lower half, as well as cut-outs for the magnetic components and the flexures. However, it is made of brass to increase the actuator's moving mass. The inner surface is a regular hexagon with faces of 1.443 in. (36.65 mm). The ring's outer diameter is 3.18 in. (80.8 mm), and the overall height is 1.15 in. (29.2 mm), which is slightly shorter than the inner ring to ensure the moving mass does not strike the vacuum bonnet.

These pieces are fastened together with machine screws. This allows the actuator to be disassembled for inspection during testing. Adhesives could be used to lock some components in place, but the associated outgassing can be a problem in certain scientific instruments.

3.2.2 Performance Evaluation

With the actuator configuration specified, some of the previous expressions may be evaluated.

The magnets were modelled as rectangular bars using the average width of the chamfered pieces: $l_m = 2.79$ mm, $h_m = 6.0$ mm, and $d_m = 20.0$ mm; no attempt was made to account for any flux focusing caused by the chamfers. Neglecting fringe effects, the same dimensions were used for the air-gap cross-sectional area: $h_a = 6.0$ mm and $d_a = 20.0$ mm. The length of the air-gap flux path was taken as $l_a = 3.05$ mm.

Using these dimensions, the slope of the load line as given by Equation (3.6) is $(2l_m A_a / l_a A_m) = 2 \times 2.79/3.05 = 1.83$. This is somewhat higher than the slope at $BH_{\max}$ listed in Table 3.1 for NdFeB, although the performance loss is probably not

too severe. The magnetic parameter α_{ma} is

$$\alpha_{ma} = \frac{12.3}{11.3}\frac{120}{120}\frac{3.05}{5.58} = 0.595$$

so the flux density in the permanent magnets and in the air gaps ($A_a = A_m$) is

$$B_a = B_m = B_R/(1 + \alpha_{ma}) = 0.77 \text{ T} \tag{3.17}$$

Based on a much more detailed analysis, Hollis *et al.* reported an average gap flux density of 0.6 T for an air gap of 6.35 mm and $30 \times 12 \times 6.35$ mm NdFeB magnets [41]. The figures for the multi-axis actuator therefore look reasonable.

The cross-sectional area of the return plate is somewhat smaller than the magnet's cross-sectional area: $h_r = 3.18$ mm and $d_r = 20.0$ mm. This concentrates the flux density in the return plate, resulting in a value of $(A_m/A_r)B_m = (6.0/3.18)0.77 = 1.5$ T. The saturation flux density for low-carbon steel is 2.1 T [51], so it is unlikely that the return plates will saturate.

The other expressions are affected by the coil design. The force constant per turn is given by Equation (3.10): $2d_aB_a = 31$ mN/A·turn. This expression also appears in Equations (3.14) and (3.16). Noting that $l_w = 92.2$ mm and $A_c = 14.7$ mm^2, and assuming a fill factor of $\beta = 0.5$, these equations may be evaluated parametrically as functions of F and r_w. Figure 3-5 shows the current and voltage requirements for various wire gauges. In order to avoid extreme values of current or voltage, the coils were made from 33 AWG wire, which was spliced to 26 AWG wire for connection to the drive electronics.

Having selected the wire gauge, the coil may be fully characterized. The radius of 33 AWG wire is approximately 0.09 mm. From Equation (3.11), the total number of turns in the coil is 290, so each forcer has a force constant of 9.0 N/A. Considering the smaller air gap and the greater number of turns in the multi-axis actuator's forcer, this force constant is comparable to the 6.2 N/A value measured by Hollis *et al.* [41].

The electrical properties of the coil may also be calculated. The resistance of each coil, Equation (3.13), is 18 Ω. This is considerably higher than the input impedance of most shakers, making the power amplifiers recommended for these shakers inappro-

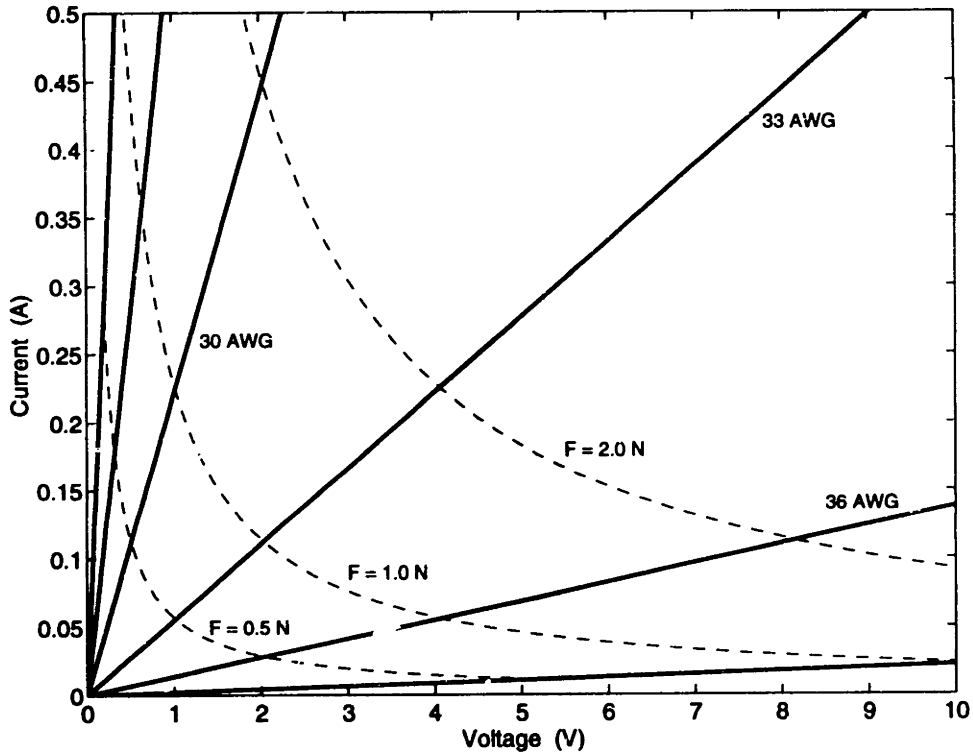

Figure 3-5: Current and voltage required to generate specified force levels for various coil wire gauges. Six wire gauges are shown (solid lines): 26 AWG, 28 AWG, 30 AWG, 33 AWG, 36 AWG, and 40 AWG. Dashed lines indicate curves of constant force.

priate for the multi-axis actuator. The power consumption is determined by the force level at which the actuator is driven. From Equation (3.15), a normalized measure is $P/F^2 = 0.23$ W/N^2. Unless large forces are required, the dissipation of this power should not pose any problems thermally.

3.2.3 Dynamics

The purpose of each forcer is to generate vertical reaction forces with which the cryocooler vibration may be cancelled. In the electrodynamic system, the reaction forces are provided by the Lorentz force. But this force is applied to both the coil and the magnets. The net transmitted force is greatly affected by the multi-axis actuator's configuration.

Each forcer consists of two pairs of magnets and a forcer. One pair of magnets and the coil are attached to the actuator's inner ring; the other pair of magnets is attached

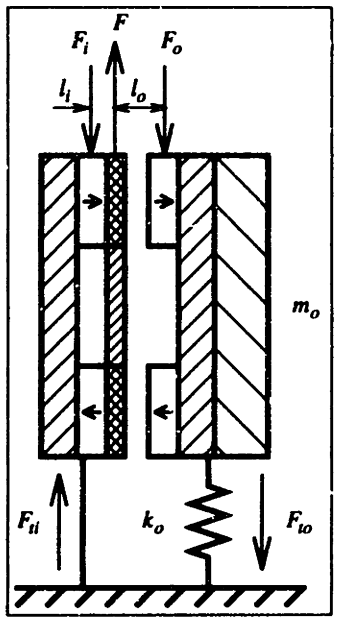

Figure 3-6: Single degree-of-freedom model of the forcer dynamics, indicating applied and transmitted forces. The flexure stiffness is represented by k_o, and the mass of the outer ring is represented by m_o.

to the outer ring. Flexures connect the outer ring to the inner ring. Dynamically, the flexures may be modelled as springs supporting the mass of the outer ring. For example, Figure 3-6 shows a model of a single forcer.

The Lorentz force F is shown acting through the center of the coil, and the forces F_i and F_o are assumed to act through the centers of the magnets. The net transmitted force is $F_t = F_{ti} - F_{to}$. Since the inner ring is directly connected to the base, neither F nor F_i are attenuated, thus $F_{ti} = F - F_i$. The outer ring, on the other hand, is connected through the spring, which isolates the outer ring at high frequencies

$$F_{to} = \frac{F_o}{1 - (\omega/\omega_o)^2} \tag{3.18}$$

where $\omega_o = \sqrt{k_o/m_o}$. The net transmitted force is then

$$F_t = \frac{-(\omega/\omega_o)^2}{1 - (\omega/\omega_o)^2} \alpha_l F \tag{3.19}$$

where $\alpha_l = 1/2$ is a transmission factor to account for the fact that only one pair of magnets is free to move. Below resonance the forcer acts like a displacement actuator, so the transmitted force is greatly attenuated and there is a sign change.

Above resonance the forcer acts like a force actuator, although the high-frequency gain is reduced by the transmission factor.

The transmission factor effectively reduces the actuator's force constant. With the multi-axis actuator's configuration, the transmission factor is $\alpha_l = 1/2$, and the reduced force constant is $0.5 \times 9.0 = 4.5$ N/A. This is the "price" of the simplified mechanical configuration. If both the inner and the outer magnets had been supported by flexures, the full force constant of 9.0 N/A would have been retained.

For computational purposes, the full force constant may be used if it is noted that it refers to the Lorentz force rather than the transmitted force. The transmission factor relates these two forces. For example, to apply a 1.0 N force to the base, the required Lorentz force is $1.0/0.50 = 2.0$ N, and the actuator must be driven with $2.0/9.0 = 0.22$ A of current. Notice that the force levels in Figure 3-5 refer to the Lorentz force, not the transmitted force.

3.2.4 Flexures

The natural frequency ω_o plays an important role in Equation (3.19). This frequency is determined by the transverse stiffness of the flexures and the mass of the outer ring. In order to design these elements, an acceptable natural frequency was selected, and trade-offs on parameter values were conducted.

Several factors affect the choice of a natural frequency. First and foremost is the frequency dependence of the actuator's gain (Figure 3-7). The magnitude of the transmissibility drops below α_l for $\omega < \omega_o/\sqrt{2}$, further decreasing the actuator's effective force constant. To avoid this performance loss, the natural frequency should be as low as possible. But low natural frequencies lead to large static deflections: $y_{st} = g/\omega_o^2$ where g is the acceleration due to gravity. These deflections can result in significant stresses and can affect the alignment of components. A common lower bound on the natural frequency is 20 Hz, for which the static deflection is 0.6 mm. In the case of spacecraft applications, the launch environment often places further restrictions on the natural frequencies. For example, instrument resonances below 50 Hz are prohibited on the NASA EOS platforms [19].

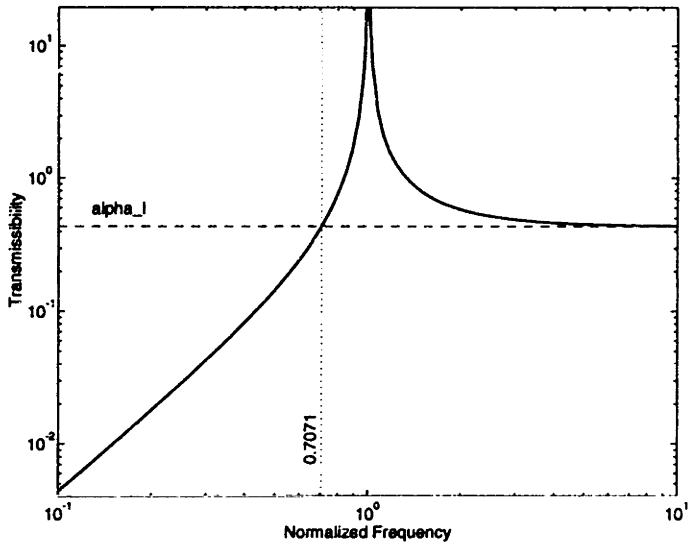

Figure 3-7: Transmissibility as a function of the normalized frequency, ω/ω_o.

An additional complication with the cryocooler cancellation application is the fact that the drive frequency of the Hughes cooler varies between 25 and 31 Hz. The resonance should be kept out of this bandwidth and the bandwidths of the harmonics, *i.e.* 50–62 Hz, 75–93 Hz, etc. Rather than attempting to place the resonance between 20 and 25 Hz, the resonance was moved above the bandwidth of the cooler's fundamental. A design value of 40 Hz was selected to maximize the margin for error. Furthermore, this natural frequency does not sacrifice too much of the actuator's force constant since $40/\sqrt{2} = 28$ Hz, which is the center of the bandwidth of the cooler's fundamental.

A single-blade flexure design was chosen for simplicity. Each flexure consists of a thin beam of rectangular cross-section. One end is clamped between the upper and lower halves of the inner ring, and the other end is clamped between the halves of the outer ring. For design purposes, let b denote the width of the flexure, h the thickness, and l the distance between the clamps. The equivalent spring constant may be derived by considering the force required to impose a tip displacement y_{tip} on a clamped-guided beam [52]

$$F = \left(12EI/l^3\right) y_{\text{tip}} = k_o\, y_{\text{tip}} \tag{3.20}$$

where $I = bh^3/12$ for a beam of rectangular cross-section. The equivalent spring constant is therefore

$$k_o = bh^3 E/l^3 \tag{3.21}$$

Three flexures support the outer ring, so each flexure supports a mass $m_o = M/3$ where M is the mass of the outer ring. The natural frequency is then $\omega_o^2 = 3k_o/M$. Substituting Equation (3.21) into this expression and letting $f_o = \omega_o/2\pi$, the relationship between the flexure's width and the natural frequency may be established

$$b = \frac{4\pi^2 f_o^2 M}{3E}\left(\frac{l}{h}\right)^3 \tag{3.22}$$

The values of M and l are determined by the actuator's configuration, while E depends on the choice of material for the flexures. Shim stock is available in discrete thicknesses, which determines h.

Another important parameter to consider when designing the flexures is the root bending stress. The stress due to the weight of the outer ring is a useful measure by which to compare designs; motion of the outer ring will incur additional stresses. For a clamped-guided beam subject to a tip load $gM/3$, the maximum stress is

$$\begin{aligned} \sigma_{\max} &= g\frac{lM}{bh^2} \\ &= \frac{3gE}{4\pi^2 f_o^2}\frac{h}{l^2} \end{aligned} \tag{3.23}$$

Notice that if the flexures are designed for a certain natural frequency, the maximum stress due to the static load is independent of the mass of the outer ring (assuming linear behavior).

A number of possible designs were compared. Two different outer rings were considered. The aluminum one ($\rho = 2800$ kg/m^3) has a mass of 0.14 kg, while the brass one ($\rho = 8400$ kg/m^3) has a mass of 0.32 kg. Some of this mass was due to the steel return plates and the rare-earth magnets and was therefore not affected by the choice of material.

The flexure length was always $l = 0.445$ in. (11.30 mm). Two different flexure materials were examined. Beryllium copper (BeCu) has a Young's modulus of 130 GPa

Table 3.2: Flexure width and root bending stress for 40 Hz bounce mode.

Aluminum Outer Ring $M = 0.14$ kg

h (mm)	b (mm)		σ_{max} (MPa)		$\sigma_{max}/\sigma_{yield}$	
	BeCu	SS	BeCu	SS	BeCu	SS
0.127	16.0	10.9	60.2	88.1	6.2%	13%
0.254	2.00	1.37	121	176	12%	26%
0.381	0.59	0.41	181	264	19%	38%

Brass Outer Ring $M = 0.32$ kg

h (mm)	b (mm)		σ_{max} (MPa)		$\sigma_{max}/\sigma_{yield}$	
	BeCu	SS	BeCu	SS	BeCu	SS
0.127	36.5	25.0	60.2	88.1	6.2%	13%
0.254	4.56	3.12	121	176	12%	26%
0.381	1.35	0.93	181	264	19%	38%

and a yield stress of 970 MPa, while stainless steel (SS) has a Young's modulus of 190 GPa and a yield stress of 690 MPa [53]. Three different shim-stock gauges were available: 5 mil. (0.127 mm), 10 mil. (0.254 mm), and 15 mil. (0.381 mm). For each combination of parameters, the flexure width required for a 40 Hz resonance was computed, as was the corresponding root bending stress. The results are presented in Table 3.2.

Clearly some of the designs are better than others. The bending stress in the 10 mil. and 15 mil. steel flexures is considerable, which shortens the fatigue life of these flexures. On the other hand, the 5 mil. flexures are quite wide, making it difficult to find space for them in the inner and outer rings. The brass outer ring was preferred in order to reduce the motion associated with a given Lorentz force. This led to the selection of the 10 mil. BeCu flexure design.

The foregoing discussion focused on a single forcer and the associated flexure. Operating three of these units in phase generates an axial force. The natural frequency of the corresponding bounce mode is then equal to the natural frequency of each forcer, which is nominally 40 Hz.

There are also natural frequencies associated with the tip and tilt modes of the actuator. These are determined by the moment of inertia of the outer ring, the

stiffness of the flexures, and their placement in the actuator. Whereas the natural frequency of the bounce mode is $\omega_b^2 = 3k_o/M$, the natural frequency of both the tip and tilt modes may be shown to be $\omega_t^2 = (3/2)k_oR^2/J$, where R is the radius of the outer tips of the flexures and J is the outer ring's mass moment of inertia about its center of mass. The frequency of these lateral modes may be related to the frequency of the bounce mode: $\omega_t/\omega_b = \sqrt{MR^2/2J}$.

In order to calculate the outer ring's mass moment of inertia, the outer ring may be approximated by a circular cylinder of uniform density with a hexagonal cut-out through the thickness. The area moment of inertia of hexagon with sides of length A is equal to the area moment of inertia of a circle of radius $0.91A$ [54]. The expression for the mass moment of inertia of a hollow right circular cylinder is $J = (M/12)(3R_1^2 + 3R_2^2 + h^2)$ where R_1 is the outer radius, R_2 is the inner radius, and h is the height. This may be used for the outer ring by replacing R_2 with $0.91A$.

The frequency ratio is then

$$(\omega_t/\omega_b)^2 = 6R^2/\left(3R_1^2 + 2.7A^2 + h^2\right) \tag{3.24}$$

From the description of the outer ring given above, these dimensions have the values $R_1 = 40.4$ mm, $A = 36.65$ mm, and $h = 29.2$ mm. The ends of the flexures are located at $R = 1.435$ in. (36.45 mm), so $\omega_t = 0.92\omega_b$. The lateral natural frequencies of the multi-axis actuator are lower than the axial resonance. This should not cause any problems since the flexures were designed for a relatively high bounce frequency of 40 Hz. Based on this model of the outer ring, the tip and tilt resonances are then 37 Hz, which is well above the bandwidth of the cooler's fundamental.

3.3 Drive Electronics

The interface between the command signal and the force output is provided by the drive electronics. This system must perform two functions. The first is converting the command signal from global coordinates (plunge, tip, and tilt) to local coil coordinates. The second is driving each coil with the appropriate current to produce the

desired force or torque.

3.3.1 Coordinate Transformations

Both the load cells (see Chapter 2) and the electrodynamic forcers are single-axis force transducers which are oriented vertically and arranged in a triangular pattern in a horizontal plane. An intuitive coordinate system for these transducers is three vertical forces, one for each transducer (Figure 2-8). This will be referred to as the local coordinate system. Any description of a general force in the local coordinate system must also be accompanied by a description of the specific arrangement of the transducers. Data from different transducer sets may be compared more conveniently using a coordinate system that consists of a vertical force through the centroid of the triangle and two torques about orthogonal horizontal axes. This will be referred to as the global coordinate system.

The basis vectors of the global coordinate system are a natural way of describing many simple dynamic systems. For example, the first three natural frequencies of the multi-axis actuator correspond to a plunge motion and two rotations about horizontal axes. The cryocooler is another example. Its vibration is primarily axial, although torque components are also present. This decomposition suggests that a control system which consists of multiple single-input single-output loops should use the global coordinate system. Each loop then sees only a single actuator mode, and the cooler vibration is separated into large and small components. Indeed, if the small components are so small that they do not have a noticeable effect on the performance metric, the loops associated with the torque coordinates may be eliminated. This would not be possible with the local coordinate system.

Thus the force transducers operate in the local coordinate system, whereas the global coordinate system is preferable for the controller. This necessitates a pair of coordinate transformations. The direct kinematic transformation determines the global coordinates given the local ones, and the inverse kinematic transformation determines the local coordinates given the global ones. These are also called the sensor and actuator transformations, respectively.

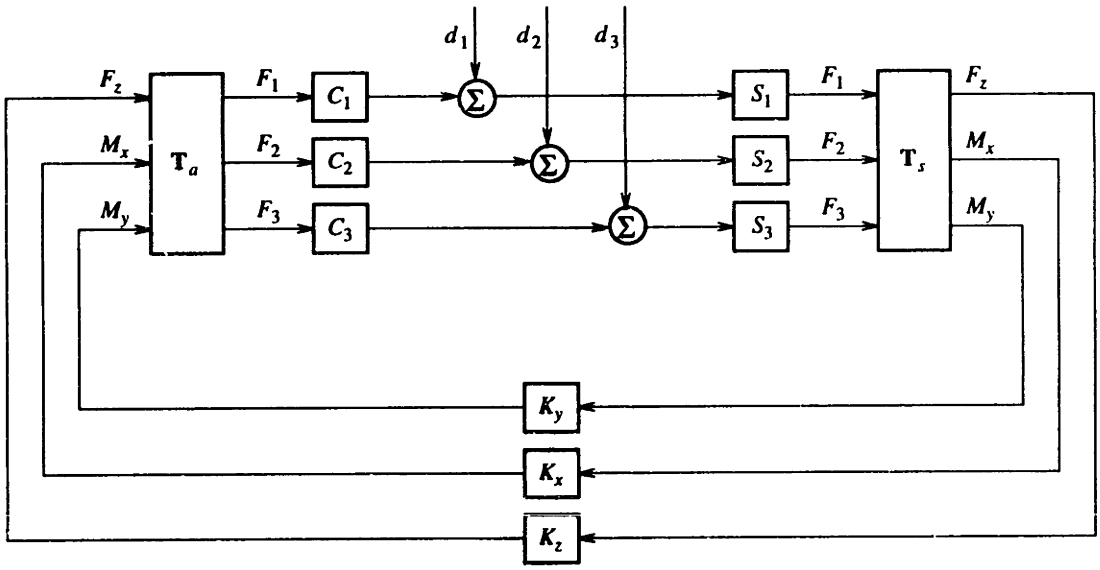

Figure 3-8: Block diagram of cancellation system, showing the transformation matrices $\mathbf{T}$, the forcers C, the disturbances d, the load cells S, and the controllers K.

Denote the forces in the global coordinate system by the column vector $\mathbf{F}_g = [F_z, M_x, M_y]$ and the forces in the local coordinate system by $\mathbf{F}_l = [F_1, F_2, F_3]$. Assume the transducers are located on a circle of radius R. Then, for the arrangement shown in Figure 2-8, the direct kinematic transformation is $\mathbf{F}_g = \mathbf{T}_s\mathbf{F}_l$ or

$$\begin{bmatrix} F_z \\ M_x \\ M_y \end{bmatrix} = \begin{bmatrix} 1 & 1 & 1 \\ -R/2 & -R/2 & R \\ -\sqrt{3}R/2 & \sqrt{3}R/2 & 0 \end{bmatrix} \begin{bmatrix} F_1 \\ F_2 \\ F_3 \end{bmatrix} \tag{3.25}$$

and the inverse kinematic transformation is $\mathbf{F}_l = \mathbf{T}_a\mathbf{F}_g$ or

$$\begin{bmatrix} F_1 \\ F_2 \\ F_3 \end{bmatrix} = \begin{bmatrix} 1/3 & -1/3R & -1/\sqrt{3}R \\ 1/3 & -1/3R & 1/\sqrt{3}R \\ 1/3 & 2/3R & 0 \end{bmatrix} \begin{bmatrix} F_z \\ M_x \\ M_y \end{bmatrix} \tag{3.26}$$

The transformation matrices $\mathbf{T}_s$ and $\mathbf{T}_a$ may be multiplied by additional matrices to scale the vectors or to account for variations in the individual transducer gains.

The transformation matrices $\mathbf{T}$ are shown in the block diagram of Figure 3-8 in relation to the forcers C, the disturbances d, the load cells S, and the controllers K.

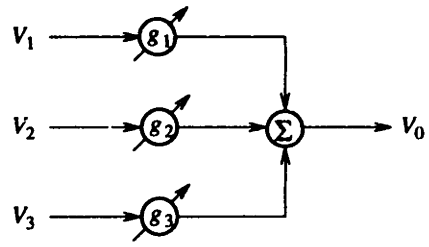

Figure 3-9: Functional elements of a variable-gain summer.

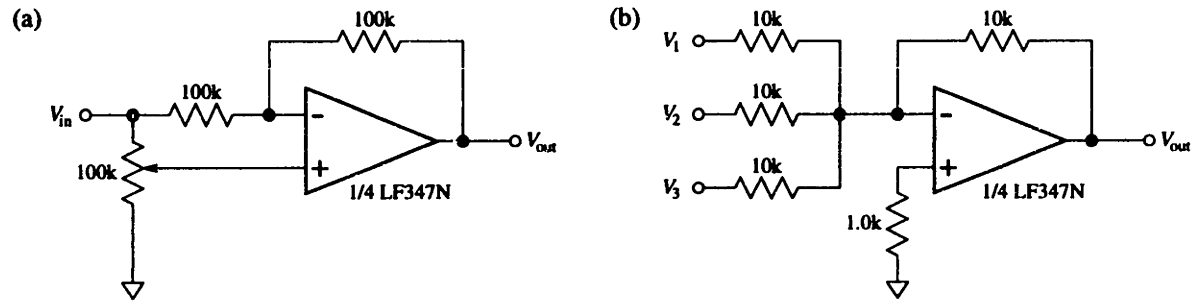

Figure 3-10: Variable-gain summer circuits: (a) variable-gain amplifier; (b) unity-gain summer.

All signals in the cryocooler force cancellation system are in analog form, making it most convenient to implement the transformation matrices with analog electronics.

One approach is to hard-wire the elements of $\mathbf{T}_s$ or $\mathbf{T}_a$ into three summers. A better choice is to implement each transformation matrix with three variable-gain summers, one of which is shown schematically in Figure 3-9. Identical circuits may then be used for both $\mathbf{T}_s$ and $\mathbf{T}_a$. Each matrix element is set using a variable-gain amplifier (Figure 3-10a) taken from Horowitz and Hill [42]. This amplifier may be adjusted to have any gain between ± 1, which allows simple calibration or even re-configuration of the transformation matrix.

Each variable-gain summer requires four op amps: three in the variable-gain stages and one in the summer (Figure 3-10b). A compact circuit may be achieved by using quad integrated circuits (ICs), which feature four op amps per package. The complete transformation-matrix circuit then occupies roughly two-thirds of a 4.5×6.5 in. printed-circuit (PC) prototyping card.

3.3.2 Power Amplifiers

The actuator transformation matrix converts the command signals from global coordinates to local coordinates. These local coordinates determine the currents with which the coils must be driven. The drive currents may be provided by power op amps configured as voltage-controlled current sources (VCCSs).

The current and voltage requirements of the multi-axis actuator are very modest for power amplifiers. From Chapter 2, the worst-case transmitted-force levels are less than 1 N per forcer, which correspond to Lorentz forces of 2.3 N per coil. The associated voltage and current levels, from Figure 3-5, are approximately 4.7 V and 0.26 A. This is well beyond the capability of conventional op amps, *e.g.* the LF411 has a maximum output current of 20 mA [42]. But power op amps can provide as much as 35 A at almost 150 V [55].

Horowitz and Hill list several power op amps with maximum output currents of 0.2–2 A [42]. A more powerful model was selected, however, based on availability. The Apex PA07A can source up to 5 A of current and can dissipate up to 67 W of power [55]. For the multi-axis actuator, two attractive features of the PA07A are its wide supply range (±12 V to ±50 V), which makes it compatible with the power supply used for the other op amps, and the fact that it was designed to drive resistive, inductive, and capacitive loads. Indeed, with a ±15 V supply, inductive loads of up to 100 mH can be safely driven with currents approaching 5 A. This is far more capability than is needed to drive the actuator's coils.

The Apex Handbook [55] describes a high-accuracy VCCS circuit for floating loads (Figure 3-11). This circuit drives the load with a current

$$I_0 = -\frac{R_2}{R_1}\frac{V_{\text{in}}}{R_s} \tag{3.27}$$

Other than the load, which represents the coil, and the power op amp itself, the most important element in this circuit is the sense resistor R_s. It should be much smaller than the impedance of the load over the operating bandwidth. Power dissipation must also be considered, since the entire current I_0 flows through the sense resistor.

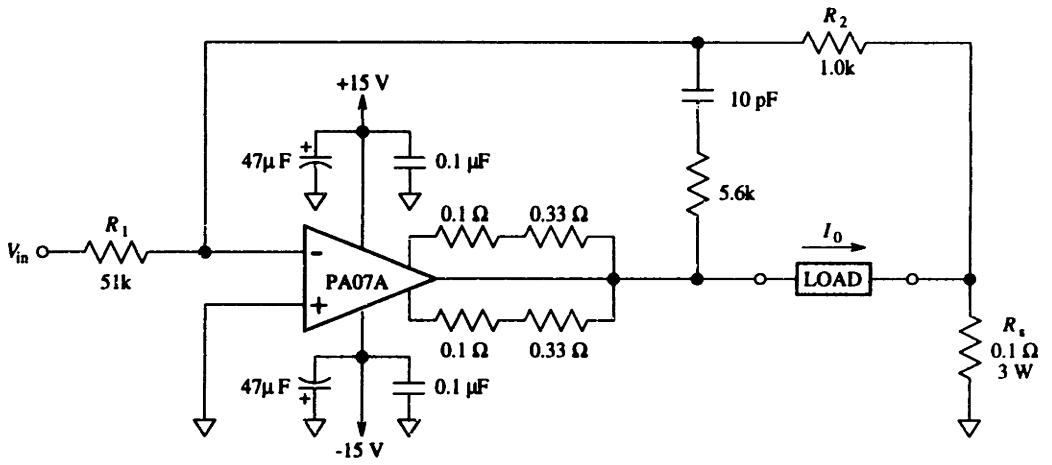

Figure 3-11: Voltage-controlled current-source circuit.

All op-amp input errors appear across this resistor, so one drawback of very small values of R_s is that these errors become more significant. The PA07A, however, has a low input-offset voltage (0.5 mV max), so a 0.1 Ω, 3 W sense resistor was selected.

Once R_s is specified, the gain of the VCCS is determined by R_1 and R_2. The feedback resistor R_2 acts as a ground-leg return impedance and should therefore be kept relatively low, *e.g.* 1 kΩ [55]. The input resistor R_1 should then be chosen to make full use of the system's dynamic range, namely, the maximum output current should correspond to an input voltage that is near full-range. During an earlier design iteration, the value of R_s was 0.33 Ω and currents as high as 0.5 A were anticipated, which led to

$$R_1 = \frac{R_2}{R_s}\frac{V_{\max}}{I_{\max}} = \frac{1000}{0.33}\frac{8.0\text{ V}}{0.5\text{ A}} = 48\text{ k}\Omega$$

Using a 51 kΩ input resistor and a 0.1 Ω sense resistor results in a VCCS gain of 0.2 A/V.

The other elements in the feedback path provide high-frequency stability. The values of these elements are not very important for the multi-axis actuator since the inductance of the coils is relatively small. However, the internal phase compensation of the PA07A is referenced to the supply lines [55], making good high-frequency grounding of these lines critical to closed-loop stability. This is accomplished with a combination of electrolytic and ceramic bypass capacitors.

The circuit also includes current-limit resistors which allow the maximum output current to be adjusted externally. As the full capability of the PA07A is not needed for the multi-axis actuator, resistor values were selected to set a current limit of 1.5 A [55]. This provides short-to-ground and short-to-supply fault protection at elevated case temperatures without sacrificing performance.

Thermal design can be critical in power op-amp applications. It is not particularly significant in the case of the multi-axis actuator because of the large margins afforded by the PA07A. Driving an 18 Ω load and using a ±15 V supply results in a maximum internal power dissipation of 3.5 W [55]. The Thermalloy 6052B TO-3 heat sink has a thermal resistance of 5.9°C/W, so the case temperature will be approximately 21°C above ambient. The junction-to-case DC thermal resistance of the PA07A is 2.6°C/W, resulting in a junction temperature 30°C above ambient. Junction temperatures as high as 125°C are considered acceptable [55], demonstrating how little demand this application puts on the power op amp.

Each coil requires its own VCCS circuit. All three may be laid out on a single 4.5 × 6.5 in. PC prototyping card. The power op amps and their heat sinks are mounted using 8-pin TO-3 mating sockets; Teflon tubing is used to prevent the PA07A pins from shorting against the anodized-aluminum heat sinks. The bypass capacitors must be placed close to the power op amps, and the ground and supply leads should be connected directly to the power supply [42]. This eliminates ground loops and ensures that IR drops along the supply leads to the power op amps do not appear on the supply voltages of the other circuits, such as the transformation matrices.

3.4 Measured Performance

None of the figures cited above were actually measured. Some are handbook values (the conductivity of copper, for example), others are design values (the coil form dimensions), and the remainder (such as the coil's resistance) are derived from simple models using these values. Many of these figures may be verified by measuring the performance of the fabricated actuator.

Starting with the coils, the as-built dimensions are in good agreement with the design values. Each coil consists of 280 turns (vs. 290 above) of 33 AWG wire rated to 220°C. The resistance measured at the 26 AWG leads was 15.1 Ω on average. This is somewhat lower than the 18 Ω value computed above, which increases the slope of the lines in Figure 3-5, *i.e.* a given value of current requires *less* voltage. The measured inductance was 0.72 mH.

There are comparable discrepancies with the mass and stiffness estimates. The total mass of the actuator is 0.559 kg, of which 0.177 kg is the inner ring and 0.372 kg is the outer ring. The outer ring is therefore more massive than had been assumed (0.32 kg). Yet the measured bounce frequency of 46 Hz is considerably greater than the design value of 40 Hz; the flexures must be stiffer than assumed.

There are two distinct sources of error in the stiffness estimates. The first is errors in the parameter values used to compute the flexure stiffness. These values include the flexure dimensions and the material properties of beryllium copper. The other source of error is the model itself. The stiffness in Equation (3.21) was derived on the basis of linear beam theory. As will be discussed in the next chapter, the actuator exhibits considerable nonlinear behavior, which is attributed to the flexure design. The nonlinearity acts to stiffen the flexures. For example, the static stiffness of the flexures increases by approximately 25% with a large-deflection model (Appendix A).

The tip and tilt frequencies, on the other hand, were found to be lower than the design values, 31 Hz rather than 37 Hz. This could be due to the simplified mass distribution assumed when computing the outer ring's mass moment of inertia, or the assumed radius R through which the spring forces act could be in error.

The actuator's multiple-input multiple-output (MIMO) transfer function was measured in the local coordinate system. Block ij in Figure 3-12 represents the SISO transfer function from the command voltage into coil j's VCCS to the output voltage of load cell i. The tip and tilt resonances at 31 Hz are clearly visible, as is the plunge resonance at 46 Hz. These modes are quite lightly damped (1–2%). The next set of modes lies between 330 Hz and 430 Hz and is attributed to vacuum-bonnet dynamics. Between 46 Hz and 330 Hz, the transfer function is relatively free of dynamics and is

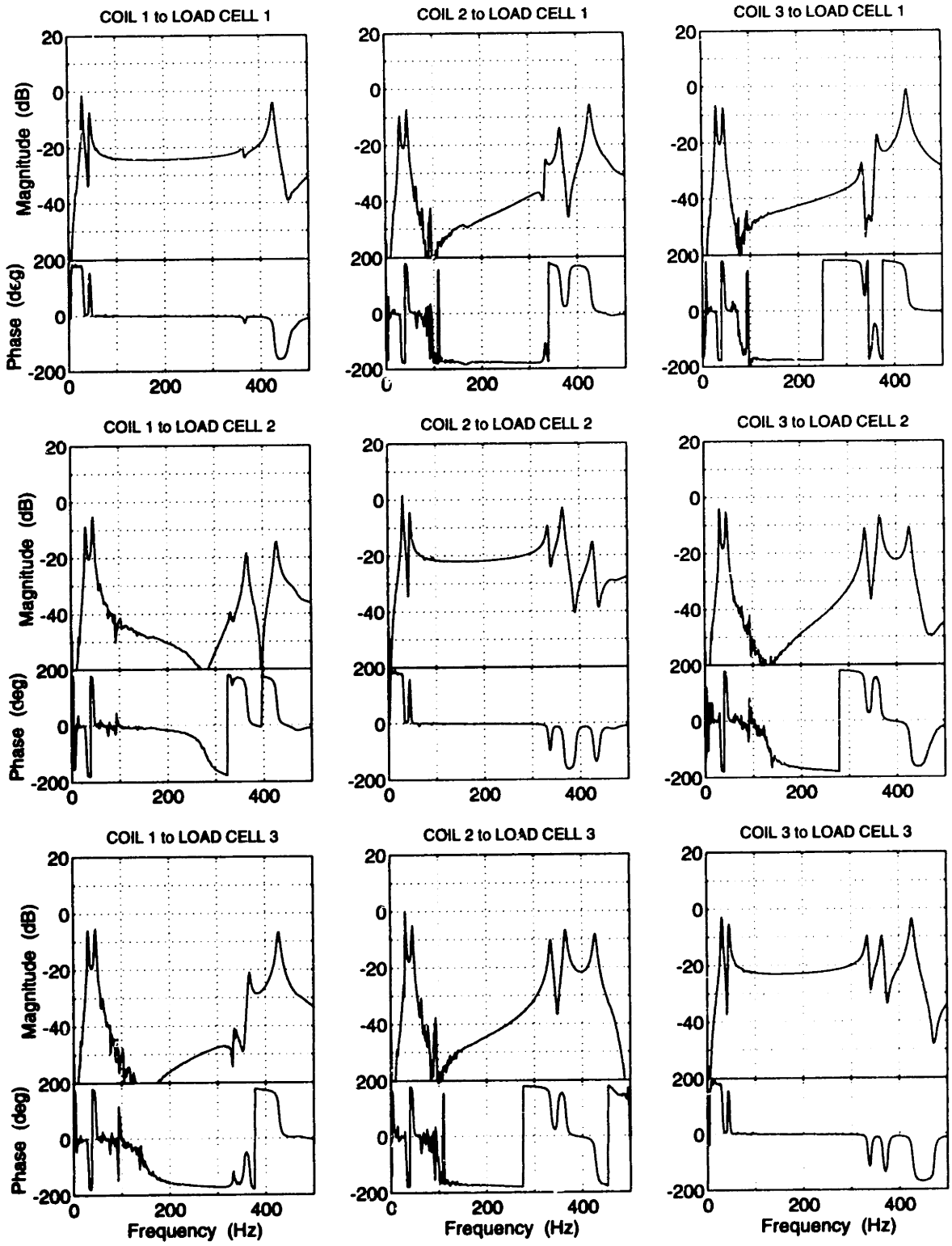

Figure 3-12: Actuator MIMO transfer function in local coordinates.

diagonally dominant.

This region was used to determine the actuator's force constant. During separate calibration tests, the VCCS's gain was found to be −0.197 A/V and the load cell's gain was found to be 0.112 V/N. The effective force constant of the forcers is therefore 3.2 N/A on average, which compares well with the design value of 3.9 N/A.

The actuator's MIMO transfer function was also measured in the global coordinate system. This was done by inserting transformation-matrix circuits at the input and the output of the multi-axis actuator as shown in Figure 3-8. The elements of the transformation matrices were adjusted to account for individual gain variations in the VCCSs, the coils, and the load cells. The measured circuit gains were

$$\mathbf{T}_s = \begin{bmatrix} +0.944 & +0.944 & +0.951 \\ -0.466 & -0.466 & +0.946 \\ -0.815 & +0.814 & -0.004 \end{bmatrix}$$

$$\mathbf{T}_a = \begin{bmatrix} +0.948 & -0.474 & -0.822 \\ +0.928 & -0.445 & +0.768 \\ +0.946 & +0.944 & -0.004 \end{bmatrix}$$

The load cells are located on a circle of radius $R = 1.025$ in. (26.04 mm) and have a gain of 0.112 V/N, so $\mathbf{T}_s$ corresponds to sensor gains of 0.106 V/N and 4.027 V/N·m in global coordinates. That is, an applied axial force $F_z = 1.0$ N will produce an axial-force signal $V_z = 0.106$ V after the transformation-matrix circuit. Similarly, the forcers are located on a circle of radius $R = 1.010$ in. (26.65 mm) and have a gain of 0.63 N/V, so $\mathbf{T}_a$ corresponds to actuator gains of 1.76 N/V and 22.5×10^{-3} N·m/V in global coordinates.

Only one of the plunge, tip, or tilt modes appears in each diagonal entry of the 3×3 transfer function in global coordinates (Figure 3-13). This reduces the phase variation of the actuator dynamics near the cooler's first and second harmonics, which occur at 25–31 Hz and 50–62 Hz, respectively. Away from the resonances, there appears to be little coupling between the two torque components M_x and M_y. The coupling between the torque components and the axial force F_z can only be considered once

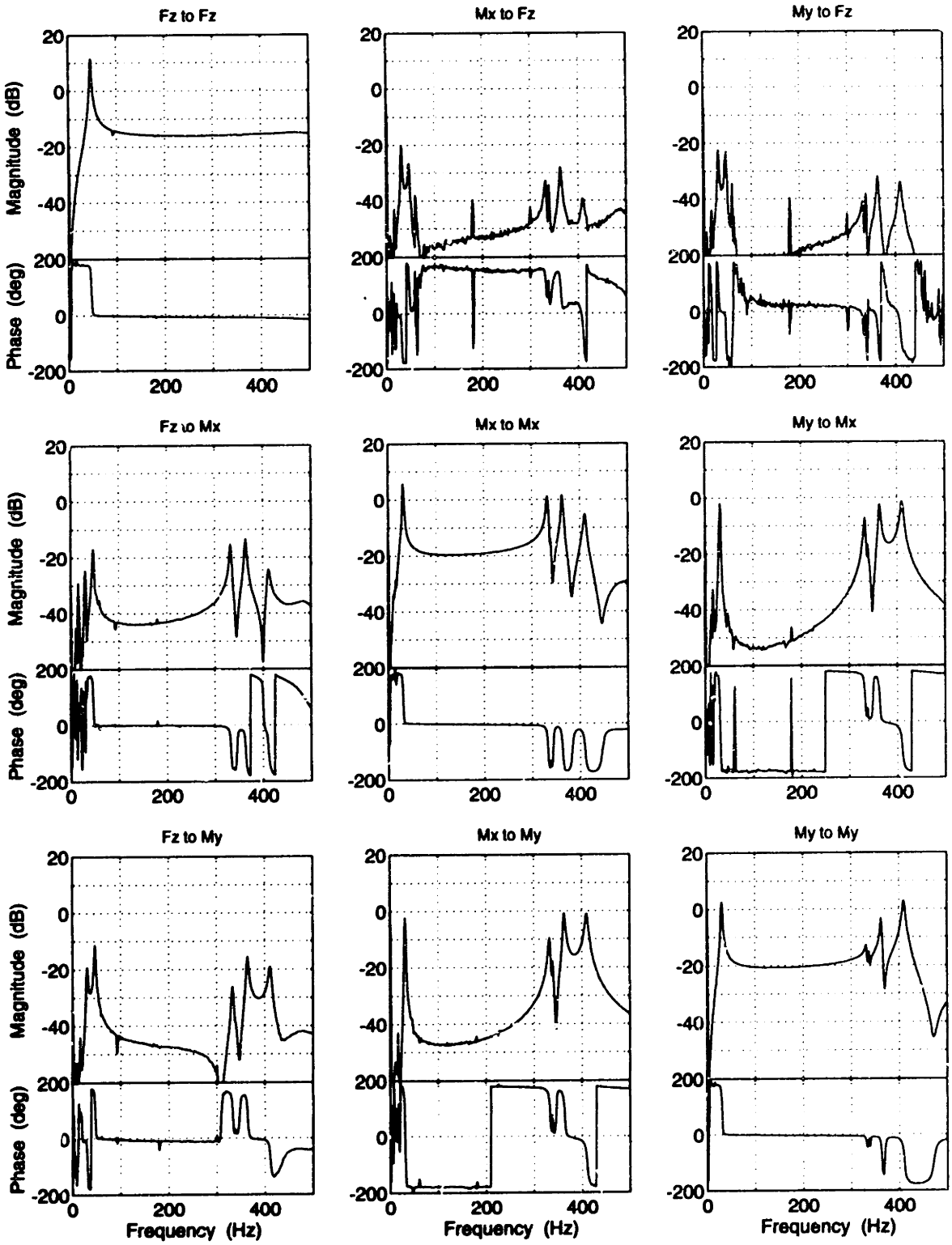

Figure 3-13: Actuator MIMO transfer function in global coordinates.

the components have been normalized—F_z has different units than M_x or M_y.

A simple, albeit rather arbitrary, normalization is to use the loop voltages. This amounts to normalizing the input components by the sensor gains and the output components by the actuator gains; no consideration is given to a performance metric. Comparing Figures 3-12 and 3-13, no significant change in the coupling of the off-diagonal and the diagonal elements is visible. A much more diagonally-dominant transfer function may be obtained by modifying T_a, but the physical interpretation of the plunge, tip, and tilt SISO loops is then lost.

3.5 Summary

The multi-axis actuator consists of three electrodynamic forcers housed in an inner ring and an outer ring. Three single-blade flexures couple the rings.

The actuator was designed to be compatible with the expander of the Hughes cryocooler. The size and shape of the rings allow both the expander and the actuator to be mounted on an existing vacuum bonnet. The flexures and the outer ring are such that the actuator's first few modes lie between the cooler's first and second harmonics. The cooler's vibration levels dictated the sizing of the forcing elements.

Each forcer relies on a tightly-wound coil and a four-magnet two-return-plate magnetic circuit to generate vertical Lorentz forces. Only the outer pair of magnets is allowed to move in this arrangement; both the inner pair and the coil are attached to the actuator's stationary inner ring. The use of rare-earth permanent magnets results in a high force constant (3.2 N/A) despite the unusual configuration.

The coils are driven by analog voltage-controlled current sources based on power op amps. These supply a current of 0.2 A/V up to a maximum of 1.5 A, providing ample force capability to cancel the cooler's vibration in three axes simultaneously. The drive signal for each coil is generated by an analog transformation-matrix circuit on the basis of command signals in the global plunge, tip, and tilt coordinates. A similar circuit implements the inverse transformation on the load-cell signals, allowing the controller to be formulated in the global coordinate system.

Chapter 4

Nonlinear Actuator Dynamics

> ...most nonlinear problems involve algebra and or calculations which are formidable and even frightening.
>
> —K. A. V. Pandalai, 1987.

During testing of the actuator, a nonlinearity was noted. This is troublesome because the actuator is intended for use in a linear active cancellation system. One of the main effects of the nonlinearity is the generation of harmonics, even when driven with a pure sinusoid. The cancellation system will drive the actuator at a number of harmonics, and there is a concern that the nonlinearity might shift the system's energy is such a way as to degrade the active system's performance or even destabilize it.

In order to assess the effect of the nonlinearity on the closed-loop cancellation system, an analytical description of the nonlinear dynamics is derived and experimentally verified. The various harmonics in the periodic disturbance signal driving the cancellation system differ in relative amplitude by more than an order of magnitude; the nonlinear model must account for effects over a similar amplitude range.

Although nonlinear analyses tend to be very application-specific, it is believed that the analysis presented here also pertains to Oxford-type cryocoolers, in which the piston and the displacer are supported by spiral flexures. As will be shown, the actuator's nonlinearity is due to the manner in which the end points of the flexures are restrained. The spiral flexures in Oxford-type coolers are used to provide accurate

radial positioning of the moving mass and thus are also highly restrained.

After noting the behavior that first suggested the presence of a nonlinearity in the actuator, a simple model is presented to motivate further study. Galerkin's method is then applied to a nonlinear beam model to derive the actuator's nonlinear equation of motion, approximate solutions of which are obtained by means of the harmonic balance method. The concept of higher-order transfer functions is introduced in relationship to these solutions, and experimental measurements of the nonlinear actuator dynamics are presented. Finally, the nonlinear actuator is combined with a typical linear compensator in a describing-function analysis.

4.1 Initial Observations

In the course of experimentally characterizing the multi-axis actuator, some nonlinear behavior was observed. This took the form of a periodic (multi-harmonic) response to a harmonic input. Qualitatively, the following observations were made:

1. A sinusoidal input produced an output that featured the input sinusoid as well as higher harmonics, especially the second and the third harmonics.

2. The higher harmonics were of significant amplitude relative to the fundamental when the moving mass underwent large-amplitude motion, *i.e.* when the drive frequency was less than the natural frequency of the actuator's bounce mode.

3. When the amplitude of the input was increased, the second and third harmonics increased more than the fundamental.

4. The higher harmonics were significantly greater in response to a commanded force than in response to a commanded moment.

Several possible sources of nonlinearity were considered. The linearity of the power amplifiers was verified by replacing the actuator with three resistors and monitoring the output current of each amplifier. The nonlinear current-force relationship in the magnetic circuit, Equation (3.9), was quantified with measurements of the current

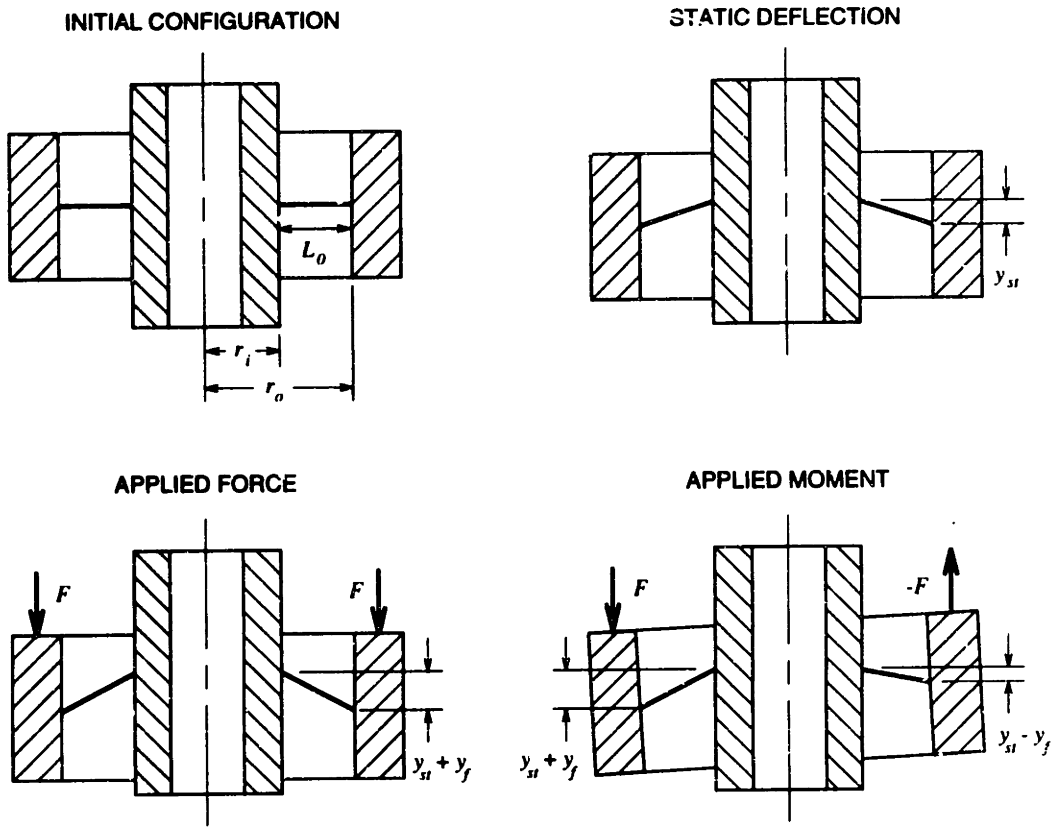

Figure 4-1: Two-flexure actuator model and effect of various loadings. Not to scale.

required to produce forces of the same order as the cryocooler forces. The actuator's nonlinear response was finally attributed to midplane stretching in the flexures that support the outer ring.

As described previously, the outer ring is supported by three flexures. One end of each flexure is clamped in the stationary inner ring, and the other end is clamped in the moving outer ring. The magnetic forcers are used to move the outer ring in either a plunge motion or in one of two perpendicular tilt motions.

Since the actuator is axially symmetric, it may be represented by a two-flexure model (Figure 4-1). The tip masses in this model represent the outer ring, which is sufficiently rigid that the masses cannot move independently. Thus, the radial position of the outer end of each flexure is determined by the outer ring. Because of this restraint, any movement of the outer ring will induce tension in the flexures, which has long been known to cause nonlinear behavior [56].

The tension is determined by several factors. Consider a simple actuator model in which the flexures are represented by pinned struts. The tension induced in these members by the motion of the outer ring can be determined directly from geometry. For example, if the outer ring undergoes a static deflection y_{st} either due to its own weight or due to an applied static load, each "flexure" is stretched from its original length L_0 to a length $L^2 = {L_0}^2 + {y_{st}}^2$, which induces an axial strain

$$\begin{aligned} \varepsilon_{st} &= (L - L_0)/L_0 \\ &= \sqrt{1 + (y_{st}/L_0)^2} - 1 \\ &\approx {y_{st}}^2/2{L_0}^2 \end{aligned}$$

This strain corresponds to an axial tension of $P_{st} = \varepsilon_{st} EA$.

When an additional force is applied to the outer ring in the same direction as the static deflection, the tip deflection of the flexures increases to $y_{st} + y_f$. The resulting axial strain is

$$\begin{aligned} \varepsilon_{+f} &\approx (y_{st} + y_f)^2/2{L_0}^2 \\ &= ({y_{st}}^2 + 2y_{st}y_f + {y_f}^2)/2{L_0}^2 \\ &= \varepsilon_{st} + \Delta\varepsilon_{+f} \end{aligned}$$

where $\Delta\varepsilon_{+f} = (2y_{st}y_f + {y_f}^2)/2{L_0}^2$. In the case of the actuator, the displacement due to the applied force is typically much less than the static deflection, *i.e.* $y_f \ll y_{st}$. If the force is applied in the opposite direction, the strain is $\varepsilon_{-f} = \varepsilon_{st} + \Delta\varepsilon_{-f}$ where $\Delta\varepsilon_{-f} = -(2y_{st}y_f - {y_f}^2)/2{L_0}^2$. The amplitude of the change in the axial strain is smaller in this direction even though the tip deflection has changed by the same amount. The static deflection introduces an asymmetry.

The asymmetry also affects the axial strain induced by an applied moment. Representing the moment by two forces of equal amplitude and opposite sign, the vertical deflection of one flexure tip is $y_{st} + y_f$, while the vertical deflection of the other is $y_{st} - y_f$. The outer ring also rotates, adding a horizontal component to the tip deflection. For small moments, the rotation angle is $\theta \approx \sin\theta = y_f/r_o$, so the horizontal

coordinate of the flexure's tip is $x_m = r_o \cos\nu \approx r_o - {y_f}^2/2r_o$ The flexures are then stretched to lengths

$$\begin{aligned} {L_+}^2 &= (x_m - r_i)^2 + (y_{st} + y_f)^2 \\ &= (L_0 - {y_f}^2/2r_o)^2 + ({y_{st}}^2 + 2y_{st}y_f + {y_f}^2) \\ {L_-}^2 &= (L_0 - {y_f}^2/2r_o)^2 + ({y_{st}}^2 - 2y_{st}y_f + {y_f}^2) \end{aligned}$$

The corresponding changes in axial strain are

$$\begin{aligned} \Delta\varepsilon_+ &\approx (2y_{st}y_f + [1 - L_0/r_o]{y_f}^2)/2{L_0}^2 \\ \Delta\varepsilon_- &\approx -(2y_{st}y_f - [1 - L_0/r_o]{y_f}^2)/2{L_0}^2 \end{aligned}$$

yielding a net change in axial strain of $\Delta\varepsilon_m \approx [1 - L_0/r_o]{y_f}^2/{L_0}^2$. Since $y_f \ll y_{st}$, the change in axial strain due to an applied moment $\Delta\varepsilon_m$ is much smaller than the change due to an applied force $\Delta\varepsilon_{\pm f}$.

Although this model is a gross simplification of the actuator dynamics, it demonstrates that motion of the outer ring will induce axial tension in the flexures, providing a mechanism for the observed actuator nonlinearity. Furthermore, it suggests that the static deflection will introduce an asymmetry and that the nonlinearity associated with an applied force will be more significant than the nonlinearity associated with an applied moment (see Observation 4). Based on these results, a more accurate model of the actuator's response to an applied force will be developed.

4.2 Nonlinear Vibration Analysis

The pinned struts in the two-flexure actuator model facilitate simple computation of the induced tension, but they do not represent the actual flexures very well. A better approximation is to model the flexures as clamped beams. The nonlinear partial differential equation that governs the deflection of the flexures may then be reduced, by means of modal analysis and Galerkin's method, to a nonlinear ordinary differential equation, namely a modified Duffing's equation. While this analysis technique has

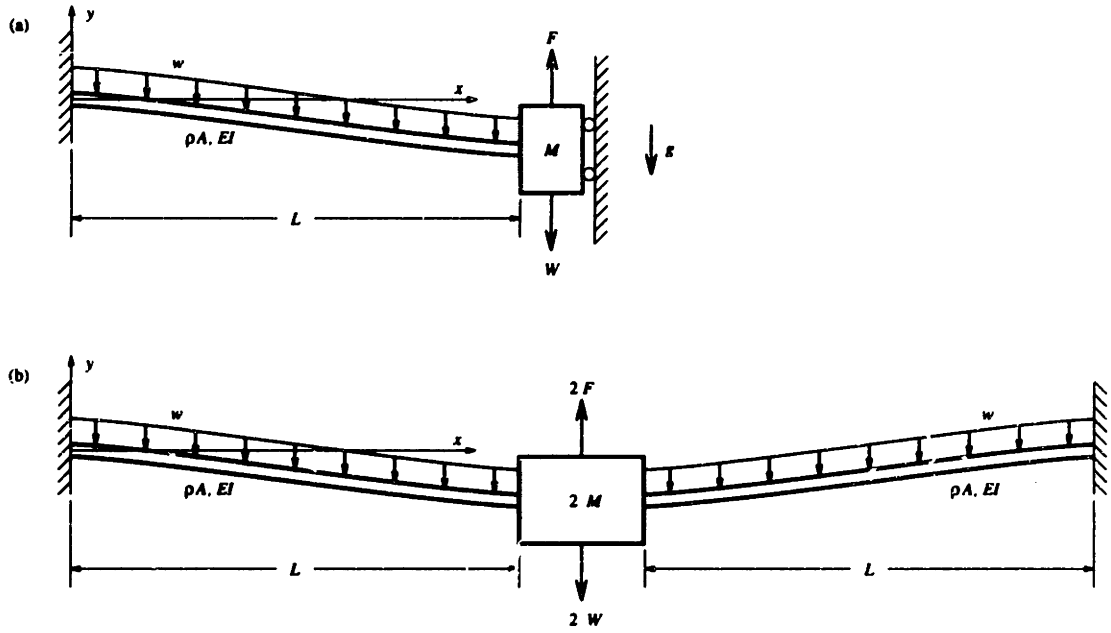

Figure 4-2: One- and two-flexure actuator models with distributed and concentrated loads. Figures are not to scale.

been used by others, the actuator model includes a unique combination of factors: the boundary conditions, the large supported mass, and the significant static deformation. The relationship between these physical aspects of the model and the parameters in Duffing's equation will be established through this analysis.

When an axial force is applied to the outer ring, each flexure bears the same load. The dynamics can then be fully described by a one-flexure model consisting of a clamped-guided beam of length L with a tip mass M subject to a force F (Figure 4-2a). Alternatively a modified two-flexure model can be used. Figure 4-2b depicts a clamped-clamped beam of length $2L$ with a central mass $2M$ subject to a force $2F$; the central mass represents the actuator's outer ring, not the stationary inner ring. Because of the symmetric loading, the dynamics of these two models will be identical. But the boundary conditions of the clamped-clamped beam are much simpler, allowing direct application of Galerkin's method.

Both of these models feature axially-restrained beams; the boundary conditions are such that longitudinal motion of either end of the beam is impossible. Any departure from the beam's initial configuration places the beam under axial tension The

resulting nonlinear vibrations were first studied by Woinowsky-Krieger [56]. He assumed the vibrations were separable in space and time. Upon approximating the spatial component with a single linear mode shape, the temporal component was found to be determined by Duffing's equation. Woinowsky-Krieger considered a pinned-pinned beam and obtained a closed-form solution of Duffing's equation using elliptic functions, while Srinivasan [57] demonstrated that excellent results could also be obtained using Galerkin's method with a one-term approximation of the temporal component. Other authors subsequently considered other boundary conditions and introduced a wide variety of techniques for solving Duffing's equation.

Several researchers used multi-mode expansions of the vibration's spatial component and observed a phenomenon unique to nonlinear systems. The normal modes of a linear system are only coupled through the damping terms, which are usually small for structural systems, effectively decoupling the modes. McDonald [58] observed that the nonlinear restoring forces provide additional coupling and that the nth natural frequency depends on the amplitude of all modes, rather than just the amplitude of the nth mode as implicitly assumed in the single-mode analyses. Bennett and Eisley [59] considered the beam's nonlinear forced response and noted the possibility of internal or coupling resonances, whereby the first modal amplitude exhibits a resonance near the third natural frequency, for example. They found that all modes of a clamped-pinned beam are coupled through Duffing's equation, while no such coupling occurs in clamped-clamped or pinned-pinned beams. However, Tseng and Dugundji [60] studied the nonlinear vibration of a buckled beam and found that a clamped-clamped beam can exhibit coupling given a sufficiently large initial static deflection. Using a perturbation technique rather than Galerkin's method, Nayfeh *et al.* [61] explained internal resonances in terms of commensurable natural frequencies, providing a simple means of assessing the degree of nonlinear coupling in a multiple-degree-of-freedom system.

The other significant feature of the actuator model is the large mass representing the outer ring. Baker [62] showed the effect of a central mass on the fundamental natural frequency of a clamped-clamped beam for mass ratios (the ratio of the con-

centrated mass to the beam's mass) from 0.1 to 100. But these results were based on a linear analysis and thus are valid only for vibrations of infinitesimal amplitude. Shaker [63] examined the fundamental natural frequency of an axially-loaded cantilever with a tip mass, but once again it was a linear vibration analysis; the axial load was independent of the beam's deformation.

The effect of both an axial restraint *and* a concentrated mass was considered by Saito *et al.* [64]. They analyzed the forced response of a pinned-pinned beam with a concentrated mass at an arbitrary location, and they included the effect of gravity by means of an initial static deflection. Except for the boundary conditions, this corresponds to the clamped-clamped actuator model, making the problem formulation in [64] very pertinent. Unfortunately the results are not as useful. Saito *et al.* consider very slender, lightly loaded beams, ones with slenderness ratios greater than 600 and mass ratios less than 10, whereas the actuator model has a slenderness ratio of approximately 150 and a mass ratio of about 1200. Furthermore, their frequency response curves combine the amplitude and phase of the first three harmonics into a single root-sum-square amplitude, which is insufficient for a closed-loop describing-function analysis.

Applying the analysis technique of Saito *et al.* to the two-flexure actuator model, consider a clamped-clamped uniform beam of length $2L$ supporting a central mass $2M$. A force $2F$ is applied at the central mass, and the beam is oriented such that the transverse deformations $y(x,t)$ are parallel with the gravity vector. Assume the beam obeys Bernoulli-Euler beam theory. Including an axial tension P and a uniformly distributed viscous damping term c, but neglecting the effects of shear deformation and rotatory inertia, the governing partial differential equation is

$$EI\frac{\partial^4 y}{\partial x^4} - P\frac{\partial^2 y}{\partial x^2} + c\frac{\partial y}{\partial t} + [\rho A + 2M\delta(x-L)]\frac{\partial^2 y}{\partial t^2} = \\ -w + 2(F-W)\delta(x-L) \qquad (4.1)$$

where E is Young's modulus of the beam, I is the moment of inertia of the beam's cross-section, ρ is the beam's density, A is the beam's cross-sectional area, $w = \rho Ag$ is the weight per unit length of the beam, $2W = 2Mg$ is the weight of the central

mass, and $\delta(x)$ is the Dirac delta function. The boundary conditions are

$$y = \partial y/\partial x = 0 \qquad \text{at } x = 0 \text{ and } x = 2L \tag{4.2}$$

The applied force may include both static and dynamic components. For example, in addition to providing the dynamic loads, the magnetic forcers could be used to offload some of the weight of the outer ring. In this analysis, however, it will be assumed that the applied force is harmonic: $2F = 2A_f \sin \omega_f t$.

Due to the restraint imposed by the fixed ends, the axial tension P is determined by the deformation of the beam. The tension must be such that the increase in length of the beam's neutral axis due to tension is equal to the unconstrained foreshortening due to curvature. If the clamps are spaced such that there is no axial load when the beam is undeflected, $y(x,t) = 0$, then the axial tension is

$$P = \frac{EA}{4L} \int_0^{2L} \left(\frac{\partial y}{\partial x}\right)^2 dx \tag{4.3}$$

Assume the vibration is separable in space and time, so that a solution of Equation (4.1) may be expressed as

$$y(x,t) = Y_0(x)q_0 + \sum_{n=1}^{\infty} Y_n(x)q_n(t) \tag{4.4}$$

where $Y_n(x)$ is the nth mode shape and q_n is the nth generalized coordinate; the first term represents the beam's static deflection. Analysis of the beam's linear vibration about its nonlinear static deflection showed that only the first mode plays a significant role in the linear forced response of the actuator model in the bandwidth of interest. Furthermore, it was found that the first mode does not parametrically excite higher modes through internal resonances. The nonlinear forced response will therefore be well approximated by retaining the static deflection and the first vibration mode in the expansion of the beam's transverse deformations:

$$y(x,t) = Y_0(x)q_0 + Y_1(x)q_1(t) \tag{4.5}$$

Rather than attempting to obtain the exact solution of the partial differential

equation, an approximate method is used. The traditional choice for nonlinear systems is Galerkin's method [65]. As described by Meirovitch [66], in this method the spatial component of the solution is assumed to be represented by a series of n comparison functions, which satisfy both the geometric and the natural boundary conditions. In general these functions will not satisfy the differential equation, so an error term is produced when the comparison functions are substituted into the differential equation. The generalized coordinates associated with the n comparison functions are determined by insisting that the integral of the weighted error over the domain be zero, where the weighting functions are the comparison functions. The accuracy of the results may be improved either by including more comparison functions or by selecting comparison functions that are better approximations of the system's eigenfunctions.

A wide variety of comparison functions are available for the actuator model, due in part to the use of the two-flexure model. The geometric boundary conditions, Equation (4.2), of the clamped-clamped beam are much easier to satisfy than the eigenvalue-dependent natural boundary condition associated with the clamped-guided beam of the one-flexure model. Possible comparison functions include polynomials, trigonometric series, hyperbolic trigonometric series, and assorted combinations of these terms.

An attractive choice is the deflection curve obtained from a linear analysis of the beam's static deflection. This function is derived from the differential equation, albeit under the assumption of infinitesimal amplitudes, and yet it is not much more complicated than an *ad hoc* selection of trigonometric functions. The clamped-clamped beam is statically indeterminate. However, the reactions may be found using the moment-area method, after which the deflection curve $y(x)$ may be determined through double integration of the beam equation [52]. For the combination of a uniform distributed load along the entire length of the beam and a concentrated central

load, the deflection curve of a clamped-clamped beam is

$$y(x) = \begin{cases} -W_b/(12EI)\left[(3\mu+2)Lx^2 - 2(\mu+1)x^3 + x^4/(2L)\right], & 0 \le x \le L \\ -W_b/(12EI)[(3\mu+2)L(2L-x)^2 - 2(\mu+1)(2L-x)^3 & \\ \qquad + (2L-x)^4/(2L)], & L \le x \le 2L \end{cases} \tag{4.6}$$

where $2W_b = 2Lw$ is the weight of the beam and $\mu = W/W_b$ is the ratio of the weight of the central mass to the weight of the beam. Of course, μ is also the mass ratio referred to above. The normalized shape of this curve matches the nonlinear deflection curve for $\mu < 3000$ and also corresponds closely to the first linear vibration mode shape. Both the nonlinear static deflection curve and the linear mode shape include hyperbolic trigonometric terms, whereas $y(x)$ is a polynomial, which makes the evaluation of the integral of the weighted error in Galerkin's method much easier.

A single comparison function $Y(x)$ is used for both the static deflection $Y_0(x)$ and the first mode shape $Y_1(x)$. In accordance with the work of Saito *et al.*, the comparison function is normalized by its value at mid-span, while the generalized coordinates q_0 and $q_1(t)$ are combined into a single coordinate that represents the beam's net deflection at mid-span, $q(t) = q_0 + q_1(t)$. Normalizing this generalized coordinate by the radius of gyration of the beam's cross-section, $r_g = \sqrt{I/A}$, yields $\overline{q}(t)$. The assumed solution is then

$$y(x,t) = [Y(x)/Y(L)]r_g\,\overline{q}(t) = \phi(x)\overline{q}(t) \tag{4.7}$$

where

$$\phi(x) = \begin{cases} r_g\, y_a(x)/y_a(L), & 0 \le x \le L \\ r_g\, y_b(x)/y_a(L), & L \le x \le 2L \end{cases}$$

$$\begin{aligned} y_a(x) &= [2(3\mu+2)L^2x^2 - 4(\mu+1)Lx^3 + x^4]/L^4 \\ y_b(x) &= [-8\mu L^4 + 24\mu L^3 x - 2(9\mu-2)L^2x^2 + 4(\mu-1)Lx^3 + x^4]/L^4 \end{aligned}$$

The unknown variable in this expression is the nondimensional generalized coordinate $\overline{q}(t)$. The error associated with the assumed solution is found by substituting Equation (4.7) into Equations (4.1) and (4.2). Galerkin's method then determines

the generalized coordinate, which must be such that the integral of the weighted error vanishes:

$$\int_0^{2L} \left\{ w + 2[W - A_f \sin\omega_f t]\delta(x-L) + [\rho A + 2M\delta(x-L)]\phi \frac{d^2\bar{q}}{dt^2} + c\phi \frac{d\bar{q}}{dt} + EI\frac{d^4\phi}{dx^4}\bar{q} - \frac{EA}{4L}\int_0^{2L}\left(\frac{d\phi}{dx}\bar{q}\right)^2 dx \frac{d^2\phi}{dx^2}\bar{q} \right\} \phi(x)\, dx = 0 \quad (4.8)$$

Most of these terms may be evaluated by direct integration. Note however that $EI\, d^4\phi(x)/dx^4 = w_i(x)$, where $w_i(x)$ is the load intensity that results in the assumed deflection curve [52]. This contributes an additional Dirac delta function because of the concentrated load. Thus, the nondimensional generalized coordinate must satisfy

$$\frac{d^2\bar{q}}{dt^2} + \frac{cL}{M_b}\frac{D_2}{D_1}\frac{d\bar{q}}{dt} + \frac{EI}{M_b L^3}\left[\frac{D_3}{D_1}\bar{q} + \frac{D_4}{D_1 {D_5}^2}\bar{q}^3 + \frac{D_5 D_6}{D_1}\bar{d}\right] = \frac{EI}{M_b L^3}\frac{{D_5}^2}{D_1}\bar{d}\bar{F}\sin\omega_f t \quad (4.9)$$

where $2M_b = 2\rho AL$ is the mass of the beam, $\bar{d} = W_b L^3/EIr_g$ is a nondimensional displacement, $\bar{F} = A_f/W_b$ is a nondimensional force, and

$$\begin{aligned} D_1 &= 4\left[\mu^3 + (48/35)\mu^2 + (67/105)\mu + 32/315\right] \\ D_2 &= (52/35)\mu^2 + (163/105)\mu + 128/315 \\ D_3 &= 16\left[3\mu^2 + 3\mu + 4/5\right] \\ D_4 &= 32\left[(3/5)\mu^2 + (3/5)\mu + 16/105\right]^2 \\ D_5 &= 2\mu + 1 \\ D_6 &= 2\left[\mu^2 + \mu + 4/15\right] \end{aligned}$$

Both the cubic stiffness term due to the axial restraint and the static forcing due to the gravity load can be seen in this expression.

Recall that $\bar{q}$ has both a static and a dynamic component. The weight of the beam and the weight of the central mass cause an initial static deflection. This appears in the nondimensional generalized coordinate as $\bar{q}_0 = q_0/r_g$, which may be evaluated by setting $\bar{F} = 0$ and eliminating the time derivatives in Equation (4.9):

$$D_4\bar{q}_d^{\,3} + D_3\bar{q}_d + D_6\bar{d} = 0 \quad (4.10)$$

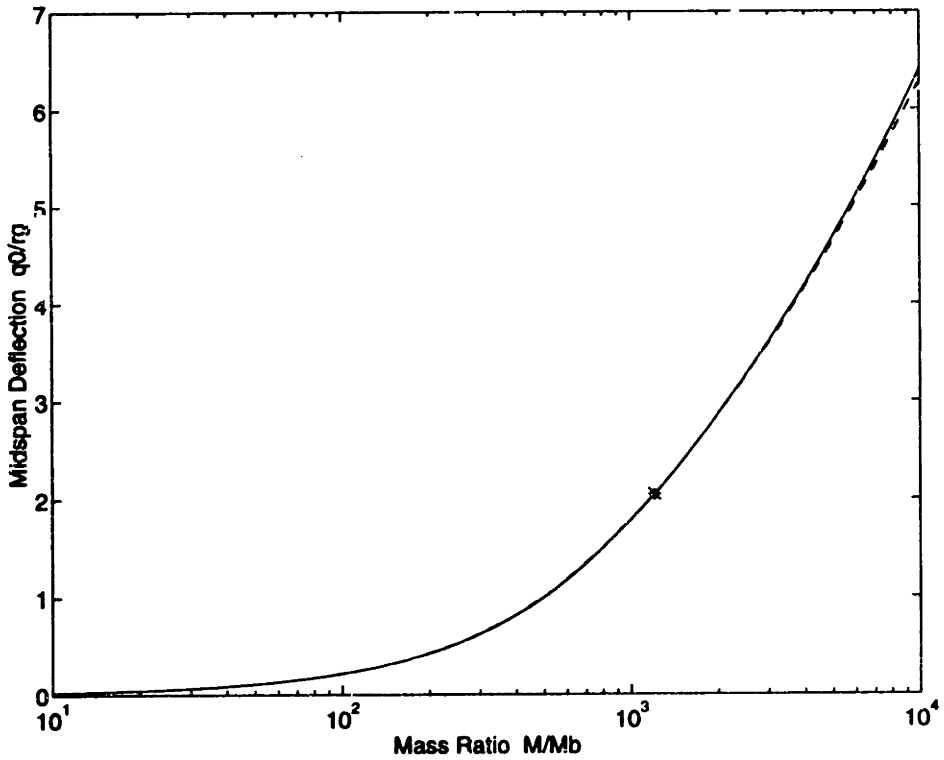

Figure 4-3: Nondimensional mid-span static deflection as a function of the system's mass ratio. Solid line: exact solution; dashed line: Equation (4.10); $*$: mass ratio of actuator.

where $\bar{q}_d = \bar{q}_0/D_5$. In the coordinate system of Figure 4-2, the initial static deflection is negative, so $\bar{q}_d < 0$.

The accuracy of the assumed solution may be checked by comparing q_0 with the exact large-amplitude static deflection for a centrally-loaded clamped-clamped beam. Figure 4-3 shows the nondimensional mid-span static deflection as a function of the system's mass ratio. Two curves are included. One was computed using Equation (4.10) while the other represents the exact solution. The close agreement between these two solutions over a wide range of mass ratios indicates that the chosen comparison function is a good approximation of the nonlinear static deflection.

The dynamic component of $\bar{q}$ defines the beam's natural frequency. Consider the free response of an undamped beam, $\bar{F} = 0$ and $c = 0$. Let $\bar{q} = \bar{q}_0 + \bar{q}_1$, and substitute Equation (4.10) into Equation (4.9). The linear natural frequency ω_1 is then obtained

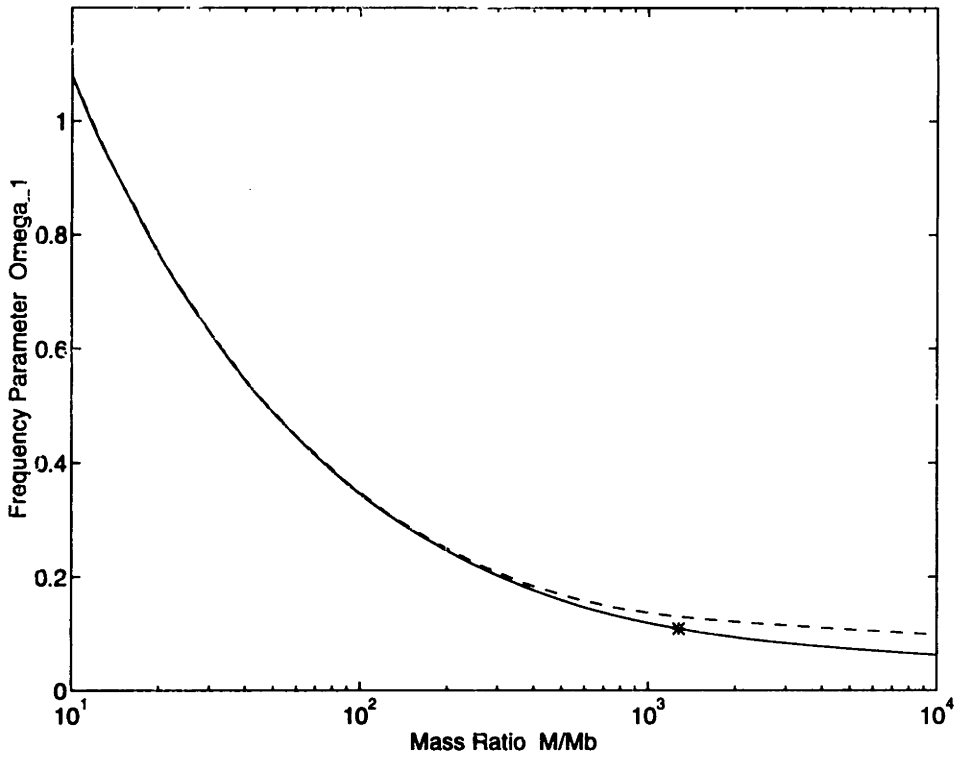

Figure 4-4: Linear natural frequency as a function of the system's mass ratio. Solid line: exact solution; dashed line: Equation (4.11); $*$: mass ratio of actuator.

by assuming a harmonic response and neglecting higher-order terms in $\bar{q}_1$:

$$\omega_1{}^2 = \left[(D_3 + 3D_4\bar{q}_d{}^2)/D_1\right](EI/M_bL^3) \tag{4.11}$$

This expression includes the effect of the axial tension caused by the static deflection but neglects the change in the tension due to the vibration.

The variation of the linear natural frequency with the system's mass ratio is shown in Figure 4-4. The frequency parameter $\Omega_1 = \omega_1\sqrt{M_bL^3/EI}$ may be obtained from Equation (4.11) once the nonlinear static deflection is known. The exact solution determined from the eigenproblem's transcendental equation is also shown. Both solutions exhibit a $1/\sqrt{\mu}$ behavior for moderate mass ratios, as expected of a mass on a spring. As the mass ratio increases, the static deflection increases, as does the effect of the axial restraint. For large-amplitude static deflections, the induced axial tension serves to stiffen the beam, counteracting the effect of the increasing mass and causing the natural frequency to level out. The quantitative agreement between the

two solutions is obviously not as good as in the previous figure. The actuator has a mass ratio of 1200, at which point the natural frequency computed with Galerkin's method is approximately 20% greater than the exact solution. Thus, the polynomial comparison function appears to be sufficient to study the general behavior of the actuator model, although any quantitative results must be treated with caution.

Finally, the nonlinear equation of motion may be expressed in a form similar to the usual mass-spring-damper equation of motion. Let the system's damping ratio be $\zeta = cLD_2/2M_bD_1\omega_1$. Introduce a nondimensional time τ such that $n_t\tau = \omega_f t$ where n_t is an integer, and let $\omega_t = n_t\omega_1/\omega_f$. The generalized coordinate is then governed by

$$\ddot{\overline{q}} + 2\zeta\omega_t\dot{\overline{q}} + {\omega_t}^2\left(\alpha_0 + \alpha_1\overline{q} + \alpha_3\overline{q}^3\right) = {\omega_t}^2\alpha_f \sin n_t\tau \tag{4.12}$$

where dots represent differentiation with respect to τ, and

$$\begin{aligned}
\alpha_0 &= \overline{d}\,D_5D_6/D_7 \\
\alpha_1 &= D_3/D_7 \\
\alpha_3 &= D_4/{D_5}^2D_7 \\
\alpha_f &= \overline{d}\bar{F}\,{D_5}^2/D_7 \\
D_7 &= D_3 + 3D_4{\overline{q}_d}^2
\end{aligned}$$

The form of this equation and its factors is consistent with Reference [64].

The equation of motion may also be expressed in terms of the vibration about the initial static deflection:

$$\ddot{\overline{q}}_1 + 2\zeta\omega_t\dot{\overline{q}}_1 + {\omega_t}^2\left(\overline{q}_1 + \alpha_2{\overline{q}_1}^2 + \alpha_3{\overline{q}_1}^3\right) = {\omega_t}^2\alpha_f \sin n_t\tau \tag{4.13}$$

where

$$\alpha_2 = 3\overline{q}_d\,D_4/D_5D_7$$

In addition to the usual cubic term, this Duffing's equation includes a quadratic term to account for the shift in the equilibrium position caused by the beam's static deflection. Either form of the equation of motion reduces to the standard Duffing's equation if the static deflection is eliminated, $\overline{q}_d = 0$.

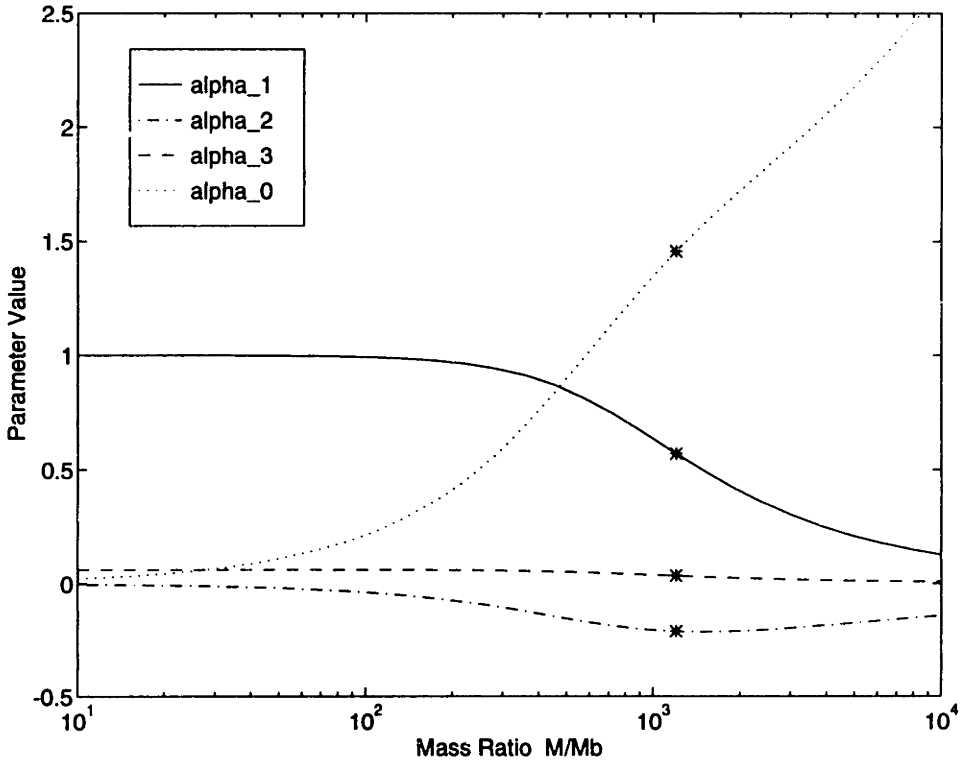

Figure 4-5: Parameters α_i in Duffing's equation as a function of the system's mass ratio. $*$: mass ratio of actuator.

The character of the system's vibration is determined in large part by the amplitude of the parameters α_i, which are shown in Figure 4-5 as functions of the system's mass ratio. The static parameter α_0 becomes significant for large mass ratios, $\mu > 400$, dominating the linear parameter α_1. Since $\overline{q}_d < 0$, the quadratic parameter α_2 is always negative (a softening spring) and is of moderate amplitude for $\mu \approx 1000$. The cubic parameter α_3 is always positive and thus acts as a hardening spring. It is much greater than α_2 for small μ but becomes rather insignificant for $\mu > 300$; notice that only α_2 and α_3 appear in Equation (4.13). Of course, the relative ordering of these terms will also be affected by the amplitude of $\overline{q}$.

4.3 Steady-State Solutions

Despite the apparent simplicity of Duffing's equation, its solutions are known to include a surprising variety of behavior, ranging from quasi-harmonic vibrations to chaotic motion [67]. Approximate methods of solving Duffing's equation are based on assumptions of the type of behavior exhibited for a given set of parameter values. These assumptions can have a great effect on the solution.

The variety of behavior makes it difficult to take advantage of existing solutions of Duffing's equation. Most analyses consider only the standard, or symmetric, form of the equation, which does not adequately describe the actuator model. The asymmetric form includes both the quadratic and the cubic terms—the parameter values will determine which term dominates. Although some solutions to the asymmetric Duffing's equation have been presented [64], they do not include the parameter values associated with the actuator model. Furthermore, these solutions only provide a root-sum-square response amplitude. The goal here is to derive the amplitude and phase of the actuator's multi-harmonic frequency response.

As noted in Section 4.1, the actuator's steady-state response to a harmonic input was experimentally observed to be periodic. The most significant components of the response occurred at the drive frequency and the next two harmonics. These higher harmonics may be included in an approximate solution of Equation (4.12) most easily through the use of the harmonic balance method.

The harmonic balance method is widely used in the study of nonlinear vibrations. One advantage that it has over perturbation techniques is that it is not restricted to weakly nonlinear problems, making the resulting solution valid over a wide range of parameter values. Rapid convergence to the exact solution is ensured for smooth systems by the similarity to a Fourier decomposition [65]. Furthermore, the harmonic balance method may be shown to be formally equivalent to Galerkin's method with trigonometric temporal comparison functions [65], which complements the application to the beam equation of Galerkin's method with spatial comparison functions in Equation (4.8).

The harmonic balance method may be applied to either form of the equation of motion. Hayashi [68] notes that it is usually preferable to use the first form, Equation (4.12), since it contains only a single nonlinear term. Based on the experimental observations, assume that the steady-state solution of Duffing's equation may be expressed as

$$\overline{q}(\tau) = a_0 + \sum_{k=1}^{3}(a_k \cos k\tau + b_k \sin k\tau) \tag{4.14}$$

Then substitute this assumed solution into the nonlinear equation of motion, Equation (4.12), group all similar trigonometric terms, and require that the coefficients of these terms vanish. The result is a set of seven coupled algebraic equations for the seven unknowns that appear in Equation (4.14):

$$\begin{aligned}
\alpha_1 a_0 + \alpha_3 L_0 + \alpha_0 &= 0 \\
-a_1 + 2\zeta\omega_t b_1 + {\omega_t}^2(\alpha_1 a_1 + \alpha_3 L_1) &= 0 \\
-b_1 - 2\zeta\omega_t a_1 + {\omega_t}^2(\alpha_1 b_1 + \alpha_3 L_2) &= {\omega_t}^2\alpha_f\delta_{n_t 1} \\
-4a_2 + 4\zeta\omega_t b_2 + {\omega_t}^2(\alpha_1 a_2 + \alpha_3 L_3) &= 0 \\
-4b_2 - 4\zeta\omega_t a_2 + {\omega_t}^2(\alpha_1 b_2 + \alpha_3 L_4) &= {\omega_t}^2\alpha_f\delta_{n_t 2} \\
-9a_3 + 6\zeta\omega_t b_3 + {\omega_t}^2(\alpha_1 a_3 + \alpha_3 L_5) &= 0 \\
-9b_3 - 6\zeta\omega_t a_3 + {\omega_t}^2(\alpha_1 b_3 + \alpha_3 L_6) &= {\omega_t}^2\alpha_f\delta_{n_t 3}
\end{aligned} \tag{4.15}$$

where $\delta_{n_t i}$ is the Kronecker delta and

$$\begin{aligned}
L_0 &= a_0^3 + (3/2)(a_1^2 + b_1^2 + a_2^2 + b_2^2 + a_3^2 + b_3^2)a_0 \\
&\quad + (3/4)(a_1^2 a_2 + 2a_1 b_1 b_2 + 2a_1 a_2 a_3 + 2a_1 b_2 b_3 - b_1^2 a_2 + 2b_1 a_2 b_3 - 2b_1 b_2 a_3) \\
L_1 &= 3(a_0 a_1 + a_1 a_2 + b_1 b_2 + a_2 a_3 + b_2 b_3)a_0 \\
&\quad + (3/4)(a_1^3 + a_1^2 a_3 + a_1 b_1^2 + 2a_1 b_1 b_3 + 2a_1 a_2^2 + 2a_1 b_2^2 + 2a_1 a_3^2 + 2a_1 b_3^2 \\
&\quad\quad - b_1^2 a_3 + a_2^2 a_3 + 2a_2 b_2 b_3 - b_2^2 a_3) \\
L_2 &= 3(a_0 b_1 + a_1 b_2 - b_1 a_2 + a_2 b_3 - b_2 a_3)a_0 \\
&\quad + (3/4)(a_1^2 b_1 + a_1^2 b_3 - 2a_1 b_1 a_3 + b_1^3 - b_1^2 b_3 + 2b_1 a_2^2 + 2b_1 b_2^2 + 2b_1 a_3^2 \\
&\quad\quad + 2b_1 b_3^2 - a_2^2 b_3 + 2a_2 b_2 a_3 + b_2^2 b_3)
\end{aligned}$$

$$
\begin{aligned}
L_3 &= (3/2)(2a_0a_2 + a_1^2 + 2a_1a_3 - b_1^2 + 2b_1b_3)a_0 \\
&\quad + (3/4)(2a_1^2a_2 + 2a_1a_2a_3 + 2a_1b_2b_3 + 2b_1^2a_2 - 2b_1a_2b_3 + 2b_1b_2a_3 + a_2^3 \\
&\quad\quad + a_2b_2^2 + 2a_2a_3^2 + 2a_2b_3^2) \\
L_4 &= 3(a_0b_2 + a_1b_1 + a_1b_3 - b_1a_3)a_0 \\
&\quad + (3/4)(2a_1^2b_2 + 2a_1a_2b_3 - 2a_1b_2a_3 + 2b_1^2b_2 + 2b_1a_2a_3 + 2b_1b_2b_3 + a_2^2b_2 \\
&\quad\quad + b_2^3 + 2b_2a_3^2 + 2b_2b_3^2) \\
L_5 &= 3(a_0a_3 + a_1a_2 - b_1b_2)a_0 \\
&\quad + (1/4)(a_1^3 + 6a_1^2a_3 - 3a_1b_1^2 + 3a_1a_2^2 - 3a_1b_2^2 + 6b_1^2a_3 + 6b_1a_2b_2 + 6a_2^2a_3 \\
&\quad\quad + 6b_2^2a_3 + 3a_3^3 + 3a_3b_3^2) \\
L_6 &= 3(a_0b_3 + a_1b_2 + b_1a_2)a_0 \\
&\quad + (1/4)(3a_1^2b_1 + 6a_1^2b_3 + 6a_1a_2b_2 - b_1^3 + 6b_1^2b_3 - 3b_1a_2^2 + 3b_1b_2^2 + 6a_2^2b_3 \\
&\quad\quad + 6b_2^2b_3 + 3a_3^2b_3 + 3b_3^3)
\end{aligned}
$$

The terms L_i are presented in a form that highlights the presence of the static term a_0. Also notice that each term L_i contains every term a_k and b_k, so the harmonics are fully coupled in this set of equations. The terms L_i are taken from an expansion of $\bar{q}^3(\tau)$ that was computed using symbolic algebra software (Maple V); it is believed that the expansion in Saito *et al.* [64] contains two errors.

It is important to note that $a_0 \neq \bar{q}_0$. The first equation in Equation (4.15) reduces to Equation (4.10) only if $a_k = b_k = 0$ for $k = 1, 2, 3$. In other words, when the beam is at rest, the static deflection is simply the deflection due to the gravity loads. But any dynamic response, whether free or forced, contributes an additional static component to the deflection. The cause of this component is apparent in Equation (4.13): the quadratic term will have a nonzero mean for any vibration of nonzero amplitude.

The forcing parameter α_f appears in three equations, although not simultaneously. The harmonic that is directly excited by α_f is determined by the parameter n_t, which defines the time scale of the solution. If $n_t = 1$, the assumed solution includes the drive frequency and two higher harmonics, whereas subharmonics may be included by selecting $n_t > 1$. Tseng and Dugundji [69] used this to study various super-

and subharmonic resonances. Experimentally, no subharmonics were observed in the actuator's response, so $n_t = 1$ is sufficient here.

The seven coupled algebraic equations may be solved numerically. However, Duffing's equation is known to have multiple solutions, some of which are unstable. The initial guess used to start the numerical routines will therefore have a significant impact on the calculated solution. Insight may be gained by considering approximate solutions of Equation (4.15).

4.3.1 Simple Harmonic Motion

The dominant component in the actuator's response over much of the bandwidth of interest is the component at the drive frequency, making simple harmonic motion a good first approximation. Furthermore, if the system is assumed to be undamped, there are only two non-zero terms in the solution, namely a_0 and b_1.

Expressions in a_0 and b_1 may be derived by eliminating the coefficients of all other components in Equation (4.15). It is also convenient to introduce the amplitude variables $r_0^2 = a_0^2$ and $r_1^2 = b_1^2$. Normalize the forcing frequency by the linear natural frequency and let $\Omega_f = \omega_f/\omega_1$. Then

$$\begin{aligned} R_0 a_0 + \alpha_0 &= 0 \\ R_1 b_1 &= \alpha_f \end{aligned} \tag{4.16}$$

where

$$\begin{aligned} R_0 &= \alpha_1 + \alpha_3 r_0^2 + (3/2)\alpha_3 r_1^2 \\ R_1 &= \alpha_1 - \Omega_f^2 + 3\alpha_3 r_0^2 + (3/4)\alpha_3 r_1^2 \end{aligned}$$

There are many cases in which the static deflection will be negligible. For example, beams with low aspect ratios and light loading will have little static deflection. Perhaps the beam is oriented such that the deformations are perpendicular to gravity, or perhaps a suspension system (electromagnetic or otherwise) is used to offload the beam. Finally, the static deflection will be eliminated on orbit, which is an important consideration given the spacecraft-borne cryocooler application proposed for

this actuator. If there is no static deflection, the static component may be eliminated from the assumed solution, $a_0 = 0$. Also, since $\bar{q}_d = 0$, the linear parameter becomes $\alpha_1 = 1$ for all values of μ, leaving

$$\left[1 + (3/4)\alpha_3 r_1^2 - \hat{\Omega}_f^2\right] b_1 = \alpha_f \tag{4.17}$$

which is the usual expression for the undamped Duffing oscillator.

Nonlinear Natural Frequency

The nonlinear natural frequency may be determined from these expressions by setting $\alpha_f = 0$. Rather than being a single number, the nonlinear natural frequency is a function of the free vibration's amplitude. The frequency-amplitude relationship defines the so-called backbone of both the fundamental component and the static component.

In the case of the symmetric cubic nonlinearity, *i.e.* when there is no static deflection, Equation (4.17) yields

$$\Omega^2(r_1) = [\omega(r_1)/\omega_1]^2 = 1 + (3/4)\alpha_3 r_1^2 \tag{4.18}$$

For $\alpha_3 > 0$, this displays the classic hardening-spring behavior: the natural frequency increases with increasing amplitude.

In the case of the asymmetric cubic nonlinearity, *i.e.* when there is a static deflection, the backbone is most easily expressed in terms of the amplitude of the fundamental component:

$$\begin{aligned} [\alpha_1 + \alpha_3 a_0^2 + (3/2)\alpha_3 r_1^2]\, a_0 + \alpha_0 &= 0 \\ \Omega^2(r_1) = \alpha_1 + 3\alpha_3 r_0^2 + (3/4)\alpha_3 r_1^2 & \end{aligned} \tag{4.19}$$

Thus, for positive parameters α_0, α_1, and α_3, the static deflection a_0 is always negative. Additionally, as r_1 increases, the amplitude of the static deflection decreases from its intial value $|\bar{q}_0|$; the component due to the vibration, $a_0 - \bar{q}_0$, is always positive and increases with increasing r_1 . From Figure 4-5, the linear parameter α_1 is always less than one and the cubic parameter α_3 is quite small, so Ω^2 can actually be less

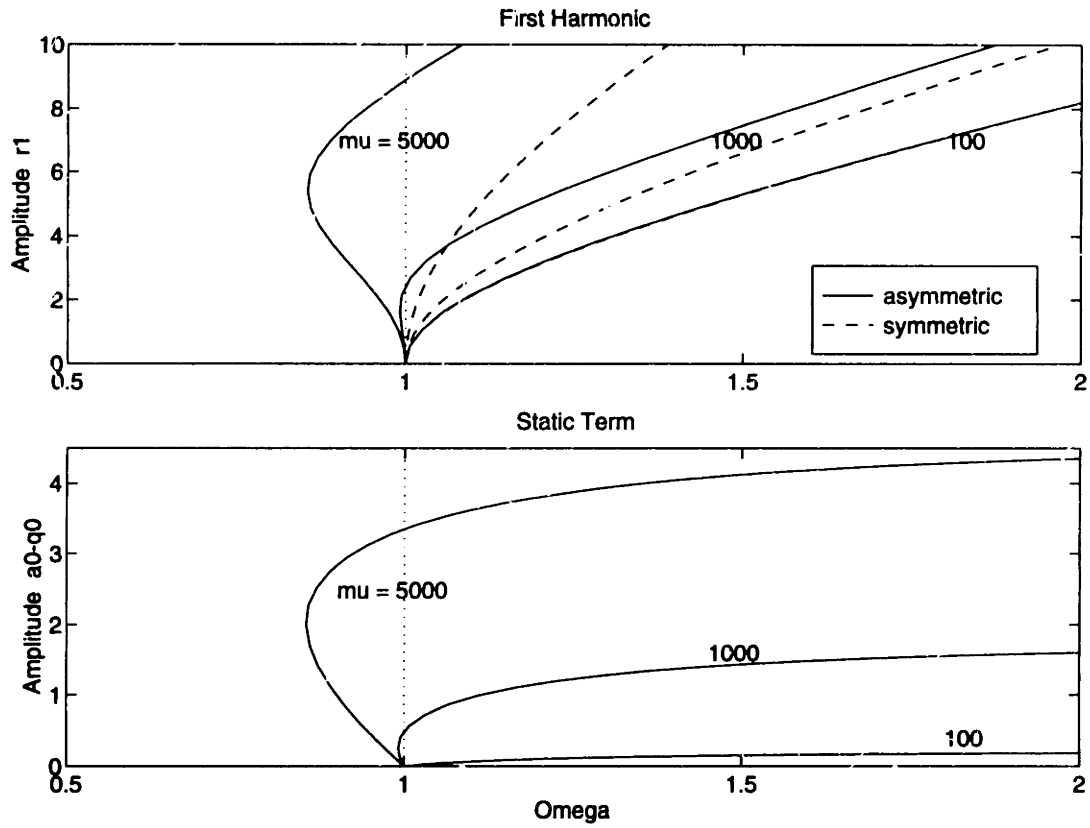

Figure 4-6: Static and harmonic backbones of the symmetric and asymmetric cubic nonlinearities for three mass ratios: $\mu = 100$, 1000, and 5000.

than one for small values of r_1, implying that the nonlinear natural frequency is less than the linear natural frequency. The system must therefore exhibit softening-spring behavior at low amplitudes.

The backbones of the symmetric and the asymmetric cubic nonlinearities are compared in Figure 4-6. The effect of the system's mass ratio is also depicted. For $\mu = 100$ the two harmonic backbones are virtually identical. The static deflection is negligible for such a mass ratio; note the small value of α_0 for $\mu = 100$ in Figure 4-5. There is a considerable difference between the backbones for $\mu = 1000$. The backbone for the symmetric nonlinearity bends over to the right, which is a defining characteristic of a hardening spring. Furthermore, this behavior is exhibited at all amplitudes. The backbone of the asymmetric nonlinearity, on the other hand, is almost vertical for $r_1 < 2$, after which the hardening behavior becomes apparent. The asymmetric backbone always lies to the left of the symmetric backbone, indicating

that the asymmetric system has a lower nonlinear natural frequency at all amplitudes. The difference between the backbones is even more pronounced for larger mass ratios. For $\mu = 5000$ the asymmetric backbone displays a large region in which it bends over to the left, acting as a softening spring. This continuous transition from softening to hardening behavior was also noted by Saito *et al.* [64] and by Nayfeh and Mook [70].

Forced Response

Equations (4.16) and (4.17) describe the forced response of the asymmetric and the symmetric nonlinearities, respectively. The actuator model has a mass ratio of approximatley 1200, for which the parameters in the equations of motion are $\alpha_0 = 1.46$, $\alpha_1 = 0.57$, $\alpha_2 = -0.21$, and $\alpha_3 = 0.03$. When used in the cancellation system, the actuator must generate forces on the same order as the disturbances created by the cryocooler. Based on measurements of the cryocooler's axial force, let $\bar{F} = 100$. The forcing parameter α_f then has a value of 0.12.

Using these parameter values, the forced response of both the symmetric and the asymmetric systems was computed as a function of the forcing frequency $\Omega_f = \omega_f/\omega_1$. As seen in Figure 4-7, the forced response has the same general character as that of a linear system with one major exception: the nonlinearity bends the resonance over, so the solution can be multi-valued. Three distinct portions of the response may be identified. There is an in-phase response to the left of the backbone, an out-of-phase response at low amplitudes to the right of the backbone, and an unstable branch at high amplitudes to the right of the backbone.

Stability

Determining the stability of a periodic solution to a nonlinear equation is in general quite difficult. For example, Hayashi [68] discusses a procedure whereby the stability is determined through the application of Floquet theory to Hill's equation (a multi-harmonic version of Mathieu's equation). A much simpler approach that is sufficient for a qualitative understanding of the solution's stability is a linear analysis of a perturbation of the steady-state solution [71].

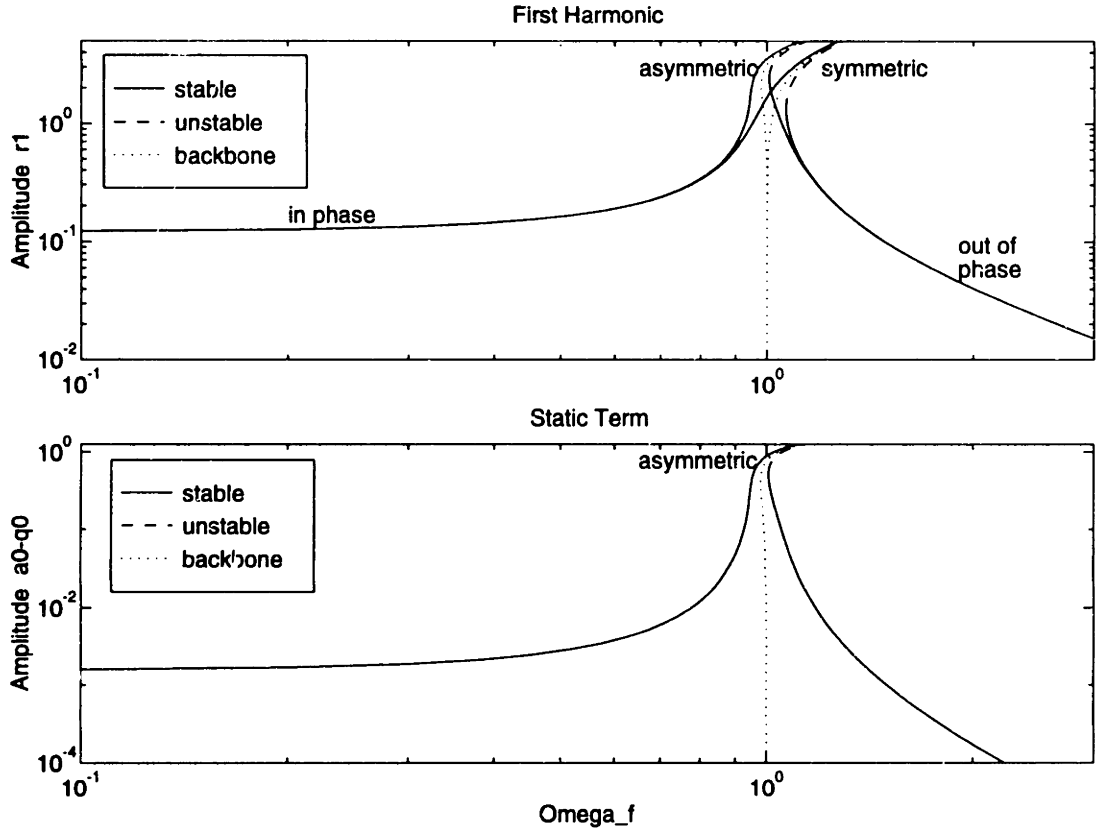

Figure 4-7: Forced response of the undamped symmetric and asymmetric systems as functions of the forcing frequency, $\Omega_f = \omega_f/\omega_1$.

For ease of exposition, consider the symmetric cubic nonlinearity:

$$\Omega_f \ddot{x} + x + \alpha_3 x^3 = \alpha_f \sin \tau \tag{4.20}$$

where τ is the nondimensional time introduced above. The simple harmonic solution of this equation is $x = b \sin \tau$. The coefficient b in the harmonic solution is determined by Equation (4.17), which may also be written as

$$(3/4)\alpha_3 b^3 - \alpha_f = \left(\Omega_f^2 - 1\right) b \tag{4.21}$$

or $z_1(b) = z_2(b)$. The left-hand side of this equation, $z_1(b)$, includes the nonlinear term and the forcing amplitude, while the right-hand side, $z_2(b)$, includes the forcing frequency. The frequency response for a given system may be determined by plotting the function $z_1(b)$ as well as a family of curves $z_2(b, \Omega_f)$ [72]. The values of b at which z_2 intersects z_1 define the response of the system (Figure 4-8). Notice that there are

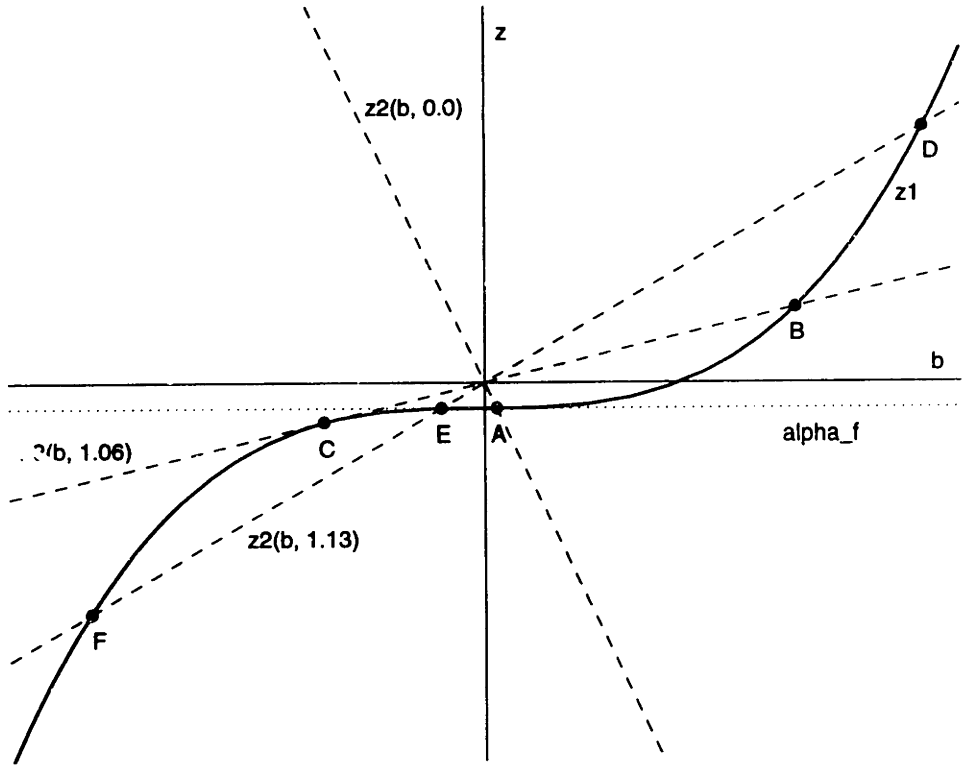

Figure 4-8: Geometric derivation of the frequency response of a system with a symmetric cubic nonlinearity.

three such intersections for sufficiently large Ω_f.

Each intersection represents an equilibrium point (a steady-state solution). Denote the associated coefficient by b_0. Now assume the solution is subject to a time-varying perturbation

$$x(\tau) = a(\tau)\cos\tau + [b_0 + b(\tau)]\sin\tau \tag{4.22}$$

Substitute this solution into Equation (4.20), and assume the perturbation is of infinitesimal amplitude and is only slowly time-varying. Noting that b_0 is an equilibrium value, the harmonic balance method yields two autonomous first-order differential equations in $a(\tau)$ and $b(\tau)$, namely

$$\begin{bmatrix} \dot{a} \\ \dot{b} \end{bmatrix} = \begin{bmatrix} 0 & A_1/2\Omega_f^2 \\ -A_2/2\Omega_f^2 & 0 \end{bmatrix} \begin{bmatrix} a \\ b \end{bmatrix} \tag{4.23}$$

where

$$\begin{aligned} A_1 &= 1 - \Omega_f^2 + (9/4)\alpha_3 b_0^2 \\ &= \frac{dz_1}{db}(b_0) - \frac{dz_2}{db}(b_0) \end{aligned}$$

$$\begin{aligned} A_2 &= 1 - \Omega_f^2 + (3/4)\alpha_3 b_0^2 \\ &= \alpha_f / b_0 \end{aligned}$$

The perturbation will remain bounded if this system is stable, *i.e.* if the matrix in Equation (4.23) has a positive determinant. This corresponds to the condition $A_1 A_2 > 0$; the terms A_1 and A_2 must have the same sign. The sign of the second term is simply the sign of the equilibrium coefficient b_0, while the sign of A_1 is determined by the difference in the slopes of $z_1(b)$ and $z_2(b)$ at b_0. For example, if $z_1(b_0^+) > z_2(b_0^+)$ where b_0^+ is immediately to the right of b_0, then $A_1 > 0$.

The graphical analysis may be used to explain the multi-valued nature of the frequency response. The in-phase response corresponds to the positive coefficients defined by the points A, B, and D in Figure 4-8. Both A_1 and A_2 are always positive at these points, so the in-phase response is a stable solution. The out-of-phase response is determined by the points C and E, which only occurs for sufficiently large forcing frequencies Ω_f. As Ω_f increases, the central intersection approaches the z axis and b tends to zero. Both A_1 and A_2 are always negative for the central intersection so the out-of-phase response is also a stable solution. The third response, defined by the points C and F, comes into existence at the same forcing frequency as the out-of-phase response, but the corresponding coefficient b increases in amplitude with increasing Ω_f. Furthermore, the values of A_1 and A_2 for this response are of different signs: A_1 is positive, while A_2 is negative. The large-amplitude out-of-phase response therefore represents an unstable solution. Any perturbation will move the system from this solution to one of the stable ones, making the unstable solution almost impossible to observe experimentally. It may also be difficult to determine numerically in the case of the coupled equations, Equation (4.16); much better conditioning is obtained by solving for r_1^2 rather than r_1.

The bifurcation between the unstable branch and the out-of-phase response occurs when $z_2(b, \Omega_f)$ is tangent to $z_1(b)$, as is apparent in Figure 4-8. Increasing Ω_f beyond this bifurcation point increases the amplitude of the unstable solution and decreases the amplitude of the out-of-phase response. Thus, the stability boundary in the system's frequency response (Figure 4-7) is defined by the location of a vertical tangent. This criterion was used to determine the stable and unstable branches of the asymmetric system's response.

4.3.2 Two-Harmonic Motion

As an improved approximation, include two harmonics in the response of the undamped system. The additional harmonic may be the second or the third.

The quadratic term in Equation (4.13) causes the second harmonic to appear as a cosine component: $\sin^2 \tau = (1/2)(1 - \cos 2\tau)$. An expression is therefore needed to determine a_2. Introducing the second-harmonic amplitude $r_2^2 = a_2^2$, Equation (4.15) may be rearranged to yield

$$\begin{aligned} (R_0 a_0 + \alpha_0) a_0 &= (1/2) R_2 r_2^2 \\ \left(R_1 - 2R_2 r_2^2 / r_1^2\right)^2 r_1^2 &= \alpha_f^2 \\ R_2^2 r_2^2 &= (9/4) \alpha_3^2 r_0^2 r_1^4 \end{aligned} \tag{4.24}$$

where

$$\begin{aligned} R_0 &= \alpha_1 + \alpha_3 r_0^2 + (3/2)\alpha_3 (r_1^2 + r_2^2) \\ R_1 &= \alpha_1 - \Omega_f^2 + 3\alpha_3 r_0^2 + (3/4)\alpha_3 (r_1^2 + 2r_2^2) \\ R_2 &= \alpha_1 - 4\Omega_f^2 + 3\alpha_3 r_0^2 + (3/4)\alpha_3 (2r_1^2 + r_2^2) \end{aligned}$$

Notice that when there is no static deflection, $r_0 = a_0 = 0$, the second harmonic vanishes; the symmetric system's response includes only odd harmonics.

The forced response of the asymmetric system was determined numerically using the parameter values associated with the actuator model. The amplitude of each component as a function of the forcing frequency is shown in Figure 4-9, which also includes the backbones ($\alpha_f = 0$) and the simple harmonic solution. In-phase ($b_1 =$

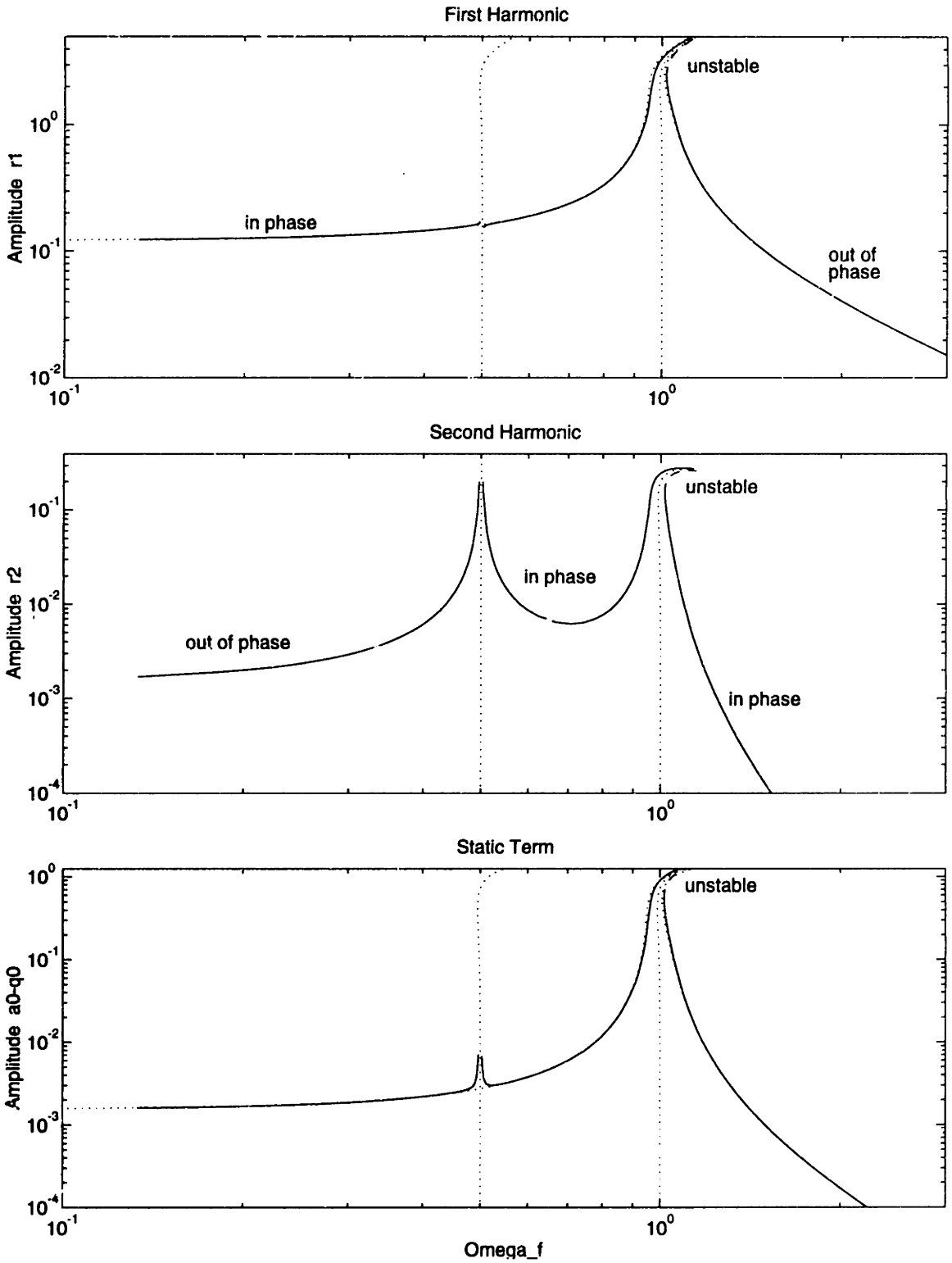

Figure 4-9: Forced response of the undamped asymmetric system as a function of the forcing frequency, $\Omega_f = \omega_f/\omega_1$. This solution includes the fundamental and the second harmonic. The backbones and the simple harmonic solution are denoted by dotted lines.

$+r_1$ or $a_2 = +r_2$), out-of-phase ($b_1 = -r_1$ or $a_2 = -r_2$), and unstable solutions are once again present. For the chosen forcing level ($\bar{F} = 100$, $\alpha_f = 0.12$), the second harmonic is almost two orders of magnitude smaller than the fundamental, and therefore the two-harmonic solution differs only slightly from the simple harmonic solution. The differences arise near the primary resonance ($\Omega_f \approx 1$) and near the second-order superharmonic resonance ($\Omega_f \approx 1/2$). Damping will of course limit the possible amplitudes at these resonances.

The third harmonic appears as a sine component due to the cubic term in Equation (4.13): $\sin^3\tau = (1/4)(3\sin\tau - \sin 3\tau)$. As was done for the second harmonic, introduce the third-harmonic amplitude $r_3^2 = b_3^2$ and rearrange Equation (4.15):

$$\begin{aligned} R_0 a_0 + \alpha_0 &= 0 \\ \left(R_1 - 3R_3 r_3^2/r_1^2\right)^2 r_1^2 &= \alpha_f^2 \\ R_3^2 r_3^2 &= (1/16)\alpha_3^2 r_1^6 \end{aligned} \tag{4.25}$$

where

$$\begin{aligned} R_0 &= \alpha_1 + \alpha_3 r_0^2 + (3/2)\alpha_3(r_1^2 + r_3^2) \\ R_1 &= \alpha_1 - \Omega_f^2 + 3\alpha_3 r_0^2 + (3/4)\alpha_3(r_1^2 + 2r_3^2) \\ R_3 &= \alpha_1 - 9\Omega_f^2 + 3\alpha_3 r_0^2 + (3/4)\alpha_3 r_3^2(2r_1^2 + r_3^2) \end{aligned}$$

In the absence of static deflection, these equations reduce to the system considered by Tseng and Dugundji [69] and by Szemplińska-Stupnicka [73].

The forced response is presented in Figure 4-10. This is very similar to the response that included the second harmonic. However, the third harmonic is even smaller than the second harmonic: it is almost four orders of magnitude smaller than the fundamental for this forcing amplitude and hence perturbs the simple harmonic solution much less. The other difference is that the superharmonic resonance occurs at $\Omega_f \approx 1/3$.

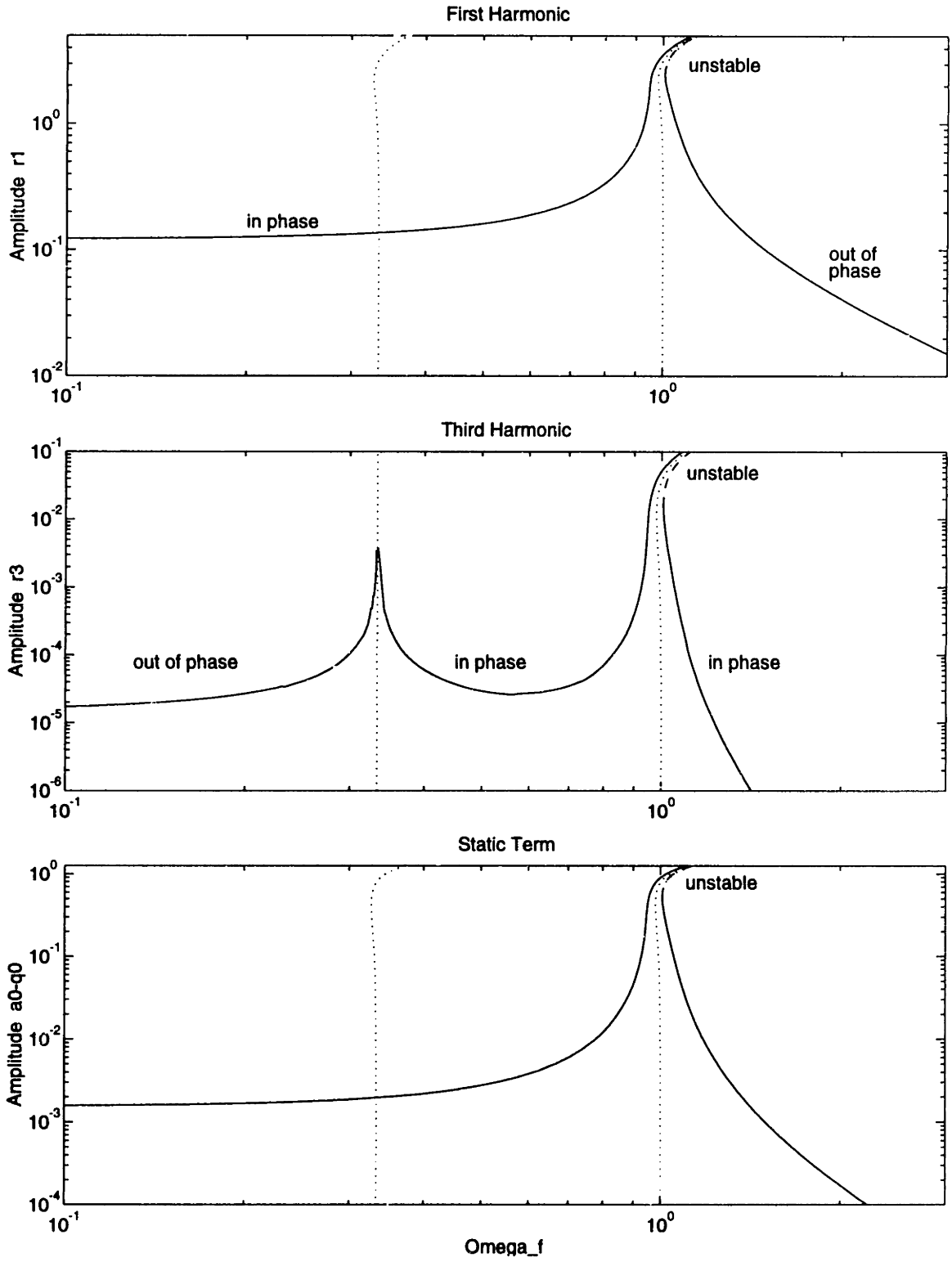

Figure 4-10: Forced response of the undamped asymmetric system as a function of the forcing frequency, $\Omega_f = \omega_f/\omega_1$. This solution includes the fundamental and the third harmonic. The backbones and the simple harmonic solution are denoted by dotted lines.

4.3.3 Three-Harmonic Motion

The full three-harmonic solution of the forced response of a damped asymmetric cubic oscillator may be determined by solving Equation (4.15) numerically, with both undamped two-harmonic solutions acting as initial guesses. The backbones, the initial guesses, and the stable branches of the solution are shown in Figure 4-11. This solution closely resembles the two-harmonic solution that includes the second harmonic—the addition of the small third harmonic has little effect on the static component, the fundamental, or the second harmonic. Notice, however, that the third harmonic is significantly modified by the presence of the second harmonic, especially near the second-order superharmonic resonance.

The wrapped phase of the various harmonic components is also shown in Figure 4-11. The effect of the damping ($\zeta = 0.01$) is clearly visible near the resonances. Burgess [74] showed the effect of various levels of damping on the phase of the third harmonic in the immediate vicinity of the third-order superharmonic resonance, and Szemplińska-Stupnicka [73] presented the phase of both the fundamental and the third harmonic over a wide range of forcing frequencies. However, both of these authors studied strongly nonlinear systems with symmetric cubic characteristics, *e.g.* the parameters were $\alpha_1 = 1$ and $\alpha_3 = 1$ with $\zeta = 0.2$ in Reference [73]. The phase of the solution in Figure 4-11 has quite a different character, due to both the lower level of the nonlinearity and the presence of the second-order superharmonic resonance, which will clearly be important when considering the effect of the nonlinearity on a closed-loop control system.

The three-harmonic solution is also shown for a lower forcing amplitude: $\bar{F} = 20$ rather than $\bar{F} = 100$. Because of the nonlinearity, the response is not simply a scaled version of the large-amplitude solution. The response near the primary resonance, for example, is fundamentally different at the lower forcing amplitude; it is no longer multi-valued. The fact that the primary resonance is not distorted at this amplitude is due to the asymmetry of the system: the softening quadratic term cancels the stiffening cubic term. In the case of a symmetric system, some distortion would be present at all forcing amplitudes.

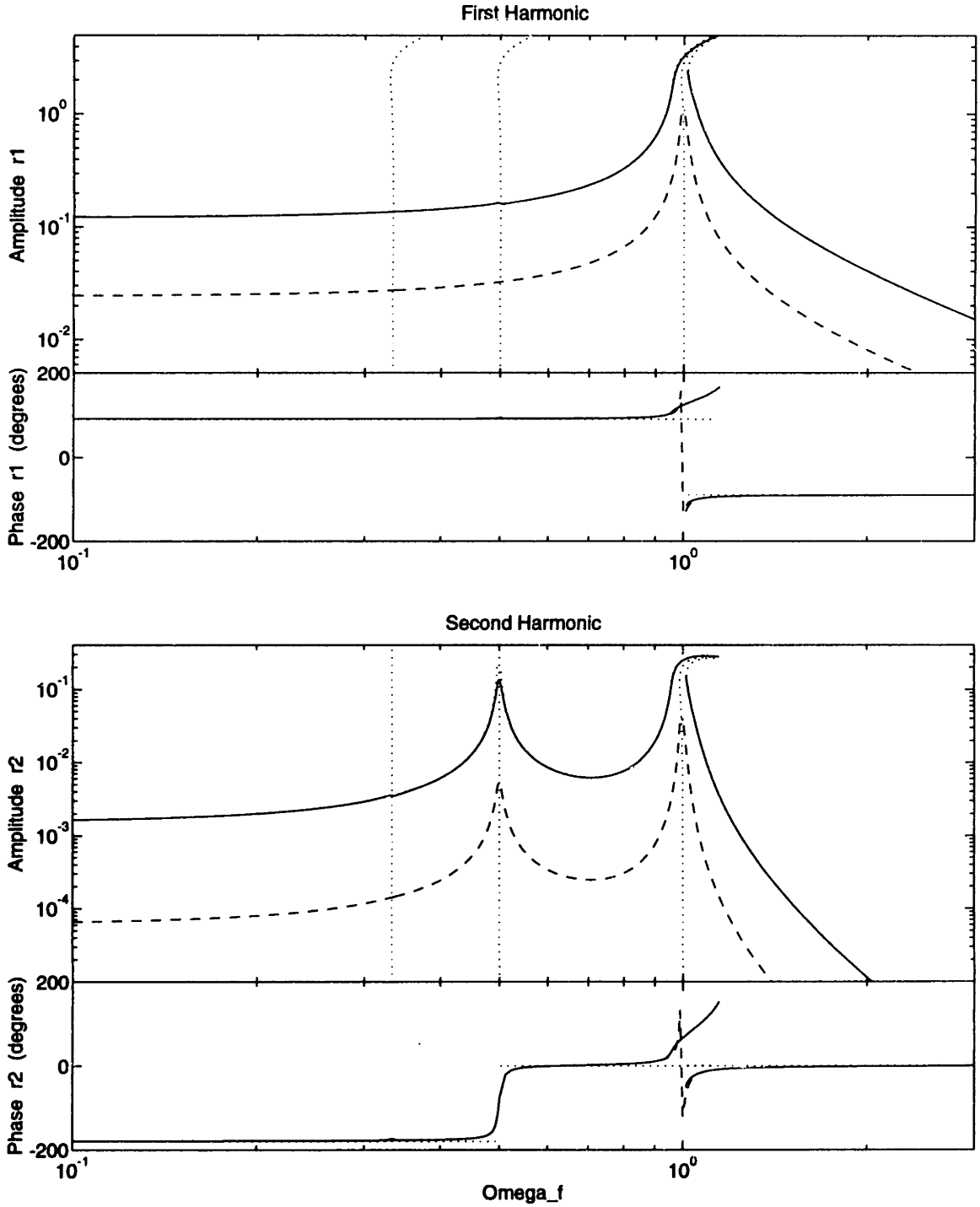

Figure 4-11: Stable forced response of the damped asymmetric system as a function of the forcing frequency, $\Omega_f = \omega_f/\omega_1$. Three-harmonic solution shown for two forcing amplitudes: $\bar{F} = 100$ (solid line) and $\bar{F} = 20$ (dashed line). The backbones and the two-harmonic solutions are denoted by dotted lines.

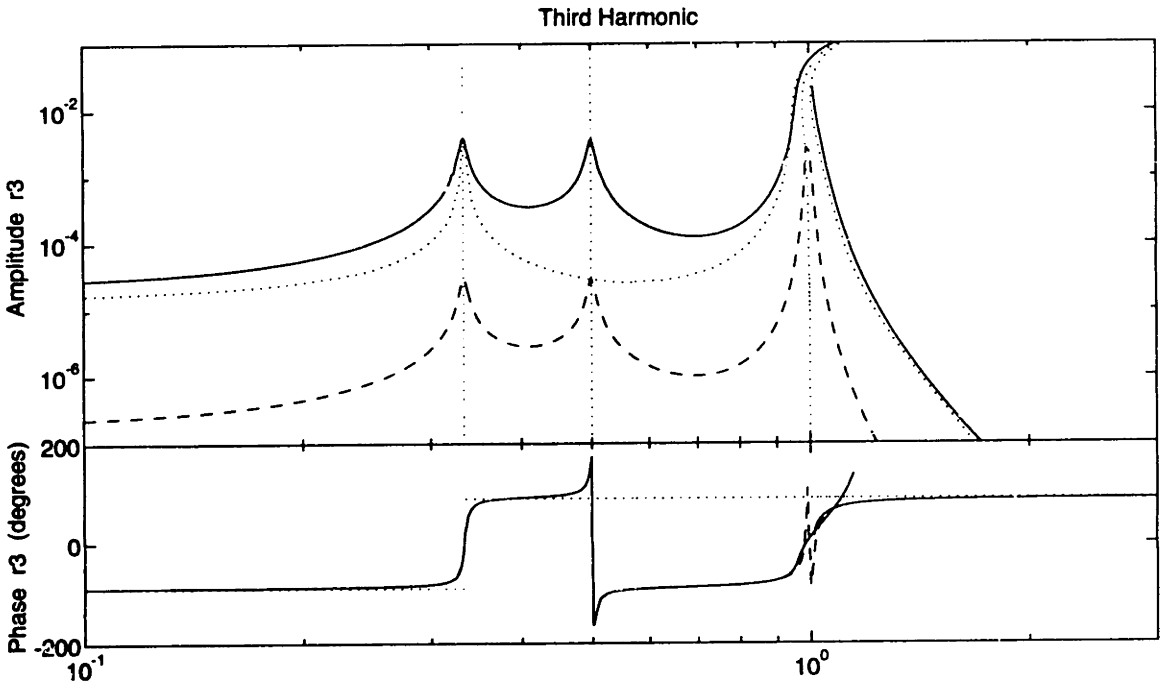
Third Harmonic
Amplitude r3
10^{-2}
10^{-4}
10^{-6}
Phase r3 (degrees)
200
0
-200
10^{-1}
10^{0}

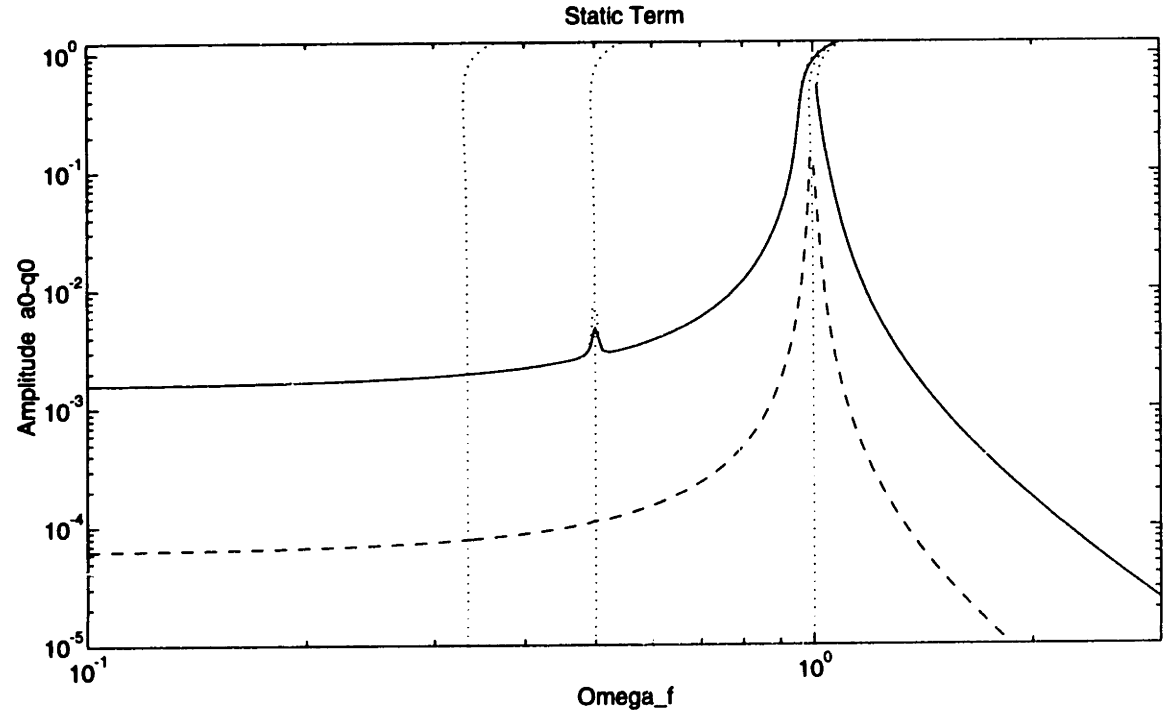
Static Term
Amplitude a0-q0
10^{0}
10^{-1}
10^{-2}
10^{-3}
10^{-4}
10^{-5}
10^{-1}
10^{0}
Omega_f

The scaling of the solution is also noteworthy. Both the forcing amplitude and the amplitude of the fundamental decreased by a factor of five, while the amplitude of the second harmonic decreased by a factor of $5^2 = 25$, and the amplitude of the third harmonic decreased by a factor of $5^3 = 125$, as might be expected. Since each component of the solution is scaled differently, a single frequency response function cannot be used to characterize the system's forced response, as is done with linear systems. However, this concept can be extended to higher-order transfer functions.

4.4 Higher-Order Transfer Functions

Even if several transfer functions are needed to characterize the response of a nonlinear system, this is preferable to having to compute a separate solution for each forcing amplitude. A simple yet theoretically rigorous approach for describing the frequency-domain response of nonlinear systems has been developed for the analysis of nonlinear circuits [75–77]. This approach is based on the application of Volterra series, which requires that the nonlinear characteristic is a polynomial and that the system is stable, causal, and time invariant. Although this approach cannot be used with dead zones, saturation, or hysteretic nonlinearities, it is applicable to a broad class of nonlinearities encountered in structural dynamics, including Duffing's equation, as has been discussed by several authors [78–80].

Just as a linear transfer function may be defined as the Fourier transform of an impulse response function, an nth-order transfer function may be defined as the multi-dimensional Fourier transform of the nth-order Volterra kernel. This leads to the elegant result that when a system is excited with a harmonic input, $Ae^{j\omega t}$, the frequency response of the nth output harmonic is given by the principal diagonal of the nth-order transfer function. This relationship forms the basis of the probing method of transfer-function identification [75].

Unfortunately additional terms in the input result in intermodulation components in the output. This is true even of the negative-frequency input components associated with a physical harmonic excitation, $A\cos\omega t = (1/2)A\,(e^{j\omega t} + e^{-j\omega t})$. The

intermodulation process causes each output harmonic to be affected by an infinite series of multi-dimensional transfer functions. Frequency-domain identification then relies on testing at several different input amplitudes to isolate the effect of each transfer function [77].

If it is not necessary to extract the individual Volterra kernels or their transforms, an nth-order frequency response function may be defined directly in terms of the nth output harmonic:

$$H_n(nf) = 2^{n-1}Y(nf)/X^n(f) \tag{4.26}$$

where $X(f)$ and $Y(nf)$ are the spectral amplitude and phase of the input signal and the nth output harmonic, respectively. Unlike the Volterra kernels, this frequency response function is amplitude dependent. The factor 2^{n-1} ensures that $H_n(nf)$ converges to the transform of the nth-order Volterra kernel as the input amplitude tends to zero.

This definition is well-suited for the experimental verification of nonlinear structural dynamics models. For example, Storer and Tomlinson [79] recently measured the first-, the second-, and the third-order frequency response functions of a clamped-clamped beam with significant initial curvature. Without an *a priori* model, however, the amplitude dependence of $H_n(nf)$ complicates interpretation of the results. Tasks such as parameter estimation or system identification are better handled with random-excitation techniques [81,82].

An experimental verification of the nonlinear actuator model was undertaken. A sine-dwell testing technique was adopted: the actuator was driven at a frequency of interest, time-domain averages of both the input and the output signals were collected, after which the frequency was changed to the next point of interest. In some runs the frequency was increased and in others it was decreased in order to obtain data on both sides of the jump phenomena in the multi-valued region. The time-domain averages were Fourier transformed to yield $X(f)$ and $Y(f)$, and values at the first three output harmonics were substituted into Equation (4.26).

Recognizing the inherent amplitude dependence of the harmonic transfer function technique, the results are compared with the transfer function estimates derived from

the numerical solution of the model's forced response (Section 4.3). One additional modification must be made. The output signal was obtained from the load cell system, so these are accelerance-type transfer functions rather than the receptance type that has been presented in this chapter. The transfer functions are easily modified:

$$\begin{aligned} H_{1A}(f) &= -\omega^2 H_{1R}(f) \\ H_{2A}(2f) &= -4\omega^2 H_{2R}(2f) \\ H_{3A}(3f) &= -9\omega^2 H_{3R}(3f) \end{aligned} \tag{4.27}$$

where A denotes accelerance and R receptance.

Two sets of data were collected. The first consisted of one run at an input level of 300 mV and one run at 500 mV. Amplitude and phase data were obtained in both runs. The resulting accelerance-type transfer function estimates are shown in Figure 4-12, where they are compared with the transfer function estimates derived from the forced response of the model. Only two parameters were adjusted manually to achieve a good fit: one parameter normalized the frequencies, and the other accounted for the sensor gain. The transfer functions match the model well. The model indicates that amplitude dependence is only to be expected near the primary resonance, and indeed the measurements display little variation between the different forcing levels. The exception is the third-order transfer function beyond the primary resonance. This appears to be a signal-to-noise problem—notice how the transfer function's level depends on the amplitude of the input. There are higher-order extensions of the coherence function [82,83] which might prove useful in tracking down the source of this behavior.

The second set featured three runs. In two of them, amplitude and phase data were obtained with input levels of 100 mV and 500 mV. In the third run, a modified measurement technique was used. This technique was based on autospectra rather than time-domain signals. While the phase information was lost, the data could be acquired much more quickly using the Tektronix Fourier Analyzer. This facilitated an investigation of the transfer functions near the multi-valued regions. The results from all three runs are shown in Figure 4-13; the estimates from the actuator model

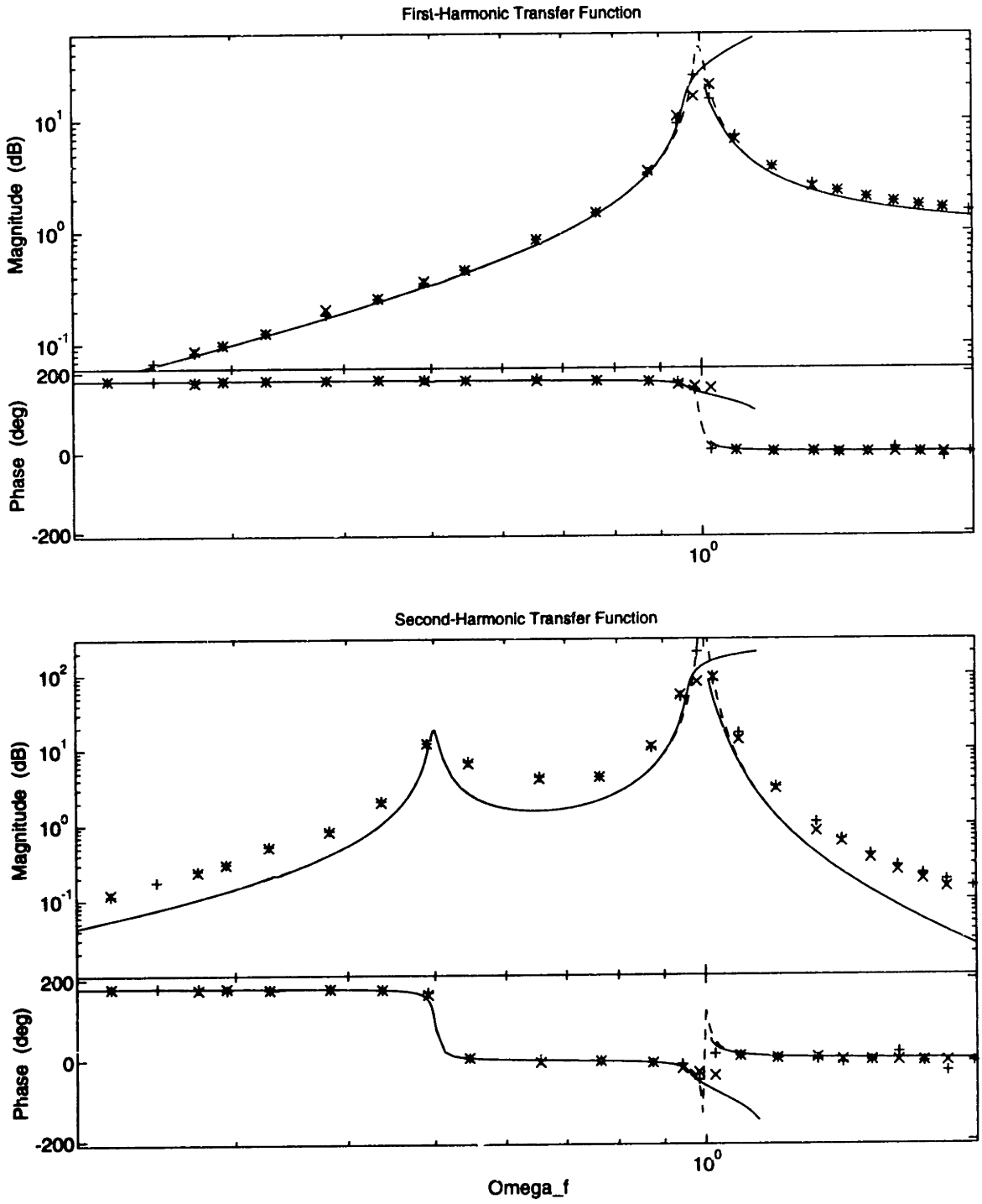

Figure 4-12: Estimated transfer functions using forced response of actuator model at two amplitudes: $\bar{F} = 100$ (solid line) and $\bar{F} = 20$ (dashed line). Experimental data shown for two amplitudes: 300 mV (+), and 500 mV (×).

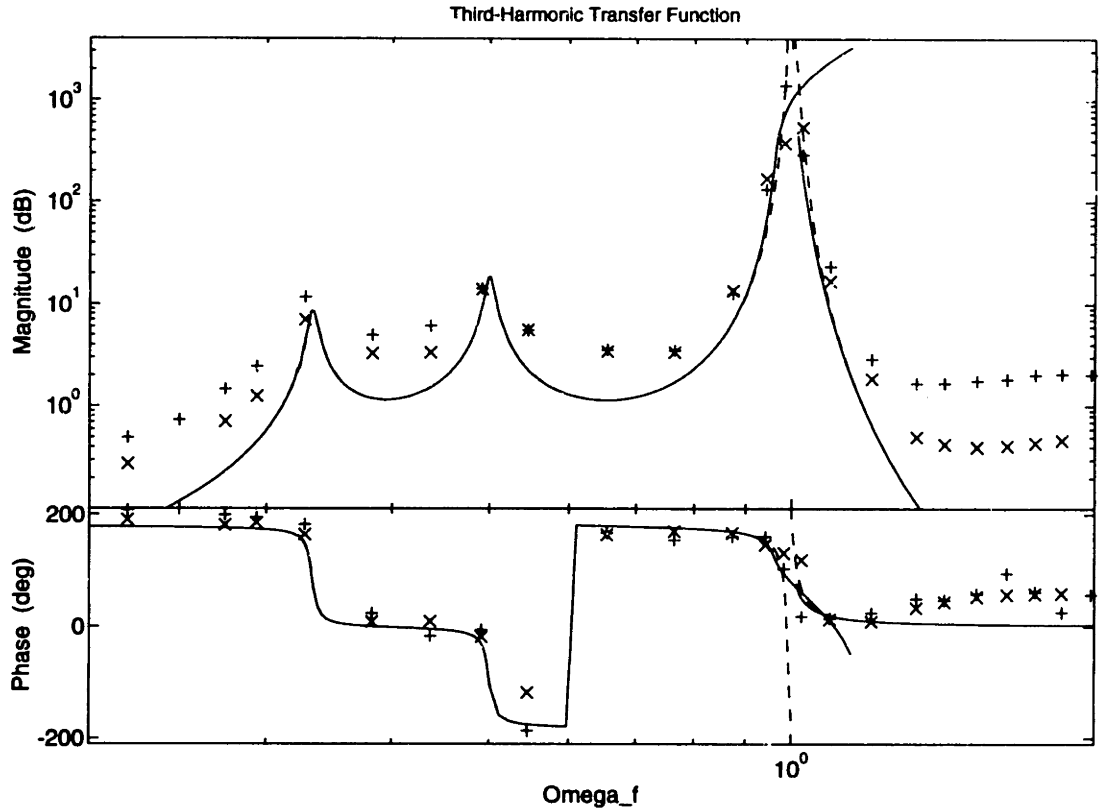

are also included. Only the first- and second-order transfer functions are shown for the lower forcing amplitude; the reponse was too noisy to make good measurements at the third harmonic.

The second set of data was collected approximately a week after the first set. It appears that the system changed quite dramatically in this time period. Additional dynamics are now clearly visible in the region $0.6 \leq \Omega_f \leq 0.8$. These are thought to be due to the lateral torque modes of the actuator, which lie in this region. One possibility is that the actuator transformation matrix was not properly calibrated during the second set. A commanded axial force could then produce a noticeable torque response. Another possibility is damage to one or more flexures.

The measurements near the primary resonance instability display the classic jump phenomenon: two stable solutions exist for a narrow band of frequencies. Approaching the resonance from a higher frequency led to different response than when it was approached from a lower frequency. It was also possible to force the response from one solution to the other by either knocking or restraining the actuator's reaction mass.

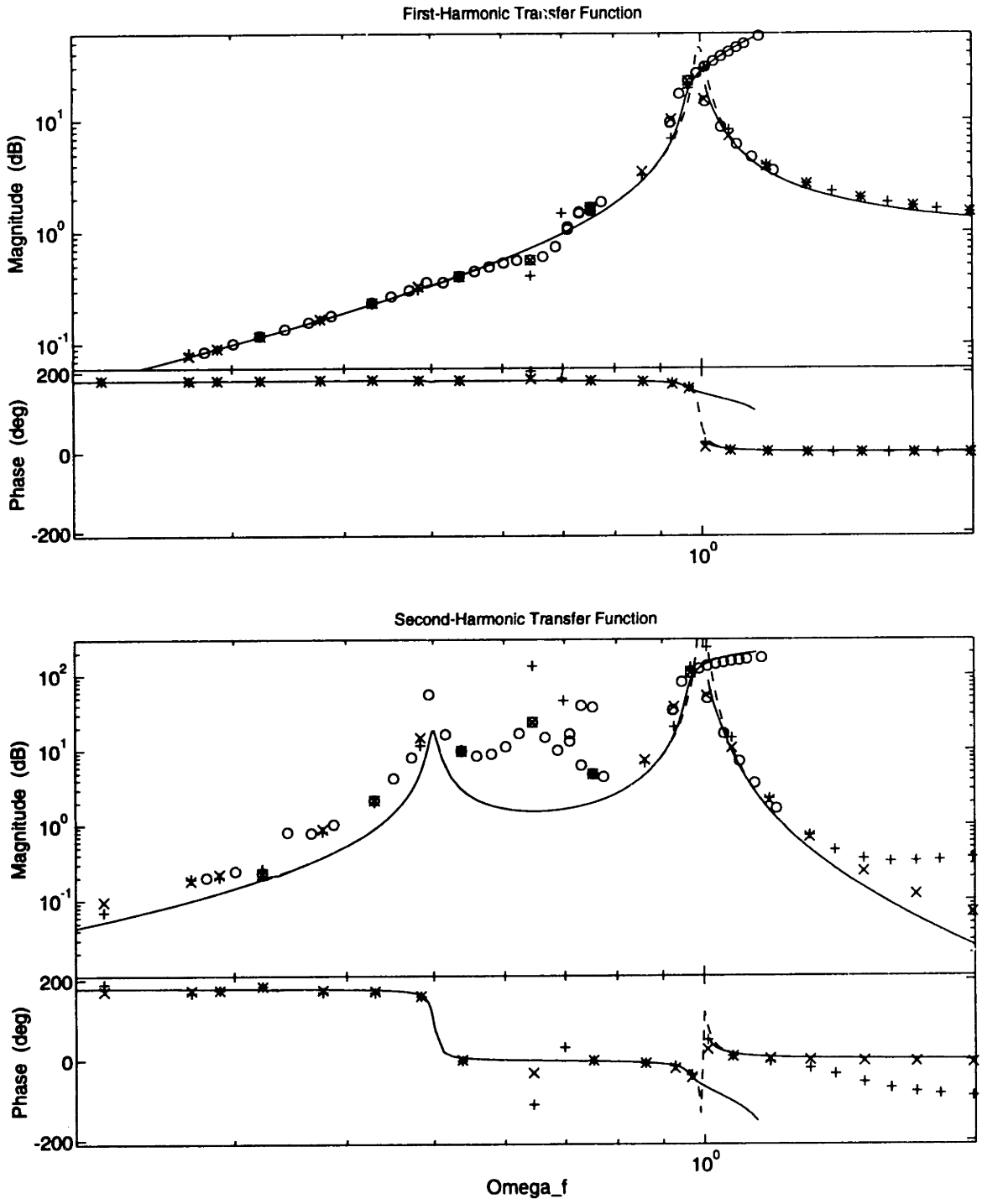

Figure 4-13: Estimated transfer functions using forced response of actuator model at two amplitudes: $\bar{F} = 100$ (solid line) and $\bar{F} = 20$ (dashed line). Experimental data shown for two amplitudes: 100 mV (+), and 500 mV (o, ×).

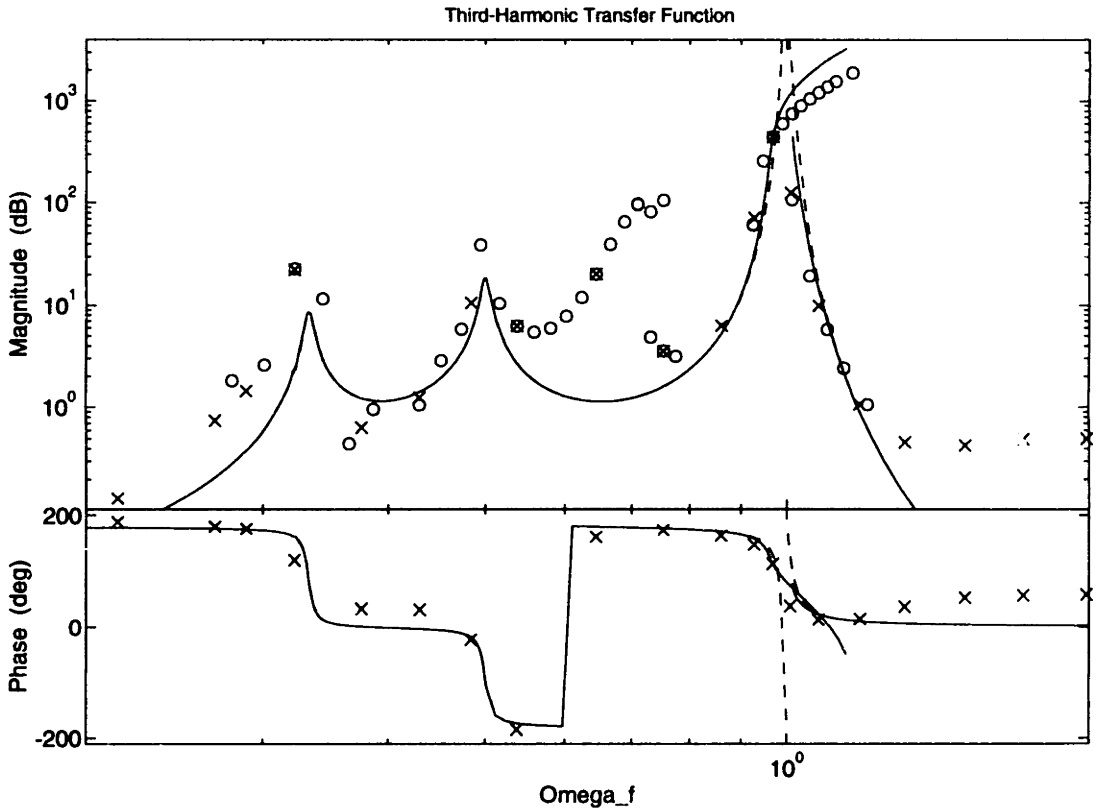

Details such as the amplitude's slope in this region and the multi-valued bandwidth correlate well with the model, indicating the parameters represent the model well. If greater accuracy were required, these measurements could be useful in determining the actuator's damping ratio and the effective mass ratio.

4.5 Effect on Linear Cancellation

The good agreement between the model and the experimental data provides confidence that the model captures the predominant component of the actuator's nonlinear response. The model may therefore be used to assess the effect of employing such an actuator in a typical linear cancellation system. This was the original motivation for developing the actuator model.

The behavior of both the actuator and the controller must be considered here. Sievers and von Flotow [84] noted that many of the narrowband disturbance rejection

schemes are equivalent to the classical compensator

$$K(s) = \frac{k_1 s + k_2}{s^2 + \omega_0^2} \tag{4.28}$$

which is a second-order bandpass filter centered on the disturbance frequency ω_0. Several of these filters may be used to cancel a periodic disturbance, with each filter tuned to a different harmonic. In this case the input to the actuator will consist of a sum of harmonics.

Using the nonlinear actuator with several bandpass filters certainly has the potential for trouble. As noted in connection with Equation (4.15), the harmonics in the actuator's output are fully coupled, making it possible to destabilize the closed-loop system. The effect of the harmonic coupling may be examined most conveniently with describing functions [85].

Given the bandpass nature of $K(s)$, the actuator's static deflection is of no direct significance here, so consider the actuator's equation of motion that includes the quadratic term, Equation (4.13). Let the nondimensional displacement of the mass be $y = \bar{q}_1$ and let the forcing term be u_L. The equation of motion is then

$$\ddot{y} + 2\zeta\omega_t\dot{y} + {\omega_t}^2\left(y + \alpha_2 y^2 + \alpha_3 y^3\right) = {\omega_t}^2 u_L \tag{4.29}$$

This equation represents an implicit dynamic nonlinearity: the nonlinearity is described in terms of the output variable y rather than the input variable u_L. Such a nonlinearity poses a formidable problem for describing-function analysis.

The linear dynamics and the amplitude nonlinearity may be separated by expressing the equation of motion in a feedback form [71]:

$$\ddot{y} + 2\zeta\omega_t\dot{y} + {\omega_t}^2 y = {\omega_t}^2 u \tag{4.30}$$

where

$$u = u_L + u_{NL} = u_L + \alpha_2 y^2 + \alpha_3 y^3$$

The nonlinear term u_{NL} in the local feedback loop is now a frequency-independent explicit nonlinearity, which is much easier to handle with describing functions.

Since each compensator $K_n(s)$ produces a sinusoid of frequency $n\omega_0$, the nonlinear element is best modelled with a multi-sinusoid-input describing function [85]. For simplicity, the two-controller case, which features two sinusoids, will be presented here. Additional controllers greatly complicate the algebra without fundamentally affecting the solution.

The two-sinusoid-input describing function (TSIDF) associated with a low-order polynomial characterisitic may be calculated by direct expansion. The characterisitic of the actuator's nonlinearity is

$$u_{NL} = \alpha_2 y^2 + \alpha_3 y^3 \tag{4.31}$$

Let the input be a pair of sinusoids of arbitrary amplitude and phase

$$y = A\cos\omega t + B\cos(\gamma\omega t + \theta) \tag{4.32}$$

The describing functions are found by substituting y into Equation (4.31), expanding the trigonometric terms, and retaining the output harmonics at ωt and $\gamma\omega t$. The describing functions N_A and N_B relate these output harmonics to the input harmonics of Equation (4.32):

$$N_A(A, B, \gamma, \theta) = u_{NL}(\omega)/y(\omega) \tag{4.33}$$

$$N_B(A, B, \gamma, \theta) = u_{NL}(\gamma\omega)/y(\gamma\omega) \tag{4.34}$$

The second harmonic in the actuator's response was found to be much more significant than the third harmonic, so the greatest coupling should occur between a first-harmonic controller and a second-harmonic controller. With $\gamma = 2$, it may be shown that the describing functions are

$$N_A(A, B, \gamma, \theta) = \alpha_2 B e^{j\theta} + \alpha_3(3/4)\left(A^2 + 2B^2\right) \tag{4.35}$$

$$N_B(A, B, \gamma, \theta) = \alpha_2\left(A^2/2B\right)e^{-j\theta} + \alpha_3(3/4)\left(2A^2 + B^2\right) \tag{4.36}$$

Notice that these are both complex and dependent on θ.

The effect of the actuator nonlinearity on the closed-loop cancellation system may

be determined. Denote the actuator's linear dynamics by $G_L(s)$, the TSIDFs by $N(A,B)$, and the controllers by $K(s) = K_1(s) + K_2(s)$. The s^2 block converts the actuator's displacement output y into a force y_f. It may be shown that the sensitivity transfer function for this system is

$$\frac{E(s)}{D(s)} = \left[1 + \frac{s^2 G_L(s) K(s)}{1 + N(A,B) G_L(s)}\right]^{-1} \tag{4.37}$$

The effect of the nonlinearity on performance may be assessed with an equivalent plant transfer function

$$G_{EQ}(s) = \frac{G_L(s)}{1 + N(A,B) G_L(s)} \tag{4.38}$$

The describing-function modifies the actuator's large-amplitude gain.

On the other hand, the effect on stability may be assessed with an equivalent controller. The system's characteristic equation is

$$1 + s^2 G_L(s) \left[K(s) + N(A,B)/s^2\right] = 0 \tag{4.39}$$

so the equivalent controller is

$$K_{EQ}(s) = K(s) + N(A,B)/s^2 \tag{4.40}$$

This may also be expressed in terms of a multiplicative error. Notice that the effect of the nonlinearity rolls off as s^2: the nonlinearity is a function of displacement, whereas the control output is a function of force or acceleration.

Given N_A, N_B, G_{EQ}, and K_{EQ}, the closed-loop system may be analysed using an expected range of A, B, and θ, the system parameters α_2 and α_3 are also important here. However, unless the actuator is being driven very hard (large A, B) or unless the actuator is very nonlinear (large α_2, α_3), the nonlinearity will have little effect on the system. By design, the controllers have high gain at the disturbance frequencies, swamping the effect of $N(A,B)$ in K_{EQ}. Furthermore, for the electrodynamic actuator the parameters are indeed small: $\alpha_2 = -0.21$ and $\alpha_3 = 0.03$. And based on the cryocooler vibration levels, A and B are on the order of 0.1 (in the nondimensional units consistent with the values of α_2 and α_3). Thus the magnitude of $N(A,B)$ is

much less than one, and the nonlinearity may be negelected.

The describing function analysis therefore indicates that the actuator nonlinearity has little effect on an active multi-harmonic cancellation system for the parameter values associated with the electrodynamic actuator and the cryocooler vibration. For different parameter values, the equivalent plant and controller expressions may be used to investigate the effect of the nonlinearity. Finally, it should be noted that this describing-function analysis only provides information about the system at the frequencies associated with the two narrowband controllers; the effect of the nonlinearity may still be visible at the uncontrolled harmonics.

4.6 Summary

A model of the actuator's nonlinearity was developed based on the assumption that the cause was the axial tension induced in the beam by both the static deflection and the vibration. Galerkin's method was used to derive numerical values for the parameters in Duffing's equation. A harmonic steady-state solution was assumed, and the unknown coefficients were determined with the harmonic balance method. This revealed a softening-hardening behavior due to the asymmetry caused by the static deflection. The various backbones and the amplitude and phase of the forced response were then obtained numerically. These results were not previously available for the asymmetric Duffing's equation.

A simplified definition of a higher-order transfer function was presented. Based directly on the output harmonics in response to a single-harmonic input, this definition is amplitude-dependent. But for the forcing levels associated with the cryocooler vibration, this dependence only affected the primary resonance. Experimental measurements of the first-, the second-, and the third-order transfer functions were found to be in good agreement with the numerical solutions, even in the multi-valued region near the primary resonance. This demonstrated that the nonlinear behavior was accurately modelled by the asymmetric Duffing's equation and that the parameters derived from the flexure model were indeed representative of the system.

The feasibility of using the nonlinear actuator in a typical active cancellation system was examined by means of describing functions. The nonlinear model was rearranged to separate the linear dynamics and the nonlinear amplitude dependence, allowing the direct computation of two-sinusoid-input describing functions. These describing functions were then used to determine an equivalent linear plant and an equivalent linear controller at the controlled harmonics. For the parameters associated with the electrodynamic actuator and the cryocooler vibration, neither of these equivalent systems was affected by the nonlinearity. This indicates that the nonlinear actuator may safely be used with linear narrowband controllers in this application. In other applications, the significance of the nonlinearity may be assessed via the general expressions for the equivalent linear plant and controller.

Chapter 5

Controller Design and Realization

> Until recently, the design and use of circuit configurations based on the conscious employment of nonlinear analog computing elements and formulations has been the recondite province of a few diehard experts in specialized areas of application.
>
> —D. H. Sheingold, 1974.

Many control techniques are available for closed-loop cancellation of periodic disturbances. A popular technique is adaptive feedforward cancellation. This has proven effective in a wide variety of applications and yet is remarkably easy to implement. Adaptation is typically based on Widrow's least-mean-square (LMS) algorithm or some variant thereof.

For vibration cancellation, the most important variant is the filtered-x LMS (FXLMS) algorithm, which is examined in detail in this chapter. After deriving the ideal behavior of the continuous-time FXLMS algorithm, consideration is given to factors that might limit performance. Bearing these effects in mind, a realization based on analog circuitry is discussed. The resulting FXLMS filter is then characterized in terms of its input-output properties.

5.1 Adaptive Feedforward Disturbance Rejection

The general approach to disturbance rejection using an adaptive feedforward filter is shown in Figure 5-1. The objective is to cancel a disturbance $d(t)$ using a cancella-

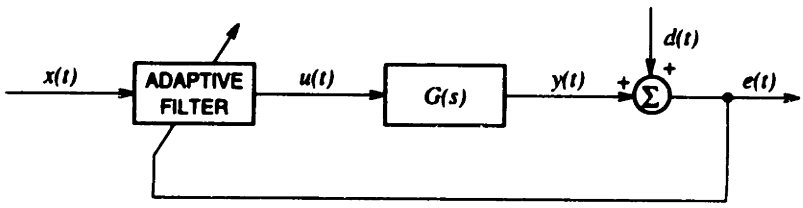

Figure 5-1: Adaptive feedforward disturbance rejection.

tion signal $y(t)$, which is produced by a plant $G(s)$ based on a control signal $u(t)$. In adaptive feedforward cancellation, $u(t)$ is a filtered version of a reference signal $x(t)$ which is correlated in an unknown way with the disturbance. The filter in the feedforward path is adapted based on the error signal $e(t)$.

Many alternatives have been proposed for both the adaptation algorithm and the structure of the feedforward filter [86]. The approach that has proven the most successful is an adaptive transversal filter governed by the LMS algorithm. The derivation in Reference [86] is presented in discrete time; an equivalent continuous-time algorithm is developed here.

5.1.1 Stochastic Disturbance Rejection

If the disturbance is a stationary stochastic signal, and if the correlation of the reference signal with the disturbance is known, the feedforward filter need not be adaptive. The optimal unconstrained fixed filter is then given by Wiener filter theory [87], where optimality is defined in terms of minimizing the average power of the error signal.

Consider the case where there is no plant in the feedforward path, so $y(t) = u(t)$. Assume the (fixed) feedforward filter is an N-stage transversal filter such that the filter output is

$$y(t) = \sum_{n=1}^{N} w_n x_n(t) = \mathbf{w}^T \mathbf{x}(t) \tag{5.1}$$

where $\mathbf{w} = [w_1, w_2, \ldots, w_N]^T$ is the filter weight vector and $\mathbf{x}(t) = [x_1(t), x_2(t), \ldots, x_N(t)]^T$ is a vector of filter inputs derived from the reference signal. For example, the elements $x_n(t)$ might be obtained from a tapped delay line.

From Figure 5-1, the error at time t is

$$\begin{aligned} e(t) &= d(t) + y(t) \\ &= d(t) + \mathbf{w}^T\mathbf{x}(t) \end{aligned} \tag{5.2}$$

The mean square error is therefore

$$\begin{aligned} \xi &= E[e^2(t)] \\ &= E[d^2(t)] + 2\mathbf{w}^T E[d(t)\mathbf{x}(t)] + \mathbf{w}^T E[\mathbf{x}(t)\mathbf{x}^T(t)]\mathbf{w} \end{aligned} \tag{5.3}$$

where $E[\cdot]$ denotes the expected value of $[\cdot]$; recall that the filter weights $\mathbf{w}$ are fixed. Let the reference correlation matrix be $\mathbf{R} = E[\mathbf{x}(t)\mathbf{x}^T(t)]$ and let the cross-correlation vector be $\mathbf{p} = E[d(t)\mathbf{x}(t)]$. Then the mean square error is

$$\xi = E[d^2(t)] + 2\mathbf{w}^T\mathbf{p} + \mathbf{w}^T\mathbf{R}\mathbf{w} \tag{5.4}$$

This defines a performance surface which is a quadratic function of $\mathbf{w}$.

The optimal filter is given by the weight vector that minimizes the mean square error. The gradient of ξ is

$$\nabla = \partial\xi/\partial\mathbf{w} = 2(\mathbf{p} + \mathbf{R}\mathbf{w}) \tag{5.5}$$

The optimal weight vector is found by setting the gradient to zero. Assuming that $\mathbf{R}$ is nonsingular, this yields

$$\mathbf{w}_{\text{opt}} = -\mathbf{R}^{-1}\mathbf{p} \tag{5.6}$$

which is the matrix form of the Wiener-Hopf equation [88].

Unfortunately, in most cases neither $\mathbf{R}$ nor $\mathbf{p}$ is known. This motivates using an adaptive filter, in which the weights are modified based on a gradient estimate. Rather than using a gradient-search technique, Widrow and Hoff [89] suggested taking the instantaneous square error as an estimate of the mean square error, $\hat{\xi}(t) = e^2(t)$. The corresponding gradient estimate is

$$\hat{\nabla}(t) = \partial\hat{\xi}(t)/\partial\mathbf{w}$$

$$
\begin{aligned}
&= 2e(t)\,\partial e(t)/\partial \mathbf{w} \\
&= 2e(t)\mathbf{x}(t) \qquad (5.7)
\end{aligned}
$$

This instantaneous estimate of the gradient may then be used to drive a steepest-descent adaptive algorithm

$$
\begin{aligned}
\dot{\mathbf{w}}(t) &= -\mu\hat{\nabla}(t) \\
&= -2\mu e(t)\mathbf{x}(t) \qquad (5.8)
\end{aligned}
$$

where μ is an adaptation parameter that controls how quickly the weight adaptation process descends the performance surface.

It may be shown that the weight vector governed by Equation (5.8) converges in the mean to the optimal weight vector. Under steady-state conditions, the variation of the mean of the weights is by definition zero, $E[\dot{\mathbf{w}}_{ss}(t)] = 0$. Setting the expected value of Equation (5.8) to zero and substituting Equation (5.2) yields

$$
\mathbf{p} + \mathbf{R}E[\mathbf{w}_{ss}(t)] = 0
$$

$$
E[\mathbf{w}_{ss}(t)] = -\mathbf{R}^{-1}\mathbf{p} = \mathbf{w}_{opt} \qquad (5.9)
$$

This convergence in the mean is due to the fact that the instantaneous square error is an unbiased estimate of the mean square error, *i.e.* $E[\hat{\xi}(t)] = \xi$.

The continuous-time LMS algorithm may be summarized as

$$
\begin{aligned}
e(t) &= d(t) + y(t) \qquad (5.10) \\
y(t) &= \mathbf{w}^T(t)\mathbf{x}(t) \qquad (5.11) \\
\dot{\mathbf{w}}(t) &= -2\mu e(t)\mathbf{x}(t) \qquad (5.12)
\end{aligned}
$$

This is in agreement with Karni and Zeng [90], given that they define the error as $e(t) = d(t) - y(t)$. Several features make the LMS algorithm attractive for implementation: it requires no squaring, averaging, or differentiation; no weight-vector perturbation is necessary; and no storage is needed.

If the cancellation signal is not equal to the filter output, $y(t) \neq u(t)$, the presence

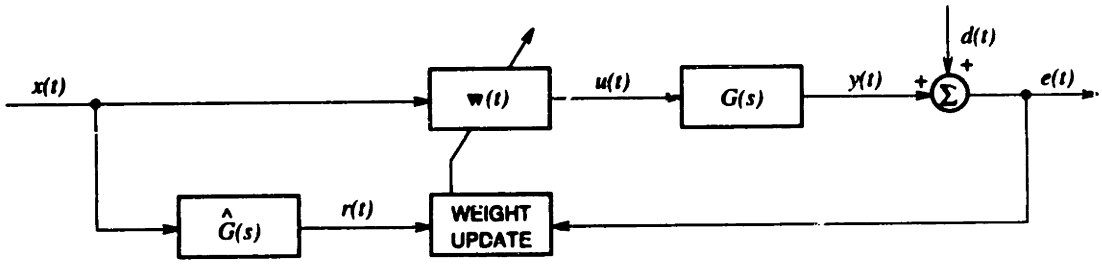

Figure 5-2: Adaptive feedforward disturbance rejection with the filtered-x LMS algorithm.

of the plant $G(s)$ must be accounted for. It was noted by several authors [91–93] that this could be done by filtering the reference signal $x(t)$ through $\hat{G}(s)$, an estimate of the plant. This is the filtered-x LMS algorithm. Denoting the filtered reference signal by $r(t)$, the continuous-time FXLMS algorithm is

$$e(t) = d(t) + y(t) \tag{5.13}$$

$$y(t) = g(t) * u(t) \tag{5.14}$$

$$u(t) = \mathbf{w}^T(t)\mathbf{x}(t) \tag{5.15}$$

$$\dot{\mathbf{w}}(t) = -2\mu e(t)\mathbf{r}(t) \tag{5.16}$$

$$\mathbf{r}(t) = \hat{g}(t) * \mathbf{x}(t) \tag{5.17}$$

where $*$ denotes convolution, $g(t)$ is the impulse response function of the plant, and $\hat{g}(t)$ is the impulse response function of the plant estimate. The FXLMS system is illustrated in Figure 5-2.

5.1.2 Harmonic Disturbance Rejection

While the LMS algorithm was motivated by stochastic-signal filtering, it also provides excellent harmonic disturbance rejection. Glover [94] demonstrated that this behavior is best analyzed by explicitly accounting for the harmonic nature of the reference signal in this application. Elliott *et al.* [95] applied the same discrete-time analysis technique to the filtered-x LMS algorithm.

In both cases it was shown that the relationship between the error signal and the output of the adaptive filter may be described by an equivalent linear transfer

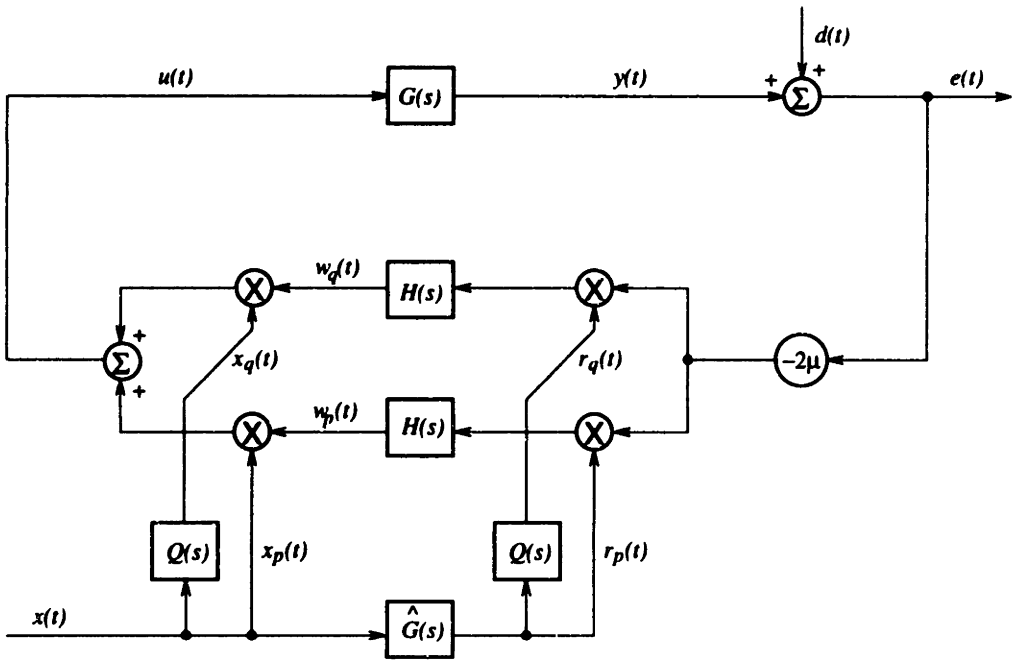

Figure 5-3: Two-weight continuous-time filtered-x LMS adaptive feedforward disturbance rejection.

function under certain conditions. Specifically, with a periodic reference signal the LMS algorithm acts as a second-order bandpass filter. This results in a notch at the reference frequency in the sensitivity transfer function, *i.e.* the transfer function from the disturbance to the error. Notice that this behavior is *not* indicated by the stochastic analysis: if the reference and error signals are sinusoids of different frequency, the cross-correlation is zero, the Wiener weights are identically zero, and no cancellation is possible. The difference is that the harmonic analysis allows a dynamic weight solution to develop.

Glover's analysis technique may be applied to the continuous-time FXLMS algorithm. Consider the two-weight filter shown in Figure 5-3; this is the minimum number of weights needed for perfect rejection of a harmonic disturbance. Based on Equation (5.16), $H(s)$ represents an integrator. In an ideal system, the reference signal $x(t)$ is harmonic at frequency ω_x and the filters $Q(s)$ produce the quadrature reference components, *i.e.* $Q(s)$ introduces a 90° phase shift at the reference frequency ω_x. The in-phase and quadrature channels of the adaptive filter are identified by the subscripts p and q, respectively.

Glover's analysis consists of tracing the error signal around the loop in the transform domain. As a preliminary step, consider the various reference signals that modulate the error signal. Assume the in-phase reference signal is a cosine

$$x_p(t) = A_x \cos \omega_x t \tag{5.18}$$

The Fourier transform of this signal is

$$X_p(j\omega) = \pi A_x \left[\delta(j\omega + j\omega_x) + \delta(j\omega - j\omega_x)\right] \tag{5.19}$$

In the transform domain, the quadrature reference signal is then

$$X_q(j\omega) = \pi A_x Q(j\omega) \left[\delta(j\omega + j\omega_x) + \delta(j\omega - j\omega_x)\right] \tag{5.20}$$

while the filtered reference signals are

$$R_p(j\omega) = \pi A_x \hat{G}(j\omega) \left[\delta(j\omega + j\omega_x) + \delta(j\omega - j\omega_x)\right] \tag{5.21}$$

$$R_q(j\omega) = \pi A_x \hat{G}(j\omega) Q(j\omega) \left[\delta(j\omega + j\omega_x) + \delta(j\omega - j\omega_x)\right] \tag{5.22}$$

After passing through the gain stage, the error signal is correlated with the filtered reference signal. For example, the output of the first in-phase multiplier is

$$m_{1p}(t) = -2\mu e(t) r_p(t) \tag{5.23}$$

The Fourier transform of this signal may be determined using the convolution theorem

$$\begin{aligned} M_{1p}(j\omega) &= \frac{-2\mu}{2\pi} E(j\omega) * R_p(j\omega) \\ &= -(\mu/\pi) \int_{-\infty}^{\infty} E(j\omega_1) R_p(j\omega - j\omega_1)\, d\omega_1 \\ &= -\mu A_x \left[\hat{G}(-j\omega_x) E(j\omega + j\omega_x) + \hat{G}(j\omega_x) E(j\omega - j\omega_x)\right] \end{aligned} \tag{5.24}$$

Similarly, the output of the first quadrature multiplier is

$$\begin{aligned} M_{1q}(j\omega) = -\mu A_x \big[&\hat{G}(-j\omega_x) Q(-j\omega_x) E(j\omega + j\omega_x) \\ &+ \hat{G}(j\omega_x) Q(j\omega_x) E(j\omega - j\omega_x)\big] \end{aligned} \tag{5.25}$$

As may be seen by comparing Equations (5.23) and (5.16), the filter weights are

obtained by integrating the multiplier outputs. Denoting the integrators by $H(j\omega)$, the weights are

$$W_p(j\omega) = -\mu A_x H(j\omega)\left[\hat{G}(-j\omega_x)E(j\omega+j\omega_x)+\hat{G}(j\omega_x)E(j\omega-j\omega_x)\right] \quad (5.26)$$

$$W_q(j\omega) = -\mu A_x H(j\omega)\left[\hat{G}(-j\omega_x)Q(-j\omega_x)E(j\omega+j\omega_x) + \hat{G}(j\omega_x)Q(j\omega_x)E(j\omega-j\omega_x)\right] \quad (5.27)$$

These weights are then correlated with the unfiltered reference signals, yielding

$$M_{2p}(j\omega) = -\frac{\mu}{2}A_x^2\left\{H(j\omega+j\omega_x)\left[\hat{G}(-j\omega_x)E(j\omega+j2\omega_x)+\hat{G}(j\omega_x)E(j\omega)\right] + H(j\omega-j\omega_x)\left[\hat{G}(-j\omega_x)E(j\omega)+\hat{G}(j\omega_x)E(j\omega-j2\omega_x)\right]\right\} \quad (5.28)$$

$$M_{2q}(j\omega) = -\frac{\mu}{2}A_x^2\left\{H(j\omega+j\omega_x)Q(-j\omega_x)\left[\hat{G}(-j\omega_x)Q(-j\omega_x)E(j\omega+j2\omega_x) + \hat{G}(j\omega_x)Q(j\omega_x)E(j\omega)\right] + H(j\omega-j\omega_x)Q(j\omega_x) \times\left[\hat{G}(-j\omega_x)Q(-j\omega_x)E(j\omega)+\hat{G}(j\omega_x)Q(j\omega_x)E(j\omega-j2\omega_x)\right]\right\} \quad (5.29)$$

The adaptive filter output is the sum of these two multiplier outputs, so

$$U(j\omega) = -\frac{\mu}{2}A_x^2\left\{\left[1+Q(-j\omega_x)Q(j\omega_x)\right]H(j\omega+j\omega_x)\hat{G}(j\omega_x)E(j\omega) + \left[1+Q(-j\omega_x)Q(j\omega_x)\right]H(j\omega-j\omega_x)\hat{G}(-j\omega_x)E(j\omega) + \left[1+Q^2(-j\omega_x)\right]H(j\omega+j\omega_x)\hat{G}(-j\omega_x)E(j\omega+j2\omega_x) + \left[1+Q^2(j\omega_x)\right]H(j\omega-j\omega_x)\hat{G}(j\omega_x)E(j\omega-j2\omega_x)\right\} \quad (5.30)$$

This may be simplified by recalling that physical systems have real impulse response functions, so their frequency response functions must display conjugate symmetry. Thus $\hat{G}(-j\omega_x) = \hat{G}^*(j\omega_x)$ and $Q(-j\omega_x) = Q^*(j\omega_x)$, where $*$ denotes the complex conjugate. In polar notation, the filter responses are given by

$$\hat{G}(\pm j\omega_x) = \hat{A}_g(\omega_x)e^{\pm j\hat{\theta}_g(\omega_x)} \quad (5.31)$$

$$Q(\pm j\omega_x) = A_q(\omega_x)e^{\pm j\theta_q(\omega_x)} \quad (5.32)$$

Although the gain and phase of these filters may be general functions of frequency, the adaptive filter output is affected only by the response at ω_x, due to the harmonic

nature of the reference signal. The adaptive filter output is then

$$\begin{aligned} U(j\omega) &= -\frac{\mu}{2}A_x^2\hat{A}_g\left\{(1+A_q^2)\left[e^{j\hat{\theta}_g}H(j\omega+j\omega_x)+e^{-j\hat{\theta}_g}H(j\omega-j\omega_x)\right]E(j\omega)\right. \\ &\quad +\left[1+A_q^2e^{-j2\theta_q}\right]e^{-j\hat{\theta}_g}H(j\omega+j\omega_x)\,E(j\omega+j2\omega_x) \\ &\quad \left.+\left[1+A_q^2e^{j2\theta_q}\right]e^{j\hat{\theta}_g}H(j\omega-j\omega_x)\,E(j\omega-j2\omega_x)\right\} \end{aligned} \tag{5.33}$$

This expression for $U(j\omega)$ has the same character as the response of the discrete-time LMS filter. As noted by Glover [94], there are two components to the adaptive filter's response. The first component represents the filter's linear response: the output $U(j\omega)$ is a linear function of $E(j\omega)$. The second component represents the filter's nonlinear response: signal intermodulation causes input components at $\omega \pm 2\omega_x$ to appear in the output at ω. The LMS algorithm may only be approximated by a linear transfer function if the nonlinear component of its response is negligible.

In an ideal implementation of the two-weight FXLMS filter, the quadrature filter $Q(s)$ has unity gain and 90° of phase at the reference frequency ω_x, so $A_q = 1$ and $\theta_q = 90°$. Substituting these values into Equation (5.33) eliminates the nonlinear component of the adaptive filter's response, leaving

$$U(j\omega) = -\mu A_x^2\hat{A}_g\left[e^{j\hat{\theta}_g}H(j\omega+j\omega_x)+e^{-j\hat{\theta}_g}H(j\omega-j\omega_x)\right]E(j\omega) \tag{5.34}$$

If $H(s)$ is an integrator, $H(s) = 1/s$, then the equivalent linear transfer function is

$$-K(s) = \frac{U(s)}{E(s)} = -2\mu A_x^2\hat{A}_g\,\frac{s\cos\hat{\theta}_g+\omega_x\sin\hat{\theta}_g}{s^2+\omega_x^2} \tag{5.35}$$

Sievers and von Flotow [84] derived a similar expression for $K(s)$. However, they assumed the reference signal was of unit amplitude, $A_x = 1$, so they did not include the A_x^2 term. In the measurements reported below, this term was found to have a strong effect on the performance of the adaptive filter.

As shown by Equation (5.35), the FXLMS adaptive filter is equivalent to a second-order bandpass filter with the center frequency determined by the reference signal. The ideal adaptive feedforward system may therefore be considered a standard feedback system for the purpose of stability and performance analysis. The compensator

dynamics $K(s)$ feature a complex-conjugate pole pair at $s = \pm j\omega_x$ and a real zero at $s = -\omega_x \tan\hat{\theta}_g$. The bandwidth over which the compensator gain exceeds 0 dB is determined by the zero location and by the gain factors μ, A_x, and $\hat{A}_g$.

The closed-loop disturbance rejection achieved by such a controller may be derived from the sensitivity transfer function, which is the transfer function from the disturbance to the closed-loop error

$$S(s) = \frac{E(s)}{D(s)} = \frac{1}{1 + G(s)K(s)} \tag{5.36}$$

Thus the undamped poles in $K(s)$ at ω_x ensure that disturbances at the reference frequency are completely cancelled, *i.e.* $S(j\omega_x) = 0$. It should be noted that $K(j\omega)$ is positive real. In the case of the LMS algorithm ($G = 1$), this implies that disturbance rejection is achieved at all frequencies, since $|S(j\omega)| < 1$ for all ω. On the other hand, given any plant dynamics, Bode's gain-phase theorem [96] dictates that

$$\int_0^\infty \ln|S(j\omega)|\, d\omega = 0 \tag{5.37}$$

so the sensitivity must be greater than one over some bandwidth, implying some disturbance amplification with the filtered-x LMS algorithm. Freudenberg and Looze [97] showed that this increase in sensitivity is not spread out over an arbitrarily large bandwidth, but rather appears as a peak near cross-over (the so-called push-pop phenomenon). Morgan and Thi [98] proposed using a cascade of FXLMS filters to limit the amplitude of this sensitivity peak for time-delay plants.

The effect of the reference filter $\hat{G}(s)$ on the closed-loop system may be shown by computing the residue of GK at the compensator poles. This will determine the closed-loop behavior for small gains provided there are no plant dynamics in the compensator bandwidth. Consider, for example, the residue at $s = j\omega_x$

$$\begin{aligned} \text{Res}[G(s)K(s);\, s = j\omega_x] &= 2\mu A_x^2 \hat{A}_g G(s) \left.\frac{s\cos\hat{\theta}_g + \omega_x \sin\hat{\theta}_g}{s + j\omega_x}\right|_{s=j\omega_x} \\ &= \mu A_x^2 \hat{A}_g A_g(\omega_x)\, e^{j\theta_g(\omega_x)}\, e^{-j\hat{\theta}_g} \end{aligned} \tag{5.38}$$

which suggests several possible choices for $\hat{G}(j\omega_x) = \hat{A}_g e^{j\hat{\theta}_g}$.

The phase of the residue at the open-loop pole determines the root-locus departure angle. A departure angle of 180° is desirable for several reasons: it stabilizes the closed-loop system, it maximizes the phase margin, and it minimizes the sensitivity at ω_x. This departure angle may be achieved by selecting $\hat{\theta}_g = \theta(j\omega_x)$, resulting in a residue with 0° of phase. The importance of matching the plant's phase at the reference frequency is widely recognized. Indeed, the precursor to the FXLMS algorithm was the delayed LMS algorithm [99, 100], in which a delay is introduced into the reference path to match the delay in the plant. For narrowband applications, this is equivalent to matching the phase at ω_x.

If the departure angle is 180°, for small gains the closed-loop poles may be approximated by

$$s = -\mu A_x^2 \hat{A}_g A_g(\omega_x) \pm j\omega_x \tag{5.39}$$

which implies that the time constant of the closed-loop system is $1/\mu A_x^2 \hat{A}_g A_g(\omega_x)$. In the usual implementation of the FXLMS algorithm, the reference filter gain is matched to the plant gain at the reference frequency, $\hat{A}_g = A_g(\omega_x)$. The plant therefore has a direct effect on the closed-loop time constant. Another option is $\hat{A}_g = 1/A_g(\omega_x)$, which eliminates the effect of the plant. This may be viewed as the single-error equivalent of the modified multiple-error LMS algorithm proposed by Sievers and von Flotow [84], in which they suggested taking as the reference filter

$$\mathbf{G}_{\text{LMS}} = \left(\hat{\mathbf{G}}\hat{\mathbf{G}}^H\right)^{-1} \hat{\mathbf{G}} \tag{5.40}$$

where H indicates the conjugate transpose and $\hat{\mathbf{G}} = \mathbf{G}(j\omega_x)$ is an estimate of the plant transfer-function matrix at the reference frequency. This choice of $\hat{A}_g$ is also equivalent to the use of the decoupling matrix in higher-harmonic control [101].

5.2 Factors Affecting Performance

Before developing a practical realization of the two-weight filtered-x LMS filter, the factors affecting the filter's performance should be considered. This will indicate which aspects of the filter deserve the most attention. Factors relating to the quadra-

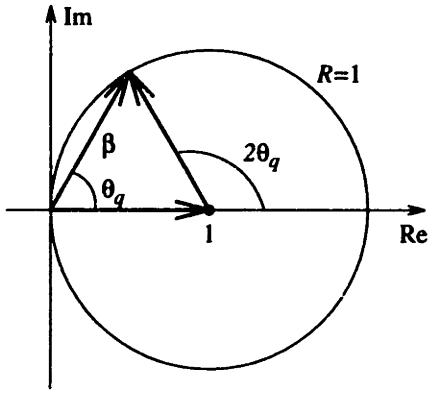

Figure 5-4: Geometric interpretation of $1 + e^{j2\theta_q} = \beta e^{j\theta_q}$.

ture filters, the integrators, the reference signal, and the plant will be examined here. In the adaptive feedforward control of sound, an additional limiting factor is the feedback from the plant output to the reference signal [102]. This path is negligible in the cryocooler vibration application and so will not be considered.

5.2.1 Imperfect Quadrature

The general expression for the output of the FXLMS filter is given by Equation (5.33). The nonlinear portion of the response consists of two frequency-shifted components multiplied by the factors $(1+A_q^2 e^{\pm j2\theta_q})$. These components are eliminated in the ideal adaptive filter since $A_q = 1$ and $\theta_q = 90°$. Imperfect quadrature results in imperfect cancellation of the filter's nonlinear response.

Consider the effect of a phase error; assume that $A_q = 1$. The factors amplifying the nonlinear frequency-shifted components are

$$1 + e^{\pm j2\theta_q} = (2\cos\theta_q)e^{\pm j\theta_q} \tag{5.41}$$

Glover [94] denotes this factor by $\beta(\theta_q, N)e^{\pm j\theta_q}$ where N is the number of filter weights. For the two-weight filter, $\beta(\theta_q, 2) = 2\cos\theta_q$; a geometric interpretation is presented in Figure 5-4.

The linear component of the filter's response, on the other hand, is shown in Equation (5.33) to be multiplied by the factor $1 + A_q^2 = 2 = N$; each channel contributes

an identical linear component to the output. Since both the linear and the nonlinear components are filtered by $H(j\omega \pm j\omega_x)$, the ratio of the nonlinear-component gain to the linear-component gain is $\beta(\theta_q, N)/N$. Small values of this ratio indicate that the nonlinear components are probably negligible, so the FXLMS filter may be approximated by the LTI transfer function $K(s)$ of Equation (5.35).

Expressing the phase of the quadrature filter as $\theta_q = 90° - \Delta\theta_q$, the gain ratio is $\beta(\theta_q, N)/N = \sin\Delta\theta_q$, or $\beta(\theta_q, N)/N = \Delta\theta_q$ for small phase errors ($\Delta\theta_q$ in radians). For example, a phase error of 5° results in a gain ratio of $\beta/N = 0.087 = -21$ dB. This suggests that the adaptive filter is not sensitive to small phase errors in the quadrature filter.

There are several ways that the frequency-shifted components may affect the adaptive filter's performance. In the case of a periodic error signal, energy is redistributed among the harmonics. For example, if an LMS filter ($G = \hat{G} = 1$) is used to cancel the first harmonic of a disturbance with harmonics at ω_x and $3\omega_x$, the open-loop filter output at the reference frequency is

$$\begin{aligned} Y(j\omega_x) &= -\mu A_x^2 \Big\{ [H(j2\omega_x) + H(0)]E(j\omega_x) + (\beta/N)\left[e^{-j\theta_q} H(j2\omega_x)E(j3\omega_x)\right. \\ &\qquad \left. + e^{j\theta_q} H(0)E(-j\omega_x)\right]\Big\} \end{aligned} \tag{5.42}$$

Since the error is a physical signal, the positive- and negative-frequency components are related: $E(-j\omega_x) = E^*(j\omega_x)$, or $E(-j\omega_x) = e^{-j2\theta_1}E(j\omega_x)$ where θ_1 is the phase of $E(j\omega_x)$. For most implementations, $H(s)$ is a good approximation of an integrator, so $|H(0)| \gg |H(j2\omega_x)|$. Neglecting the $H(j2\omega_x)$ terms, the open-loop output is

$$Y(j\omega_x) = -\mu A_x^2 H(0)\left[1 + (\beta/N)e^{j\theta_q}e^{-j2\theta_1}\right] E(j\omega_x) \tag{5.43}$$

Thus, at the reference frequency, the frequency-shifted components appear as a multiplicative error.

This error will change the closed-loop disturbance rejection if $H(0)$ is finite. For large values of $H(0)$, a worst-case variation of 1 dB is produced by a gain ratio of $\beta/N = 0.12$, which corresponds to a phase error of 7°. This demonstrates the performance robustness of the adaptive filter to small phase errors in the quadrature

filter when the adaptive filter is used to cancel a periodic disturbance.

The other case that deserves attention occurs when there are additional components in the error signal. Components that are not harmonically related to the reference frequency might be due to a second cooler operating at a slightly different speed or they might be due to near-by structural resonances.

Assume, for example, that the disturbance includes components at ω_x and $\omega_2 = \omega_x + \Delta\omega$. Retaining the dominant terms in $H(s)$, the open-loop output of an LMS filter has significant components at

$$Y(\pm j\omega_x) = -\mu A_x^2 H(0)\left[E(\pm j\omega_x) + (\beta/N)e^{\pm j\theta_q}E(\mp j\omega_x)\right] \quad (5.44)$$

$$Y(\pm j(\omega_x + \Delta\omega)) = -\mu A_x^2 H(\pm\Delta\omega)\left[E(\pm j(\omega_x + \Delta\omega)) + (\beta/N)e^{\pm j\theta_q}E(\mp j(\omega_x - \Delta\omega))\right] \quad (5.45)$$

$$Y(\pm j(\omega_x - \Delta\omega)) = -\mu A_x^2 H(\mp\Delta\omega)\left[E(\pm j(\omega_x - \Delta\omega)) + (\beta/N)e^{\pm j\theta_q}E(\mp j(\omega_x + \Delta\omega))\right] \quad (5.46)$$

Equation (5.44) is equivalent to Equation (5.43), so the multiplicative error at the reference frequency is present in this case too. However, Equations (5.45) and (5.46) represent a new phenomenon: a disturbance at $\omega_x + \Delta\omega$ is "mirrored" about the reference frequency and appears at $\omega_x - \Delta\omega$. These components will be coupled in the closed-loop system, although they will be gain-stabilized for small values of β/N. This behavior was observed recently by Snyder and Tanaka [103]; unfortunately they provided no indication of the magnitude of β/N. If the disturbance spectrum contains large components near the reference frequency, the quadrature filter phase must be implemented with better accuracy than suggested by the amplitude of the multiplicative error.

5.2.2 Leaky Integrator

The perfect disturbance rejection achieved by the ideal FXLMS filter at the reference frequency is due to the integrators in the error path. There are, however, some problems with this arrangement. It is difficult to collect open-loop data, *e.g.* the

loop transfer function, since the weights quickly saturate. Similarly, DC errors in the multiplier outputs can saturate the weights in the closed-loop system [102]. An undamped compensator can also be very sensitive to interaction with structural modes if there is insufficient frequency separation [104].

The tendency to saturate may be eliminated, and the stability robustness may be improved, by changing $H(s)$ from an integrator to a lowpass filter. This corresponds to the leaky LMS algorithm [86]. The algorithm's forgetting factor is set by the corner frequency of the lowpass filter. For example, consider the first-order lowpass filter

$$H(s) = A_h/(s + \alpha_h) \tag{5.47}$$

Substituting this into the response of the ideal two-weight FXLMS filter, Equation (5.34), yields an equivalent linear transfer function

$$K(s) = 2\mu A_x^2 A_h \hat{A}_g \frac{(s + \alpha_h)\cos\hat{\theta}_g + \omega_x \sin\hat{\theta}_g}{(s + \alpha_h)^2 + \omega_x^2} \tag{5.48}$$

The compensator poles and zero have been shifted by α_h, *i.e.* the zero is now at $s = -\alpha_h - \omega_x \tan\hat{\theta}_g$ and the poles are at $s = -\alpha_h \pm j\omega_x$. These poles have a natural frequency of $\omega_n = \omega_x\sqrt{1 + (\alpha_h/\omega_x)^2}$ and a damping ratio of $\zeta = \alpha_h/\omega_n$, which is approximately α_h/ω_x for low corner frequencies ($\alpha_h \ll \omega_x$).

The leaky FXLMS algorithm changes two aspects of the closed-loop system. The closed-loop time constant for small gains is $1/(\alpha_h + \mu A_x^2 A_h \hat{A}_g A_g)$. This is slightly smaller than the time constant with an integrator, implying faster convergence. On the other hand, the disturbance rejection at the reference frequency is reduced. For $\alpha_h \ll \omega_x$ and $\hat{\theta}_g = \theta_g(\omega_x)$, the minimum sensitivity is

$$S(j\omega_x) = 1/(1 + \mu A_x^2 A_h \hat{A}_g A_g/\alpha_h) \tag{5.49}$$

Notice that for a fixed α_h, the compensator damping decreases with increasing ω_x, whereas the peak disturbance rejection is independent of ω_x. The loop gain may be adjusted to provide a given level of disturbance rejection; this will also affect the compensator's bandwidth.

5.2.3 Integration Bias Error

A recurring problem in analog circuits is bias error. It is particularly troubling in adaptive filtering since the purpose of the multiplier/integrator combination is to shift to DC the harmonic of interest in the error signal. AC coupling would therefore eliminate the useful information as well as the bias error.

Assume that bias terms $N_p\delta(j\omega)$ and $N_q\delta(j\omega)$ are added to the in-phase and quadrature weights, Equations (5.26) and (5.27), respectively. It may be shown that for $H(0) \gg H(j2\omega_x)$, the output of the ideal LMS filter at the reference frequency is

$$Y(\pm j\omega_x) = -\mu A_x^2 H(0) E(\pm j\omega_x) + (1/2) A_x A_n e^{\pm j\theta_n} \tag{5.50}$$

where $A_n^2 = N_p^2 + N_q^2$ and $\tan\theta_n = N_q/N_p$. The closed-loop error signal at the reference frequency is then

$$\left[1 + \mu A_x^2 H(0)\right] E(\pm j\omega_x) = D(\pm j\omega_x) + (1/2) A_x A_n e^{\pm j\theta_n} \tag{5.51}$$

The bias error appears in the closed-loop error as an additional disturbance at the reference frequency. If $D(\pm j\omega_x) = A_d e^{\pm j\theta_d}$, then

$$S(\pm j\omega_x) = \frac{1 + (A_x A_n / 2A_d) e^{\pm j(\theta_n - \theta_d)}}{1 + \mu A_x^2 H(0)} \tag{5.52}$$

The closed-loop disturbance rejection will be affected if $H(0)$ is finite. In the worst case, the disturbance rejection level will be decreased by a factor of $(1 + A_x A_n / 2A_d)$. This may be used to determine an acceptable level of bias error.

5.2.4 Noisy Reference Signal

In deriving the equivalent linear transfer function for the adaptive filter, it was assumed that the reference signal was a pure tone. The addition of noise to this signal will degrade the filter's performance. Shensa [105] found that the depth of the notch in the sensitivity function decreases with the reference signal-to-noise ratio, *i.e.* the disturbance rejection decreases with increasing noise levels. He also developed expressions to account for the considerable difference between the notch depth measured

with a white noise disturbance and the notch depth measured with a harmonic disturbance.

A much simpler approximation may be derived based on the stochastic behavior of the LMS algorithm. Nelson and Elliott [102] demonstrated that the presence of a reference filter does not affect the minimum mean square error. The reduction in the power spectral density of the error signal may be expressed as

$$\frac{[S_{ee}]_{\min}(\omega)}{S_{dd}(\omega)} = 1 - \frac{|S_{xd}(\omega)|^2}{S_{xx}(\omega)S_{dd}(\omega)} = 1 - \gamma_{xd}^2(\omega) \tag{5.53}$$

where $\gamma_{xd}^2(\omega)$ is the ordinary coherence function between $x(t)$ and $d(t)$.

Assume the reference signal is a harmonic of amplitude A_x at a frequency ω_x, and assume the reference noise has a power spectral density N_0. The signal-to-noise ratio in the reference path at the reference frequency is then

$$\mathrm{SNR}_x(\omega_x) = A_x^2/2N_0 \tag{5.54}$$

If the disturbance is a harmonic of amplitude A_d at ω_x, the ordinary coherence function is then

$$\gamma_{xd}^2(\omega_x) = \frac{\mathrm{SNR}_x(\omega_x)}{1 + \mathrm{SNR}_x(\omega_x)} \tag{5.55}$$

and the fractional reduction in the power spectral density of the error is

$$\frac{[S_{ee}]_{\min}(\omega)}{S_{dd}(\omega)} = \frac{1}{1 + \mathrm{SNR}_x(\omega_x)} \tag{5.56}$$

Therefore, with a reasonable reference SNR, the disturbance power at the reference harmonic is reduced by $1/\mathrm{SNR}_x$. This also gives the reduction in amplitude of the disturbance harmonic if the SNR is expressed in dB.

5.2.5 Periodic Reference Signal

Rather than additive white noise, the reference signal might be contaminated by additional harmonics. The transform-domain analysis presented above may be repeated for this case.

For simplicity, consider the LMS algorithm and assume $A_q = 1$. Replacing Equa-

tion (5.18) with

$$x_p(t) = \sum_{m=1}^{M} A_m \cos(\omega_m t + \theta_m) \tag{5.57}$$

where the frequencies need not be harmonically related, it may be shown that the adaptive filter output is

$$\begin{aligned} Y(j\omega) \;=\; & -\mu E(j\omega) \sum_{m=1}^{M} A_m^2 \left[H(j\omega + j\omega_m) + H(j\omega - j\omega_m)\right] \\ & - \frac{\mu}{2} \sum_{m=1}^{M} \sum_{\substack{n=1 \\ n\neq m}}^{M} A_m A_n e^{\pm j(\theta_m - \theta_n)} e^{\mp j(\theta_{qm} - \theta_{qn})/2} \beta\left([\theta_{qm} - \theta_{qn}]/2, N\right) \\ & \quad \times H(j\omega \pm j\omega_m)\, E(j\omega \pm j[\omega_m - \omega_n]) \\ & - \frac{\mu}{2} \sum_{m=1}^{M} \sum_{n=1}^{M} A_m A_n e^{\pm j(\theta_m + \theta_n)} e^{\mp j(\theta_{qm} + \theta_{qn})/2} \beta\left([\theta_{qm} + \theta_{qn}]/2, N\right) \\ & \quad \times H(j\omega \pm j\omega_m)\, E(j\omega \pm j[\omega_m + \omega_n]) \end{aligned} \tag{5.58}$$

where $\theta_{qm} = \theta_q(\omega_m)$.

There are now three components in the filter's response: a linear component proportional to $E(j\omega)$, a nonlinear difference component proportional to $E(j\omega \pm j[\omega_m - \omega_n])$, and a nonlinear sum component proportional to $E(j\omega \pm j[\omega_m + \omega_n])$. The sum component may be eliminated with ideal quadrature, *i.e.* $\theta_q(\omega_m) = 90°$ for all ω_m. T' is is not easy to implement; recall that $A_q(\omega_m) = 1$ for all ω_m. However, even if it were implemented, the nonlinear difference components would not be eliminated. As was done previously, a gain ratio may be defined: the ratio of the gain of the mnth difference component to the gain of the ℓth linear component is

$$\Gamma_{\ell mn} = (A_m A_n / A_\ell^2)\, \beta([\theta_{qm} - \theta_{qn}]/2, N)/N \tag{5.59}$$

If $\theta_{qm} = \theta_{qn}$, this reduces to $A_m A_n / A_\ell^2$.

The nonlinear components have the same effect as was discussed in relation to imperfect quadrature. There are simply more of them now. While Chen and Lewis [106] succeeded in simultaneously cancelling two harmonics using a two-weight filter, several nonlinear components of significant amplitude are apparent in Figure 5a of Reference [106]. In discrete-time filter analysis, these components are controlled by

providing many more weights than suggested by the number of harmonics, *e.g.* Glover used a 64-weight filter to cancel three harmonics [94]. This has the effect of reducing β/N. With the two-weight filter, the only solution is to minimize the amplitudes of the additional harmonics in the reference signal. Phase-locked loops or various filters may be used to generate a reference signal with little harmonic distortion, as will be shown below.

5.2.6 Plant Modes

The compensator zero in the adaptive filter's equivalent linear transfer function is selected to phase-stabilize the closed-loop compensator poles. Closed-loop plant poles are typically assumed to lie far enough from the (narrowband) compensator dynamics that they are gain-stabilized. However, the need to gain-stabilize the plant poles limits the achievable disturbance rejection in the case of the leaky FXLMS algorithm, because the compensator has finite gain at the reference frequency.

The multi-axis actuator brings this issue to the fore, since its poles are lightly damped and they lie between the cooler's first and second harmonics. As shown in Chapter 3, the dynamics of each axis may be modelled as a damped second-order highpass filter, say

$$G(s) = \frac{k_p s^2}{s^2 + 2\zeta_p \omega_p s + \omega_p^2} \tag{5.60}$$

Assume the adaptive filter is well approximated by a linear transfer function. In the case of the leaky FXLMS, the compensator may be expressed as

$$K(s) = \frac{k_c \left[k_1 s + (k_2 + \zeta_c k_1)\omega_c\right]}{s^2 + 2\zeta_c \omega_c s + \omega_c^2} \tag{5.61}$$

The gains k_1 and k_2 may be chosen to match the plant phase at ω_c. Outside the half-power bandwidth of $G(s)$, the plant is approximately real, so choose $k_1 = \pm 1$, $k_2 = 0$. This puts the compensator zero near the origin and provides the correct sign to stabilize the closed-loop system.

The loop dynamics therefore include two plant zeros at the origin, a compensator zero near the origin, a pair of complex poles at ω_p due to the plant, and another pair

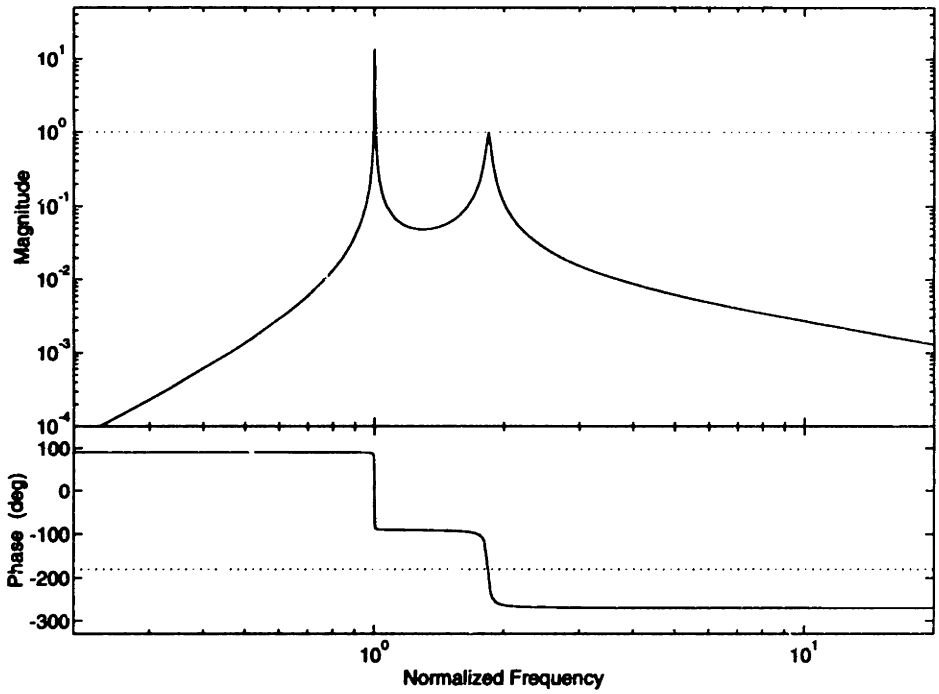

Figure 5-5: Bode plot for leaky FXLMS controller and second-order plant. Shown for $\omega_c/\omega_p = 0.54$, $\zeta_c = 0.04\%$, and $\zeta_p = 1\%$.

at ω_c due to the compensator. The corresponding Bode plot is shown in Figure 5-5 for the condition $\omega_c < \omega_p$.

If both pole pairs are lightly damped, the magnitude of the loop transfer function at the plant poles is

$$|GK(\omega_p)| = \frac{k_c k_p \omega_p}{2\zeta_p \left|\omega_c^2 - \omega_p^2\right|} \tag{5.62}$$

while the magnitude at the compensator poles is

$$|GK(\omega_c)| = \frac{k_c k_p \omega_c}{2\zeta_c \left|\omega_p^2 - \omega_c^2\right|} \tag{5.63}$$

Combining these two equations yields

$$|GK(\omega_c)| = \frac{\omega_c/\omega_p}{\zeta_c/\zeta_p} |GK(\omega_p)| \tag{5.64}$$

Performance is determined by $|GK(\omega_c)|$ while stability is determined by $|GK(\omega_p)|$, so this expression highlights the performance/stability trade-off in terms of the frequency ratio and the damping ratio quotient.

Consider the cryocooler vibration cancellation system. The actuator's axial resonance is at $f_p = 46$ Hz and its damping ratio is $\zeta_p \approx 1$–2%. At the cooler's first harmonic, the compensator poles are at $f_c = 25$ Hz and $\zeta_c = 0.04\%$, assuming the lowpass filter's corner frequency is 0.01 Hz. The maximum stable loop gain at ω_c is therefore 23 dB. Much higher gains can be achieved when the compensator poles are faster than the plant poles. For example, at the cooler's second harmonic ($f_c = 50$ Hz, $\zeta_c = 0.02\%$), the maximum stable gain is 35 dB. If greater levels of disturbance rejection are required, the parameters in Equation (5.64) must be modified or additional dynamics must be introduced to stabilize the system at higher loop gains. The use of additional dynamics will be demonstrated in the next chapter.

5.3 Implementation

The two-weight continuous-time FXLMS filter is straightforward to implement. Most of the elements in Figure 5-3 may be realized directly with analog ICs and discrete components. While not pursued here, it should be noted that there have been several examples of custom ICs that implement a complete LMS filter using MOS technology [107–109]. The results of the previous section suggest that the generation of the reference signal and the implementation of the quadrature filters deserve particular attention in order to linearize the filter's response. Some noteworthy features of the multiplier and the integrator blocks will also be presented.

5.3.1 Reference Signal

Ideally, the reference signal consists of a single noise-free harmonic at the disturbance frequency; the phase of this harmonic is immaterial. Furthermore, the reference signal should not be affected by the adaptive filter's output. A useful signal in tactical-cooler vibration cancellation is provided by the cooler's drive current. However, it contains many harmonics of the cooler's drive frequency and therefore cannot be used directly as a reference signal for a two-weight adaptive filter.

Many techniques are available to derive valid reference signals from such a signal.

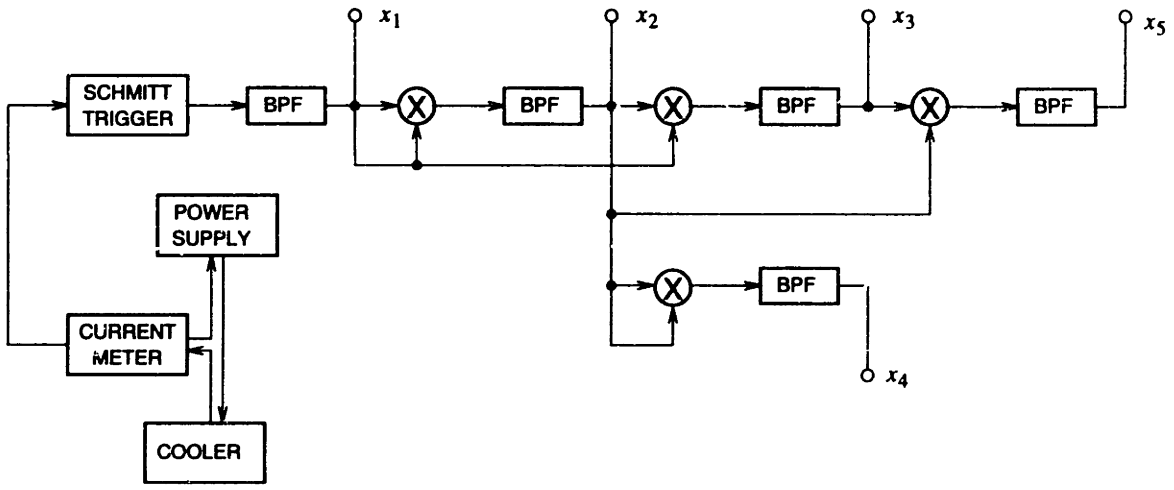

Figure 5-6: Functional block diagram of the reference-signal generation network. BPF denotes a bandpass filter.

Elliott *et al.* [110] discuss three techniques, namely filtering by fixed filters, filtering by tracking filters, and harmonic generation by phase-locked loops. As the cooler drive frequency varies over a small known range (approximately 25 Hz to 31 Hz), the reference signal for the first harmonic may be extracted from the drive current by fixed filtering. However, in order for this approach to be successful at higher harmonics, high-order filters are necessary. Instead, reference signals for the higher harmonics may be obtained by modulating the first-harmonic reference signal and then using low-order filters to reduce unwanted components in the output. Reference signals for the cooler's first five harmonics were generated in this way.

A functional block diagram of the reference-signal generation network is shown in Figure 5-6. The drive current amplitude was found to vary somewhat with the operating conditions of the cryocooler. Since the adaptive filter's gain is proportional to the square of the reference signal's amplitude, a Schmitt trigger is included in the network to generate a constant-amplitude square wave at the cooler's drive frequency ω_d. The square wave is bandpass filtered to produce the first-harmonic reference signal $x_1(t) = \cos(\omega_d t + \theta_1)$. This signal is then squared using an analog multiplier IC. Neglecting the phase of $x_1(t)$, the multiplier output is

$$x_1^2(t) = (1/2)(1 + \cos 2\omega_d t)$$

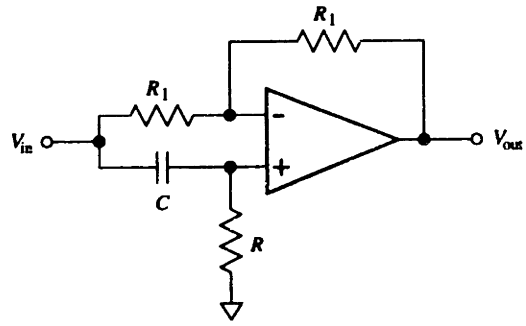

Figure 5-7: Circuit diagram for a noninverting unity-gain allpass filter, which has 90° of phase at $\omega_c = 1/RC$.

Higher harmonics are still present in this signal, but they are much smaller than in the drive current. A bandpass filter produces $x_2(t) = \cos(\omega_d t + \theta_1)$, which is then modulated with $x_1(t)$. This process is continued to generate $x_3(t)$, $x_4(t)$, and $x_5(t)$:

$$\begin{aligned} x_1(t)x_2(t) &= (1/2)(\cos\omega_d t + \cos 3\omega_d t) \xrightarrow{\text{BPF}} x_3(t) = \cos(3\omega_d t + \theta_3) \\ x_2^2(t) &= (1/2)(1 + \cos 4\omega_d t) \xrightarrow{\text{BPF}} x_4(t) = \cos(4\omega_d t + \theta_4) \\ x_2(t)x_3(t) &= (1/2)(\cos\omega_d t + \cos 5\omega_d t) \xrightarrow{\text{BPF}} x_5(t) = \cos(5\omega_d t + \theta_5) \end{aligned}$$

where BPF denotes bandpass filtering. The multiplier and filter gains in this network may be adjusted to keep the amplitude of each reference signal near full range (10 V for the multipliers).

5.3.2 Quadrature Filters

Ideally, a quadrature filter has unit gain and 90° of phase. While an integrator has 90° of phase at all frequencies, its gain varies as a function of frequency. Not only does this fail to cancel the nonlinear components in the output of the adaptive filter, but it changes the linear-component gain in Equation (5.33), which will in turn change the closed-loop disturbance rejection. A better choice for the quadrature filter is an allpass filter.

A first-order allpass filter has constant gain at all frequencies and 90° of phase at its "corner" frequency. It may be implemented with a single op amp, and some realizations allow tuning by means of a single resistor. For example, Figure 5-7 shows

a noninverting unit-gain allpass circuit [111], for which the transfer function is

$$\frac{V_{\text{out}}}{V_{\text{in}}} = \frac{s - 1/RC}{s + 1/RC} \tag{5.65}$$

This has 90° of phase at $s = \pm j\omega_c$ where $\omega_c = 1/RC$.

The corner frequency of the allpass filter may be tuned to a nominal cooler drive frequency. Variations in this frequency will result in variations in the phase of the allpass filter. Denoting this phase by $\theta_q(\omega)$, it may be shown that

$$\tan\theta_q(\omega) = \frac{2\omega\omega_c}{\omega^2 - \omega_c^2} \tag{5.66}$$

For the Hughes tactical cooler, the drive frequency varies by a factor of 0.11 about its geometric mean, which implies that $\theta_q = 90° \pm 6°$. As shown above, phase errors of this magnitude have little effect on the FXLMS algorithm (unless there are strong additional in-band disturbances).

5.3.3 Multipliers and Integrators

The error path within the adaptive filter includes two multipliers and an integrator. The multipliers should display good linearity, the integrator should be slightly leaky, and the integrator bias error should be minimized.

Analog multiplier ICs are available from several manufacturers. However a standard "jellybean" multiplier comparable to a 741 op amp does not exist. Functionality, linearity, noise, and cost vary widely from model to model. As cryocooler vibration cancellation is a narrowband low-frequency application, output error was considered more important than unity-gain bandwidth or noise. And since four multipliers are required per two-weight filter, cost and the need for external components were also significant factors.

The output equation that includes the major errors of a practical multiplier is of the form

$$Z = kk_eXY \pm \{kk_e(XY_0 \pm X_0Y) \pm Z_0 \pm f(X,Y)\} \tag{5.67}$$

where X and Y are the inputs, Z is the output, and k is the nominal scale factor

Table 5.1: Comparison of analog multiplier ICs. The manufacturer codes represent Analog Devices (AD) and Burr-Brown (BB). FS denotes full scale, *e.g.* 1% FS of a ±10 V signal is ±0.1 V.

Model	Mfg	Total Error (% FS)	X Feedthru (% FS)	Y Feedthru (% FS)	Z_0 (± mV)	Price ($)
AD633J	AD	2	1	0.4	50	5.25
AD632A	BB	1	0.3	0.1	30	18.70
MPY634B	BB	0.5	0.3	0.1	15	34.55
AD534L	AD	0.25	0.12	0.1	10	66.30

(typically $k = 0.1$). The error terms include a scale-factor error k_e, offsets X_0, Y_0, and Z_0, and an input nonlinearity $f(X, Y)$. The feedthrough terms XY_0 and X_0Y can be particularly troublesome in modulation applications. Separate specifications for X and Y feedthrough are provided since multipliers are not symmetric devices [112]. A "total error" that includes all these error terms is also commonly cited.

The previous generation of four-quadrant multiplier ICs have feedthrough terms of 0.5%–4% of full scale. While models such as Motorola's MC1595 or Raytheon's RC4200 are inexpensive ($5–10 per unit), they require extensive trimming circuitry. Furthermore, they are transconductance devices, sourcing a current proportional to the product of the inputs. A single-ended voltage signal (V_{out}) is usually preferred, so additional external components include an op amp and a precision resistor network for accurate current-to-voltage conversion.

Modern multipliers are laser-trimmed for much better accuracy without external trimming, although the offsets may be reduced still further with optional trim pots. They also feature internal current-to-voltage conversion. However, they are much more expensive. Table 5.1 compares several of these multipliers. The errors shown represent maximum values listed in the various data sheets; manufacturers often cite "typical" values that are 2–10 times smaller. The quoted prices, taken from 1992/93 price lists, are for 1–24 units; quantity discounts are always available.

The AD633J was selected for use in the FXLMS filter. This multiplier offers linearity and cost that is comparable to the older multipliers without the need for external components.

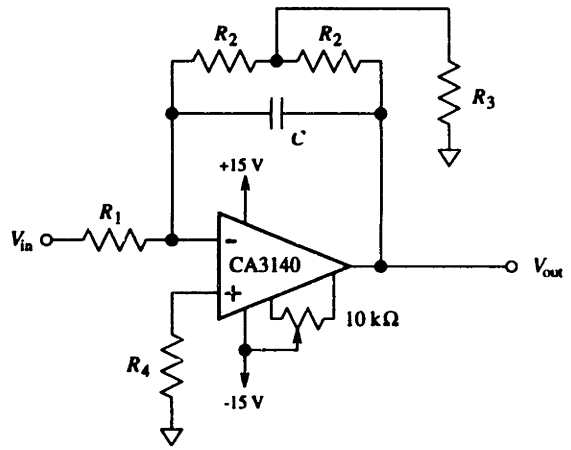

Figure 5-8: Circuit diagram for the leaky integrator. Component values are $C = 4.7\,\mu\text{F}$, $R_1 = R_2 = 240\,\text{k}\Omega$, $R_3 = 11\,\text{k}\Omega$, and $R_4 = 130\,\text{k}\Omega$.

The integrator was implemented with a modified Miller circuit [42]. As shown in Figure 5-8, a T-network in the feedback path is used to roll off the integral effect at low frequencies. The effective resistance of the T-network is

$$R_{\text{eff}} = (2 + R_2/R_3)\, R_2 \tag{5.68}$$

which allows low corner frequencies to be achieved with reasonable component values. Using the nominal component values given in Figure 5-8, the leaky integrator has a time constant of $\tau_c = R_{\text{eff}}C = 27$ seconds. This corresponds to a corner frequency of 0.006 Hz. The DC gain is 28 dB.

Large values of DC gain and large resistor values can result in significant integrator bias error due to op amp characteristics such as offset voltage and bias current. The offset voltage of the first multiplier will also contribute to this error.

Several steps were taken to minimize the error, since it directly affects the adaptive filter's performance. A compensator resistor R_4 was used to present the same DC driving resistance to both op amp inputs. A low-noise MOSFET op amp (the CA3140E) with negligible bias current was selected. And a trim pot was included to adjust the op amp's offset. Due to the behavior of the multiplier, it was found that the trimming is best done with the reference signal applied but with the error input grounded. The integrator bias error could then be reduced to 5–10 mV.

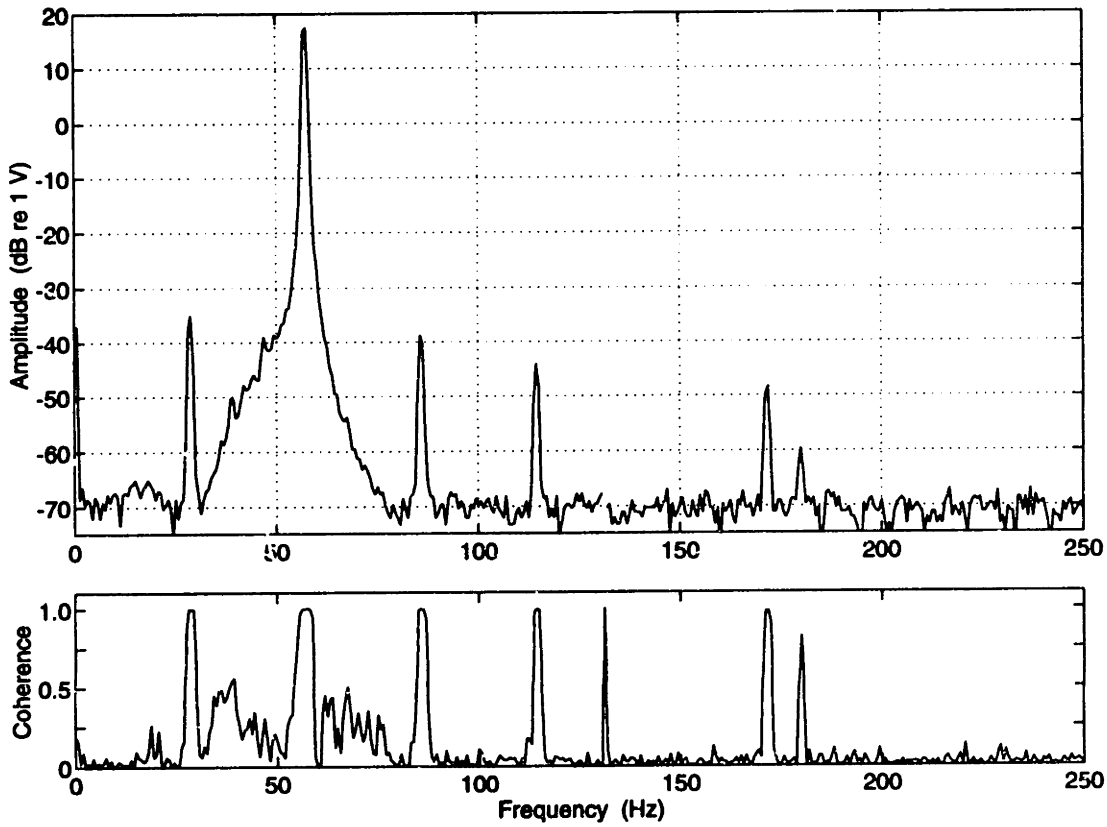

Figure 5-9: Spectrum of the second-harmonic reference signal.

5.4 Measured Performance

The circuits of the previous section were constructed on 4.5×6.5″ prototyping cards. One card was needed for the reference-signal generation network, and each two-weight FXLMS filter was placed on a separate card. In addition to the quadrature filters, the multipliers, and the integrators, each FXLMS card includes an allpass reference filter, a summer, variable-gain input and output stages, an optional inverter, and a DIP switch to select the error signal (one of F_z, M_x, M_y) and the reference signal (one of $x_1, \ldots, x_5$). The open-loop performance of these components is reported here.

5.4.1 Reference Signal

High-quality reference signals were obtained from the generation network. A typical spectrum, of x_2 in particular, is shown in Figure 5-9. In all five reference signals, the broadband noise is more than 80 dB below the primary harmonic. The measured

coherence function between $x_2(t)$ and the axial force $F_z(t)$ is also shown in Figure 5-9; the average value for γ^2_{xd} at the primary harmonic is 0.9990. While other harmonics are apparent in the spectrum, they are at least 30 dB (and typically 40 dB) smaller than the primary harmonic. Based on these figures, high levels of cancellation should be achievable, and the nonlinear components in the adaptive filter's output due to the additional reference-signal harmonics should be negligible.

The bandpass filter used to extract the second harmonic is shown in Figure 5-10; the other filters have similar characteristics. As the passband is not flat, there is some variation in the amplitude of the resulting reference signal. For example, Figure 5-11 depicts the variation in the amplitude of several of the harmonics in $x_2(t)$ as a function of the cooler drive frequency. The reference signals for the higher harmonics display greater variation due to the cascade nature of the generation network; the value of γ^2_{xd} at the primary harmonic also decreases slightly. The closed-loop disturbance rejection will therefore be a function of the drive frequency,

5.4.2 LMS Input-Output Behavior

The input-output behavior of a two-weight FXLMS filter was then characterized in conjuction with the reference-signal generation network. The adaptive filter output was observed for both harmonic and stochastic error signals.

Using the first-harmonic output of the reference-signal generation network, the reference signal was sinusoidal and had a frequency of 28 Hz. The quadrature filters were adjusted to have 90° of phase at 28 Hz, and the reference filter (the plant model) was adjusted to have 35° of phase at this frequency. Using the first-harmonic reference signal, a 2 V sinusoidal error signal at 26 Hz served as the input and resulted in the adaptive filter output shown in Figure 5-12. I must be emphasized that the frequency of the error harmonic is *not* equal to the reference frequency; the system is displaying the non-Wiener solution. The harmonic content of the output spectrum may be interpreted in light of expressions such as Equations (5.44)–(5.46) and Equation (5.58). Note however that Figure 5-12 shows the output over a broad bandwidth due to a harmonic input, while the equations express the output at one

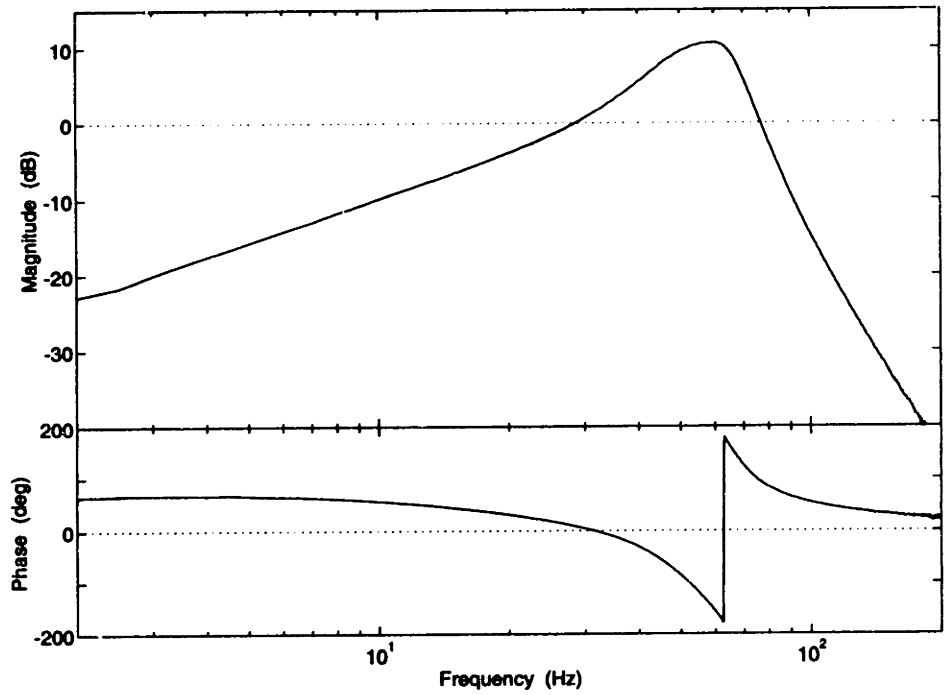

Figure 5-10: Bandpass filter used to extract the second-harmonic reference signal.

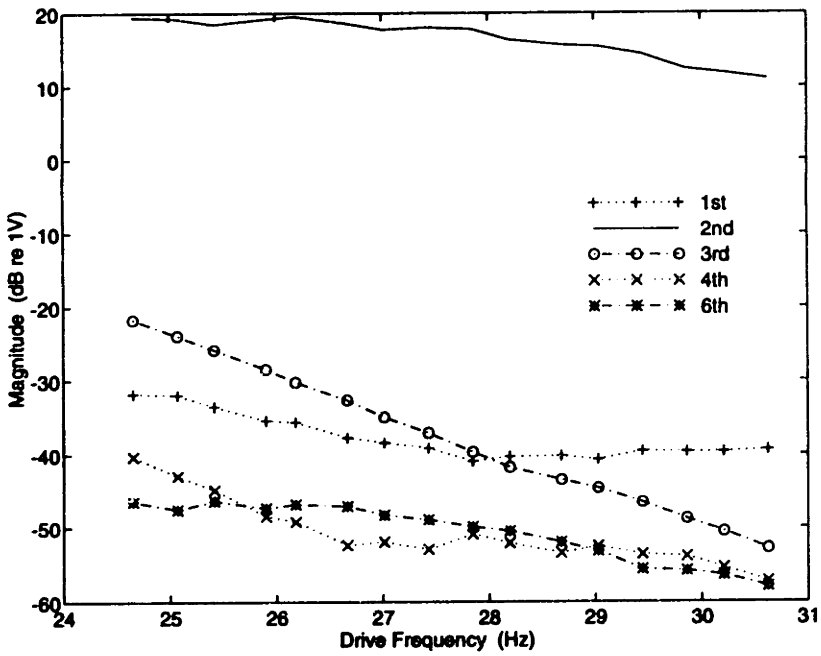

Figure 5-11: Amplitude of the predominant harmonics in the second-harmonic reference signal as a function of the cooler drive frequency.

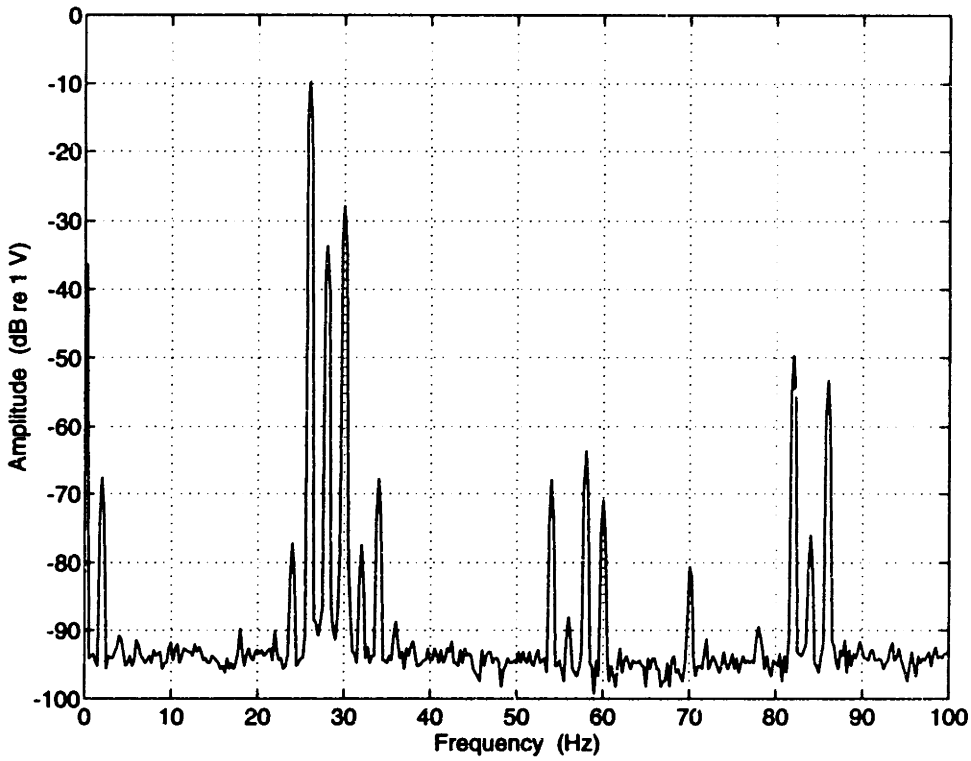

Figure 5-12: Adaptive filter output in response to an input harmonic at 26 Hz. Sinusoidal reference signal is at 28 Hz.

frequency due to all input components.

The predominant component in the output spectrum occurs at the input frequency of 26 Hz; this is the linear component of the filter's response. The components at DC and at harmonics of the 28-Hz reference frequency are due to multiplier output errors, *e.g.* reference signal feedthrough. These components did not change when the input amplitude or frequency was varied. Aside from some low-level harmonics such as 60 Hz line noise and a 70 Hz harmonic due to the Fourier analyzer (the screen refresh rate), the other components are mirror images of the disturbance about the various reference harmonics. This phenomenon was noted above in relation to quadrature error. The ratio of the amplitude of the mirrored harmonics to the amplitude of the primary harmonic was found to be independent of the input amplitude and the input frequency. The adaptive filter appears to be approximately linear here—the linear response is roughly 20 dB greater than any other component.

The equivalent transfer function was measured using random excitation. The

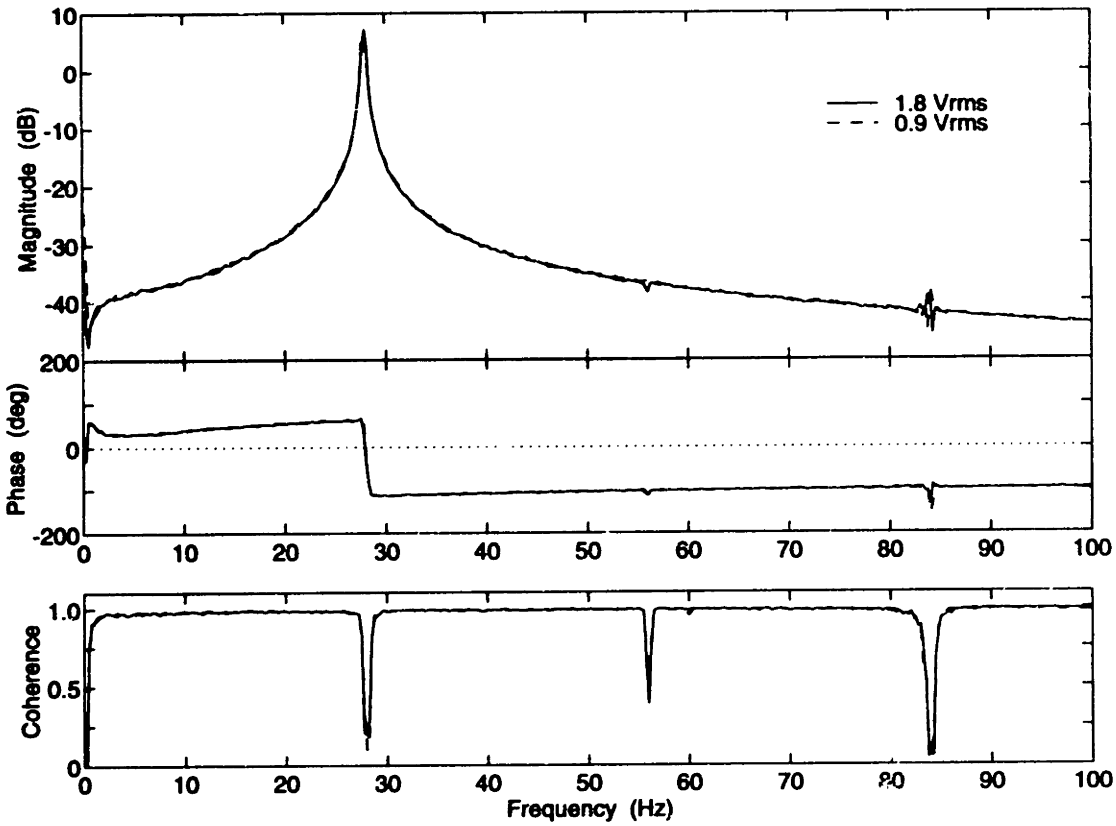

Figure 5-13: Adaptive filter's input-output transfer function with a sinusoidal reference signal at 28 Hz. Results for two excitation levels are shown.

magnitude and phase of the transfer function, as well as the coherence function, is shown in Figure 5-13 for two input amplitudes. The lightly-damped second-order bandpass nature of this transfer function is clearly evident. The linearity is demonstrated by the close agreement of the two measurements and by the high value of the coherence function away from harmonics of the reference frequency. Feedthrough and the mirrored harmonics seen in Figure 5-12 distort the transfer function at these frequencies. The distortion makes it difficult to determine the transfer function's magnitude at the reference frequency, a value of obvious interest for calculations of the closed-loop disturbance rejection. Different peak values were found using different excitation bandwidths. Finally, notice the effect of the reference filter on the phase: it is not symmetric about 0°, but instead has been shifted downwards. The phase at the reference frequency is approximately $-25°$, which will roughly offset the assumed phase (35°) of the plant at this frequency.

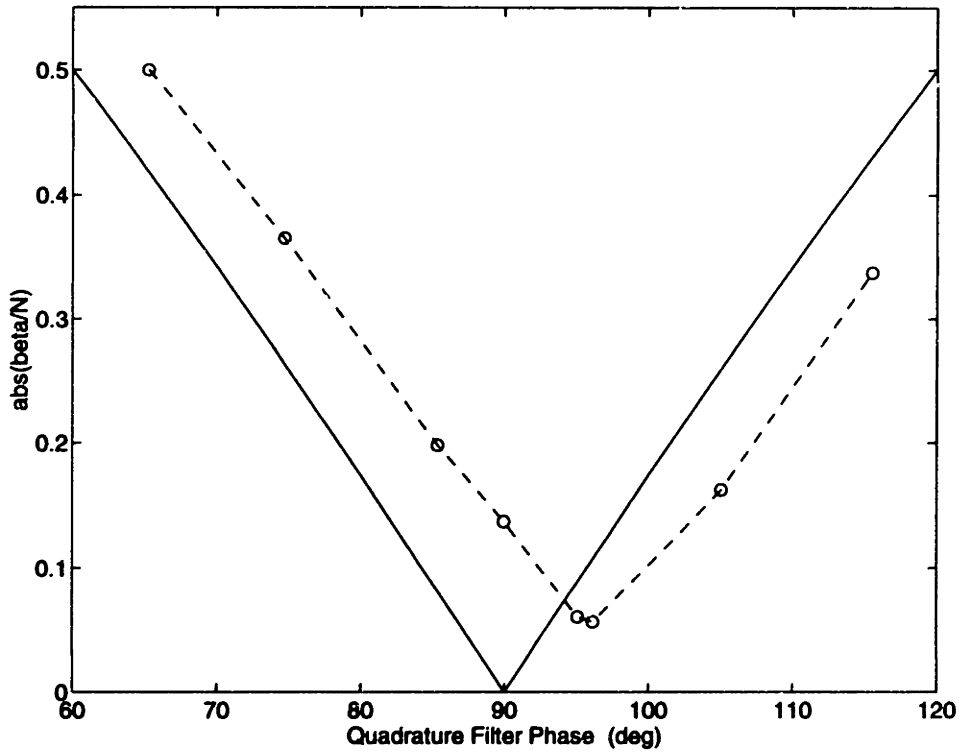

Figure 5-14: Ratio of nonlinear component gain to linear component gain as a function of the quadrature filter phase. Solid line: analysis; dashed line: experimental measurements.

5.4.3 Imperfect Quadrature

The effect of imperfect quadrature was investigated by deliberately mistuning both quadrature filters by the same amount ($\pm 0.5°$). For each value of θ_q, the ratio of the most significant nonlinear component to the linear component was computed. This ratio is shown as a function of θ_q in Figure 5-14 and is compared to the analytical expression of Equation (5.41): $|\beta/N| = |\cos\theta_q|$. The measurements are in good agreement with the analysis, although a shift in the apparent phase of the quadrature filters is evident. While the weight multipliers might introduce a small phase shift, a more likely explanation of the shift in β_{min} is amplitude errors in the quadrature filters—consider the effect of shifting the center and changing the radius of the circle in Figure 5-4.

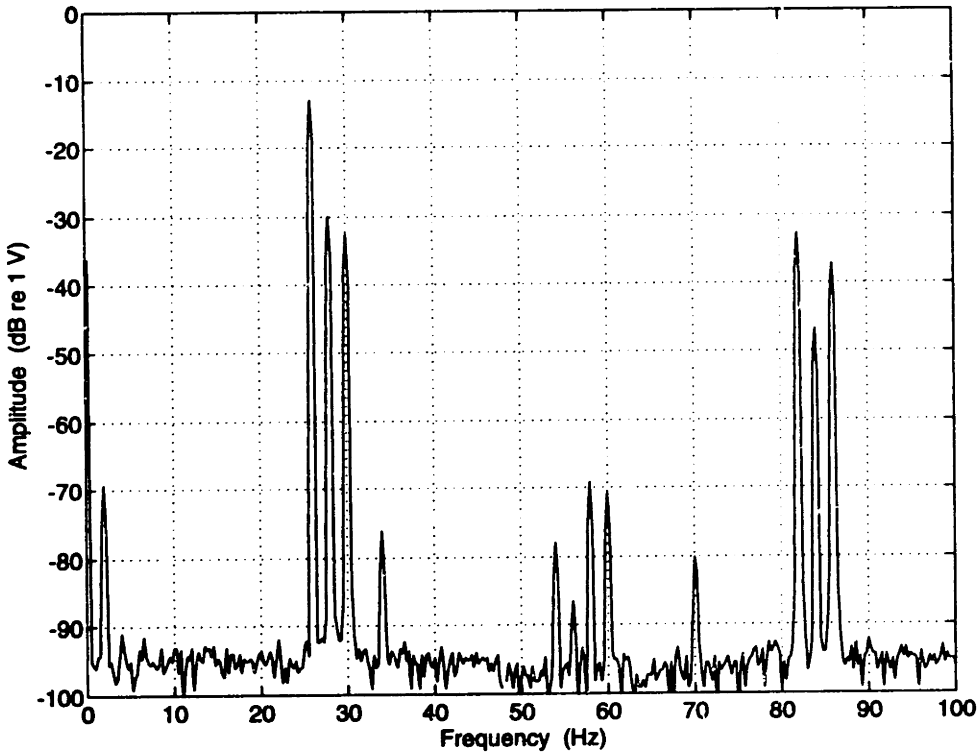

Figure 5-15: Adaptive filter output in response to an input harmonic at 26 Hz. Triangular reference signal is at 28 Hz.

5.4.4 Periodic Reference Signal

The effect of a periodic reference signal on the adaptive filter's input-output behavior was characterized by applying a 28-Hz triangular reference signal directly to the filter; the reference-signal generation network was bypassed. The amplitudes of the first three harmonics in the sinusoidal reference signal and in the triangular reference signal are compared in Table 5.2. The output spectrum in response to a sinusoidal error at 26 Hz is shown in Figure 5-15. The most significant change from the output with a sinusoidal reference signal (Figure 5-12) is the increase in the amplitude of the three components between 80 Hz and 90 Hz.

The transfer function measured with random excitation and a triangular reference signal is compared to the harmonic-reference transfer function in Figure 5-16. Due to the smaller first harmonic in the triangular reference signal, there is a uniform loss of gain of approximately 3 dB. More significantly, there is a dramatic loss of coherence in a sizable bandwidth around the third harmonic. While there is some suggestion

Table 5.2: Comparison of the harmonic content of a sinusoidal reference signal and a triangular reference signal.

Signal Type	A_1 (dB)	A_2 (dB)	A_3 (dB)
Sinusoid	16.3	-36.5	-21.0
Triangle	14.7	-39.3	-3.6

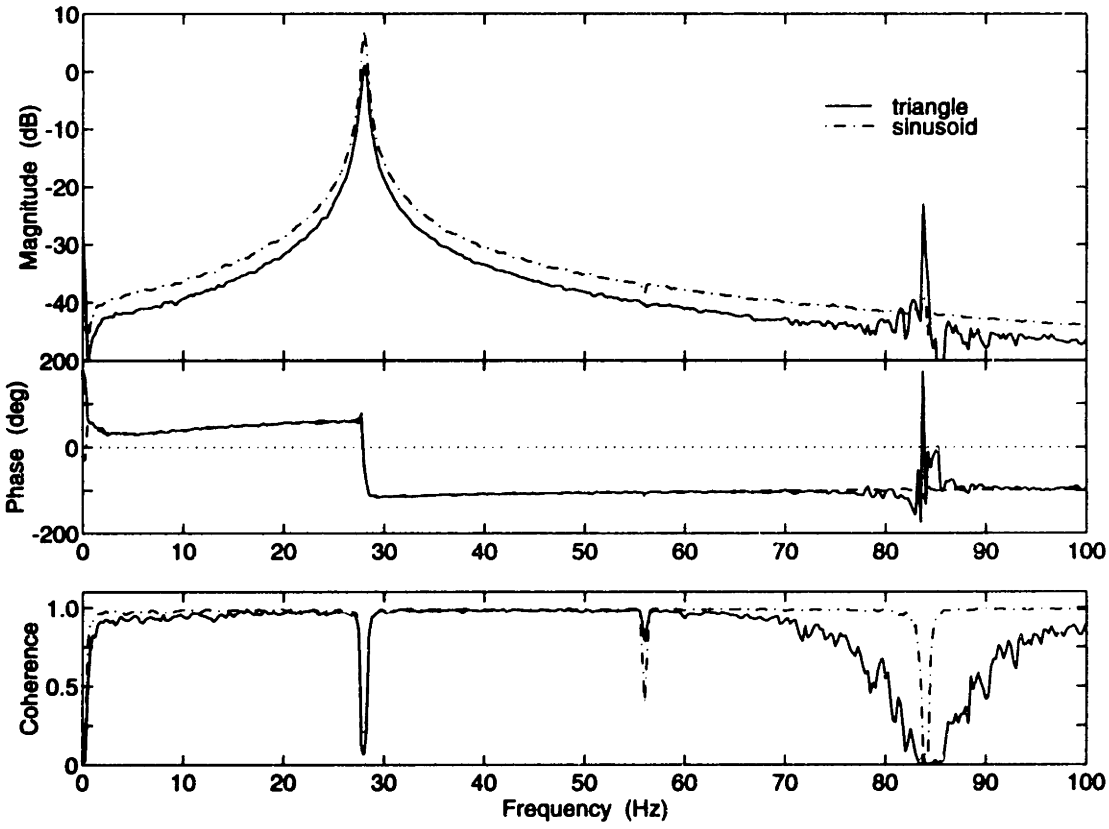

Figure 5-16: Comparison of the adaptive filter's input-output transfer function with a triangular reference signal and with a sinusoidal reference signal.

of a peak in the transfer function within this bandwidth, the two-weight filter is not able to act as a linear "comb" filter with one pair of complex poles at ω_x and another at $3\omega_x$.

5.5 Summary

This chapter concentrated on a two-weight adaptive filter governed by the continuous-time filtered-x LMS algorithm. The ideal behavior of this filter was considered in terms of both stochastic and harmonic disturbances. By analyzing the response of the filter in the transform domain, expressions were derived that explicitly showed the linear and the nonlinear components in the output. If the nonlinear components are negligible, the adaptive filter acts like a linear second-order bandpass filter.

Consideration was then given to factors that affect the performance of the FXLMS filter. For example, quadrature phase errors and additional harmonics in the reference signal were both found to result in stronger nonlinear components. On the other hand, factors such as integrator leakage and bias error, noise in the reference signal, and plant modes all affected the closed-loop disturbance rejection that could be achieved at the reference frequency.

With these factors in mind, circuit realizations based on analog components were proposed to implement a two-weight FXLMS filter. The input-output behavior of such a filter was measured and was found to be well approximated by a linear transfer function. Furthermore, the analysis of the limiting factors was experimentally verified both for quadrature phase error and for a periodic reference signal. The agreement between the analysis and the measured behavior provides confidence that these analog adaptive feedforward filters can indeed be used for active vibration cancellation.

Chapter 6

Cancellation System Performance

All words,
And no performance!

—P. Massinger, 1624.

Various elements of the cancellation system have been examined in isolation in the previous chapters. After characterizing the disturbance, the actuator's force capability was verified and its multi-axis coupling measured. The input-output behavior of the adaptive feedforward controller was then analyzed. Under certain conditions, the controller is well approximated by a linear transfer function, as was experimentally confirmed with a two-weight analog implementation. These elements will be combined in this chapter to form an active multi-axis vibration cancellation system.

The closed-loop performance of the system is presented for various operating conditions. In order to improve both performance and stability, some fixed filters are added to the elements discussed above; loop transfer function measurements provide confidence in the overall system. Steady-state and transient cancellation results are discussed for cases that include single and multiple harmonics, single and multiple axes, and fixed and varying disturbance frequencies.

6.1 Fixed Filters

The block diagram of Figure 5-3 includes all the functional elements theoretically required for adaptive feedforward vibration cancellation. Since the closed-loop can-

cellation is proportional to the loop gain (for $GK \gg 1$), it is beneficial to maximize the loop gain at the disturbance frequencies. This may be accomplished, for example, by using integrators in the error path, $H(s) = 1/s$. However, if leaky integrators are used, the gain must be increased at other points in the loop.

It is not always possible to achieve the desired levels of cancellation by simply increasing the adaptation parameter μ. While this increases the gain at the disturbance frequencies, it also increases the controller bandwidth (the frequency range over which the compensator gain exceeds 0 dB). The high-μ approach can have practical consequences, such as excessive signal levels or slew rates for the op amps and multipliers, as well as more fundamental consequences, such as destabilized plant modes. These problems may be avoided by modifying the loop dynamics, using techniques such as fixed filters, local feedback, or even adaptive filters.

Consideration should first be given to fixed filters, since they offer a simple means of improving the cancellation system's performance. As discussed by Morgan and Sanford [113], the filtered-x LMS architecture provides three convenient locations for additional filtering: bandpass filters may be placed in the error path; lowpass filters may be placed in the weight path; and plant-equalization (or compensation) filters may be placed in the control path. While the same net effect on the loop transfer function can be achieved from any of these locations, the various signals within the loop will not be the same in each case. Each filter is best suited at overcoming different performance limitations.

Two distinct factors limit the gain of the cryocooler vibration cancellation system. The first is the significant high-frequency content of the error signals, and the second is the lightly damped structural modes of the the multi-axis actuator. Performance improvements were achieved through the use of error filters and compensation filters.

6.1.1 Error Filters

The highly impulsive nature of the Hughes cryocooler's axial vibration virtually ensures that structural modes of the foundation will be excited. Unless the structural modes are heavily damped, they will greatly amplify any cooler harmonics that fall

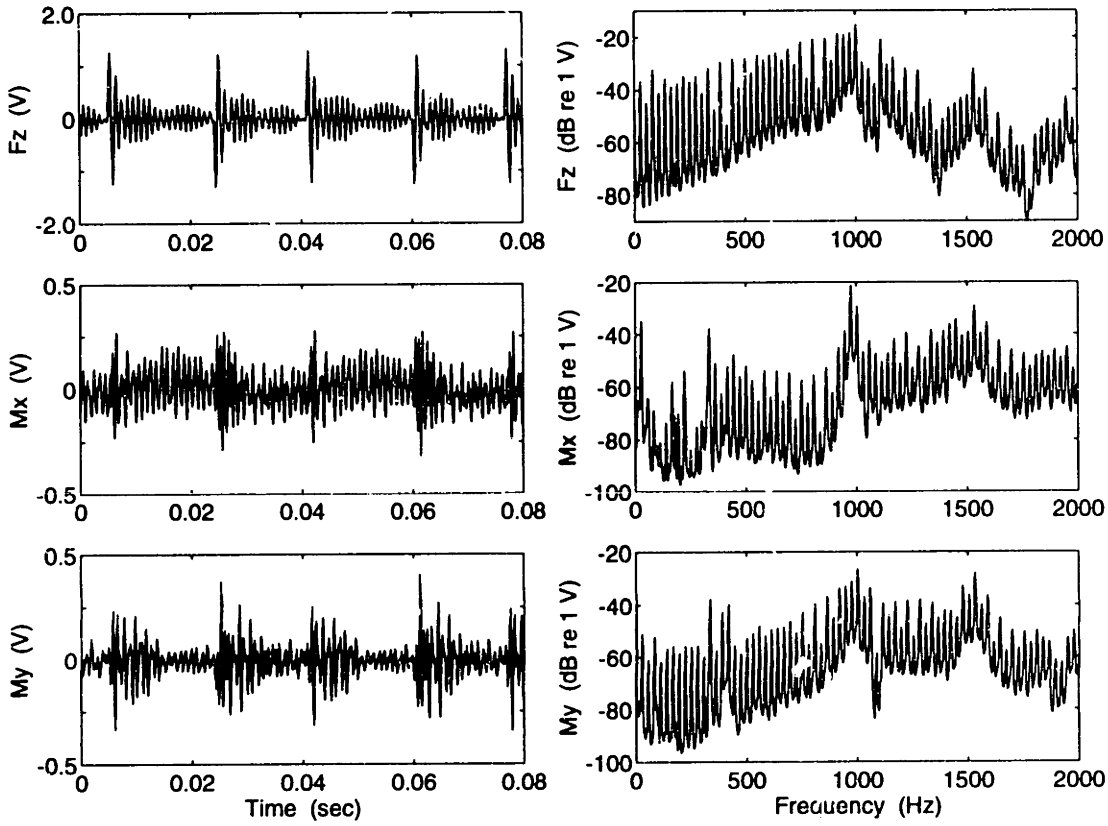

Figure 6-1: Error signals caused by cryocooler vibration.

within their half-power bandwidth. These harmonics will then dominate the error signal measured by the cancellation system's load cells, as was seen in Chapter 2. The vibration measurements of Figure 2-9 are presented in Figure 6-1 directly as error signals, *i.e.* without the sensor gains. The spectral bandwidth has been extended to highlight the structural modes near 1 kHz.

A general solution to this problem is to incorporate sufficient passive damping in the mount to avoid exciting the structural modes. If it were not for the displacer's impact, the interaction with the foundation modes would not cause so much difficulty. Rather than redesigning the mount, an alternative solution was developed specifically for the system at hand since most coolers do not have impacting displacers.

The dynamics of the foundation do not change significantly during the various phases of testing, so a fixed filter may be used to reduce the measured response near the foundation modes. A lowpass notch filter was designed to provide almost 18 dB attenuation at 1 kHz and approximately 14 dB of low-frequency gain (Figure 6-2).

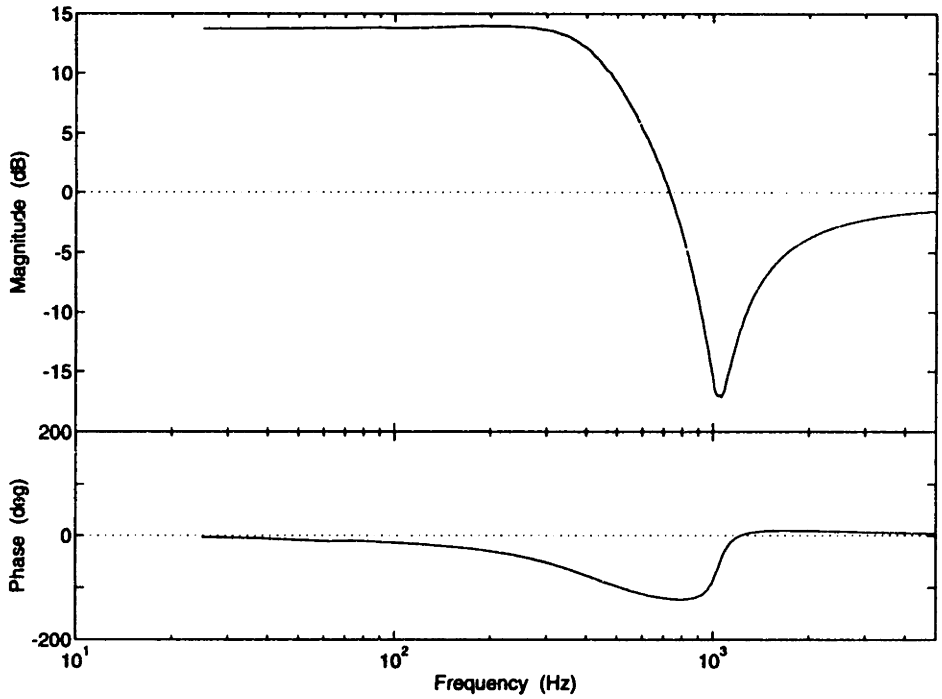

Figure 6-2: Error-filter transfer function.

The associated phase loss is less than 22° at the cooler's fifth harmonic, which can be accounted for with the reference filter. A Boctor single-op-amp circuit [111] was used to implement the notch; one was constructed for each error channel.

The filtered error signals are shown in Figure 6-3. The response at 1 kHz has practically been eliminated. The axial vibration is now dominated by the impact, while the lower-frequency lateral modes (300–400 Hz) have been revealed in M_x and M_y. There is also a strong fundamental component to the M_x vibration. The first five harmonics represent a greater percentage of power in the filtered error signals than in the direct signals, allowing higher loop gains at the reference frequencies before the op amps start clipping the input to the FXLMS filters.

6.1.2 Compensation Filters

The dynamics of the multi-axis actuator were discussed in Chapter 3. As shown in Figure 3-13, over the first 300 Hz the actuator behaves like three loosely-coupled second-order highpass filters. The axial resonance is at 46 Hz, and the lateral ones are at 31 Hz. All three modes are lightly damped, $\zeta \approx 1$–2%. The need to gain-stabilize

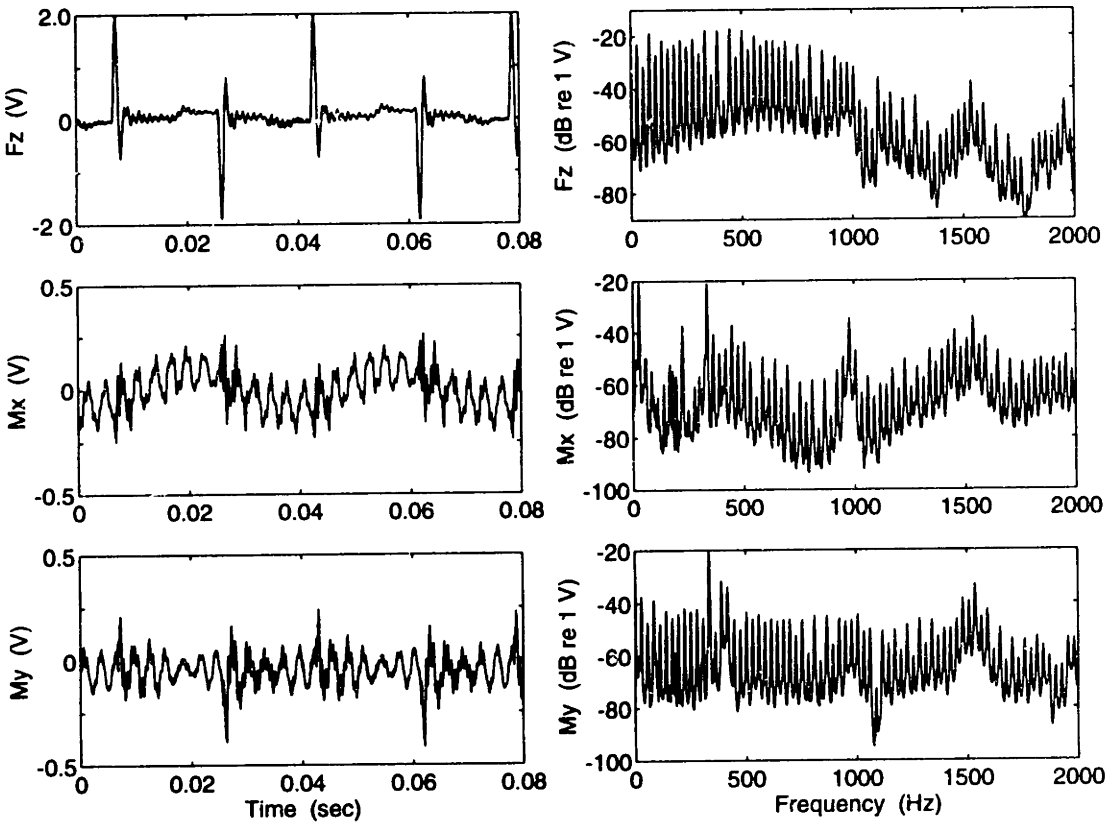

Figure 6-3: Effect of error filters on open-loop error signals.

these modes compromises the achievable levels of vibration cancellation. For example, as was demonstrated in Chapter 5, only about 23 dB of cancellation is possible at the first axial harmonic.

Performance improvements may be realized by decreasing the natural frequencies of the actuator, by adding damping to the flexures, or by phase-stabilising the plant poles. In order to be done successfully, the first two options involve substantial modifications to the actuator. Instead, a compensation filter was added to each control path to stabilize the plant poles.

The compensation filters basically represent an attempt to invert the plant. A pair of lag-lead networks were used to reduce the plant phase below the resonance. The first network was AC-coupled to prevent transmission of any bias errors from the LMS filters. A lightly-damped adjustable notch, implemented with a biquad circuit [111], was used to limit the magnitude of the resonance. The transfer function of the axial compensation filter is shown in Figure 6-4.

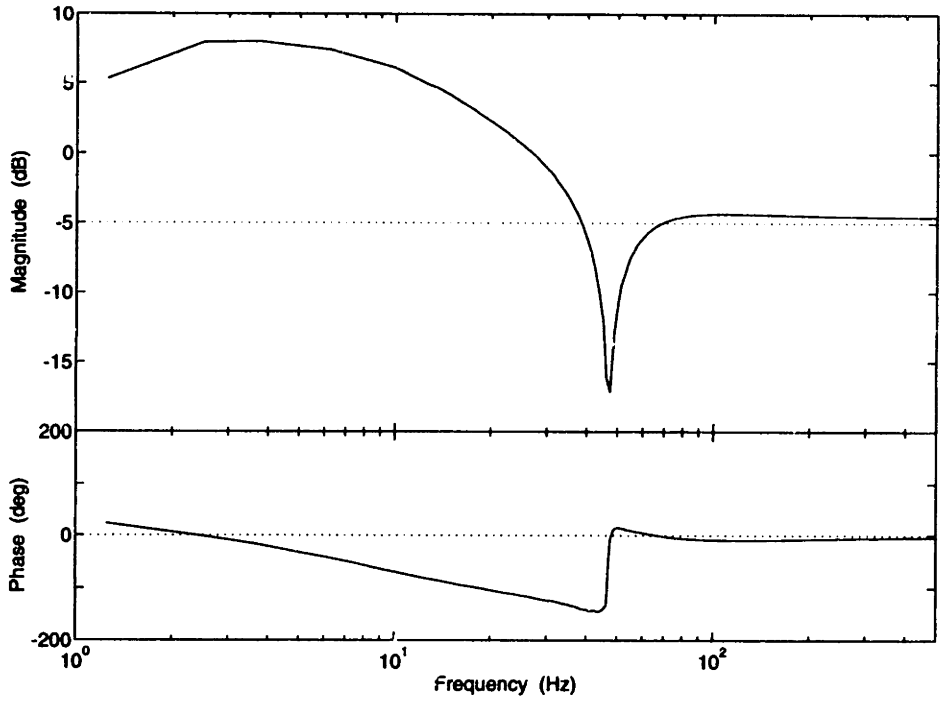

Figure 6-4: Axial compensation-filter transfer function.

This is not a robust solution to the problem of lightly-damped actuator modes; careful tuning of the notch is obviously critical to the success of these filters. In an attempt to improve the resolution with which the notch could be tuned, the feedback resistor that determines the notch's natural frequency was implemented with a fixed resistor and a trim pot in series. However, this also had the effect of limiting the range over which the notch could be varied. Good tuning could be achieved with the axial resonance, but the lateral modes softened over the course of six months, gradually moving below the notch's frequency range (and right onto the cooler's drive frequency). Although these circuits could be modified, the effort would probably be better spent redesigning the flexures, which are really the source of the problem.

Both the cancellation filters and the error filters may be considered part of the plant for the purpose of setting the reference filters in the LMS controllers. The measured plant transfer-function matrix incorporating these filters is presented in Figure 6-5. Notice the good cancellation of the F_z mode, while the M_y mode still has a significant region with a large loss of phase. The phase lag due to the error filters is visible in all elements of the matrix, although this should not be a problem with a

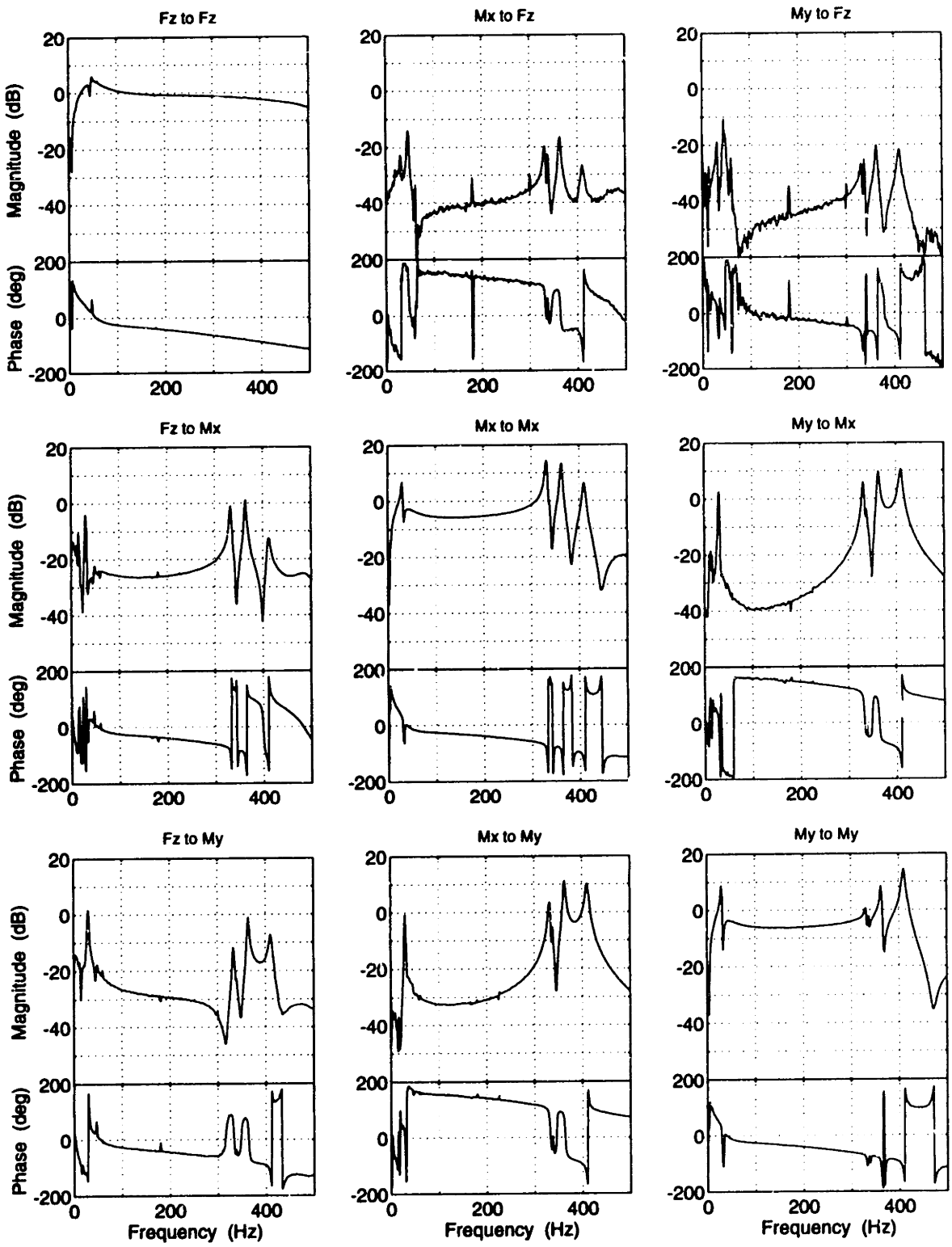

Figure 6-5: Plant transfer-function matrix including cancellation filters and error filters.

narrowband control scheme. The error filters also contribute approximately 14 dB of gain over this bandwidth (cf. Figure 3-13). The single-input single-output filters do not affect the coupling of the axes.

6.2 Loop Transfer Functions

Seven FXLMS controllers were fabricated, six on prototyping cards and one on a protoboard. The reference-signal generation network provides reference signals for the first five harmonics of the cooler's drive frequency. As there was no externally-defined performance metric, the (unfiltered) error signals were used; the sensor gains (0.106 V/N and 4.03 V/N·m) therefore act as scale factors. Based on Figure 6-1, five controllers were assigned to the axial vibration, one per harmonic, and one controller was assigned to each lateral error signal. The lateral controllers were adjusted to cancel the first harmonic.

The measured transfer-function matrix (Figure 6-5) was used to determine the plant's phase at the first five harmonics of the cooler's average drive frequency, 28 Hz. The allpass filters that serve as the reference filters in the FXLMS controllers were then tuned to match the plant phase at a given harmonic.

Loop transfer functions were measured from the error filter input to the output of the sensor transformation matrix. Figure 6-6 shows the axial transfer function using one FXLMS controller (for the second harmonic) and using five controllers. The M_x loop transfer function is shown in Figure 6-7. These transfer functions are the product of the plant's transfer function (Figure 6-5) and the controller's transfer function (Figure 5-13). Due to implementation details, an inverter was not included in the measured loop, so closed-loop stability of these systems should be assessed using negative-feedback rules, *i.e.* a gain of 0 dB and a phase of $\pm 180°$ corresponds to marginal stability.

Figures 6-6 and 6-7 illustrate the narrowband nature of the system. The peak gains are lower than expected, although this could be due to insufficient frequency resolution; notice the decreasing damping with increasing frequency. The reference

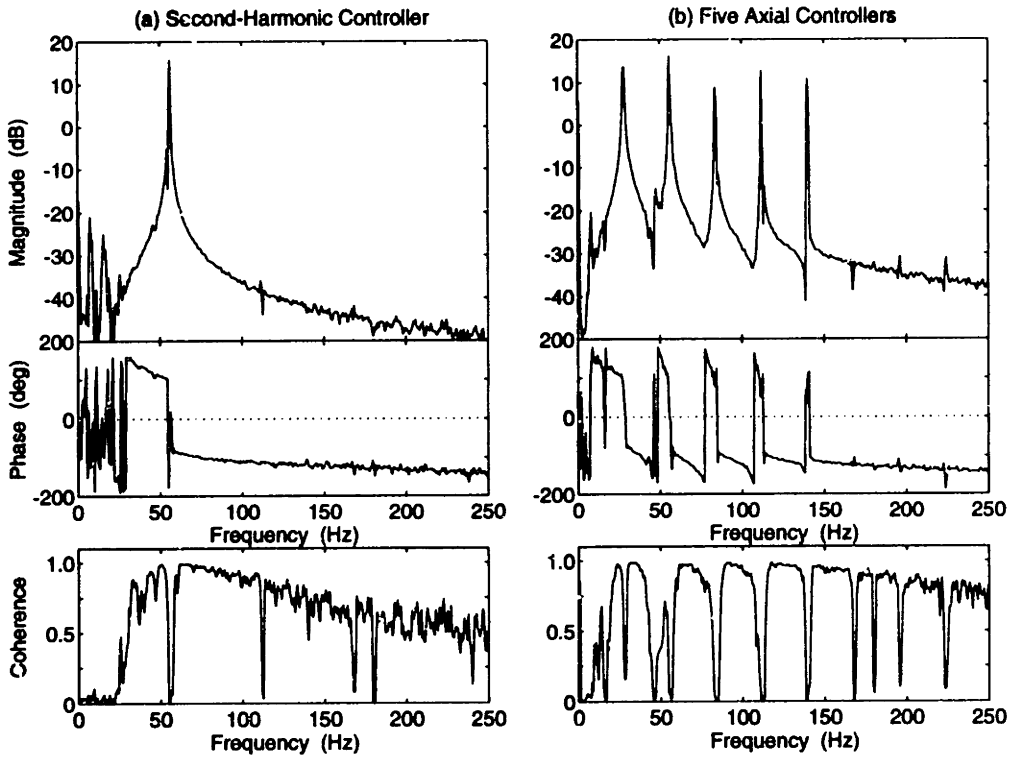

Figure 6-6: Axial loop transfer functions. (a) Second-harmonic controller; (b) five axial controllers.

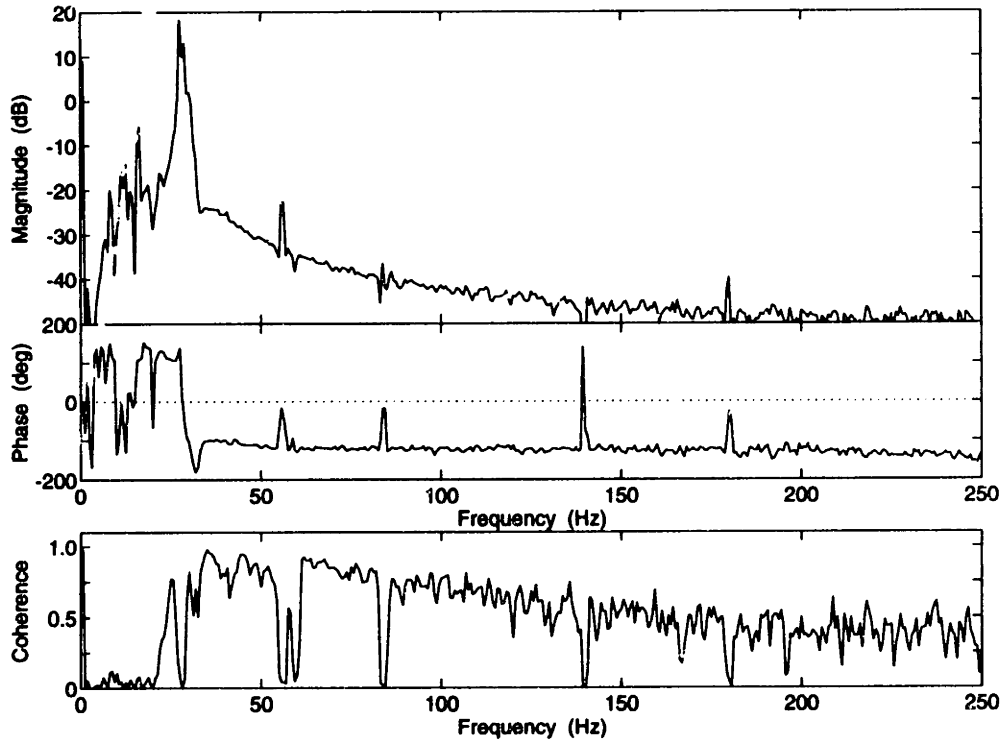

Figure 6-7: M_x loop transfer function with first-harmonic controller.

filters successfully phase-stabilized the compensator poles. Both the controller roll-off and the compensation filters gain-stabilized the plant poles, although there is very little margin associated with the M_x resonance at 31 Hz. The low-frequency features are primarily due to resonances of the vacuum system fittings.

As with Figure 5-13, the coherence drops at harmonics of the drive frequency due to the nonlinear components in the output of the controllers; these components might also distort the measured peak gains. Sharp drops in the coherence also occur at the structural resonances and at the harmonics of the 60 Hz electrical noise. The gradual loss of coherence at higher frequencies is due to insufficient excitation of the system. This could be improved by breaking the loop at a different point.

6.3 Single-Axis Cancellation

A variety of tests were conducted to assess the system's performance when used to cancel vibration along or about a single axis. Both the steady-state response and the transient response are shown for separate cases of axial and lateral cancellation. Some frequency-tracking results are also presented. These tests not only demonstrate the performance of the cancellation system, they reinforce many of the observations made in the previous chapters, as will be noted.

6.3.1 Axial Cancellation

As the various nonlinearities in the actuator and in the controllers suggested the possibility of coupling between the harmonics, the steady-state performance of each controller was measured on its own and in conjunction with the other controllers.

Typical open- and closed-loop axial vibration spectra are shown in Figure 6-8 for a single FXLMS controller, tuned to the third harmonic in this case. Roughly 34 dB of cancellation was achieved at the target harmonic, while the other harmonics were almost completely unaffected. (The frequency shift that is visible above 150 Hz is due to slight variations in the cooler's drive frequency during testing.) The harmonic cancellation levels associated with the various controllers are presented in Table 6.1;

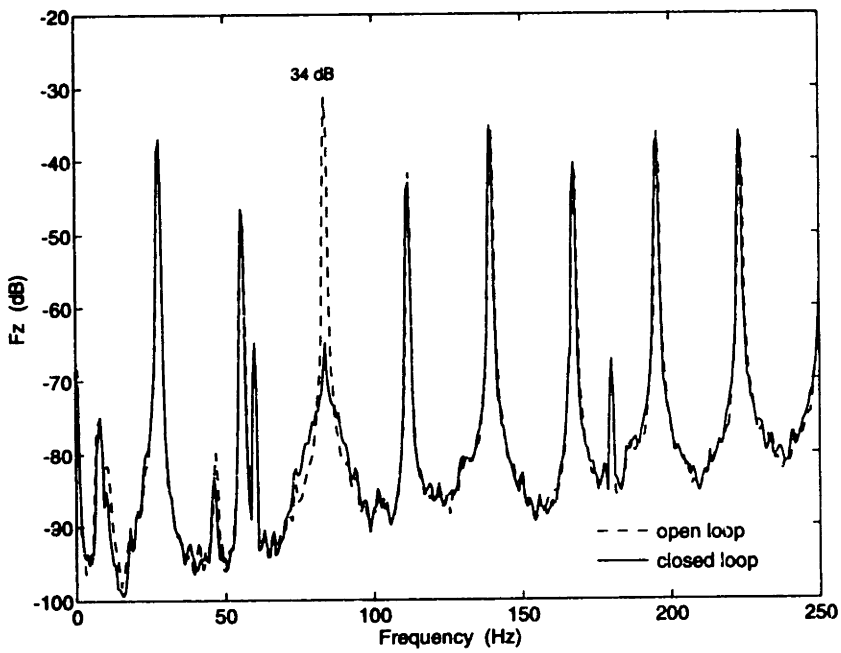

Figure 6-8: Open- and closed-loop axial vibration spectra with the third-harmonic axial controller.

positive values indicate cancellation while negative values indicate amplification. The greatest off-diagonal entry in the table occurs at the second harmonic in conjunction with first-harmonic cancellation. This is consistent with the observations in Chapter 4 regarding the frequency dependence of the actuator's nonlinearity: the higher harmonics in the actuator's response are most significant when the actuator is driven at frequencies below its bounce resonance (46 Hz).

The reduction in the RMS vibration computed over the first five harmonics is also shown in Table 6.1 for each controller. As all the harmonics are of significant amplitude, cancelling a single one does not have much effect on the RMS vibration levels.

Rather significant coupling with the lateral vibrations was observed for some harmonics. The lateral cancellation levels associated with the axial controllers are presented in Table 6.2. While the cross-axis coupling is occassionally beneficial, contributing a few dB of unintended cancellation, it can also substantially increase the lateral vibration levels, *c.g.* the third, fourth, and fifth M_x harmonics are increased by 12–22 dB.

Table 6.1: Axial cancellation levels achieved at the first five harmonics with a single axial controller.

Controller	Axial Cancellation (dB)					RMS (dB)
	1	2	3	4	5	1–5
1	31.9	2.7	0.1	1.5	-0.8	0.9
2	-0.1	31.4	0.1	0.2	0.0	0.1
3	0.3	-0.4	33.7	1.3	-0.5	3.5
4	0.2	-0.1	-0.1	30.8	1.5	0.4
5	0.4	-1.0	-0.1	0.5	28.6	1.3

Table 6.2: Lateral cancellation levels achieved at the first five harmonics with a single axial controller.

Controller	M_x Cancellation (dB)					M_y Cancellation (dB)				
	1	2	3	4	5	1	2	3	4	5
1	-0.3	-0.2	-0.3	0.0	-0.8	-7.6	-0.6	0.3	1.7	-0.6
2	0.1	0.7	0.0	1.2	0.4	0.3	1.0	0.2	0.2	0.1
3	-0.5	-0.5	-12.0	2.4	-0.5	0.1	-0.7	3.7	1.3	-0.3
4	0.3	-0.9	0.7	-22.4	-1.2	0.4	-0.8	-0.1	2.4	1.4
5	0.3	-1.0	-1.0	-3.2	-12.9	0.5	-0.8	0.0	0.6	2.8

Multiple axial harmonics were then cancelled simultaneously. Open- and closed-loop spectra were recorded using from one to five controllers, starting with the third-harmonic controller and then adding the next most effective one based on the rms reductions in Table 6.1. Axial and lateral vibration levels are given in Tables 6.3 and 6.4, respectively. The entry in the "controllers" column indicates which controllers were used in a particular test, *e.g.* the code 10100 indicates that the first-harmonic and the third-harmonic axial controllers were included in the loop. The resulting F_z, M_x, and M_y spectra are shown in Figure 6-9 for the five-controller case; cancellation levels that exceed ±3 dB are indicated in this figure.

There is considerable variation among the vibration levels measured for the different combinations of controllers. For example, the difference between the single-controller and the multi-controller axial cancellation at a given harmonic exceeds 6 dB in some cases. Based on the loop transfer function (Figure 6-6), the cancellation at a given harmonic should be independent of the other harmonics and thus should

Table 6.3: Axial cancellation levels achieved at the first five harmonics with multiple axial controllers.

Controllers	Axial Cancellation (dB)					RMS (dB)
	1	2	3	4	5	1–5
00100	0.3	-0.4	33.7	1.3	-0.5	3.5
10100	29.6	2.7	27.2	1.2	0.7	5.6
10101	33.1	2.7	34.7	0.7	24.0	13.8
10111	34.5	2.2	40.2	29.0	29.5	20.4
11111	33.2	23.4	39.8	24.9	30.3	27.0

Table 6.4: Lateral cancellation levels achieved at the first five harmonics with multiple axial controllers.

Controllers	M_x Cancellation (dB)					M_y Cancellation (dB)				
	1	2	3	4	5	1	2	3	4	5
00100	-0.5	-0.5	-12.0	2.4	-0.5	0.1	-0.7	3.7	1.3	-0.3
10100	0.2	0.5	-11.8	-3.0	0.6	-9.4	0.4	3.5	0.6	0.6
10101	-0.9	0.6	-11.5	-2.5	-10.3	-10.7	0.6	3.7	0.7	3.0
10111	-0.2	0.6	-11.2	-9.1	-10.8	-10.9	0.5	3.8	2.9	2.6
11111	0.0	0.1	-11.1	-8.2	-10.5	-10.9	0.2	3.6	3.1	3.0

remain constant. However the loop transfer function masks many of the details associated with the FXLMS controllers. Changes in the reference signal levels have a strong effect on the closed-loop cancellation, as shown in the last chapter. Changes in the disturbance levels generated by the cooler modify signal-to-noise ratios, which also affects the cancellation. Finally, the nonlinear components in the output of the controllers provide some coupling between the harmonics, and so could be expected to account for some of the variation seen in the multiple-controller cases. It was not possible to assign a specific cause to the observed variation.

The lateral cancellation exhibited less variation between the single-controller results and the multiple-controller results. There was one exception to this: the fourth-harmonic axial controller caused a 22 dB increase in the fourth harmonic of M_x when used alone, and yet the increase was less than 10 dB when multiple axial controllers were used. This was traced to an unusually low open-loop value of the fourth harmonic of M_x in the single-controller run; the closed-loop levels are actually comparable in

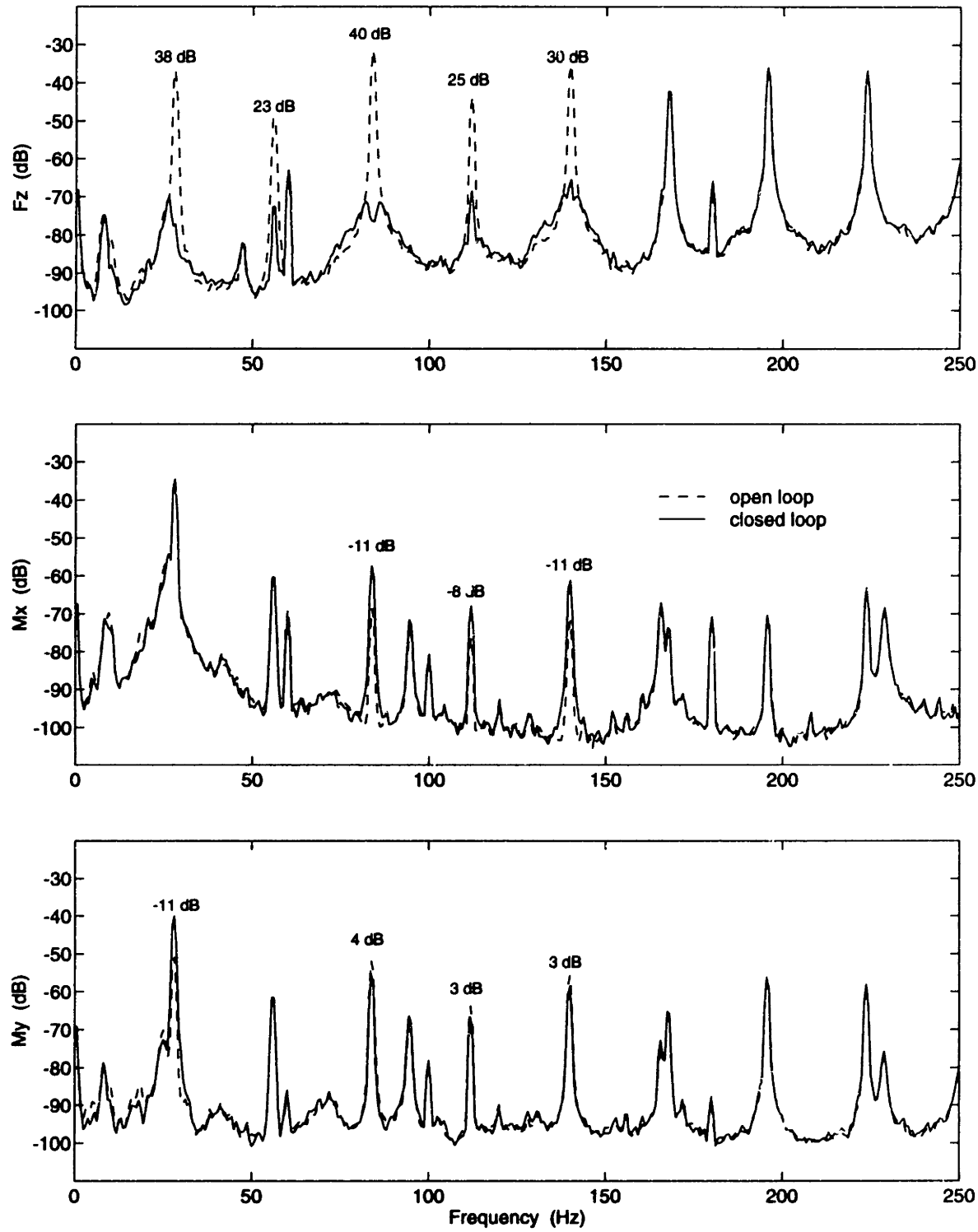

Figure 6-9: Open- and closed-loop vibration spectra with five axial controllers.

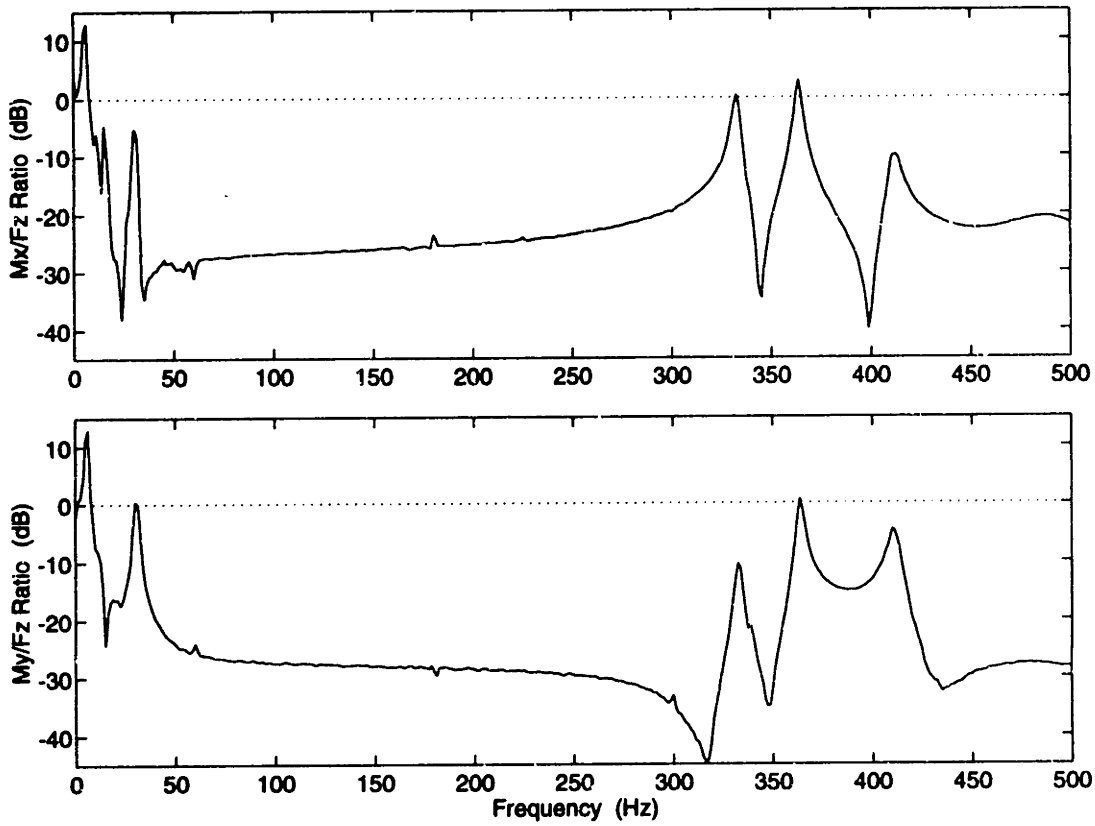

Figure 6-10: Ratios of lateral to axial actuator output in response to a commanded axial force.

the single- and multiple-controller cases.

The cross-axis coupling may be understood by examining the plant's transfer-function matrix (Figure 6-5). In particular, consider the three-dimensional response to a commanded axial force. The relative amplitude of the off-diagonal response (the two torques in this case) to the diagonal response (the axial force) provides a good indication of the plant's cross-axis coupling. Rather than reducing the entire matrix to as few functions as possible, as is done with the dominance ratio [32], two specific ratios are retained: M_{xo}/F_{zo} and M_{yo}/F_{zo}, where the subscript o denotes an output quantity. These ratios are shown as functions of frequency in Figure 6-10.

Based on this figure, it would appear that cross-axis coupling is a problem only near the lateral resonances. But Figure 6-10 only provides half the story. The other half lies in the open-loop disturbance spectrum, see Figure 6-9 for example. The large disparity between the amplitude of the axial vibration and the lateral vibration,

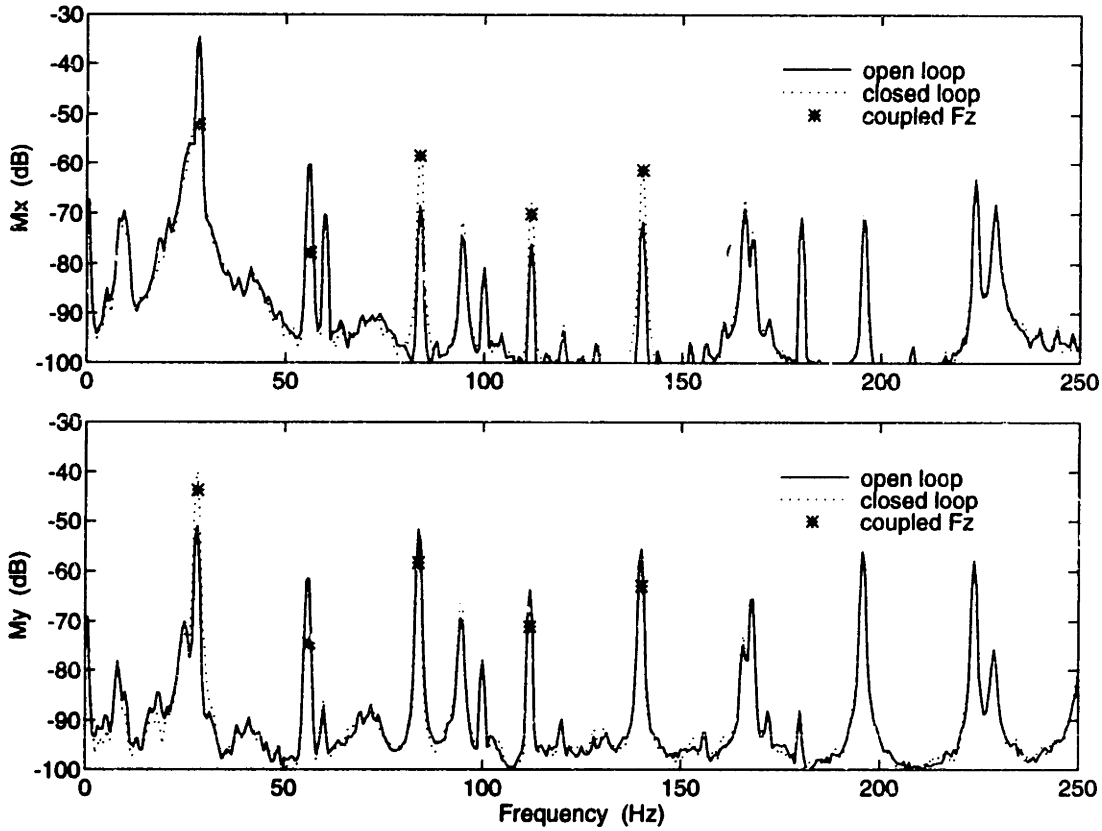

Figure 6-11: Open- and closed-loop lateral vibration spectra with five axial controllers. Also shown are the calculated lateral torques generated by the actuator when cancelling F_z.

especially at higher frequencies, means that even a small amount of coupling between the axes can have a noticeable effect.

The open- and closed-loop lateral vibration spectra from the five-controller test are repeated in Figure 6-11; the line types have been changed to better distinguish the harmonics with closed-loop amplification. Also shown in this figure is the calculated lateral vibration caused by the cross-axis coupling in the actuator. This was computed by assuming that, at the controlled harmonics, the actuator must generate forces of the same amplitude as the open-loop axial vibration. These levels were then multiplied by the torque/force ratios of Figure 6-10 to arrive at the torque levels indicated in Figure 6-11. These levels appear to correlate well with the measured closed-loop lateral vibration. At the harmonics that exhibited large increases due to the cancellation system, the spurious actuator-generated torques are significantly greater than the cooler-generated torques. Furthermore, at the harmonics that

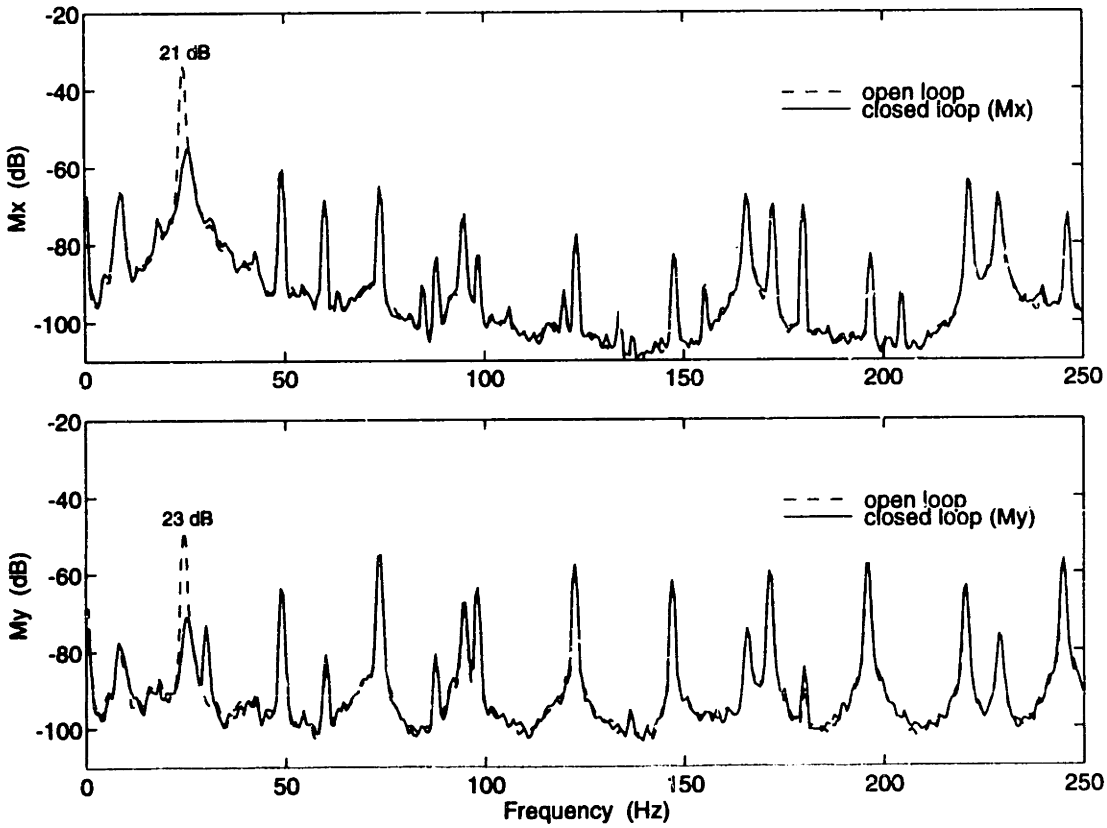

Figure 6-12: Open- and closed-loop lateral vibration spectra with first-harmonic lateral controllers. The two controllers were not operated simultaneously.

showed some closed-loop reduction the two torques are within 10 dB, as required for cancellation levels of 3–4 dB.

This example demonstrates that the off-diagonal response to single-axis cancellation is determined by both the actuator's multi-axis coupling and the multi-axis nature of the disturbance.

6.3.2 Lateral Cancellation

The lateral vibration levels generated by the cryocooler are significantly lower than the axial ones. Rather than repeating the investigation of single- and multi-controller performance on the lateral axes, each lateral axis was assigned a single controller which was tuned to the fundamental component. The performance of the M_x controller and the M_y controller is shown in Figure 6-12; no coupling was observed between the harmonics or the axes. These were single-axis tests—the two lateral loops

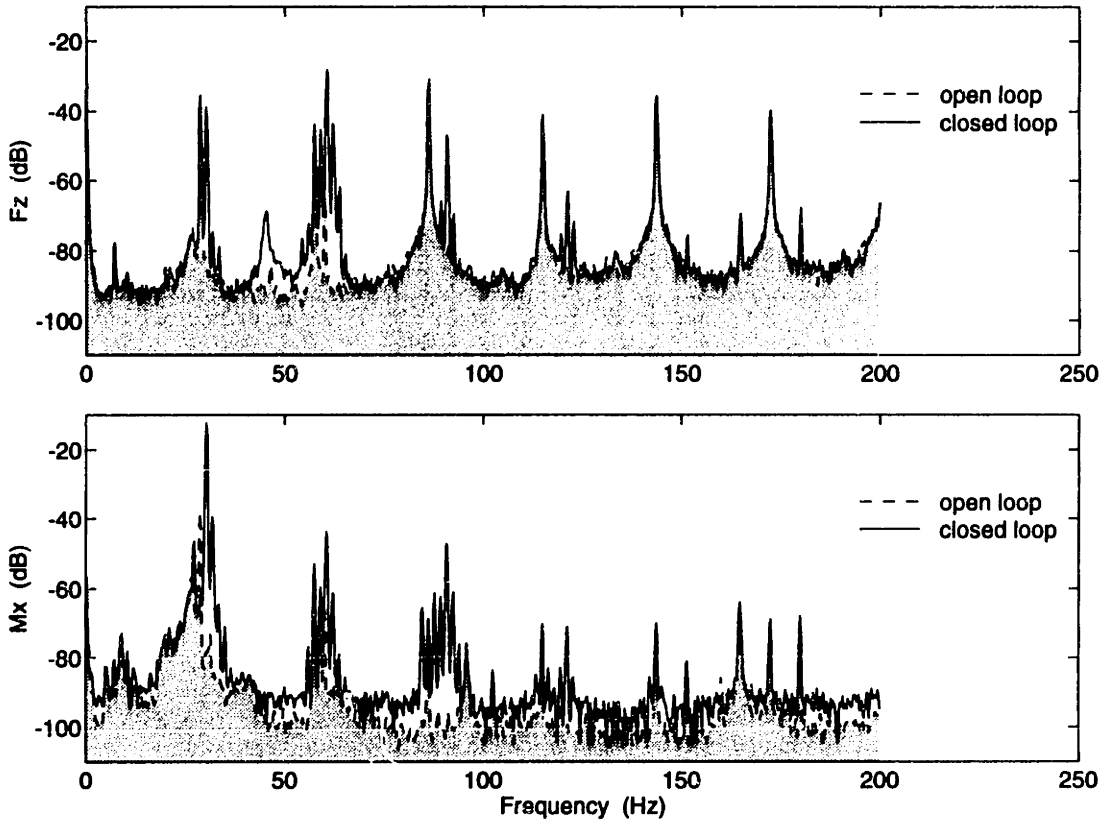

Figure 6-13: Open- and closed-loop F_z and M_x vibration spectra with a first-harmonic M_x controller.

were not closed simultaneously here.

Several steps were necessary to achieve these results. As was mentioned above, the lateral compensation filters could not be properly tuned to the lateral resonances. In order to gain-stabilize these modes, the frequency separation between the compensator poles and the plant poles was increased by decreasing the cooler's drive frequency (compare Figures 6-11 and 6-12). The controller gain was also reduced, thereby sacrificing some performance. Even after taking these measures, notice that the M_y resonance at 30 Hz has been amplified by the closed-loop system.

Attempting to implement lateral cancellation at higher drive frequencies revealed an interesting instability: the M_x error grew rapidly and then achieved steady-state after 5–10 seconds. The F_z and M_x spectra in this large-amplitude condition are shown in Figure 6-13, where the open-loop spectra have been shaded in order to emphasize the additional harmonic content of the closed-loop vibration.

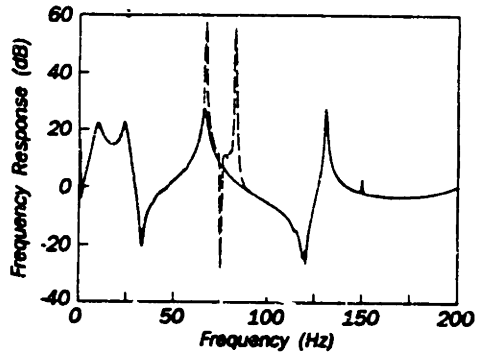

Figure 6-14: Magnitude of the transfer function from disturbance to output. Solid line: open-loop plant; dashed line: plant and four-weight FXLMS filter tuned to 75 Hz. From Reference [103].

The drive frequency is slightly greater than the natural frequency of the actuator's lateral mode. Notice that even with the large-amplitude limit cycle, almost 25 dB of cancellation has been achieved at the drive frequency. However the lateral mode is amplified by 10 dB. But the harmonic that goes unstable is the lateral mode mirrored about the drive frequency. There are additional mirrored harmonics at the second, third, and fourth harmonics of the drive frequency; these appear in both the lateral and the axial vibration. The actuator's axial mode at 46 Hz is also amplified, although this does not result in a cascade of mirrored harmonics because it is well outside the controller's bandwidth.

The failure mode depicted in Figure 6-13 is a decidely unattractive property of the LMS filter. The cause of the instability is the phase shift associated with the lateral resonance, but the generation of the additional harmonic components is due to the nonlinear terms in the adaptive filter's output, as discussed in Chapter 5. It is worth noting that this behavior is due to the modulation process and thus appears in both the continuous-time and the discrete-time LMS filter; Snyder and Tanaka [103] observed a similar response (Figure 6-14) with a four-weight discrete-time controller.

6.3.3 Transient Response

Aside from a brief mention of the closed-loop time constant, the analysis of Chapter 5 neglected the system's transient response. The convergence properties of various

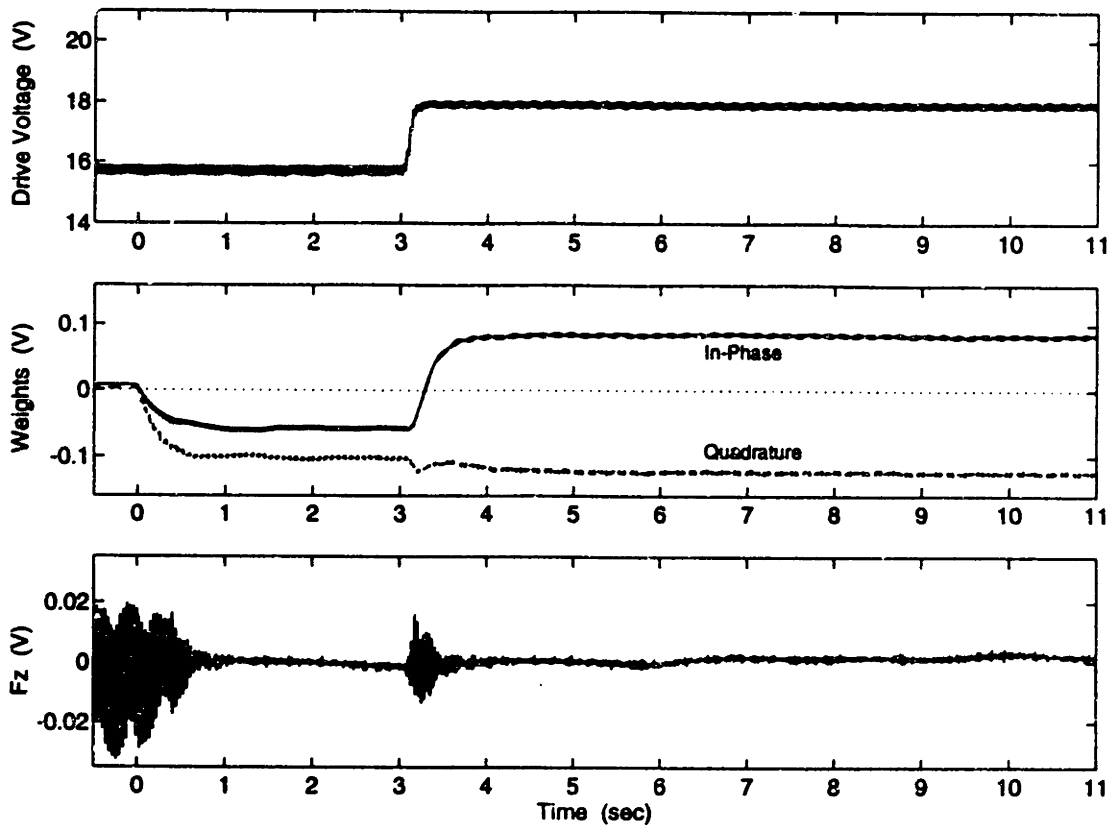

Figure 6-15: Transient response of the first-harmonic axial adaptive filter to a step change in the drive voltage. The loop is closed at $t = 0$.

adaptive filters have received considerable attention in the field of adaptive signal processing [86]. While most adaptation algorithms have comparable steady-state performance, there can be significant differences in their transient behavior [114]. This is of little concern in the cryocooler application since the long thermal time constants give the vibration cancellation system enough time to converge. For the sake of completeness, however, the transient response of the two-weight FXLMS filter was measured.

An example of the axial transient response is shown in Figure 6-15. This data was collected using a 50-Hz data bandwidth on the Tektronix Fourier Analyzer, so most of the response is due to the cooler's first and second harmonics. Four signals are presented as functions of time. The cooler's drive voltage may be varied to adjust the drive frequency: 15.5 V corresponds to 26 Hz, and 18.0 V corresponds to 31 Hz. Two controllers were used to cancel the first and second harmonics of the axial vibration;

the in-phase and quadrature weights of the first-harmonic controller are shown. The unfiltered axial error signal is also shown.

All loops are open for $t < 0$. Recall that the integrators are leaky, so their output, the weights, should go to zero when the inputs are grounded. The initial offset visible in the weights (8 mV in-phase and 2 mV quadrature) represents the integrator bias error. The integrator offset adjustments were trimmed to minimize this error.

The exponential convergence of the weights and the error is apparent when the two axial loops are closed at $t = 0$. The time constant is approximately 0.2 seconds. Some noise can be seen in the weights, which may be attributed to the higher harmonics in the error signal.

A step change in the drive voltage is made at $t = 3.0$ seconds. The weights immediately begin to adapt, although the system's time constant results in a brief period of misadjustment. A general analysis of the system during this time is quite complicated, see for example References [115–118]. Widrow *et al.* [115] discuss the trade-off between having a small time constant to track changes in the disturbance accurately and having a larger time constant to provide better steady-state performance. This decision will obviously depend on the statistics of the disturbance—does the disturbance frequency vary rapidly or not?

In addition to the step change, several other types of varying disturbances were investigated. For example, Figure 6-16 shows the transient response to a five-second ramp in the drive voltage. The initial voltage level was somewhat lower than in Figure 6-15, resulting in a smaller open-loop error. The misadjustment during the voltage ramp is only slightly larger than the steady-state error. On the other hand, rapid fluctuations in the drive voltage (Figure 6-17) resulted in a misadjustment on the same order as the open-loop error. Notice that, despite the misadjustment, the weights follow the drive voltage (and the drive frequency) at all times.

The filtered-x LMS filter appears to be capable of tracking a varying disturbance frequency. While there can be significant misadjustment with rapid changes in frequency, such changes are unusual in the cryocooler application. Even under closed-loop temperature control, cooler time constants on the order of a minute are typi-

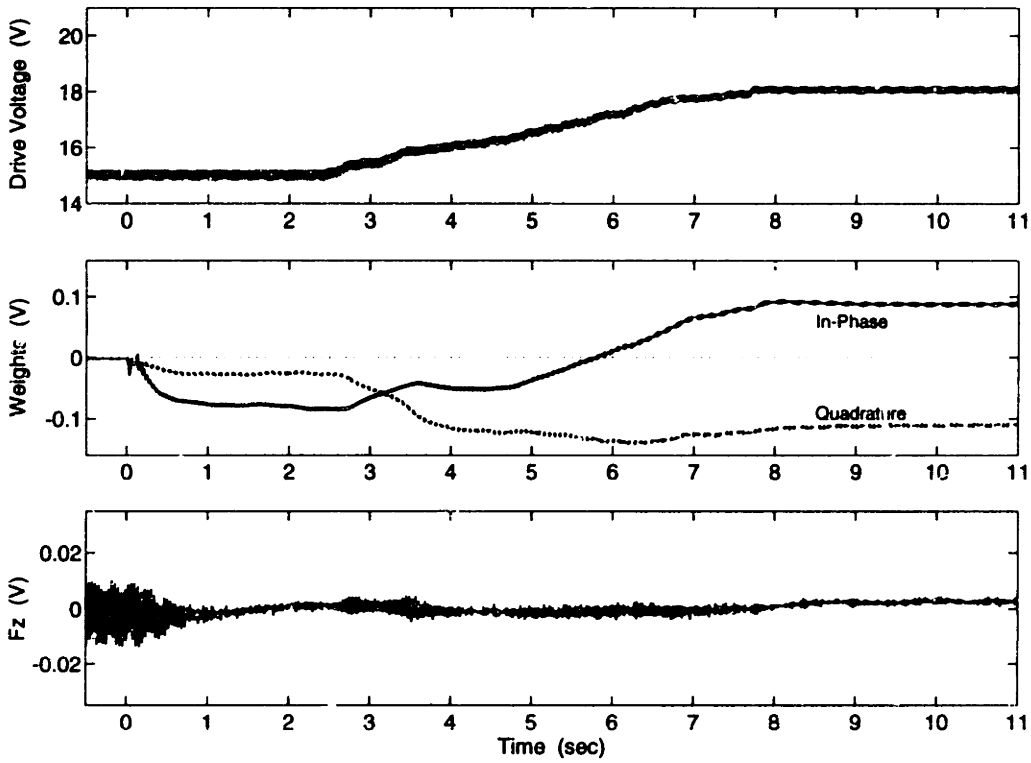

Figure 6-16: Transient response of the first-harmonic axial adaptive filter to a drive-voltage ramp. The loop is closed at $t = 0$.

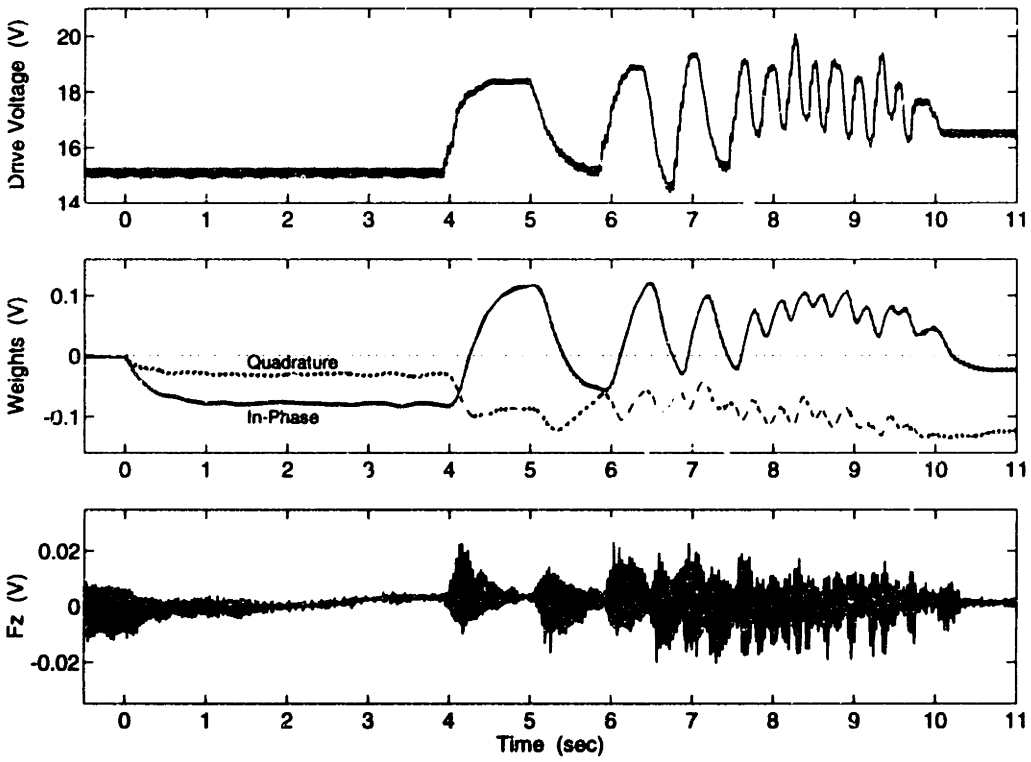

Figure 6-17: Transient response of the first-harmonic axial adaptive filter to rapid drive-voltage changes. The loop is closed at $t = 0$.

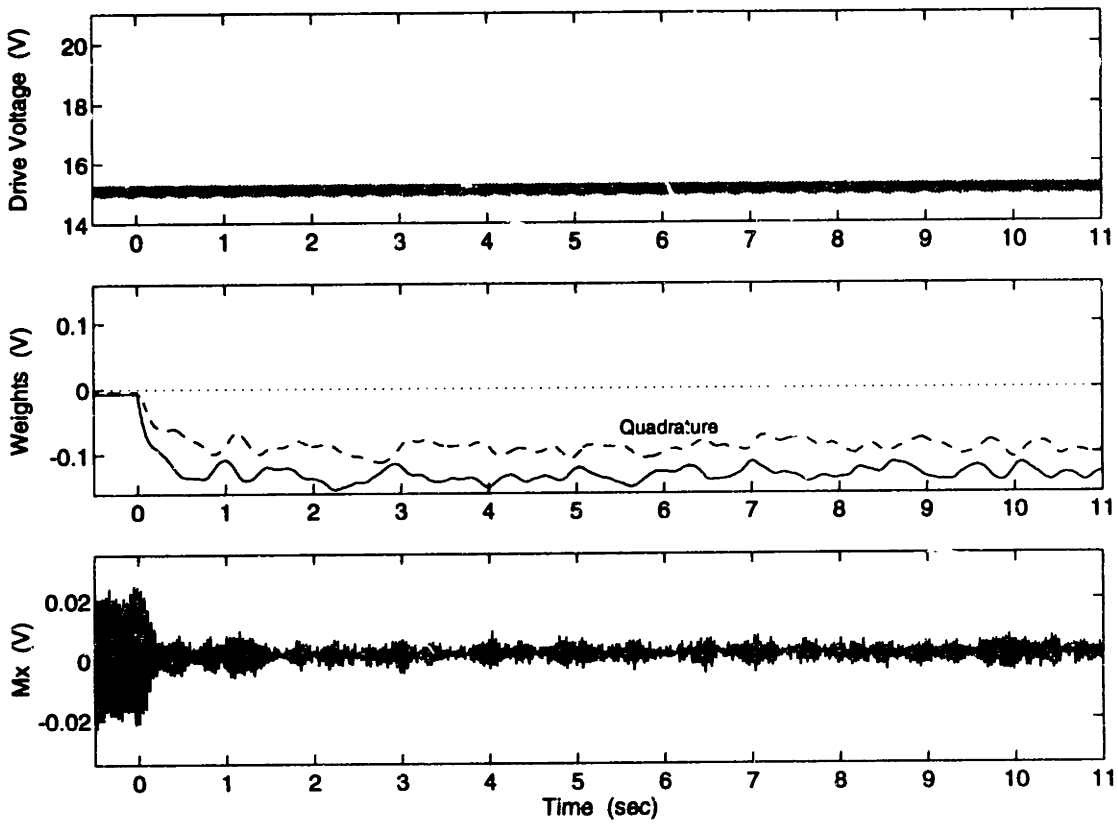

Figure 6-18: Transient response of the first-harmonic M_x adaptive filter at a low drive frequency. The loop is closed at $t = 0$.

cal [119]. The vibration cancellation system's misadjustment to such slow changes would be imperceptible.

The lateral transient response was also measured. As shown in Figure 6-18, at low drive voltages the M_x controller converged rapidly, but some low-frequency noise appears in both weights. This is most likely due to the so-called gradient noise associated with large loop gains [115]; the adaptation process is trying to converge too quickly and is thereby overshooting the optimal weight values. The loop gain on the lateral controllers had been increased in an effort to improve performance.

Increasing the drive voltage with the lateral loop closed led to the lateral instability discussed above. The transient response associated with the instability is shown in Figure 6-19; notice that the weights and the error are an order of magntiude larger than in the other transient responses. Rather than the constant-weight Wiener solution, the weights converge to the dynamic solution discussed by Glover [94]. In

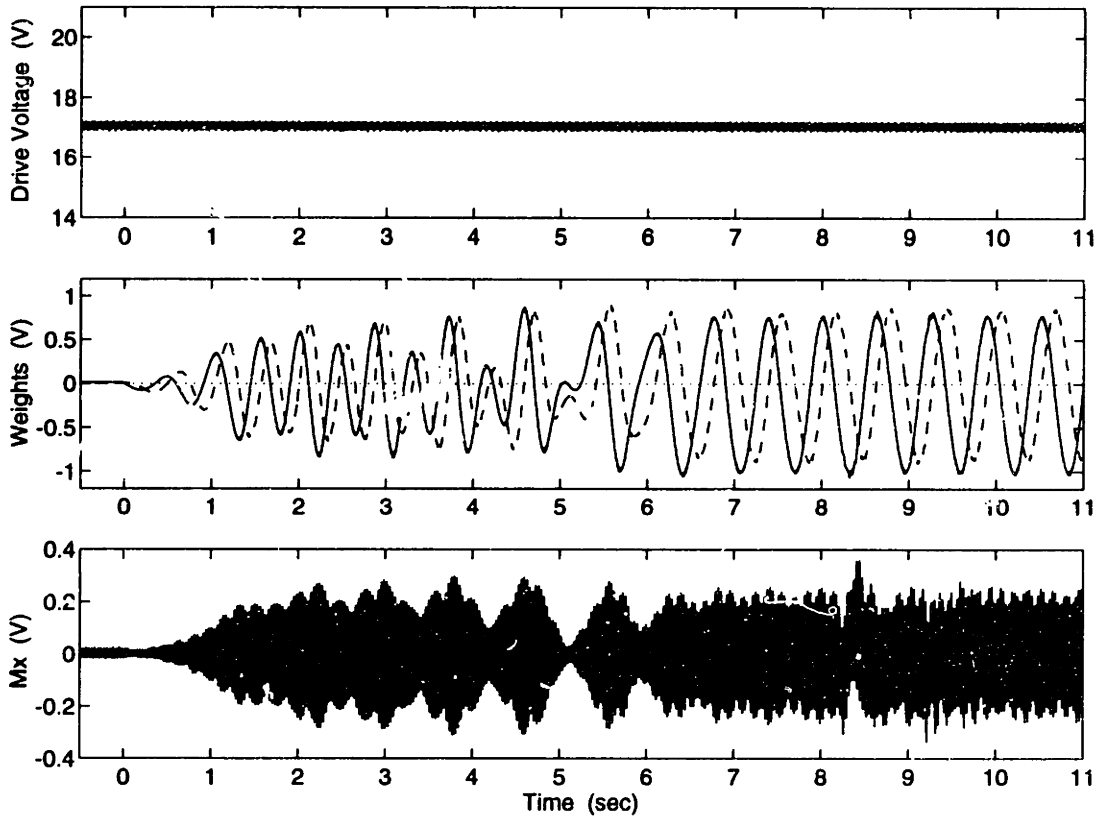

Figure 6-19: Transient response of the first-harmonic M_x adaptive filter at a high drive frequency. The loop is closed at $t = 0$.

particular, the frequency at which the weights vary is the difference between the reference frequency and the frequency of the lateral resonance. Practically, this solution can only develop if the filter implementation has sufficient range such that it is not driven into saturation.

6.3.4 Frequency-Tracking Cancellation

The frequency-tracking performance of the first-harmonic axial controller was measured. In these tests, the controller was given time to converge, the steady-state cancellation was recorded, and then the drive frequency was increased to the next setting. No gains were changed and no filters were tuned during this process.

The axial and lateral cancellation achieved at the first four harmonics is shown as a function of the drive frequency in Figure 6-20. Recall that the only controller in use here is the first-harmonic axial controller. The cancellation associated with this

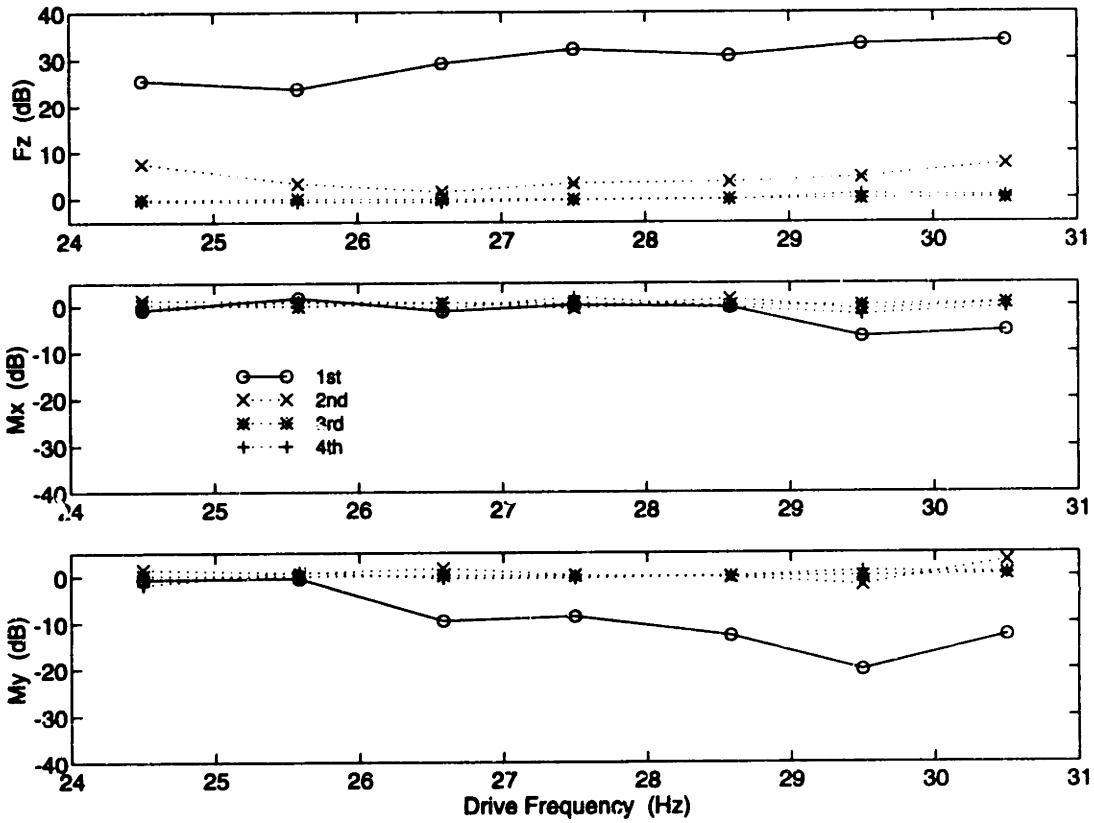

Figure 6-20: Axial and lateral cancellation achieved at the first four harmonics as a function of drive frequency.

controller increases somewhat with drive frequency. This is due in part to an increase in the amplitude of the first-harmonic reference signal and the resulting increase in loop gain. While the third and fourth harmonics of the axial vibration are unaffected by the first-harmonic controller, there is some coupling with the second harmonic. The range of drive frequencies used here lies between the actuator's second-order superharmonic resonance and its primary axial resonance; the normalized forcing frequency is $0.53 < \Omega_f < 0.66$. The increased coupling observed at either end of the drive-frequency range is due to the proximity of these resonances and is in agreement with the nonlinear actuator model of Chapter 4, *e.g.* Figure 4-13.

The coupling with the first harmonic of M_x and M_y may be explained in conjuction with Figures 6-10 and 6-11. The open-loop level of the first M_y harmonic is much smaller than the first M_x harmonic, making it much more sensitive to any coupling with F_z. As the drive frequency is increased, the coupling ratio peaks, resulting in

Table 6.5: Cancellation levels achieved at the first five harmonics with multiple controllers on multiple axes.

Loops	F_z Cancellation (dB)					RMS (dB)
	1	2	3	4	5	1–5
Z	29.3	34.0	30.3	31.8	19.4	22.0
ZX	30.0	30.8	31.0	33.0	21.7	23.5
ZXY	29.0	31.8	31.7	30.6	22.6	23.7
	M_x Cancellation (dB)					
Z	-0.2	0.7	-6.8	-12.0	-10.9	-0.1
ZX	25.8	1.2	-7.5	-12.6	-11.8	19.3
ZXY	24.2	-1.5	-7.2	-10.8	-11.8	18.1
	M_y Cancellation (dB)					
Z	-0.4	1.7	4.5	3.9	2.9	0.0
ZX	-0.8	0.7	4.2	3.6	2.6	-0.4
ZXY	17.8	6.3	4.8	3.7	3.1	11.2

greater feedthrough of the axial vibration.

6.4 Multi-Axis Cancellation

Multi-axis cancellation was implemented by simultaneously closing the single-axis cancellation loops. Once again, this was done in a step-wise fashion to investigate the coupling between these loops; some coupling had already been observed in the F_z single-axis tests.

The lower drive frequency was used to avoid destabilizing the lateral resonances. The F_z loop included five controllers, while the other loops had one controller each. Table 6.5 summarizes the cancellation levels at the first five harmonics.

The cancellation is similar, though not identical, to the single-axis results. The decreased drive frequency reduces the open-loop disturbance amplitude; it also modifies the reference signals due to the bandpass filtering in the generation network. This is believed to be the cause of the variation in the five-harmonic axial cancellation levels—the change in drive frequency from Table 6.3 to Table 6.5 has a greater effect on the F_z cancellation than the additional loops closed in Table 6.5.

The lateral axes display much the same coupling with F_z as was apparent in

Table 6.6: Cancellation levels achieved at the first five harmonics with third-harmonic controllers on multiple axes.

Loops	F_z Cancellation (dB)				
	1	2	3	4	5
Z	-0.2	-0.1	38.6	0.6	-0.4
XY	0.2	-0.1	0.3	-0.1	0.5
ZXY	-0.1	-0.4	41.3	0.0	-0.2
	M_x Cancellation (dB)				
Z	-0.3	0.6	-10.3	0.5	0.1
XY	-0.7	-0.2	5.2	-0.8	1.3
ZXY	-0.2	0.5	10.8	-0.1	0.8
	M_y Cancellation (dB)				
Z	-0.3	0.3	3.1	0.6	-0.2
XY	-1.1	-0.5	15.1	-0.1	0.6
ZXY	-0.9	0.4	12.5	0.0	-0.1

Table 6.4, although the actual numbers have changed. One significant difference is that the first M_y harmonic is no longer coupled; the drive frequency has moved away from the peak near 30 Hz in the M_y coupling ratio (Figure 6-10). As would be expected, this allows the three loops to be closed with little interaction. The open- and closed-loop spectra with all seven controllers in operation are shown in Figure 6-21.

If the lateral higher harmonics are unacceptable, additional controllers may be added. The cross-axis coupling due to the axial cancellation appears as an additional disturbance to these controllers, which affects the lateral cancellation that can be achieved. In order to demonstrate this, three controllers were used to cancel the vibration at the third harmonic, one controller per axis. The cancellation levels achieved at the first five harmonics are given in Table 6.6 for axial cancellation (Z), lateral cancellation (XY), and simultaneous axial and lateral cancellation (ZXY). The open- and closed-loop spectra for Z and ZXY are shown in Figure 6-22. As cancellation was not attempted near the lateral resonance, the higher cooler drive frequency used for the axial controller tests (Figure 6-9) could also be used here. This increased the amplitude of the reference signal, thereby increasing the controller's gain.

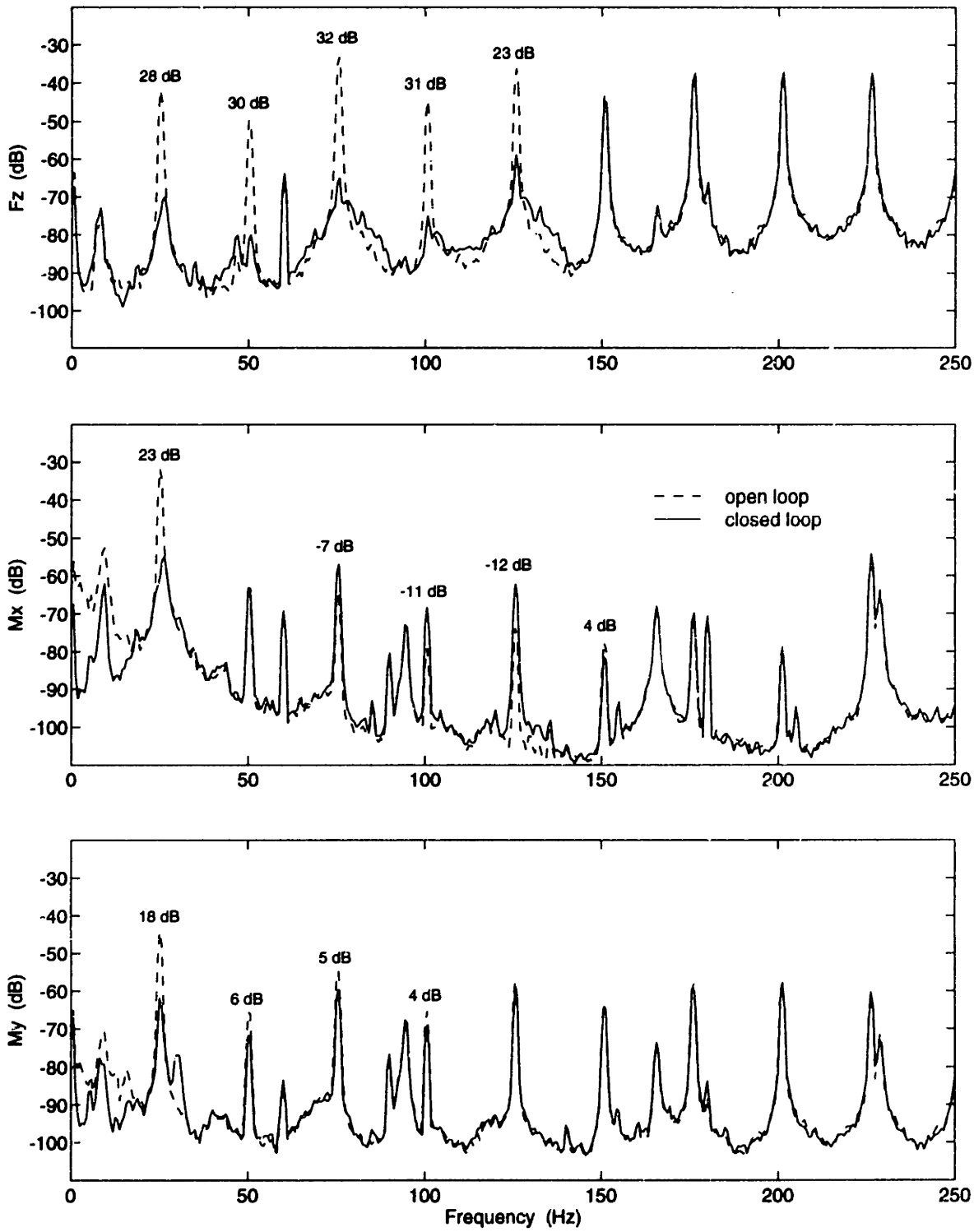

Figure 6-21: Open- and closed-loop vibration spectra with five axial controllers and two lateral controllers. All controllers were operated simultaneously.

The coupled F_z vibration appears to have quite a different effect on the lateral vibration when the lateral loops are closed. With axial cancellation alone, M_x is increased and M_y is decreased. But just the opposite occurs between the case of lateral cancellation alone, XY, and the case of axial and lateral cancellation case: the coupled F_z vibration now decreases M_x and increases M_y. It is not clear whether this is simply due to the different open- and closed-loop phase angles of the vibration, or whether this is a more complicated effect.

6.5 Summary

The closed-loop performance of the vibration cancellation system was examined in this chapter. Due to some implementation problems, several fixed filters were added to the loop in order to improve the achievable cancellation, which is proportional to the loop gain at the reference frequencies. As the FXLMS filter may be approximated by a linear transfer function, loop transfer functions were measured to provide confidence in the system before closing the loop. It appeared to be difficult to get good quantitative data from the loop transfer functions, although they did display the desired general characteristics of narrowband bandpass filters.

Single-axis and multi-axis cancellation tests were conducted. The first five harmonics of the axial vibration were cancelled, as were the fundamental components of both M_x and M_y. Some coupling was seen between the first and the second harmonics, especially for F_z, but the cross-axis coupling was much more significant. This was interpreted in terms of the actuator's coupling ratios, and good agreement with the closed-loop coupling was found.

The transient response of the adaptive filter was measured. The filter is able to track rapid variations in the cooler's drive frequency, although significant output error due to misadjustment is visible during the filter's convergence period. The amplitude of the misadjustment error appears to increase with the variation frequency.

Multi-axis cancellation achieved significant reductions in all three vibration components despite the cross-axis coupling. This was demonstrated at the first harmonic,

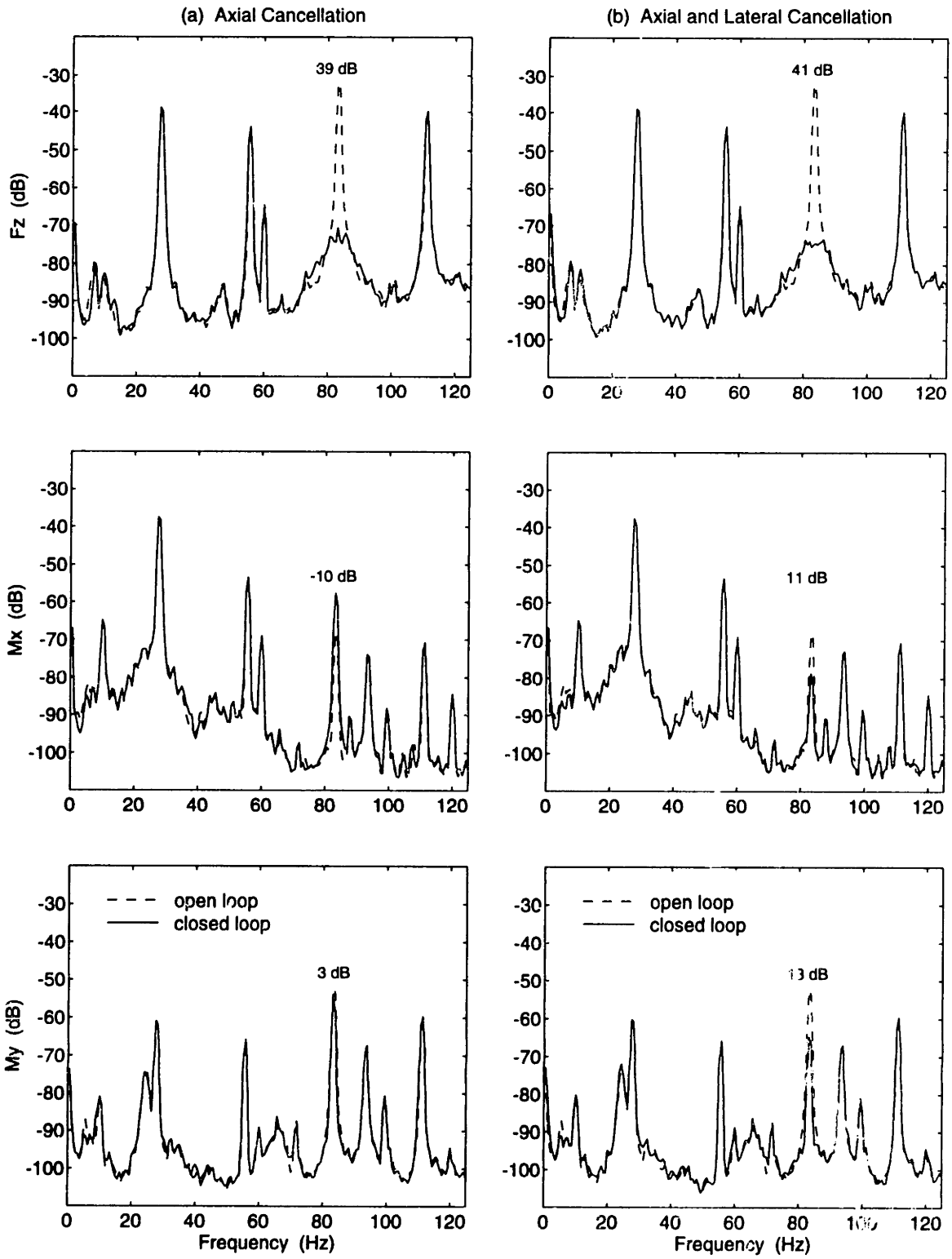

Figure 6-22: Open- and closed-loop vibration spectra with third-harmonic controllers. (a) Axial cancellation only; (b) axial and lateral cancellation.

which did not exhibit stong cross-axis coupling, and at the 3rd harmonic, which did exhibit strong coupling. A multi-axis multi-harmonic cancellation system may therefore be implemented using a set of single-axis single-harmonic FXLMS controllers.

Chapter 7

Conclusions

7.1 Summary

The subject of cryocooler vibration reduction was investigated in this thesis. Specifically, a novel active cancellation system based on adaptive feedforward control was designed, analyzed, implemented, and tested. The system includes a set of single-axis narrowband analog controllers that may be combined to provide multi-axis, multi-harmonic cancellation; the sensors and the multi-axis actuator are arranged for cancellation of the cooler's axial vibration and its torque about two orthogonal lateral axes. The experimental results verify that high levels of multi-axis cancellation may be achieved with this system.

The architecture of the active cancellation system was selected after considering the characteristics of the cryocooler and of a typical precision-pointing instrument. Simplified models of the cryocooler vibration facilitated preliminary sizing of the sensors and actuators used by the active system. These models were confirmed with multi-axis measurements of the vibration generated by the expander of a Hughes tactical cooler. Three types of actuators were considered: electromagnetic, electrodynamic, and piezoelectric. The electrodynamic actuator was selected on the basis of its mechanical simplicity and its low-power drive electronics.

The detailed design and analysis of a custom multi-axis electrodynamic actuator was pursued. Trade-offs based on first-order analyses were conducted for many of

the actuator's elements, including the magnetic circuit, the coils, the flexures, and the overall mechanical configuration. The use of rare-earth permanent magnets and relatively narrow air gaps results in a high force constant, making low-power drive electronics sufficient to generate the force levels required for cryocooler vibration cancellation. The measured performance confirmed that these levels could be achieved with ample current margin.

Testing also revealed significant higher harmonics in the actuator's response to a sinusoidal input, indicating an actuator nonlinearity. There was concern that the nonlinearity would couple the harmonics in a multi-harmonic cancellation system, reducing the system's performance or even destabilizing it. This concern was addressed by developing an analytical model of the nonlinearity, which was attributed to in-plane tension in the actuator's flexures. The harmonic content of the actuator's response was predicted with the nonlinear actuator model, and it was found to be in good agreement with the measurements. A describing-function analysis based on the nonlinear model showed that the nonlinearity will not adversely affect the active cancellation system for the parameter values associated with the experimental implementation.

The operation of an adaptive feedforward controller was then examined. The controller is based on the filtered-x least-mean-square (FXLMS) algorithm employed widely in the active control of sound and vibration; a continuous-time version was considered here. The behavior of the controller under ideal conditions was derived, and the performance limitations imposed by various implementation-related factors were investigated. For example, while leaky integrators help prevent the controller from saturating, they also limit the achievable cancellation, which makes factors like integrator bias error and the presence of lightly-damped plant modes more significant. Performance is also compromised by phase errors in the quadrature filters and by harmonic distortion in the reference signal—these factors result in nonlinear frequency-shifted components in the adaptive filter's output.

An analog realization of a two-weight FXLMS controller was proposed. The input-output behavior of one such controller was measured and was found to be in good

agreement with the analysis: the input-output transfer function was approximately linear and clearly had the features of a second-order bandpass filter. Furthermore, the effect of quadrature phase errors and the effect of additional harmonic components in the reference signal were experimentally confirmed. Some additional distortion due to the analog multiplier ICs was observed at the harmonics of the reference frequency.

Several extra elements were added to the FXLMS controllers and the multi-axis actuator in order to improve the performance of the vibration cancellation system. Error filters reduced the high-frequency content of the load cell signals, allowing greater gains (and cancellation levels) to be achieved before the electronics saturated. Compensation filters helped gain-stabilize the actuator modes, although good tuning was not achieved with the lateral channels due to long-term changes in the tip and tilt frequencies. Measured loop transfer functions verified the ability of the reference filters in the FXLMS controllers to phase-stabilize the compensator poles.

Closed-loop cancellation was successfully demonstrated with the FXLMS controllers. The single-axis, single-harmonic controllers were combined to form a multi-axis, multi-harmonic cancellation system. Coupling between the axes and between the harmonics was measured and accounted for; the coupling did not have a significant impact on the system's performance. The steady-state and transient response of the system was measured for fixed and varying disturbance frequencies. Typical cancellation levels were on the order of 30 dB for the axial vibration and 20 dB for the lateral torques.

7.2 Conclusions and Contributions

1. This research has demonstrated the utility of adaptive feedforward control for the active cancellation of cryocooler vibration. The cancellation approach has several advantages over other vibration reduction techniques. Unlike isolation, it does not require wholesale modification of the cooler's support structure. Unlike waveform cancellation, it does not require that the cooler's drive signal be available for modification—the cooler need not even be driven by a periodic

signal. And unlike fixed-frequency feedback control, it does not require that the control electronics be slaved to the cooler electronics to provide precise tuning of the compensator dynamics—this tuning is done adaptively.

2. A single-degree-of-freedom model of a cryocooler expander with an impacting displacer was developed. The model is based on parameters that are physically meaningful and are relatively easy to determine without actually measuring the expander's vibration, making the model useful for initial sizing of cancellation system components. The model provided good estimates of the expander's axial vibration as a function of drive frequency. These estimates include the higher harmonics as well as the fundamental component at the drive frequency. The model therefore represents a considerable advance on the linear model suggested by the cooler's manufacturer [14] which does not account for any of the higher harmonics.

3. Multi-axis measurements were made of the vibration generated by the expander of a Hughes 7014H 1/4-W split Stirling cryocooler; the cooler that was tested had a rotary compressor. The axial vibration is extremely impulsive due to the displacer striking the bumpers at the top and bottom of each stroke. The peak amplitude of about 12 N includes many harmonics, each on the order of 0.1 N. The peak amplitude of the lateral torques is approximately 6 N·cm, and the harmonics are on the order of 0.04 N·cm. This is a much more complete description of the vibration associated with a tactical cooler's expander than previously available in the literature; Gully and Hanes [14] discussed only the axial vibration generated by the expander of a 1 W tactical cooler.

4. A unique electrodynamic actuator with multi-axis capability was designed, analyzed, fabricated, and tested. It consists of three electrodynamic forcing elements housed in two concentric rings. Each forcing element combines a tightly-wound coil with a four-magnet two-return-plate magnetic circuit. The coil and half the magnetic circuit are supported by the stationary inner ring, while the other half of the magnetic circuit is housed in the moving outer ring, which is

connected by blade flexures to the inner ring. The effective force constant of each forcing element is approximately 3.2 N/A. The drive current for each coil is provided by a power op amp configured as a voltage-controlled current source with a 1.5 A current limit. Combined with the force constant, this current source ensures that the actuator can simultaneously cancel many of the cooler's axial and lateral harmonics.

5. The multi-axis actuator dynamics were effectively decoupled from one another by a pair of analog transformation-matrix circuits, one operating on the actuator command signals, and the other operating on the sensor output signals. The resulting F_z, M_x, and M_y channels each feature a single actuator mode over the first 300 Hz, with the axial resonance occurring at 46 Hz and the lateral resonances occurring at 31 Hz. Over the 300 Hz bandwidth, the coupling between the lateral channels is about -30 dB, while the coupling between the axial channel and either lateral channel is about -25 dB. There is much greater coupling between all channels near the resonances.

6. The actuator exhibited considerable nonlinear dynamics. The blade flexures are restrained by the inner and the outer ring, so any relative displacement of these rings induces axial tension in the flexures. A flexure model that accounted for this tension was derived, resulting in a modified form of Duffing's equation that includes both a quadratic stiffness and a cubic stiffness. The quadratic stiffness represents the effect of the outer ring's static deflection, while the cubic stiffness represents the effect of the outer ring's vibratory motion. The frequency response of the nonlinear model was then found by applying the harmonic balance method to an assumed three-harmonic solution. Both the derivation of the nonlinear model and the analysis of its response make use of common techniques from the field of nonlinear structural dynamics. However, several aspects of the actuator model make the results significant:

   (a) The quadratic/cubic Duffing's equation is rarely studied although it is clearly of practical relevance. The static deflection was found to be signifi-

cant in the flexure model when it exceeded the flexure's radius of gyration (approximately a third of the flexure's thickness for a rectangular cross-section).

(b) Previous solutions of the quadratic/cubic Duffing's equation [64] were expressed in terms of a root-sum-square amplitude rather than in terms of a multi-harmonic frequency response. The present results include both the amplitude and the phase of the first three harmonics in the output. This description is important when considering the use of the nonlinear actuator in a closed-loop system.

(c) Some multi-harmonic frequency responses have been derived for the cubic Duffing's equation, but only for heavily-damped systems [73, 74]. The present results apply to a lightly-damped nonlinear system. Quite apart from the lack of the quadratic stiffness, the selected range of damping can have a dramatic effect on the response of a nonlinear system.

7. The nonlinear actuator model was verified with experimental measurements. The actuator's forced response was measured at several forcing amplitudes. First-, second-, and third-order input-output transfer functions were derived from this data and compared with the nonlinear model. Good agreement was found; the model captured nonlinear effects such as superharmonic resonances and jump phenomena observed in the measured response. The experimental transfer functions are also of interest in their own right—the author is aware of only one other example of a third-order transfer function measured on a nonlinear structure [79].

8. It was shown that the nonlinear actuator can also be analyzed using describing functions. The nonlinear equation of motion may be arranged as a local feedback loop, separating the linear frequency dependence and the nonlinear amplitude dependence. The quadratic and cubic terms then appear as explicit frequency-independent nonlinearities which are easily treated with describing functions. An example is considered in which the nonlinear actuator is driven

by a two-harmonic narrowband controller. The nonlinearity is shown to have little effect on the closed-loop system for the parameter values associated with the experimental system. General expressions are presented to help assess the impact of the nonlinearity on performance and stability for other parameter values.

9. A detailed analysis was conducted of a continuous-time implementation of a two-weight FXLMS filter and a harmonic reference signal. The behavior of the discrete-time narrowband FXLMS filter is well-documented in the literature [94,95,113,84]; analogous expressions were derived for the continuous-time filter. For example,

   (a) It was shown that the narrowband FXLMS adaptive filter is equivalent to a second-order bandpass filter with the center frequency determined by the harmonic reference signal. This behavior lies outside the scope of a Wiener-filter interpretation.

   (b) It was shown that using a leaky integrator introduces damping into the bandpass filter, limiting the loop gain at the reference frequency and therefore limiting the closed-loop cancellation. If the corner frequency of the leaky integrator is α_h and the reference frequency is ω_x, the compensator's damping ratio is then $\zeta = \alpha_h/\omega_x$.

   (c) It was shown that broadband noise in the reference signal limits the closed-loop cancellation. Expressed in dB, the maximum cancellation is given by the reference signal's signal-to-noise ratio at the reference frequency.

In addition, the following original conclusions were reached:

   (a) It was shown that the effect of the plant may be eliminated from the loop by modifying the reference filter in the FXLMS algorithm. Assuming the plant's transfer function at the reference frequency is $G(\omega_x) = A_g e^{j\theta_g}$, the traditional approach is to match the plant with the reference filter:

$\hat{G}(\omega_x) = A_g e^{j\theta_g}$ [84,86,113]. The plant's effect on the system's closed-loop time constant may be eliminated by using instead $\hat{G}(\omega_x) = A_g^{-1} e^{j\theta_g}$.

(b) It was shown that integrator bias errors appear in the closed-loop error as an additional disturbance at the reference frequency. The amplitude of this disturbance is $A_x A_n/2$ where A_x is the amplitude of the reference signal and A_n is the effective amplitude of the in-phase and quadrature bias errors. When combined with a leaky FXLMS filter, which has limited gain at the reference frequency, the bias error can affect the closed-loop cancellation.

(c) It was shown that phase errors in the quadrature filters appear as a multiplicative error at the reference frequency. The magnitude of the multiplicative error is small for typical phase errors, *e.g.* -21 dB for a 5° mistuning. This indicates that, at the reference frequency, phase errors do not raise stability-robustness concerns and they have little effect on performance.

(d) It was shown that phase errors in the quadrature filters can have a significant effect on the adaptive filter's output at frequencies other than the reference frequency. The output then includes frequency-shifted components in addition to the linear response. For example, if the linear component's frequency is $\omega_x + \Delta\omega$, then the most significant nonlinear component appears at $\omega_x - \Delta\omega$, *i.e.* the linear response is mirrored about the reference frequency. The ratio of the nonlinear component's amplitude to the linear component's amplitude is given by the magnitude of the multiplicative error. Large in-band disturbances can therefore result in significant harmonic distortion of the FXLMS filter's output.

(e) It was shown that a reference signal that includes higher harmonics of the fundamental reference frequency ω_x creates nonlinear frequency-shifted components in the filter's output in much the same way as quadrature phase errors.

(f) It was shown that the need to gain-stabilize plant poles limits the closed-

loop cancellation of a leaky FXLMS filter. For example, with the second-order highpass actuator model, the maximum loop gain at the reference frequency is $(\omega_c/\omega_p)/(\zeta_c/\zeta_p)$ where the subscript c denotes compensator and the subscript p denotes plant. The cancellation may be improved by changing the frequency separation, ω_c/ω_p, by changing the damping-ratio quotient, ζ_c/ζ_p, or more drastically, by modifying the loop dynamics.

10. An analog circuit implementation of a two-weight narrowband FXLMS adaptive filter was designed, with particular attention given to the quadrature filters and to the generation of a harmonic reference signal. It was confirmed that the input-output behavior of this adaptive filter is well-approximated by a linear bandpass transfer function. The effect of quadrature phase error and of a periodic reference signal was experimentally investigated; good agreement with the analysis was found.

11. A modular cancellation system based on two-weight FXLMS controllers was fabricated and demonstrated. The system includes error filters to reduce the high-frequency content of the error signals, which had been a problem with the expander's impulsive vibration. The system also includes compensation filters to minimize the effect of the resonances in the actuator dynamics. Each two-weight FXLMS controller may be assigned to an arbitrary axis and an arbitrary harmonic, allowing a multi-axis, multi-harmonic cancellation system to be built up. The number of controllers may be easily varied to match the resources and requirements of a particular application.

12. The performance of the system was demonstrated in a variety of tests:

    (a) Single-axis, single-harmonic cancellation verified that despite all the nonlinearities in the system, there was little coupling between the harmonics. The strongest harmonic coupling consistently appeared between the first and second axial harmonics, which was attributed to the nonlinear actuator dynamics and the relative amplitudes of these two harmonics in the

cooler's axial vibration. The coupling resulted in 2–8 dB of cancellation at the second harmonic due to the first-harmonic controller.

(b) Single-axis cancellation revealed significant coupling between the axes. Although the actuator's off-diagonal response was roughly 25 dB below the diagonal response, the open-loop lateral vibration was also much smaller than the open-loop axial vibration. The combination of the actuator's coupling and the disparate open-loop vibration levels was shown to account for the observed cross-axis cancellation.

(c) Based on the system's measured transient response, the weights of the adaptive filter were found to converge with a time constant of 0.2 seconds. The system was able to track rapid changes in the cooler's drive frequency. The misadjustment error during tracking appeared to be proportional to the speed of the frequency changes.

(d) Because of poor tuning of the compensation filter, significant interaction occurred between the actuator's lateral dynamics and the lateral first-harmonic controllers. Indeed, the system was unstable for certain ranges of the cooler's drive frequency. The instability brought out the controller's nonlinear response. The lateral resonance provided a large-amplitude in-band disturbance at a frequency other than the reference frequency. Although cancellation was achieved at the reference frequency, the lateral resonance was amplified, and the lateral harmonic mirrored about the reference frequency was unstable. The filter weights did not converge to a constant value. Instead they varied sinusoidally at a frequency equal to the difference between the reference frequency and the lateral resonance. Due to the large amplitudes involved, several of the nonlinear components about the reference frequency were clearly visible (the analysis only included the dominant nonlinear component). The response at the second, third, and fourth harmonics of the reference frequency was also distorted. This behavior suggests that the narrowband FXLMS controllers must be used with considerable caution when there is the possibility of large in-

band disturbances.

(e) The multi-axis, multi-harmonic system composed of seven FXLMS controllers achieved much the same performance and exhibited basically the same coupling as each of its single-axis, single-harmonic controllers. Despite the coupling, approximately 30 dB of cancellation was achieved at each of the first five axial harmonics, and approximately 20 dB of cancellation was achieved at the fundamental of both lateral torques.

7.3 Recommendations

1. A better understanding is needed of the actual requirements associated with cryogenic optical systems. Mechanical cryocooler technology has developed considerably in the last 5–10 years, presenting the cryosystem designer with many options. Spacecraft design philosophy has also changed dramatically, as "cheaper, faster, better" missions and micro-spacecraft proliferate. A useful systems-level study might consider several classes of cryogenic instruments, such as moderate resolution survey instruments and high-resolution research instruments, as well as considering a range of cryocoolers, including low-capacity tactical coolers and high-capacity long-life coolers. A realisitic assessment of the need for vibration reduction systems could then be made. A variety of cryosystem integration issues could also be addressed:

   - Is this a single-axis problem? A three-axis problem? A six-axis problem?
   - How much passive isolation can be added to the system?
   - Is foundation flexibility a significant issue?
   - Is it worthwhile to incorporate the vibration reduction system into the cooler design?
   - Can performance be better matched to requirements through the use of a modular add-on system?
   - How much computational power is available? Are DSPs an option?

2. The vibration cancellation system presented in this thesis represents a proof-of-concept for a simple system that can be added to almost any split Stirling cooler. If there is a need for such a system, justifying further development, several areas deserve attention.

   (a) The flexures in the actuator need to be redesigned. At the very least, substantial levels of passive damping should be added. The cause of the actuator nonlinearity (the axial restraint of the flexures) can be greatly reduced by adding vertical relief flexures.

   (b) The possibility of replacing the load cells with accelerometers mounted on the expander should be considered, as this would further simplify integration with an existing cryosystem. Expected acceleration levels for typical mounting structures must be computed and compared with the sensitivity of available accelerometers. During testing, the use of additional sensors would verify that by reducing the error signals, the vibration cancellation system is indeed reducing the vibration transmitted to the focal plane.

   (c) Substantial miniaturization of the controllers is feasible. Application-specific ICs that incorporate the multiplier-integrator-multiplier functions of the error path should be easy to build. A more challenging approach would be to reduce the entire two-weight controller to a single chip; this could take advantage of the exisiting switched-capacitor LMS filter designs. Finally, the use of some digital components might simplify certain tasks, especially the generation of clean reference harmonics.

3. The analysis of the stochastic behavior of the LMS filter appears to be more advanced than the frequency-domain analysis. Establishing a closer connection between these two descriptions of the same algorithm would make available the stochastic results regarding, for example, misadjustment or the effect of noisy signals. Presently there appears to be considerable conservatism in these expressions when applied to the narrowband FXLMS filter.

4. The two-weight filtered-x LMS controller is a basic adaptive filter that achieves

good levels of performance in the vibration cancellation application. It might be possible to achieve better performance with some of the more sophisticated filters. Options include multi-weight filters (which might reduce the nonlinear components in the controller output), multiple-error filters (which might be able to account for the cross-axis coupling), and even Volterra LMS filters (which might be useful for much greater levels of actuator nonlinearity). The field of adaptive signal processing has in no sense converged on a single approach to adaptive filtering; a wide variety of techniques are under development, and new designs are always appearing. As the pitfalls and merits of the various algorithms and implementations are understood, the advanced filters should be considered for use in the vibration cancellation system.

References

[1] R. A. Hopkins, J. H. Lee, R. L. Oonk, C. D. Miller, and S. J. Nieczkoski, "Long-Lifetime Stored Cryogen Systems Using Refrigerators to Reduce Parasitic Heat Input," *Proceedings of the Sixth International Cryocoolers Conference*, G. Green and M. Knox, eds., Plymouth, MA, October 25–26, 1990, Vol. I, pp. 153–171.

[2] W. W. Burt, "Cooling of Very Large Focal Plane Arrays," *Advances in Cryogenic Engineering*, R. W. Fast, ed., Vol. 35, Part A, 1990, pp. 865–879.

[3] R. G. Ross, Jr., "Requirements for Long-Life Mechanical Cryocoolers for Space Application," *Cryogenics*, Vol. 30, No. 3, March 1990, pp. 233–238.

[4] R. J. Glaser, R. G. Ross, Jr., and D. L. Johnson, "Cryocooler Tip Motion Suppression Using Active Control of Piezoelectric Actuators," presented at the 7th International Cryocooler Conference, Santa Fe, NM, November 17–19, 1992.

[5] F. Stolfi, M. Goldowsky, J. Ricciardelli, and P. Shapiro, "A Magnetically Suspended Linearly Driven Cryogenic Refrigerator," *Refrigerators for Cryogenic Sensors*, M. Gasser, ed., NASA CP-2287, 1983, pp. 263–303.

[6] J. L. Miller, "Key Attributes and Generic Requirements for Cryocooler Application on Microsats," *Proceedings of the Sixth International Cryocoolers Conference*, G. Green and M. Knox, eds., Plymouth, MA, October 25–26, 1990, Vol. II, pp. 285–293.

[7] S. T. Werrett and G. D. Peskett, "The Pressure Modulators, Closed Cycle Coolers and Detector Cooling System in ISAMS," *Instrumentation for Optical Remote Sensing from Space*, J. S. Seeley, J. W. Lear, A. Monfils, and S. L. Russak, eds., Proc. SPIE 589, 1985, pp. 96–103.

[8] R. Boyle, E. James, P. Miller, V. Arillo, L. Sparr, and S. Castles, "Structural and Thermal Interface Characteristics of Stirling Cycle Cryocoolers for Space Applications," *Advances in Cryogenic Engineering*, R. W. Fast, ed., Vol. 37, Part B, 1992, pp. 1063–1068.

[9] L. M. Sparr, M. Schien, and L. Nuygen, "Design and Test of Potential Cryocooler Coldfinger Interfaces," presented at the Cryogenic Engineering Conference, Albuquerque, NM, July 12 16, 1993.

[10] A. Sherman, "History, Status and Future Applications of Spaceborne Cryogenic Systems," *Advances in Cryogenic Engineering*, R. W. Fast, ed., Vol. 27, 1982, pp. 1007–1029.

[11] E. Lindale and D. Lehrfeld, "Life Test Performance of a Philips Rhombic-Drive Refrigerator with Bellows Seals," *Refrigerators for Cryogenic Sensors*, M. Gasser, ed., NASA CP-2287, 1983, pp. 197–213.

[12] G. R. Pruitt, "Reliability Growth of Coolers for Advanced Optical Systems and Instruments," *Cryogenic Optical Systems and Instruments IV*, R. K. Melugin and G. R. Pruitt, eds., Proc. SPIE 1340, 1990, pp. 311–324.

[13] A. Sherman, M. Gasser, M. Goldowsky, G. Benson, and J. McCormick, "Progress on the Development of a 3- to 5-Year Lifetime Stirling Cycle Refrigerator for Space," *Advances in Cryogenic Engineering*, K. D. Timmerhaus and H. A. Snyder, eds., Vol. 25, 1980, pp. 791–800.

[14] W. J. Gully and M. W. Hanes, "Vibration Characteristics of Small Rotary and Linear Cryogenic Coolers for IR Systems," *Proceedings of the Sixth International Cryocoolers Conference*, G. Green and M. Knox, eds., Plymouth, MA, October 25–26, 1990, Vol. II, pp. 85–96.

[15] C. Minas and R. A. Ackermann, "Dynamically Balanced Gifford-McMahon Cold Head," presented at the Cryogenic Engineering Conference, Albuquerque, NM, July 12–16, 1993.

[16] T. Ellis, R. Drake, A. M. Fowler, I. Gatley, J. Heim, R. Luce, K. M. Merrill, R. Probst, and N. Buchholz, "The Simultaneous Quad-Color Infrared Imaging Device (SQIID): A Leap Forward in Infrared Cameras for Astronomy," *Cryogenic Optical Systems and Instruments V*, R. K. Melugin, ed., Proc. SPIE 1765, 1992, pp. 94–106.

[17] G. Davey, "The Oxford University Miniature Cryogenic Refrigerator," *International Conference on Advanced Infrared Detectors and Systems*, London, UK, October 29–30, 1981, IEE Conf. Publ. No. 204, p. 39.

[18] R. G. Ross, Jr., D. L. Johnson, and R. S. Sugimura, "Characterization of Miniature Stirling-Cycle Cryocoolers for Space Application," *Proceedings of the Sixth International Cryocoolers Conference*, G. Green and M. Knox, eds., Plymouth, MA, October 25–26, 1990, Vol. I, pp. 27–38.

[19] R. G. Ross, Jr., D. L. Johnson, and V. Kotsubo, "Vibration Characterization and Control of Miniature Stirling-Cycle Cryocoolers for Space Application,"

Advances in Cryogenic Engineering, R. W. Fast, ed., Vol. 37, Part B, 1992, pp. 1019–1027.

[20] D. Lehrfeld, "Split-Stirling, Linear-Resonant, Cryogenic Refrigerators for Detector Cooling," *Refrigerators for Cryogenic Sensors*, M. Gasser, ed., NASA CP-2287, 1983, pp. 215–229.

[21] R. C. Tipton, "Development of Stirling Cycle Cooler and Integration of This Cooler Into a Biological Storage Freezer," *Proceedings of the Sixth International Cryocoolers Conference*, G. Green and M. Knox, eds., Plymouth, MA, October 25–26, 1990, Vol. I, pp. 217–229.

[22] W. Newman and C. S. Keung, "A 10°K [sic] Triple-Expansion Stirling-Cycle Cryocooler," *Refrigerators for Cryogenic Sensors*, M. Gasser, ed., NASA CP-2287, 1983, pp. 141–156.

[23] B. G. Johnson, F. J. Flynn, M. S. Gaffney, D. L. Johnson, and R. G. Ross, Jr., "Demonstration of Active Vibration Control on a Stirling-Cycle Cryocooler Testbed," *Proceedings of the 1992 American Control Conference*, Vol. 2, Chicago, IL, June 24–26, 1992, pp. 1630–1631.

[24] B. G. Jones and S. R. Scull, "Development and Preflight Qualification Testing of a Range of Cryogenic Coolers for Applications from 20 K to 80 K," *Cryogenics*, Vol. 32, No. 10, 1992, pp. 850–858.

[25] J.-N. Aubrun, R. R. Clappier, K. R. Lorell, T. C. Nast, and P. J. Reshatoff, Jr., "A High-Performance Force Cancellation Control System for Linear-Drive Split-Cycle Stirling Cryocoolers," *Advances in Cryogenic Engineering*, R. W. Fast, ed., Vol. 37, Part B, 1992, pp. 1029–1036.

[26] R. G. Ross, Jr., D. L. Johnson, G. R. Mon, and G. Smedley, "Cryocooler Resonance Characterization," presented at the 1993 Space Cryogenics Workshop, San Jose, CA, July 20–21, 1993.

[27] D. L. Johnson, G. R. Mon, and R. G. Ross, Jr., "Spacecraft Cooler Characterization," presented at the 7th International Cryocooler Conference, Santa Fe, NM, November 17–19, 1992.

[28] Y.-W. A. Wu, "Demonstration of Active Vibration Control on the Hughes Cryocooler Testbed," *Proceedings of the 31st IEEE Conference on Decision and Control*, Tucson, AZ, December 16–18, 1992, Vol. 3, pp. 2580–2585.

[29] Y.-W. A. Wu, "Active Vibration Control Algorithm for Cryocooler Systems," presented at the Cryogenic Engineering Conference, Albuquerque, NM, July 12–16, 1993.

[30] M. Obal and J. M. Sater, "Adaptive Structures for Space-Based Defense Systems," presented at the 44th International Astronautical Federation Congress, Graz, Austria, October 16–22, 1993, Paper No. IAF-93-I.5-244.

[31] M. T. Chahine, H. H. Aumann, R. D. Haskins, F. G. O'Callaghan, R. A. Schindler, R. J. Pagano, and R. W. Capps, "The Atmospheric Infrared Sounder," presented at the 28th AIAA Aerospace Sciences Meeting, Reno, NV, January 8–11, 1990, Paper No. AIAA-90-0261.

[32] G. H. Blackwood, "Active Vibration Isolation for Controlled Flexible Structures," Ph.D. Thesis, Massachusetts Institute of Technology, Cambridge, MA, February 1994.

[33] R. Pagano and M. Hatch, "A Multi-Aperture Spectrometer Design for the Atmospheric Infrared Sounder (AIRS)," *International Lens Design Conference*, G. N. Lawrence, ed., Monterey, CA, June 11–14, 1990, Proc. SPIE 1354, pp. 460–471.

[34] *AIRS System Requirements Review*, Loral Infrared & Imaging Systems, Lexington, MA, October 29–30, 1991.

[35] A. K. de Jonge, "Small Split Stirling Coolers for I.R. Detectors," *International Conference on Advanced Infrared Detectors and Systems*, London, UK, October 29–30, 1981, IEE Conf. Publ. No. 204, pp. 55–59.

[36] R. G. Ross, Jr., D. L. Johnson, and V. Y. Kotsubo, "BAe 80 K Stirling Cooler Performance Characterization," JPL Internal Report D-9912, Jet Propulsion Laboratory, Pasadena, CA, May 1992.

[37] R. L. Berry, Electron Dynamics Division, Hughes Aircraft Company, personal communication, April 1992.

[38] G. H. Blackwood and A. H. von Flotow, "Active Control for Vibration Isolation Despite Resonant Structural Dynamics: A Trade Study of Sensors, Actuators and Configurations," *Second Conference on Recent Advances in Active Control of Sound and Vibration*, R. A. Burdisso, ed., Blacksburg, VA, April 28–30, 1993, pp. 482–494.

[39] B. G. Watters, R. B. Coleman, G. L. Duckworth, and E. F. Berkman, "A Perspective on Active Machinery Isolation," *Proceedings of the 27th IEEE Conference on Decision and Control*, Austin, TX, December 7–9, 1988, Vol. 3, pp. 2033–2038.

[40] G. R. Slemon, *Magnetoelectric Devices: Transducers, Transformers, and Machines*, John Wiley & Sons, Inc., New York, 1966.

[41] R. L. Hollis, S. E. Salcudean, and A. P. Allan, "A Six-Degree-of-Freedom Magnetically Levitated Variable Compliance Fine-Motion Wrist: Design, Modeling, and Control," *IEEE Transactions on Robotics and Automation*, Vol. 7, No. 3, June 1991, pp. 320–332.

[42] P. Horowitz and W. Hill, *The Art of Electronics*, 2nd ed., Cambridge University Press, Cambridge, U. K., 1989.

[43] *Products for Micropositioning*, Catalogue 108, Edition E, Physik Instrumente, Waldbronn, Germany, 1990.

[44] K. L. Napolitano, A. H. von Flotow, and E. M. Austin, "Adaptive Vibration Suppression Mount for Cryogenic Coolers," Report No. 93-06-01, CSA Engineering, Inc., Palo Alto, CA, June 1993.

[45] D. I. Jones, A. R. Owens, and R. G. Owen, "A Microgravity Isolation Mount," *Acta Astronautica*, Vol. 15, No. 6/7, June/July 1987, pp. 441–448.

[46] R. C. Fenn, J. R. Downer, V. Gondhalekar, and B. G. Johnson, "An Active Magnetic Suspension for Space-Based Microgravity Vibration Isolation," *Active Noise and Vibration Control—1990*, G. E. Warnaka, C. Radcliffe, and A. H. von Flotow, eds., NCA-Vol. 8, 1990, pp. 49–56.

[47] T. Higuchi, M. Tsuda, and S. Fujiwara, "Magnetic Supported Intelligent Hand for Automated Precise Assembly," *IECON '87: Automated Design and Manufacturing*, H. Y. K. Wo and V. K. L. Huang, eds., Proc. SPIE 857, 1987, pp. 926–933.

[48] W. H. Hayt, Jr., *Engineering Electromagnetics*, 4th ed., McGraw-Hill Book Co., New York, 1981.

[49] *High Performance Permanent Magnets*, Catalog 1, Magnet Sales & Mfg. Co., Culver City, CA, 1990.

[50] W. Morris, Electronic Equipment Engineering and Fabrication Section, Jet Propulsion Laboratory, personal communication, July 1992.

[51] P. H. Estes and A. E. Kettner, "Electrical Properties," *ASME Handbook of Metals Engineering—Design*, 2nd ed., O. J. Horger, ed., McGraw-Hill Book Co., New York, 1965.

[52] W. A. Nash, *Theory and Problems of Strength of Materials*, 2nd ed., Schaum's Outline Series, McGraw-Hill Book Co., Inc., New York, 1972.

[53] R. J. Roark, *Formulas for Stress and Strain*, 4th ed., McGraw-Hill Book Co., Inc., New York, 1965.

[54] R. D. Blevins, *Formulas for Natural Frequency and Mode Shape*, Robert E. Krieger Publishing Co., Inc., Malabar, FL, 1979.

[55] *Apex Hybrid & IC Handbook*, Vol. V, Apex Microtechnology Corp., Tucson, AZ, 1991.

[56] S. Woinowsky-Krieger, "The Effect of an Axial Force on the Vibration of Hinged Bars," *Journal of Applied Mechanics*, Vol. 17, No. 1, March 1950, pp. 35–36.

[57] A. V. Srinivasan, "Large Amplitude-Free Oscillations of Beams and Plates," *AIAA Journal*, Vol. 3, No. 10, October 1965, pp. 1951–1953.

[58] P. H. McDonald, Jr., "Nonlinear Dynamic Coupling in a Beam Vibration," *Journal of Applied Mechanics*, Vol. 22, No. 4, December 1955, pp. 573–578.

[59] J. A. Bennett and J. G. Eisley, "A Multiple Degree-of-Freedom Approach to Nonlinear Beam Vibrations," *AIAA Journal*, Vol. 8, No. 4, April 1970, pp. 734–739.

[60] W.-Y. Tseng and J. Dugundji, "Nonlinear Vibrations of a Buckled Beam Under Harmonic Excitation," *Journal of Applied Mechanics*, Vol. 38, No. 2, June 1971, pp. 467–476.

[61] A. H. Nayfeh, D. T. Mook, and S. Sridhar, "Nonlinear Analysis of the Forced Response of Structural Elements," *Journal of the Acoustical Society of America*, Vol. 55, No. 2, February 1974, pp. 281–291.

[62] W. E. Baker, "Vibration Frequencies for Uniform Beams with Central Masses," *Journal of Applied Mechanics*, Vol. 31, No. 2, June 1964, pp. 335–337.

[63] F. J. Shaker, "Effect of Axial Load on Mode Shapes and Frequencies of Beams," NASA TN D-8109, Lewis Research Center, Cleveland, OH, December 1975.

[64] H. Saito, K. Sato, and T. Yutani, "Non-Linear Forced Vibrations of a Beam Carrying Concentrated Mass Under Gravity," *Journal of Sound and Vibration*, Vol. 46, No. 4, June 22, 1976, pp. 515–525.

[65] M. Urabe, "Galerkin's Procedure for Nonlinear Periodic Systems," *Archive for Rational Mechanics and Analysis*, Vol. 20, 1965, pp. 120–152.

[66] L. Meirovitch, *Analytical Methods in Vibrations*, Macmillan Publishing Co., Inc., New York, 1967.

[67] Y. Ueda, "Explosion of Strange Attractors Exhibited by Duffing's Equation," *Annals of the New York Academy of Sciences*, Vol. 357, December 26, 1980, pp. 422-434.

[68] C. Hayashi, *Nonlinear Oscillations in Physical Systems*, McGraw-Hill Book Co., New York, 1964.

[69] W. Y. Tseng and J. Dugundji, "Nonlinear Vibrations of a Beam Under Harmonic Excitation," *Journal of Applied Mechanics*, Vol. 37, No. 2, June 1970, pp. 292–297.

[70] A. H. Nayfeh and D. T. Mook, *Nonlinear Oscillations*, John Wiley & Sons, Inc., New York, 1979.

[71] D. W. Jordan and P. Smith, *Nonlinear Ordinary Differential Equations*, 2nd ed., Oxford University Press, Oxford, 1987.

[72] W. Weaver, Jr., S. P. Timoshenko, and D. H. Young, *Vibration Problems in Engineering*, 5th ed., John Wiley & Sons, Inc., New York, 1990.

[73] W. Szemplińska-Stupnicka, "Higher Harmonic Oscillations in Heteronomous Non-Linear Systems with One Degree of Freedom," *International Journal of Non-Linear Mechanics*, Vol. 3, No. 1, 1968, pp. 17–30.

[74] J. C. Burgess, "Existence and Stability of Ultraharmonics and Subharmonics in Forced Nonlinear Oscillations (Discussion)," *Journal of Applied Mechanics*, Vol. 22, No. 2, June 1955, pp. 280–282.

[75] E. Bedrosian and S. O. Rice, "The Output Properties of Volterra Systems (Nonlinear Systems with Memory) Driven by Harmonic and Gaussian Inputs," *Proceedings of the IEEE*, Vol. 59, No. 12, December 1971, pp. 1688–1707.

[76] J. J. Bussgang, L. Ehrman, and J. W. Graham, "Analysis of Nonlinear Systems with Multiple Inputs," *Proceedings of the IEEE*, Vol. 62, No. 8, August 1974, pp. 1088–1119.

[77] S. Boyd, Y. S. Tang, and L. O. Chua, "Measuring Volterra Kernels," *IEEE Transactions on Circuits and Systems*, Vol. CAS-30, No. 8, August 1983, pp. 571–577.

[78] S. J. Gifford and G. R. Tomlinson, "Recent Advances in the Application of Functional Series to Non-Linear Structures," *Journal of Sound and Vibration*, Vol. 135, No. 2, December 8, 1989, pp. 289–317.

[79] D. M. Storer and G. R. Tomlinson, "Recent Developments in the Measurement and Interpretation of Higher Order Transfer Functions from Non-Linear Structures," *Mechanical Systems and Signal Processing*, Vol. 7, No. 2, March 1993, pp. 173–189.

[80] H. Zhang and S. A. Billings, "Analysing Non-Linear Systems in the Frequency Domain—I. The Transfer Function," *Mechanical Systems and Signal Processing*, Vol. 7, No. 6, November 1993, pp. 531–550.

[81] S. A. Billings, "Identification of Nonlinear Systems—A Survey," *IEE Proceedings*, Vol. 127, Part D, No. 6, November 1980, pp. 272–285.

[82] J. S. Bendat, *Nonlinear System Analysis and Identification from Random Data*, John Wiley & Sons, Inc., New York, 1990.

[83] J. Y. Hong, Y. C. Kim, and E. J. Powers, "On Modeling the Nonlinear Relationship Between Fluctuations with Nonlinear Transfer Functions," *Proceedings of the IEEE*, Vol. 68, No. 8, August 1980, pp. 1026–1027.

[84] L. A. Sievers and A. H. von Flotow, "Comparison and Extensions of Methods for Cancellation of Periodic Noise," *IEEE Transactions on Signal Processing*, Vol. 40, No. 10, October 1992, pp. 2377–2391.

[85] A. Gelb and W. E. Vander Velde, ***Multiple-Input Describing Functions and Nonlinear System Design***, McGraw-Hill Book Co., Inc, New York, 1968.

[86] B. Widrow and S. D. Stearns, *Adaptive Signal Processing*, Prentice-Hall, Inc., Englewood Cliffs, NJ, 1985.

[87] N. Wiener, *Extrapolation, Interpolation, and Smoothing of Stationary Time Series*, John Wiley & Sons, Inc., New York, 1949.

[88] R. G. Brown and P. Y. C. Hwang, *Introduction to Random Signals and Applied Kalman Filtering*, John Wiley & Sons, Inc., New York, 1992.

[89] B. Widrow and M. E. Hoff, "Adaptive Switching Circuits," *1960 IRE WESCON Convention Record*, Part 4, Los Angeles, CA, August 23–26, 1960, pp. 96–104.

[90] S. Karni and G. Zeng, "The Analysis of the Continuous-Time LMS Algorithm," *IEEE Transactions on Acoustics, Speech, and Signal Processing*, Vol. ASSP-37, No. 4, April 1989, pp. 595–597.

[91] D. R. Morgan, "An Analysis of Multiple Correlation Cancellation Loops with a Filter in the Auxiliary Path," *IEEE Transactions on Acoustics, Speech, and Signal Processing*, Vol. ASSP-28, No. 4, August 1980, pp. 454–467.

[92] J. C. Burgess, "Active Sound Control in a Duct: A Computer Simulation," *Journal of the Acoustical Society of America*, Vol. 70, No. 3, September 1981, pp. 715–726.

[93] B. Widrow, D. Schur, and S. Shaffer, "On Adaptive Inverse Control," *Conference Record of the 15th Asilomar Conference on Circuits, Systems & Computers*, Pacific Grove, CA, November 8–11, 1981, pp. 185–189.

[94] J. R. Glover, Jr., "Adaptive Noise Canceling Applied to Sinusoidal Interferences," *IEEE Transactions on Acoustics, Speech, and Signal Processing*, Vol. ASSP-25, No. 6, December 1977, pp. 484–491.

[95] S. J. Elliott, I. M. Stothers, and P. A. Nelson, "A Multiple Error LMS Algorithm and Its Application to the Active Control of Sound and Vibration," *IEEE Transactions on Acoustics, Speech, and Signal Processing*, Vol. ASSP-35, No. 10, October 1987, pp. 1423–1434.

[96] H. W. Bode, *Network Analysis and Feedback Amplifier Design*, D. Van Nostrand Co., Inc., Princeton, NJ, 1945.

[97] J. S. Freudenberg and D. P. Looze, "Right Half Plane Poles and Zeros and Design Tradeoffs in Feedback Systems," *IEEE Transactions on Automatic Control*, Vol. AC-30, No. 6, June 1985, pp. 555–565.

[98] D. R. Morgan and J. Thi, "A Multitone Pseudocascade Filtered-X LMS Adaptive Notch Filter," *IEEE Transactions on Signal Processing*, Vol. 41, No. 2, February 1993, pp. 946–956.

[99] B. Widrow, "Adaptive Filters," in *Aspects of Network and System Theory*, R. E. Kalman and N. DeClaris, eds., Holt, Rinehart and Winston, Inc., New York, 1971, pp. 563–587.

[100] P. Kabal, "The Stability of Adaptive Minimum Mean Square Error Equalisers Using Delayed Adjustment," *IEEE Transactions on Communications*, Vol. COM-31, 1983, pp. 430–432.

[101] S. R. Hall, and N. M. Werely, "Performance of Higher Harmonic Control Algorithms for Helicopter Vibration Reduction," *Journal of Guidance, Control, and Dynamics*, Vol. 16, No. 4, July-August 1993, pp. 793–797.

[102] P. A. Nelson and S. J. Elliott, *Active Control of Sound*, Academic Press Ltd., London, 1992.

[103] S. D. Snyder and N. Tanaka, "Modification to Overall System Response When Using Narrowband Adaptive Feedforward Control Systems," *Journal of Dynamic Systems, Measurement, and Control*, Vol. 115, No. 4, December 1993, pp. 621–626.

[104] K. B. Scribner, L. A. Sievers, and A. H. von Flotow, "Active Narrow Band Vibration Isolation of Machinery Noise from Resonant Substructures," *Active Noise and Vibration Control–1990*, G. E. Warnaka, C. Radcliffe, and A. H. von Flotow, eds., NCA-Vol. 8, 1990, pp. 101–111.

[105] M. J. Shensa, "Non-Wiener Solutions of the Adaptive Noise Canceller with a Noisy Reference," *IEEE Transactions on Acoustics, Speech, and Signal Processing*, Vol. ASSP-28, No. 4, August 1980, pp. 468–473.

[106] H. M. Chen and P. Lewis, "Adaptive Control for a Vibration Isolation Mount," *Active Noise and Vibration Control–1990*, G. E. Warnaka, C. Radcliffe, and A. H. von Flotow, eds., NCA-Vol. 8, 1990, pp. 121–124.

[107] L. W. Massengill and D. B. Mundie, "An Analog Neural Hardware Implementation Using Charge-Injection Multipliers and Neuron-Specific Gain Control," *IEEE Transactions on Neural Networks*, Vol. 3, No. 3, May 1992, pp. 354–362.

[108] U. Menzi and G. S. Moschytz, "Adaptive Switched-Capacitor Filters Based on the LMS Algorithm," *IEEE Transactions on Circuits and Systems—I. Fundamental Theory and Applications*, Vol. 40, No. 12, December 1993, pp. 929–942.

[109] H. Qiuting and G. S. Moschytz, "Analog Multiplierless LMS Adaptive FIR Filter Structures," *IEEE Transactions on Circuits and Systems—II. Analog and Digital Signal Processing*, Vol. 40, No. 12, Dec. 1993, pp. 790–794.

[110] S. J. Elliott, P. A. Nelson, and I. M. Stothers, "Active Vibration Control," International Patent, WO 88/02912, April 21, 1988.

[111] M. E. Van Valkenburg, *Analog Filter Design*, Holt, Rinehart and Winston, Inc., New York, 1982.

[112] D. H. Sheingold, ed., *Nonlinear Circuits Handbook*, Analog Devices, Inc., Norwood, MA, 1976.

[113] D. R. Morgan and C. Sanford, "A Control Theory Approach to the Stability and Transient Analysis of the Filtered-X LMS Adaptive Notch Filter," *IEEE Transactions on Signal Processing*, Vol. 40, No. 9, September 1992, pp. 2341–2346.

[114] J. C. Lee and C. K. Un, "Performance of Transform-Domain LMS Adaptive Digital Filters," *IEEE Transactions on Acoustics, Speech, and Signal Processing*, Vol. ASSP-34, No. 3, June 1986, pp. 499–510.

[115] B. Widrow, J. M. McCool, M. G. Larimore, and C. R. Johnson, Jr., "Stationary and Nonstationary Learning Characteristics of the LMS Adaptive Filter," *Proceedings of the IEEE*, Vol. 64, No. 8, August 1976, pp. 1151-1162.

[116] D. C. Farden, "Tracking Properties of Adaptive Signal Processing Algorithms," *IEEE Transactions on Acoustics, Speech, and Signal Processing*, Vol. ASSP-29, No. 3, June 1981, pp. 439–446.

[117] B. Widrow and E. Walach, "On the Statistical Efficiency of the LMS Algorithm with Nonstationary Inputs," *IEEE Transactions on Information Theory*, Vol. IT-30, No. 2, March 1984, pp. 211–221.

[118] W. A. Gardner, "Nonstationary Learning Characteristics of the LMS Algorithm," *IEEE Transactions on Circuits and Systems*, Vol. CAS-34, No. 10, October 1987, pp. 1199–1207.

[119] W. J. Gully, "Closed Loop Temperature Control for IR System Applications," *Proceedings of the 5th International Cryocooler Conference*, Monterey, CA, 1988, pp. 227–241.